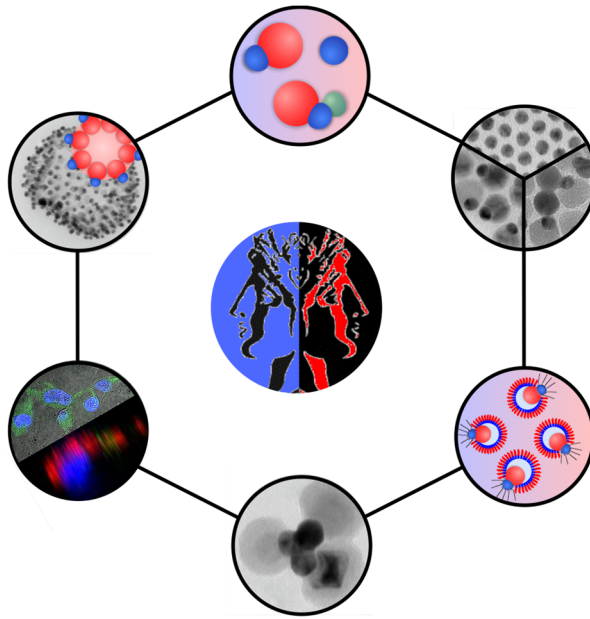


# Design of Multifunctional Janus Particles for Biomedical Applications



## Dissertation

zur Erlangung des Grades  
„Doktor der Naturwissenschaften“  
im Promotionsfach Chemie

am Fachbereich Chemie, Pharmazie und Geowissenschaften  
der Johannes Gutenberg-Universität Mainz

*Dipl.-Chem. Isabel Schick*

geb. in Wiesbaden

Mainz, 2014

Dekan:

Erster Berichterstatter:

Zweiter Berichterstatter:

Datum der mündlichen Prüfung: 13.10.2014

Die hier vorliegende Arbeit wurde in der Zeit von Oktober 2011 bis August 2014 unter der Leitung von HERRN PROF. DR. [REDACTED] und HERRN PROF. DR. [REDACTED] am Institut für Anorganische Chemie und Analytische Chemie der Johannes Gutenberg-Universität Mainz angefertigt.



*Für meine Familie*

# Abstract

Inspired by recent advancements in the synthesis and design of hetero-nanoparticles, Janus particles have become the focus of scientific attention due to their outstanding properties. Novel optical, electronic, magnetic, and superficial properties emerge in inorganic Janus particles from their unique morphology at nanoscale, as they exhibit two physically and chemically distinct surfaces, which are interconnected by solid state interfaces: (i) their multifunctionality arises from the different surface chemistry of the chosen components, enabling separate and selective surface functionalization in addition to the intrinsic multifunctionality, (ii) directed self-assembly is achieved by orthogonal functionalization of the surfaces, and (iii) their efficient interaction across the solid state interface facilitates the emergence of synergistically enhanced or even additional characteristics, which would not be accessible using single-component materials.

The present work focusses on multifunctional Janus particles and is as multi-faceted as the nanoparticles of interest. It combines the synthesis and comprehensive analysis from a chemist's viewpoint with initial results on biomedical applications. The synthesis of a variety of monodisperse multifunctional Janus particles was designed as a seed-mediated nucleation and growth process. The heterodimer nanoparticles were built up from a metal and a metal oxide domain. Here, Au, Pt, and their alloy were each chosen due to their high X-ray attenuation, making them useful for applications as computed X-ray tomography (CT) contrast agents. The unique magnetic behavior of MnO and Fe<sub>3</sub>O<sub>4</sub>, which leads to a shortening of the longitudinal and transverse relaxation time in magnetic resonance imaging (MRI), respectively, motivated their use. In particular, size and morphology of the individual domains, which were analyzed by means of (HR) TEM, DLS, UV-VIS and FT-IR spectroscopy, as well as magnetic measurements, could be precisely controlled by adjustment of the synthetic parameters. High resolution synchrotron powder diffraction was used for quantitative phase analysis of the heterodimer nanoparticles. Further, the metal oxide domains could be selectively coated with a thin silica layer, leaving the metal domain untouched. This coating enabled the efficient incorporation of fluorescent dyes and provided solubility as well as colloidal stability in polar solvents, as confirmed by dynamic light scattering. Time-resolved fluorescence spectroscopy negated an electronic interaction of the metal domains with the incorporated dyes, while confocal laser scanning microscopy revealed the particles to be highly two-photon active. These results suggest our multifunctional Janus particles to be efficient vehicles for *theranostics*, which is addressed in the second part.

The investigation of the amphiphilic character of inorganic Janus particles included an analysis of their self-assembly behavior at interfaces as well as of their impact on artificial lipid membranes, which served as a model system for the interaction with the cellular membrane. We were able to provide experimental evidence for Janus particles inducing membrane tubulation, a passive, artificial endocytotic uptake pathway, in tension-free membranes. By virtue of the intrinsic materials' characteristics, the potential of Janus particles for biomedical applications was analyzed regarding their use as multimodal contrast agents for simultaneous diagnosis by MRI and CT. Their contrast-enhancing potential as compared to spherical metal oxide nanoparticles was confirmed in several studies. As a last point, their impact on the cellular metabolism of Caki-1 and HeLa cells as well as HMEC-1 was analyzed by determination of cellular ATP levels, subsequent to investigation of the composition of their hard protein corona by label-free-liquid chromatography mass spectrometry (LC-MS) and their performance in enzyme-mimicking reactions. We show a significant impact of the chemical composition and the corresponding amphiphilic surface functionalization on the protein corona, as well as on the enzyme-like activity in peroxidase tests. Further, surface charge, size, and composition were demonstrated to affect the cell viability, though no increased cytotoxic potential was observed for Janus particles over spherical nanoparticles.

## Zusammenfassung

Die gezielte Weiterentwicklung der Synthese von Hetero-Nanopartikeln führte zur intensiven Erforschung der faszinierenden Eigenschaften von Janus-Partikeln. Ihre besondere Morphologie hinsichtlich der Kombination zweier chemisch oder physikalisch unterschiedlicher Komponenten mit definierter Phasengrenzfläche im Nanometerbereich bietet exzellente Möglichkeiten für die Erschaffung neuartiger optischer, elektronischer, magnetischer Eigenschaften: (i) ihre Multifunktionalität entsteht durch die Realisierbarkeit einer selektiven Adressierung der Oberflächen aufgrund unterschiedlicher chemischer Funktionalität, Reaktivität oder Polarität zusätzlich zur intrinsischen Funktionsvielfalt, (ii) die Kontrolle der Selbstorganisation von Janus-Partikeln kann durch orthogonale Oberflächenfunktionalisierung erzielt werden, und (iii) synergistisch verstärkte sowie neuartige Phänomene, die durch homogene Nanopartikel nicht zu erreichen sind, entstehen durch die effiziente Grenzflächenwechselwirkung der unterschiedlichen Komponenten.

Die vorliegende Arbeit beschäftigt sich mit multifunktionalen Janus-Partikeln und ist ebenso ambivalent wie die genannten Nanopartikel; sie kombiniert die Synthese und umfassende Charakterisierung aus chemischer Sicht mit vielversprechenden Ergebnissen

erster biomedizinischer Anwendungen. Zur Darstellung monodisperser Janus-Partikel, bestehend aus einer Metall- und einer Metalloxidkomponente, wurde eine Saat-Keim-vermittelte Methode entwickelt. Hierbei konnten sowohl die Größe als auch die Morphologie der einzelnen Domänen durch gezielte Anpassung der Syntheseparameter variiert werden. Dies wurde durch (HR) TEM, DLS, UV-VIS und FT-IR Spektroskopie und durch magnetische Messungen bestätigt. Dabei wurden Au, Pt, sowie AuPt aufgrund ihrer starken Absorption von Röntgenstrahlung verwendet, um eine Anwendung als Kontrastmittel für Computertomographie (CT) zu ermöglichen. MnO und Fe<sub>3</sub>O<sub>4</sub> wurden im Hinblick auf ihre besonderen magnetischen Eigenschaften auf Nanometerebene genutzt, die eine Verkürzung der Relaxationszeiten in der Magnetresonanztomographie (MRT) ermöglichen. Rietveld Verfeinerungen hochauflösender Synchrotron-Röntgendiffraktionsdaten wurden zur quantitativen Phasenanalyse verwendet. Aufgrund ihrer chemisch unterschiedlichen Oberflächen konnte die Metalloxidkomponente selektiv mit SiO<sub>2</sub> umhüllt werden, wobei die Funktionalisierung der Metalldomäne unverändert blieb. Die Umhüllung mit SiO<sub>2</sub> ermöglichte die stabile Anbindung von Fluoreszenzfarbstoffen und stellte die Löslichkeit sowie kolloidale Stabilität in polaren Lösungsmitteln sicher, eine grundlegende Voraussetzung für spätere biomedizinische Anwendungen. Zeitaufgelöste Fluoreszenz-Spektroskopie widerlegte eine mögliche elektronische Wechselwirkung zwischen inkorporierten Fluorophoren und den Metalldomänen, während eine starke 2-Photonenaktivität unter Verwendung konfokaler Lasermikroskopie nachgewiesen werden konnte. Dies sind vielversprechende Ergebnisse im Hinblick auf eine Anwendung der multifunktionalen Janus-Partikel als effiziente Trägermaterialien für therapeutische und diagnostische Zwecke, die im zweiten Teil der Arbeit näher untersucht wurden.

Schließlich wurde der amphiphile Charakter der Janus-Partikel einschließlich ihrer Selbstorganisation an Phasengrenzflächen sowie ihr Einfluss auf synthetische Lipidmembranen untersucht. Diese dienen als Modell für die Wechselwirkung mit Zellmembranen. Hierbei konnten wir zeigen, dass Janus-Partikel in spannungsfreien Membranen Tubulationen als künstlichen passiven, endozytotischen Aufnahmeweg hervorrufen. Im Hinblick auf ihre intrinsischen Materialeigenschaften wurde die Eignung der Janus-Partikel als multimodale Kontrastmittel für simultane MRT und CT Untersuchungen analysiert. Verschiedene Studien zeigten eine deutliche Signalverstärkung im Vergleich zu sphärischen Metalloxidnanopartikeln. Die Interaktion mit biologischen Systemen wurde unter drei Aspekten untersucht: die chemische Zusammensetzung der einzelnen Komponenten, sowie die orthogonale Oberflächen-funktionalisierung erwiesen sich als entscheidend (i) für die Zusammensetzung der Proteincorona nach Inkubation mit Blutplasma sowie (ii) für die Aktivität der Partikel in Tests bezüglich ihrer Enzym-ähnlichen Reaktivität. (iii) Darüber hinaus konnte gezeigt werden, dass Oberflächenladung, Größe und chemische Zusammensetzung entscheidende Faktoren für die Zellvitalität und die Beeinflussung des Zellmetabolismus von Caki-1, HeLa und HMEC-1 sind.



# List of Publications

[1] J.J. McDowell, **I. Schick**, A. Price, D. Faulkner, G. Ozin, "Pure Blue Emitting Poly(3,6-dimethoxy-9,9-dialkylsilafluorenes) Prepared via Nickel-Catalyzed Cross-Coupling of Diarylmagnesate Monomers", *Macromolecules* **2013**, *46*, 6794 – 6805.

[2] J. Rother, A. Pietuch, K. Koll, T.D. Schladt, O. Köhler, **I. Schick**, W. Tremel, A. Janshoff, "Enhanced motility of alveolar cancer cells induced by CpG-ODN-functionalized nanoparticles", *Journal of Nanoparticle Research* **2013**, *15*, 2107.

[3] **I. Schick**, S. Lorenz, D. Gehrig, A.-M. Schilman, H. Bauer, M. Panthöfer, K. Fischer, D. Strand, F. Laquai, W. Tremel, "Multifunctional Two-Photon Active Silica-Coated Au@MnO Janus Particles for Selective Dual Functionalization and Imaging", *Journal of the American Chemical Society*, **2014**, *136*, 2473 – 2483.

[4] L. Landgraf, P. Ernst, **I. Schick**, O. Köhler, H. Oehring, W. Tremel, I. Hilger, "Anti-oxidative effects and harmlessness of asymmetric Au@Fe<sub>3</sub>O<sub>4</sub> Janus particles on human blood cells", *Biomaterials* **2014**, *35*, 6986 – 6997.

[5] **I. Schick**, S. Lorenz, D. Gehrig, S. Tenzer, W. Storck, K. Fischer, D. Strand, F. Laquai, W. Tremel, "Inorganic Janus Particles for Biomedical Applications", *Beilstein Journal of Nanotechnology*, **2014** submitted.

[6] L. Landgraf, I. Müller, P. Ernst, M. Schäfer, C. Rosman, **I. Schick**, O. Köhler, H. Oehring, V.V. Breus, T. Basché, C. Sönnichsen, W. Tremel, I. Hilger, "Comparative evaluation of the impact on endothelial cells induced by different nanoparticle structures and functionalization", *Beilstein Journal of Nanotechnology*, **2014** submitted.

[7] J. Rother, **I. Schick**, W. Tremel, A. Janshoff, "Janus particles induced tubulation of lipid bilayers", **2014** in preparation.

[8] **I. Schick**, D. Gehrig, B. Balke, M. Panthöfer, F. Laquai, W. Tremel, "Composition-Dependent Communication Across Solid State Interfaces in Dumbbell-like Hetero-Nanoparticles", **2014** in preparation.

[9] **I. Schick**, S.E. Noll, W. Tremel, "Enhanced Peroxidase-Like Activity of Multi-functional Silica-Coated Janus Particles", **2014** in preparation.

# Acknowledgment



# List of Contents

<b>ABSTRACT</b> .....	<b>VI</b>
<b>ZUSAMMENFASSUNG</b> .....	<b>VII</b>
<b>LIST OF PUBLICATIONS</b> .....	<b>IX</b>
<b>ACKNOWLEDGMENT</b> .....	<b>X</b>
<b>LIST OF CONTENTS</b> .....	<b>XII</b>
<b>LIST OF FIGURES</b> .....	<b>XV</b>
<b>LIST OF TABLES</b> .....	<b>XX</b>
<b>1 INTRODUCTION</b> .....	<b>1</b>
<b>2 SYNTHESIS OF PLASMONIC NANOPARTICLES</b> .....	<b>5</b>
<b>2.1 Introduction</b> .....	<b>5</b>
<b>2.2 Gold Nanoparticles</b> .....	<b>8</b>
2.2.1 Size Control in Gold Nanoparticle Synthesis .....	9
2.2.2 Optical Characteristics of Gold Nanoparticles .....	12
2.2.3 Formation of Gold Nanoparticles .....	14
2.2.4 Self-Assembled Superlattices of Gold Nanoparticles .....	19
<b>2.3 Platinum Nanoparticles</b> .....	<b>22</b>
2.3.1 Morphology of Pt Nanoparticles .....	22
2.3.2 Optical Properties of Pt Nanoparticles .....	24
<b>2.4 Gold-Platinum Alloy Nanoparticles</b> .....	<b>25</b>
2.4.1 Synthesis of Gold-Platinum Alloy Nanoparticles .....	25
2.4.2 Compositional Analysis of Gold-Platinum Alloy Nanoparticles .....	27
2.4.3 Optical Properties of Gold-Platinum Alloy Nanoparticles .....	29
<b>2.5 Conclusion</b> .....	<b>30</b>
<b>2.6 Experimental Section</b> .....	<b>31</b>

<b>3 SYNTHESIS OF HETERODIMER NANOPARTICLES.....</b>	<b>33</b>
<b>3.1 Introduction.....</b>	<b>33</b>
<b>3.2 Au@MnO Heterodimer Nanoparticles.....</b>	<b>36</b>
3.2.1 Synthesis of Au@MnO Heterodimer Nanoparticles .....	37
3.2.2 Domain Size Control.....	40
3.2.3 Mechanism of Growth.....	44
3.2.4 Morphology of Au@MnO Heterodimer Nanoparticles .....	47
3.2.5 Magnetic Properties.....	49
<b>3.3 Au@Fe<sub>3</sub>O<sub>4</sub> Heterodimer Nanoparticles.....</b>	<b>50</b>
3.3.1 Synthesis of Au@Fe <sub>3</sub> O <sub>4</sub> Heterodimer Nanoparticles.....	51
3.3.2 Shape Control .....	54
3.3.3 Domain Size Control.....	56
3.3.4 Mechanism of Growth.....	58
3.3.5 Magnetic Properties.....	61
<b>3.4 Schottky Junctions in Heterodimer Nanoparticles.....</b>	<b>62</b>
<b>3.5 Variation of Metal Domain.....</b>	<b>67</b>
<b>3.6 Conclusion.....</b>	<b>72</b>
<b>3.7 Experimental Section .....</b>	<b>73</b>
<b>4 SURFACE MODIFICATION OF HETERODIMER NANOPARTICLES.....</b>	<b>77</b>
<b>4.1 Introduction.....</b>	<b>77</b>
<b>4.2 Silica Encapsulation of Heterodimer Nanoparticles.....</b>	<b>81</b>
4.2.2 Colloidal Stability of Au@MO <sub>x</sub> @SiO <sub>2</sub> Nanoparticles .....	85
4.2.3 Optical Imaging .....	89
<b>4.3 Conclusion.....</b>	<b>93</b>
<b>4.4 Experimental Section .....</b>	<b>94</b>
4.4.1 Instrumental Details.....	95
<b>5 HARNESSING THE JANUS CHARACTER OF HETERODIMER NANOPARTICLES.....</b>	<b>99</b>
<b>5.1 Introduction.....</b>	<b>99</b>
<b>5.2 Assembly of Janus Particles .....</b>	<b>101</b>
5.2.1 Molecular Assembly of Janus Particles.....	103
5.2.2 Assembly of Janus Particles at Interfaces .....	105
<b>5.3 Interaction Between Janus Particles and Artificial Membranes.....</b>	<b>109</b>
5.3.1 Introduction.....	109
5.3.2 Interaction of Janus Particles with GUVs.....	110
<b>5.4 Conclusion.....</b>	<b>116</b>

5.5 Experimental Section.....	117
<b>6 JANUS PARTICLES FOR MULTIMODAL BIOIMAGING.....</b>	<b>121</b>
6.1 Introduction.....	121
6.2 Tailoring Janus Particles for Bioimaging Applications.....	125
6.3 Janus Particles as CT Contrast Agents.....	131
6.4 Janus Particles as MRI Contrast Agents.....	134
6.5 Conclusion.....	136
6.6 Experimental Section.....	138
<b>7 THE TWO FACES OF JANUS PARTICLES FOR BIOMEDICAL APPLICATIONS.....</b>	<b>141</b>
7.1 Introduction.....	141
7.2 Protein Corona of Janus Particles.....	144
7.3 Janus Particles as Enzyme Mimics.....	146
7.3.1 Peroxidase-Like Activity of M@Fe <sub>3</sub> O <sub>4</sub> Janus Particles.....	147
7.3.2 Peroxidase-Like Activity of M@MnO Janus Particles.....	153
7.4 <i>In Vitro</i> Cytotoxicity of Janus Particles.....	155
7.5 Conclusion.....	162
7.6 Experimental Section.....	163
<b>8 CONCLUSION AND OUTLOOK.....</b>	<b>167</b>
<b>9 SUPPORTING INFORMATION.....</b>	<b>173</b>
<b>10 BIBLIOGRAPHY.....</b>	<b>177</b>
<b>CURRICULUM VITAE.....</b>	<b>193</b>

# List of Figures

Figure 1.1: Schematic illustration of the transition from isotropic to anisotropic nanoparticles, which are superior for their outstanding characteristics.	2
Figure 1.2: Schematic illustration of the seed-mediated synthesis of inorganic heterodimer nanoparticles and subsequent surface modification, outlining the structure of the first part of this doctoral thesis.	3
Figure 2.1: The dichroic Lycurgus Cup changes color from opaque green to translucent red when light is shown through it.[57] Reproduced from [58].	5
Figure 2.2: Average size of Au nanoparticles as a function of reaction temperature.	9
Figure 2.3: TEM images of Au nanoparticles prepared at different reaction temperatures resulting in different core sizes.	10
Figure 2.4: HR TEM images of $4.5 \text{ nm} \pm 0.6 \text{ nm}$ Au nanoparticles.	10
Figure 2.5: Refined synchrotron powder diffraction data for Au nanoparticles.	11
Figure 2.6: TEM images of Au nanoparticles showing the increased diameter upon application of a seeding-growth process.	12
Figure 2.7: UV-VIS spectra of Au nanoparticles of different core diameters, namely 4, 7, and 17 nm.	14
Figure 2.8: Photographs taken from the reaction flask equipped with temperature control and reflux condenser a) prior and b) subsequent to swift injection of the reduction solution.	15
Figure 2.9: LaMer plot showing the monomer concentration as a function of the reaction time and, therefore, illustrating the separation of nucleation and growth. Based on [72,120].	16
Figure 2.10: UV-VIS spectra of reaction snapshots of the synthesis of Au nanoparticles at room temperature after a reaction time of 30 min, 45 min, 60 min, 75 min, and 90 min.	17
Figure 2.11: TEM micrographs of reaction snapshots of the formation of Au nanoparticles at room temperature showing the temporal evolution.	18
Figure 2.12: TEM images of self-assembled Au nanoparticles.	20
Figure 2.13: TEM images of self-assembled 3D superlattices of assorted samples of oleylamine-functionalized 4 nm Au nanoparticles formed spontaneously upon drying a colloidal solution in hexane on TEM grids.	21
Figure 2.14: HR TEM images of Pt nanoparticles showing their uniform size distribution.	23
Figure 2.15: Electron diffraction of Pt nanoparticles referred to simulated pattern of Pt.	23
Figure 2.16: TEM images of truncated Pt nanocubes.	24
Figure 2.17: UV-VIS spectrum of $5.6 \text{ nm} \pm 0.5 \text{ nm}$ Pt nanoparticles.	25
Figure 2.18: HR TEM images of $\text{Au}_x\text{Pt}_{1-x}$ nanoparticles.	26

Figure 2.19: TEM images of Au <sub>x</sub> Pt <sub>1-x</sub> nanoparticles displaying the increase in diameter as well as the focusing effect upon seeding growth.	27
Figure 2.20: TEM images and compositional analysis of Au <sub>x</sub> Pt <sub>1-x</sub> nanoparticles by SEM EDS with corresponding SEM images as insets.	27
Figure 2.21: Electron diffraction of Au <sub>0.55</sub> Pt <sub>0.45</sub> nanoparticles as compared to simulated Au and Pt pattern.	29
Figure 2.22: UV-VIS spectra of Au <sub>x</sub> Pt <sub>1-x</sub> nanoparticles showing the composition-dependent damping of the surface plasmon resonance.	29
Figure 3.1: Schematic diagram showing the mechanism of formation of heterodimer nanoparticles in a non-polar solvent (top) and "flower-like" hetero-nanoparticles in a polar solvent (bottom).	35
Figure 3.2: TEM images of Au@MnO hetero-nanoparticles showing the impact of various reaction parameters.	38
Figure 3.3: FT-IR spectra of oleylamine, oleic acid, manganese(II) oleate, and Au@MnO heterodimer nanoparticles.	39
Figure 3.4: Refined synchrotron powder diffraction data for Au@MnO heterodimer nanoparticles.	40
Figure 3.5: TEM images of Au@MnO heterodimers with tunable sizes of Au and MnO domains.	41
Figure 3.6: a) TEM image of Au@MnO heterodimers, b) UV-VIS spectra of Au seeds as well as sequencing Au@MnO heterodimers.	42
Figure 3.7: UV-VIS spectra of Au@MnO heterodimers as a function of their domain sizes.	43
Figure 3.8: Dynamic light scattering results of Au and Au@MnO dispersed in <i>n</i> -heptane.	44
Figure 3.9: UV-VIS spectra of reaction snapshots of a typical Au@MnO synthesis.	45
Figure 3.10: TEM images of reaction snapshots of a typical Au@MnO synthesis.	46
Figure 3.11: Analysis of the UV-VIS spectra of the growth of Au@MnO heterodimers.	47
Figure 3.12: a) HAADF STEM image and b) Au and Mn elemental profiles of Au@MnO heterodimer nanoparticles.	47
Figure 3.13: TEM tomography of Au@MnO heterodimers.	48
Figure 3.14: HR TEM images of a single Au@MnO heterodimer nanoparticle.	48
Figure 3.15: Magnetic data of 4@25 nm Au@MnO heterodimer nanoparticles.	50
Figure 3.16: TEM images of Au@Fe <sub>3</sub> O <sub>4</sub> nanoparticles, which were prepared using Fe(CO) <sub>5</sub> as the iron oxide precursor.	52
Figure 3.17: FT-IR spectra of oleic acid, iron oleate, spherical Fe <sub>3</sub> O <sub>4</sub> , and Au@Fe <sub>3</sub> O <sub>4</sub> heterodimer nanoparticles.	53
Figure 3.18: Refined synchrotron powder diffraction data of Au@Fe <sub>3</sub> O <sub>4</sub> heterodimer nanoparticles.	54
Figure 3.19: TEM images of Au@Fe <sub>3</sub> O <sub>4</sub> heterodimers prepared with iron(III) oleate as iron oxide precursor.	55
Figure 3.20: HR TEM images of Au@Fe <sub>3</sub> O <sub>4</sub> heterodimers.	55
Figure 3.21: Dynamic light scattering results of Au and Au@Fe <sub>3</sub> O <sub>4</sub> dispersed in <i>n</i> -heptane.	56
Figure 3.22: TEM images of Au@Fe <sub>3</sub> O <sub>4</sub> heterodimers with different domain sizes of Au and Fe <sub>3</sub> O <sub>4</sub> .	57
Figure 3.23: UV-VIS spectra of Au@Fe <sub>3</sub> O <sub>4</sub> heterodimers with different domain sizes of Au and Fe <sub>3</sub> O <sub>4</sub> .	58
Figure 3.24: UV-VIS spectra of reaction snapshots of a typical Au@Fe <sub>3</sub> O <sub>4</sub> synthesis.	59



Figure 3.25: TEM images of reaction snapshots of a typical Au@Fe <sub>3</sub> O <sub>4</sub> synthesis.	60
Figure 3.26: Magnetic data of 4@20 nm Au@Fe <sub>3</sub> O <sub>4</sub> heterodimer nanoparticles in comparison to spheroidal Fe <sub>3</sub> O <sub>4</sub> nanoparticles.	62
Figure 3.27: Schematic representation of the interface communication of Au and Fe <sub>3</sub> O <sub>4</sub> within the heterodimers.	63
Figure 3.28: Comparison of the optical characteristics of Au nanoparticles, Au@MnO, as well as Au@Fe <sub>3</sub> O <sub>4</sub> heterodimers dissolved in hexane.	64
Figure 3.29: TR-PL measurements of pure Au nanoparticles as well as Au@Fe <sub>3</sub> O <sub>4</sub> and Au@MnO heterodimers.	66
Figure 3.30: TEM images of 4@18 nm Pt@Fe <sub>3</sub> O <sub>4</sub> heterodimer nanoparticles.	67
Figure 3.31: HR TEM images of Au <sub>0.55</sub> Pt <sub>0.45</sub> @Fe <sub>3</sub> O <sub>4</sub> heterodimer nanoparticles.	68
Figure 3.32: Electron diffraction pattern of Pt@Fe <sub>3</sub> O <sub>4</sub> and Au <sub>0.55</sub> Pt <sub>0.45</sub> @Fe <sub>3</sub> O <sub>4</sub> heterodimer nanoparticles referenced to simulated pattern of Fe <sub>3</sub> O <sub>4</sub> , Pt, and Au.	69
Figure 3.33: Refined synchrotron powder diffraction data for Au <sub>x</sub> Pt <sub>1-x</sub> @Fe <sub>2</sub> O <sub>3</sub> and Pt@Fe <sub>2</sub> O <sub>3</sub> .	70
Figure 3.34: Magnetic data of 8@16 nm Au <sub>x</sub> Pt <sub>1-x</sub> @Fe <sub>2</sub> O <sub>3</sub> heterodimer nanoparticles.	71
Figure 3.35: UV-VIS spectra of Au <sub>x</sub> Pt <sub>1-x</sub> @Fe <sub>2</sub> O <sub>3</sub> heterodimer nanoparticles.	71
Figure 4.1: Schematic illustration of interactions between nanoparticles in aqueous solution.	80
Figure 4.2: Schematic diagram of the silica encapsulation of Au@MO <sub>x</sub> heterodimer nanoparticles using the reverse microemulsion indicating the impact of a long-chain alkane-thiol.	82
Figure 4.3: TEM micrographs of silica-encapsulated heterodimer nanoparticles.	82
Figure 4.4: TEM images of Au@MnO@SiO <sub>2</sub> heterodimer nanoparticles with increasing thickness of the silica shell.	83
Figure 4.5: Refined synchrotron powder diffraction data for Au@MnO@SiO <sub>2</sub> and Au@MnO.	84
Figure 4.6: FT-IR spectra of Au@MnO and Au@MnO@SiO <sub>2</sub> nanoparticles.	85
Figure 4.7: Photograph of nanoparticles in a two-phase system composed and dynamic light scattering results of Au, Au@MnO, and Au@Fe <sub>3</sub> O <sub>4</sub> dispersed in <i>n</i> -heptane in comparison to Au@MnO@SiO <sub>2</sub> and Au@Fe <sub>3</sub> O <sub>4</sub> @SiO <sub>2</sub> dispersed in water.	85
Figure 4.8: Dynamic light scattering results of Au@MnO and Au@MnO@SiO <sub>2</sub> as well as Au@Fe <sub>3</sub> O <sub>4</sub> and Au@Fe <sub>3</sub> O <sub>4</sub> @SiO <sub>2</sub> dispersed in <i>n</i> -heptane and water, respectively.	87
Figure 4.9: TEM images of Au@MnO@SiO <sub>2</sub> nanoparticles with variable surface charge	88
Figure 4.10: TEM images of the degradation of MnO domains in sodium acetate buffer as a function of the incubation time.	88
Figure 4.11: UV-VIS spectra of AuMnO@SiO <sub>2</sub> , fluorescent dyes, and dye-labeled Au@MnO@SiO <sub>2</sub> nanoparticles.	89
Figure 4.12: Fluorescence images of TexasRed-Au@MnO@SiO <sub>2</sub> -ATTO 495.	90
Figure 4.13: Two-photon fluorescence images of TexasRed-Au@MnO@SiO <sub>2</sub> -ATTO 495.	90
Figure 4.14: Two-photon stability measurements of blue, green, and red regions of TR-Au@MnO@SiO <sub>2</sub> -ATTO 495 nanoparticles.	91
Figure 4.15: TR-PL measurements of pristine Au nanoparticles, pure ATTO 495, MnO@SiO <sub>2</sub> -ATTO 495, and Au@MnO@SiO <sub>2</sub> -ATTO 495 nanoparticles.	92

Figure 5.1: Summary of synthetic routes towards organic Janus particles. Reproduced from [31].	100
Figure 5.2: Synthetic routes towards inorganic Au@MnO Janus particles used within this work.	101
Figure 5.3: Kaolinite as natural Janus-type materials. Reproduced from [293].	102
Figure 5.4: Schematic representation of surface activity of Au@Fe <sub>3</sub> O <sub>4</sub> Janus particles self-assembled at the hexane-water interface. Reproduced from [299].	103
Figure 5.5: Scheme and TEM images of heterodimer nanoparticles and 1,4-benzenedimethanethiol used to link three individual particles into a trimeric colloid molecule.	104
Figure 5.6: Surface-pressure area isotherms of amphiphilic Au@MnO Janus particles.	106
Figure 5.7: Scheme of self-assembly of Janus particles at liquid interfaces depending on their functionalization.	107
Figure 5.8: TEM images of self-assembled PEG-functionalized Au@MnO Janus particles at an oil-water interface.	108
Figure 5.9: TEM images of amphiphilic ODT-Au@Fe <sub>3</sub> O <sub>4</sub> @SiO <sub>2</sub> Janus particles stabilizing toluene droplets in water.	108
Figure 5.10: Simulations of the interaction of membranes and Janus particles predict either the formation of tubes or the opening of pores, while the amphiphilic particles could also disrupt the bilayer structure due to detergent-like behavior. Adapted from Dr. Jan Rother. <sup>[314]</sup>	109
Figure 5.11: Evolution of interaction of Janus particles with GUVs over time.	111
Figure 5.12: Synthetic procedure for fabrication of PEG-conjugated SiO <sub>2</sub> -coated Janus particles.	112
Figure 5.13: Dynamic light scattering results of PEG-conjugated spherical MnO@SiO <sub>2</sub> as well as ODT-Au@MnO@SiO <sub>2</sub> Janus particles dispersed in water.	112
Figure 5.14: CLSM images of DOPC/TR-DHPE GUVs.	115
Figure 6.1: Left: <i>in vivo</i> X-ray images of mouse hind legs before injection and 2 min post tail injection of Au nanoparticles. Reproduced from [40]. Right: <i>in vivo</i> T <sub>1</sub> -weighted and T <sub>2</sub> -weighted image of mouse liver using ultra-small Fe <sub>3</sub> O <sub>4</sub> nanoparticles as dual contrast agent for MRI. Reproduced from [332].	124
Figure 6.2: TEM images of Au@Au@Fe <sub>3</sub> O <sub>4</sub> hetero-nanoparticles obtained by Au overgrowth.	126
Figure 6.3: UV-VIS spectra of Au@Au@Fe <sub>3</sub> O <sub>4</sub> hetero-nanoparticles as compared to Au@Fe <sub>3</sub> O <sub>4</sub> seed particles and Ag@Au@Fe <sub>3</sub> O <sub>4</sub> heterotrimer nanoparticles referred to Au@Fe <sub>3</sub> O <sub>4</sub> .	127
Figure 6.4: Representative TEM images showing Au@MnO seeds and Au@Au@MnO hetero-nanoparticles subsequent to Au overgrowth.	128
Figure 6.5: Schematic illustration of Au overgrowth on Au@MO <sub>x</sub> heterodimer nanoparticles and corresponding TEM images of Au@Au@MnO hetero-nanoparticles.	128
Figure 6.6: UV-VIS spectra of Au@Au@MnO hetero-nanoparticles.	129
Figure 6.7: Dynamic light scattering results of Au@Au@MnO dispersed in <i>n</i> -heptane.	130
Figure 6.8: TEM images of amphiphilic Au@Au@MnO@SiO <sub>2</sub> hetero-nanoparticles.	130
Figure 6.9: X-ray attenuation of hetero-nanoparticles.	132
Figure 6.10: T <sub>1</sub> -weighted phantom MR images of aqueous solutions nanoparticles and corresponding T <sub>1</sub> relaxivity plots.	135

Figure 7.1: Effects of the protein corona surrounding a nanoparticle. Adopted from [265].	142
Figure 7.2: Label-free LC-MS analysis of the hard protein corona of Fe <sub>3</sub> O <sub>4</sub> @SiO <sub>2</sub> , MnO@SiO <sub>2</sub> , and Au@MnO@SiO <sub>2</sub> and corresponding TEM images.	145
Figure 7.3: Picture and reaction scheme of progressive oxidation of 3,3',5,5'-tetramethylbenzidine.	147
Figure 7.4: Absorption measurements revealing the catalytic activity of Fe <sub>3</sub> O <sub>4</sub> -based nanoparticles to not be caused by degradation of nanoparticles.	148
Figure 7.5: Time-resolved UV-VIS spectra of the oxidation of TMB in the presence of H <sub>2</sub> O <sub>2</sub> and Fe <sub>3</sub> O <sub>4</sub> -based nanoparticles.	149
Figure 7.6: The reaction velocity of TMB oxidation in presence of Au@Fe <sub>3</sub> O <sub>4</sub> @SiO <sub>2</sub> or Fe <sub>3</sub> O <sub>4</sub> @SiO <sub>2</sub> nanoparticles, respectively, as a function of the substrate concentration was monitored by UV-VIS spectroscopy.	149
Figure 7.7: Steady-state kinetic assay of Au@Fe <sub>3</sub> O <sub>4</sub> @SiO <sub>2</sub> and Fe <sub>3</sub> O <sub>4</sub> @SiO <sub>2</sub> nanoparticles.	150
Figure 7.8: Comparison of peroxidase-like activity of Fe <sub>3</sub> O <sub>4</sub> @SiO <sub>2</sub> -based nanoparticles with different chemical compositions.	152
Figure 7.9: UV-VIS and TEM images of Au@MnO@SiO <sub>2</sub> nanoparticles incubated with TMB w/o H <sub>2</sub> O <sub>2</sub> in acetate buffer.	153
Figure 7.10: Pictures and corresponding UV-VIS spectra of Au@Au@MnO@SiO <sub>2</sub> and Au@AuPt@MnO@SiO <sub>2</sub> nanoparticles incubated with TMB and H <sub>2</sub> O <sub>2</sub> in acetate buffer.	154
Figure 7.11: Effect of incubation and internalization of Au@MnO@SiO <sub>2</sub> Janus particles on cell viability of Caki-1.	155
Figure 7.12: Confocal laser scanning microscopy images of HeLa cells co-incubated with Au@MnO@SiO <sub>2</sub> -ATTO495.	156
Figure 7.13: Effect of nanoparticle surface functionalization on cellular ATP level: HMEC-1 cells were incubated with increasing concentrations of Au@MnO@SiO <sub>2</sub> Janus particles.	158
Figure 7.14: Effect of incubation time on cellular ATP level and internalization of Au@MnO@SiO <sub>2</sub> -FITC Janus particles.	159
Figure 7.15: Domain size effects of MnO-based nanoparticles on cellular ATP levels.	160
Figure 7.16: Influence of chemical composition of the metal oxide domain of Janus particles on cellular ATP levels.	161

# List of Tables

Table 2.1: Comprehensive analysis of Au snapshots by TEM and UV-VIS spectroscopy.	18
Table 2.2: Compositional analysis of Au <sub>x</sub> Pt <sub>1-x</sub> nanoparticles based on the molar ratio of metal precursors used in the synthesis and subsequent SEM EDS analysis.	28
Table 3.1: Inverse decay rates $\tau$ and stretching exponent $\beta$ obtained from fitting the fluorescence dynamics to a stretched-exponential decay.	66
Table 4.1: Radii of Au and Au@MO <sub>x</sub> as intermediate stages as well as Au@MO <sub>x</sub> @SiO <sub>2</sub> nanoparticles determined by TEM and DLS.	86
Table 4.2: Inverse decay rates $\tau_1$ and $\tau_2$ obtained from fitting the fluorescence dynamics.	92
Table 5.1: Characterization of PEG-functionalized silica-coated spherical and Janus particles.	113
Table 6.1: X-ray mass attenuation constants $\mu/\rho$ in dependency of the photon energy $E$ . <sup>[343]</sup>	131
Table 6.2: Size-, concentration-, and composition-dependent X-ray attenuation of hetero-nanoparticles.	133
Table 6.3: Comparison of magnetic resonance properties of silica-coated Janus particles to spheroidal metal oxide nanoparticles.	136
Table 7.1: Comparison of the steady-state kinetic parameter of Fe <sub>3</sub> O <sub>4</sub> @SiO <sub>2</sub> and Au@Fe <sub>3</sub> O <sub>4</sub> @SiO <sub>2</sub> nanoparticles and literature data of Fe <sub>3</sub> O <sub>4</sub> nanoparticles. <sup>[379]</sup>	151
Table 7.2: Summary of domain sizes of Janus particles, core size of spherical control particles, and obtained zeta potentials $\zeta$ in aqueous solution as a function of surface functionalization.	157

# 1

## Introduction

Nanoparticles have become an indispensable part of our everyday life, as they are superior to bulk materials regarding their application in catalysis,<sup>[1,2]</sup> electronics,<sup>[3]</sup> biotechnology,<sup>[4,5]</sup> and medicine.<sup>[6–8]</sup> In recent years, the focus of nanomaterials research has moved beyond the preparation of size- and morphology-controlled, single-component particles. The design, synthesis, and properties of multi-component hetero-nanostructures have attracted much attention owing to their sophisticated structure-property relationship.<sup>[9]</sup> The expansion from single-component to well-defined hybrid nanoparticles has been shown to be advantageous for several reasons. Considering the combination of optical, magnetic, and catalytic properties within one nanoparticle, hetero-nanoparticles facilitate an advanced approach toward today's highly desired multifunctional nanoparticles used in research at the interface between materials' science,<sup>[10–14]</sup> biotechnology,<sup>[4,15,16]</sup> and medicine.<sup>[5,7,17–20]</sup> They enable access to widespread technological scenarios, as they represent artificial platforms, generating synergistically enhanced, tunable chemical and physical characteristics, or even cause the emergence of phenomena, which would not be accessible using homogeneous nanomaterials.

Janus particles are outstanding among the hetero-nanostructures owing to their asymmetry as an additional design module. Within the scope of his Nobel price lecture, Pierre Gilles de Gennes established the god Janus, who was depicted in Roman mythology as having two opposite and distinct faces, as their eponym.<sup>[21]</sup> They combine two or more components distinct in chemistry, properties, and morphology. Such particles exhibit many intriguing properties, including amphiphilic, magnetic, optical, and catalytic characteristics.<sup>[22]</sup> The interest in these particles arises from the fact that demanding problems in materials science, sensor specificity, and biomedicine can be approached, as the particles open a wide range of potential applications as catalysts,<sup>[2,10,23–25]</sup> surfactants,<sup>[26]</sup> and water-repellent coatings,<sup>[27]</sup> as well as in

drug delivery,<sup>[28]</sup> biological probing,<sup>[29,30]</sup> and biomedical imaging.<sup>[31]</sup> Moreover, the advanced surface-active properties of Janus particles with a segregated corona over particles with a uniform wettability makes them fascinating objects of current research.<sup>[32–34]</sup>

Most inorganic nanoparticles have a core surrounded by organic surface ligands. When the inorganic core contains two or more chemical species, the composition and distribution of each of those phases are crucial in addition to crystal structure, size, and shape.<sup>[35]</sup> The synthesis of hetero-nanoparticles requires an even higher degree of synthetic control as compared to single-component nanoparticles due to the enlarged variety of achievable hybrid morphologies. The most commonly engineered morphological configuration of hetero-nanoparticles is the so-called core/shell structure, where the inner nanoparticles are evenly embedded within a shell of different chemical composition, so that the overall interaction with the external environment is determined by the shell.<sup>[36]</sup> We placed emphasis on phase-segregated anisotropic hetero-nanoparticles, so-called dumbbell-like Janus particles or heterodimers, composed of a metal and a metal oxide domain (Figure 1.1). Among the myriad of available hetero-nanostructures, dumbbell-like heterodimer nanoparticles are second to none, as their well-defined morphology enables an even higher degree of control over size- and shape-dependent properties and, thus, more sophisticated applications. Although, some major problems have been overcome by intelligent design of the synthetic procedure within the last decade, the synthesis of well-defined Janus particles, specially designed for applications, is a continuing endeavor.<sup>[37]</sup>

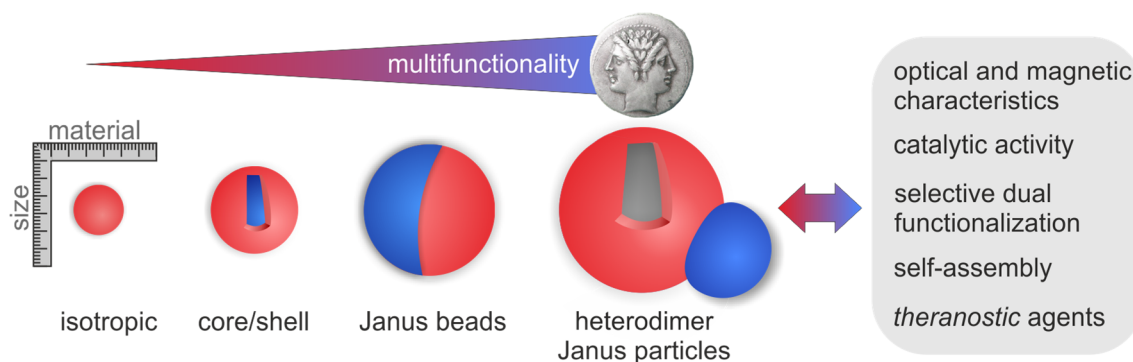


Figure 1.1: Schematic illustration of the transition from isotropic to anisotropic nanoparticles, which are superior for their outstanding characteristics.

Apart from each other, the chosen materials have been demonstrated to exhibit several unique advantages useful for biomedical applications. They are under current investigation as *theranostic* agents, which is commonly referred to as the combination of *therapeutic* and *diagnostic* features within a single nanoparticle. On the one hand, the metal domain, composed of gold, platinum, or their alloy, is chosen based on these metals' chemical stability, strong plasmonic resonance<sup>[38]</sup>, and multi-photon activity.<sup>[39]</sup> Further, the enhanced X-ray absorption together with the easiness of highly selective surface functionalization makes them nearly ideal contrast agents for computed X-ray tomography (CT).<sup>[40–44]</sup> On the other hand, magnetic metal

oxide nanoparticles are subject to ongoing research owing to their applications as contrast agents for magnetic resonance imaging (MRI). Here, the use of manganese oxide and iron oxide is investigated, as they are chemically congeneric but complementary regarding the underlying physical process of interaction with the analyzed tissue, which is responsible for the imaging process.<sup>[45–51]</sup>

In principle, this doctoral thesis is divided into two parts. The first part, comprised of Chapters 2 through 4, will focus on the progressive synthesis toward selectively functionalized heterodimer nanoparticles (Figure 1.2). Here, underlying concepts are explained as they are needed.

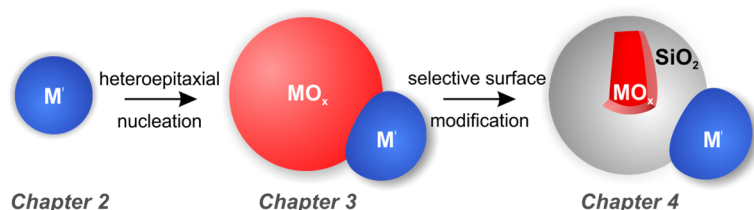


Figure 1.2: Schematic illustration of the seed-mediated synthesis of inorganic heterodimer nanoparticles and subsequent surface modification, outlining the structure of the first part of this doctoral thesis.

Chapter 2 is concerned with the synthesis of spherical, monodisperse, and size-tunable metal nanoparticles using Au nanoparticles as model system and followed by the establishment of composition-tunable  $\text{Au}_x\text{Pt}_{1-x}$  alloy nanoparticles. The exceptionally narrow size distribution of all investigated metal nanoparticles was displayed by well-defined properties, for instance the characteristic surface plasmon resonance. The uniformity of size of polycrystalline metal nanoparticles, which enabled the fabrication of self-assembled superlattices, can be ascribed to a precise separation of nucleation and growth, as postulated by the fundamental LaMer model.

Chapter 3 is devoted to the heteroepitaxial growth of metal oxide domains on preformed metal nanoparticles in a seed-mediated nucleation and growth technique. Here,  $\text{Au@MnO}$  heterodimer nanoparticles are introduced as novel dumbbell-like hetero-nanostructures, which were comprehensively analyzed and compared to  $\text{Au@Fe}_3\text{O}_4$  heterodimer nanoparticles, a frequently used system. Independent of the chemical composition of the metal oxide domain, the facile control over morphology and domain sizes is demonstrated and exploited to adjust the particles' characteristics. Owing to the strong coupling between the two components sharing a common interface in heterodimer nanoparticles, the distinct electronic structure of MnO and  $\text{Fe}_3\text{O}_4$ , respectively, is illustrated to bias the interfacial communication across the solid state interface and, thus, to control their intrinsic optical and magnetic characteristics.

In Chapter 4, the advantageous potential of hetero-nanoparticles is explored by selective surface modification. In the present case, the metal oxide domains are coated with a silica shell of tunable thickness, which enables the efficient incorporation of fluorescent dyes and

subsequent conjugation of functional groups. The distinguished wetting of the chemically different surfaces is exploited to leave the noble metal domain untouched and, thus, available for specific targeting. Au@MnO@SiO<sub>2</sub> heterodimer nanoparticles are water-soluble, colloiddally stable, and highly two-photon active.

In the second part, comprised of Chapters 5 through 7, the intrinsic Janus character of dumbbell-like hetero-nanoparticles is demonstrated, and its impact on the interactions at the nano-bio interface is addressed.

Chapter 5 presents initial results on the self-assembly of Janus particles at air-water and oil-water interfaces and highlights their impact on artificial membranes. Giant unilamellar vesicles function as model system for the cellular membrane to investigate membrane tubulations and vesiculations as passive, artificial endocytotic uptake pathways of Janus particles. This study provides experimental evidence of effects of amphiphilic Janus particles on lipid bilayers, which have been predicted by recent coarse-grained simulations.<sup>[52,53]</sup>

Chapter 6 is an example of the application of Janus particles as multimodal contrast agents in biomedical applications. In the present case, sequential overgrowth of Au on preformed heterodimer nanoparticles is useful to adjust the domain size ratio, which is required due to the distinct sensitivity of different imaging techniques. However, the narrow size distribution, the selective addressability, and thus, the Janus character are maintained. By virtue of the X-ray attenuation of the noble metal domains and the magnetic properties of the metal oxide domains, Janus particles have great potential for simultaneous optical, CT, and MR bioimaging.

Chapter 7 illustrates the two faces of Janus particles for biomedical applications, as their enhanced intrinsic reactivity, anisotropy, and sophisticated surface functionalization can be both advantageous and hazardous to living organisms. We provide insight into different stages of interaction between Janus particles and biological systems: the initial contact leads to the dynamic formation of a protein corona, and the reactivity and chemical stability determines the enzyme-like behavior, which finally contributes to the fate of cells after internalization. In order to assess the benefits of inorganic Janus particles over single-component particles, factors such as chemical composition of the core materials, particle morphology and size, surface charge and presence of amino groups, as well as incubation time are analyzed.



# Part I



# 2

## Synthesis of Plasmonic Nanoparticles

This chapter contains parts of an adapted reproduction of *Journal of the American Chemical Society* **2014**, 136, 2473 – 2483,<sup>[54]</sup> reproduced with permission of the American Chemical Society Copyright 2014.

### 2.1 Introduction

The optical properties of metal nanoparticles have been studied for a long time, starting with Faraday's investigations of colloidal gold.<sup>[55]</sup> But even prior to systematic examination, they were used in stained glass windows, ornaments, and pieces of jewelry for their beauty and resilience.<sup>[38]</sup> The most prominent example is likely the Lycurgus Cup, which was fabricated by Romans in the 4<sup>th</sup> century AD. This dichroic glass changes color depending on the viewing direction, *i.e.* reflection versus transmission, due to the incorporation of gold and silver colloids (Figure 2.1).<sup>[56]</sup>



Figure 2.1: The dichroic Lycurgus Cup changes color from opaque green to translucent red when light is shown through it.<sup>[57]</sup> Reproduced from [58].

In 1908, this color variation of colloidal gold with size encouraged Gustav Mie to extend the theory of light extinction to small metal particles,<sup>[59]</sup> which is still of particular importance to

current research. Thus, even centuries after the focus of research first turned to metal colloids, there is no evidence of sagging interest due to the wide range of fascinating properties and the large variety of possible applications, for instance in catalysis,<sup>[1,14,60,61]</sup> electronics,<sup>[62]</sup> photonics,<sup>[63]</sup> sensing,<sup>[64–66]</sup> imaging,<sup>[39,67,68]</sup> and medicine.<sup>[40,69]</sup>

The underlying principle of chemistry at nanoscale dimensions can be described in terms of a structure-property relationship, as the drastic changes in size and shape dictate the characteristics.<sup>[35]</sup> Since Faraday's preliminary work on Au colloids, much progress has been made regarding the synthesis of metal nanoparticles with well-defined sizes and morphologies. They reveal a unique size- and shape-dependency of their optical properties and give significance to the control of their physical parameters including size, shape, composition, and structure. Thus, the preparation of uniformly sized nanoparticles has received considerable critical consideration. Regarding the precise control over the size and shape of nanoparticles, solution-phase colloidal chemistry is favored, though only small scale production is commonly workable. Generally speaking, nanoparticle synthesis can be divided into three phases, which are the nucleation, the evolution of nuclei into seeds, and, finally, the growth of seeds into nanoparticles. According to Skrabalak *et al.*, seeds are defined as something larger than nuclei, so that structure fluctuation has to be considered no longer an option.<sup>[70]</sup> LaMer and co-workers pioneered the research on the preparation of uniform colloidal particles, although micron-sized particles were analyzed.<sup>[71]</sup> They revealed the separation of nucleation and growth to be crucial in order to obtain uniform particles. The formation mechanism of nanoparticles often closely resembles that of micron-sized nanoparticles, though the high surface-to-volume ratio brings an unknown factor to the mechanism.<sup>[72]</sup>

As it is the heart of nanoparticle-based research, many synthetic techniques have been developed, where one of two approaches are commonly applied: the one-pot<sup>[73]</sup> or the hot-injection method.<sup>[74]</sup> They differ according to their origin of nucleation. In the one-pot methods, the slow heating of a precursor mixture leads to thermal decomposition and subsequent nucleation, while for the hot-injection methods the rapid injection of a cold precursor into a hot reaction mixture causes a short nucleation event. The appropriate choice is strongly dependent on the chemical reaction behind the nanoparticle formation, as nowadays many pathways are known, including thermal decomposition, non-hydrolytic sol-gel processes, and reduction utilizing a multiplicity of reducing agents. More sophisticated shapes of nanoparticles are often obtained by a seeding-growth, whereby additional surfactants control the anisotropic growth on the seed particles. Generally, the synthetic tunability of noble metal nanoparticles stretches over the size range of 1 nm to more than 100 nm and enables the formation of various geometries including spheres, cubes, rods, prism, triangles, stars, and branched structures.<sup>[72,75,76]</sup>

Of the various groups of noble metal nanomaterials, Au nanoparticles exhibit unique size- and shape-dependent optical properties, facile surface chemistry, and chemical

resistance.<sup>[17]</sup> They show an unusually high polarizability of optical frequencies arising from the excitation of localized surface plasmon resonances (SPR).<sup>[77,78]</sup> Au nanoparticles generate an intense optical signal, are durable, and apt to bind molecules of interest in a controlled fashion without photo-bleaching, a major drawback of common fluorescent dyes.<sup>[79]</sup> Furthermore, their strong X-ray absorption coefficient together with the easiness of thiol functionalization makes them nearly ideal contrast agents for computer tomography.<sup>[80]</sup> Additionally, gold nanoparticles have promising therapeutic properties as photo-thermal agents: being behind this is the effective conversion of absorbed light into localized heat. Thus, the local temperature around gold nanoparticles can be increased by laser illumination through the tunable surface plasmon bands in the near infrared region (NIR).<sup>[16,81–83]</sup>

Moreover, gold rods showed strong two-photon activity in cellular imaging.<sup>[45,84–87]</sup> Generally speaking, multi-photon microscopy possesses some advantages over conventional confocal microscopy: (i) the fluorescence background is reduced because of the relatively low two-photon cross-section of most biomolecules responsible for autofluorescence, (ii) photo-bleaching is decreased by selective excitation of the focal volume, and (iii) the penetration depth in scattering samples is increased by using excitation light within the optical transmission window of biological tissues (near-infrared (NIR) spectral range, 700 - 1000 nm).<sup>[78]</sup>

In recent years, there has been an increasing interest in nanoparticles of platinum group metals due to their size- and shape-dependent catalytic properties.<sup>[35]</sup> In fact, the noble metals gold and platinum exhibit similar chemical properties at bulk scales, which is attributed to their neighboring relationship in the periodic system of elements. However, this affinity gets lost upon decreasing the crystal dimensions down to a few nanometers. For instance, the miscibility gap of bulk gold and platinum vanishes at nanoscale.<sup>[88]</sup> The most prominent characteristic of gold nanoparticles is their shape-dependent optical scattering process. Conversely, platinum nanoparticles show a rather featureless response to light excitation in the visible range.<sup>[89]</sup>

Nanocrystalline intermetallic compounds and alloys are novel materials and emerge as potentially more important materials than monometallic nanoparticles.<sup>[90,91]</sup> Gold-Platinum alloy nanoparticles have stimulated increasing research interest based on their electronic properties<sup>[92]</sup> and enhanced catalytic activity as compared to gold and platinum nanoparticles.<sup>[93]</sup> They are discussed as next generation heterogeneous catalysts for their conceivably low-cost high performance. Even though many methods for preparing high quality monometallic nanoparticles are known, the controlled synthesis of bimetallic nanoparticles is much more difficult and remains challenging.<sup>[49,94]</sup>

Here, we report the synthesis of gold, platinum, and their alloy nanoparticles as model system for metallic nanoparticles. Upon facile adjustment of a reported procedure, we were able to fabricate spherical Au nanoparticles with an exceptionally narrow size distribution leading to well-defined properties. Moreover, the uniformity was evidenced by the formation of self-

assembled superlattices. We observed significant differences between Au, Pt, and Au<sub>x</sub>Pt<sub>1-x</sub> at nanoscale regarding e.g. their optical properties and crystal structure, although some common features remain. Therefore, we separately discuss the preparation and comprehensive characterization of Au and Pt nanoparticles within the first and second part of this chapter and conclude with their combination in the form of alloy nanoparticles.

## 2.2 Gold Nanoparticles

Gold nanoparticles are chemically the most stable metal nanoparticles and are a major area of interest within the field of several materials science. Spheroidal gold nanoparticles can be taken as one extreme case of the even more studied gold nanorods. These are commonly prepared using a seed-mediated growth process in aqueous solution. Their anisotropic growth is triggered by rod-shaped micelles of detergents such as CTAB, thus dictating the shape of reaction templates.<sup>[95,96]</sup> Gold nanorods are especially widely used in colorimetric sensing,<sup>[97,98]</sup> diagnostics,<sup>[40,99]</sup> and cancer treatment,<sup>[100]</sup> known as hyperthermia.<sup>[101]</sup>

Nowadays, a plethora of synthetic routes to spherical gold nanoparticles has been developed, although the preparation of small nanoparticles, *i.e.* core sizes below 10 nm, was challenging for a long time. The major fraction of synthetic procedures utilizes strong reducing agents (e.g. NaBH<sub>4</sub>, LiBH<sub>4</sub>) in aqueous media.<sup>[72]</sup> Introduced by Turkevitch *et al.* in 1951, the citrate reduction of HAuCl<sub>4</sub> in water remained the most popular synthesis of ca 20 nm Au nanoparticles for many years.<sup>[102]</sup> A break-through regarding the preparation of small Au nanoparticles was reported in 1994 by Brust *et al.* subsequent to the detection of Schmid's extraordinary cluster [Au<sub>55</sub>(PPh<sub>3</sub>)<sub>12</sub>Cl<sub>6</sub>] in 1981.<sup>[103]</sup> This so-called Brust-Schiffrin method facilitated the synthesis of stable nanoparticles of enhanced uniformity in the range between 1.5 nm and 5.2 nm.<sup>[104]</sup> In fact, the synthesis was inspired by Faraday's two-phase approach<sup>[55]</sup> and is performed as a reduction of AuCl<sub>4</sub><sup>-</sup> by NaBH<sub>4</sub> in toluene, subsequent to a phase-transfer reaction.

In this study, the particles were intended to be applied as seeds in nonpolar solvents to form metal-metal oxide Janus particles, so that the hydrophobic functionalization of the nanoparticles was one of the decisive factors for the choice of preparation technique. Moreover, a precise size control was desired in order to obtain highly uniform seed particles for the designated subsequent seeding-growth reaction. This was not achievable by the Brust-Schiffrin technique in due form. In previous studies, the use of amine borane complexes for the synthesis of monodisperse, thiol-functionalized gold particles was reported.<sup>[105]</sup> For instance, as a part of the detailed examination of the catalytic activity, Peng *et al.* demonstrated a facile aprotic synthesis of monodisperse size-tunable Au nanoparticles.<sup>[106]</sup>

### 2.2.1 Size Control in Gold Nanoparticle Synthesis

The bottom-up synthesis of hydrophobic gold nanoparticles was adapted from the procedure reported by Peng and co-workers.<sup>[106]</sup> The authors report control over the particle diameter from 2 nm to 10 nm by adjusting the reaction temperature between 40 °C and 2 °C. Moreover, a certain loss of control is declared concerning the size distribution for the larger particles. This is attributed to solubility problems at low temperatures of the precursor tetrachloroauric acid in the reaction mixture containing tetralin and oleylamine.<sup>[106]</sup> Based on this reported chemical protocol, we obtained monodisperse Au nanoparticles in the range of 3 nm to 9 nm. However, the procedure was adjusted as the solubility problems started significantly above 2 °C. Additional problems due to the high melting point of oleylamine of 18 - 26 °C were observed, and, thus, the amount of stabilizing ligand available was decreased. Therefore, only syntheses above 8 °C were performed, where the solubility was sufficient to obtain monodisperse nanoparticles. The comparison of the obtained nanoparticle sizes with literature data shows a monotone decrease in diameter with increasing temperature (Figure 2.2). However, the slope for the obtained data was significantly steeper than in literature. This was ascribed to the difficulties of experimental execution at low temperatures.

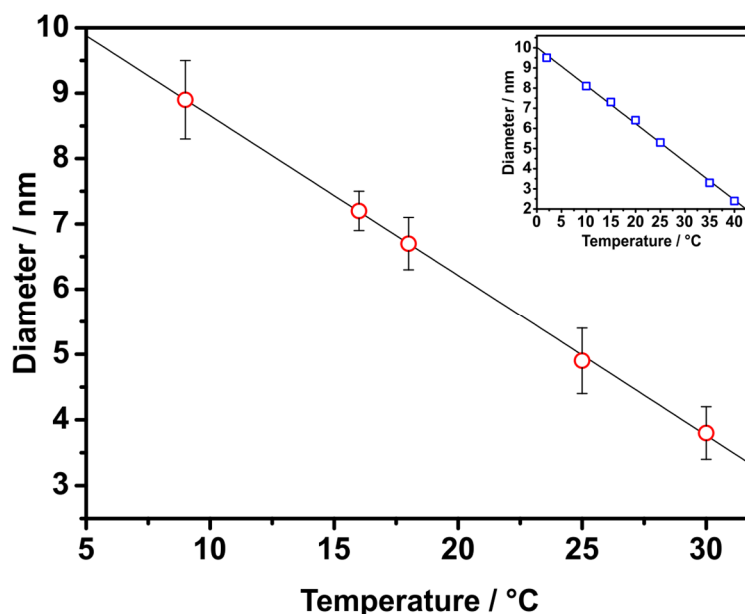


Figure 2.2: Average size of Au nanoparticles as a function of reaction temperature. The size was determined from the corresponding TEM images. The inset displays reported literature data.<sup>[106]</sup>

As nucleation requires a distinct amount of energy, the number of nuclei formed at lower temperatures is limited by the provided thermal energy. In fact, the critical free energy  $\Delta G_c$  to form a stable nucleus correlates with the temperature in a  $T^{-2}$  dependence. The higher the temperature, the more nuclei that are formed, and, thus, the smaller the resulting nanoparticles will grow due to the restricted amount of precursor available. Moreover, the temperature dependence can also be ascribed to the reducing rate of gold cations by the amine-borane

complex. Zheng *et al.* reported an increased reduction rate of AuPPh<sub>3</sub>Cl for various amine-borane complexes upon raising reaction temperature.<sup>[105]</sup>

Transmission electron microscopy, TEM, images show the uniform size distribution of the gold nanoparticles prepared at different reaction temperatures (Figure 2.3). Aside from the increase in diameter, crystal facets became much more distinct. Independent of their size, the particles tended to self-assemble into hexagonally-ordered arrays, which continued to the typical close packing upon increasing the concentration of gold particles.

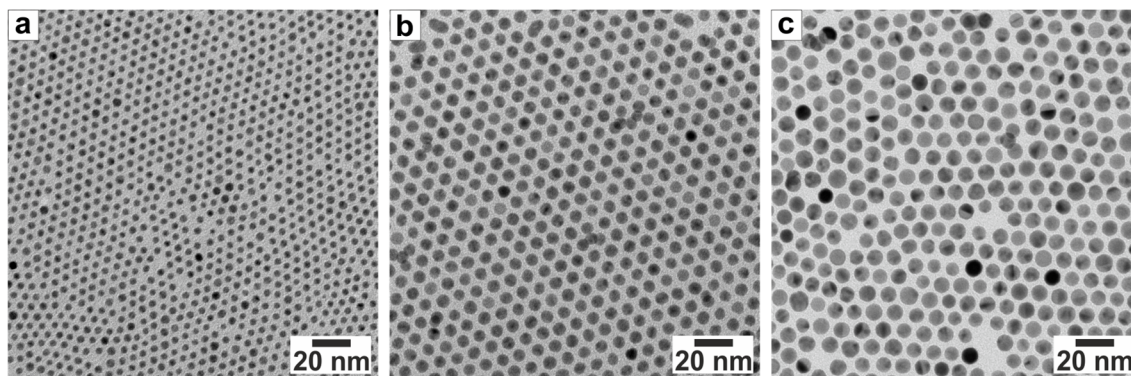


Figure 2.3: TEM images of Au nanoparticles prepared at different reaction temperatures resulting in different core sizes: a) the reaction at room temperature obtained  $3.8 \pm 0.4$  nm, b) at  $16^\circ\text{C}$  the diameter was  $7.2 \text{ nm} \pm 0.3$  nm, and lowering the temperature even further to c)  $9^\circ\text{C}$  resulted in a diameter of  $8.9 \text{ nm} \pm 0.6$  nm. All images were taken with the same magnification.

High-resolution TEM images confirmed the existence of clearly faceted, crystalline gold particles, even for the smaller core sizes (Figure 2.4a). The nanoparticles were multiply twinned, which was confirmed by two (or more) sets of peaks in electron diffraction. In fact, planar defects, *i.e.* twins or stacking faults, are commonly observed in Au nanoparticles. That is because Au has one of the lowest energy barriers to stacking faults among the *fcc* metals.<sup>[70]</sup> The structure of the particles was identified by electron diffraction as *fcc* structure with terminating, close-packed (111) and (100) planes, as known from literature.<sup>[107–109]</sup>

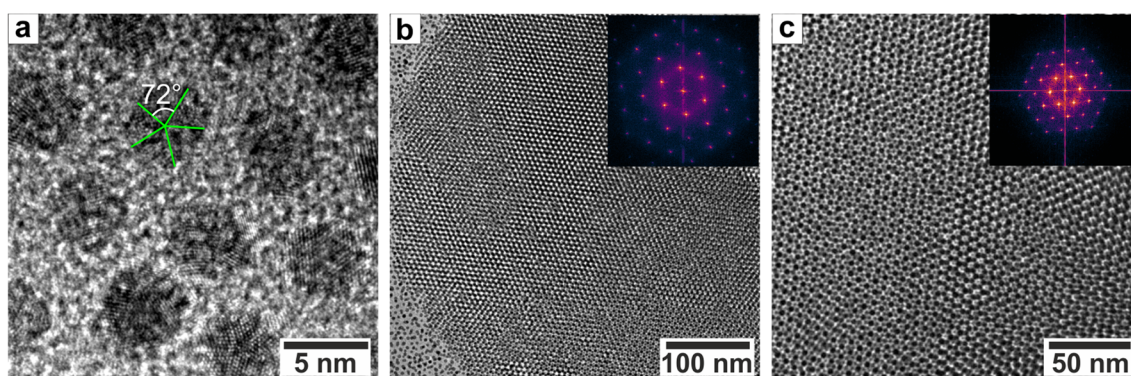


Figure 2.4: HR TEM images of  $4.5 \text{ nm} \pm 0.6$  nm Au nanoparticles. a) High magnification showing the structure to be mixed single- as well as polycrystalline; b) and c) self-assembled 3D *fcc* superlattices with corresponding FFT images as insets indicating the (111)<sub>SL</sub>-oriented array of Au nanoparticles. The FFT images are shown in pseudo-colors (ImageJ, look up table: gem). The HR TEM measurements were performed by [REDACTED].

Furthermore, HR TEM images of 3D self-assembled superlattices in Figure 2.4b and c showed the typical face-centered cubic packing of the particles oriented along the (111)<sub>SL</sub>-plane.



This became evident in the sixfold symmetry in fast Fourier transformations (FFT) of the corresponding images (insets of Figure 2.4). Hereafter, the subscript “SL” designates the planes and directions in the superlattices.

High resolution synchrotron diffraction data were collected at the beamline 11-BM at the Advanced Photon Source (APS) of the Argonne National Laboratory. The data provide the advantage of high resolution, low sample absorption, and no sample fluorescence. Figure 2.5 displays the quantitative phase analysis by means of Rietveld refinement of room temperature synchrotron data of Au nanoparticles. Reflection profiles were modelled according to the fundamental parameter approach and a log normal distribution of spherical crystallites. The particle diameter was determined by TEM to  $5.3 \text{ nm} \pm 0.5 \text{ nm}$ , where the occurrence of contrast differences within individual particles indicated them to be composed of multiple crystallites (inset of Figure 2.5), which was in good accordance to HR TEM analysis. According to the synchrotron diffraction data the crystallite distribution refines an expectation value of  $1.39(1) \text{ nm}$ , a maximum of  $0.516(5) \text{ nm}$ , and a variance of  $1.84(4) \text{ nm}$  (see Table S1).

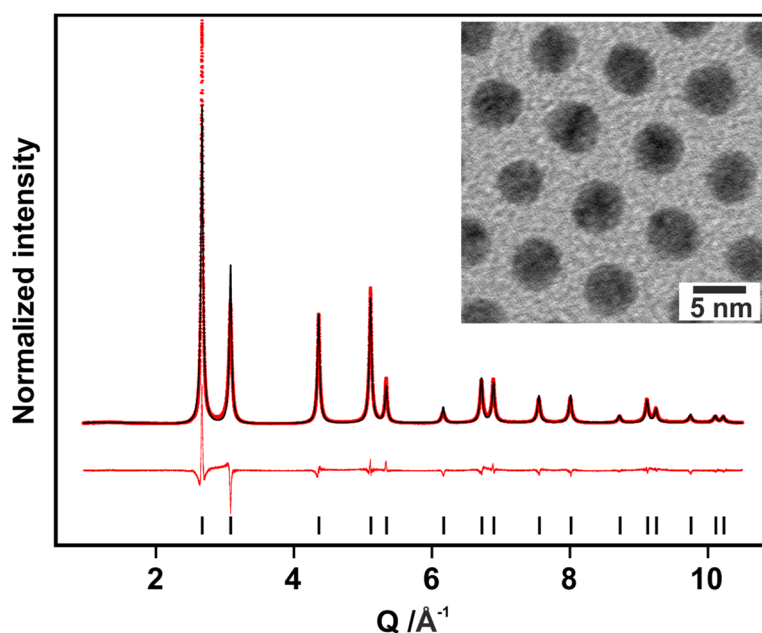


Figure 2.5: Refined synchrotron powder diffraction data for Au nanoparticles (red dots), including profile fit (black solid line), and profile difference (red solid line). The refined peak positions are indicated by black tick marks. Inset: corresponding TEM image. The data were refined by [REDACTED].

Considering the difficulties in reproduction of literature descriptions regarding the preparation of large, *i.e.*  $> 10 \text{ nm}$ , monodisperse gold nanoparticles, the synthesis was changed to a two-step procedure. Nonetheless, the room temperature synthesis was maintained as the first step. Subsequently, the as-prepared gold particles were used as seeds for a seeding-growth process to enlarge the diameter of the particles. A key aspect of the seeding-growth technique is the usage of small nanoparticles as the center of nucleation to obtain the desired core size.<sup>[110]</sup> This concept has been applied to gold particles for a long time, however, it was only reported applying various experimental techniques in aqueous media so far.<sup>[74,110–112]</sup> In

terms of avoiding secondary nucleation, the seeding-growth technique is superior to a one-step seeding method regarding the uniformity of the resulting nanoparticles.<sup>[111]</sup> Similarly, this approach was successfully realized for hydrophobic gold nanoparticles in nonpolar solvents within this work. More precisely, the as-prepared, small gold particles were added to a solution of tetrachloroauric acid in a 1:1 mixture of toluene and oleylamine and, then, heated to reflux for 2 hours. The reduction of the gold salt was achieved by oleylamine as weak reducing agent at elevated temperatures. Therefore, the reduction took place rather slowly facilitating the growth of the particles towards secondary nucleation. The increase in diameter was controlled by the ratio of tetrachloroauric acid to gold particles, while the seeding-growth process could be repeated until the desired diameter was obtained. Despite the enlargement of the diameter, the size distribution was narrowed. For instance, the enlargement reaction of  $6.0 \text{ nm} \pm 0.6 \text{ nm}$  (10.0 %) to  $10.5 \text{ nm} \pm 0.5 \text{ nm}$  (4.8 %) reduced the standard deviation by half (Figure 2.6).

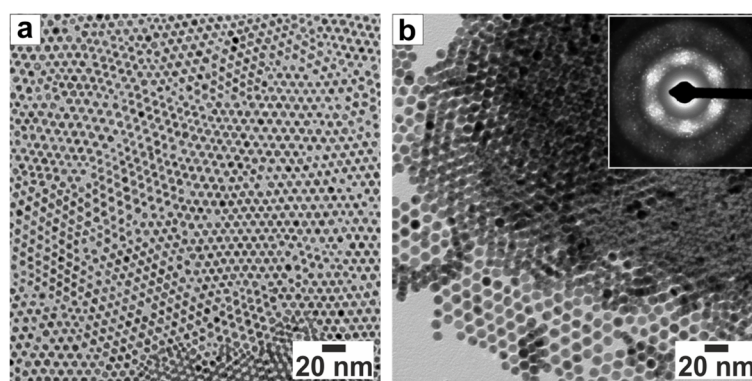


Figure 2.6: TEM images of Au nanoparticles showing the increased diameter upon application of a seeding-growth process: a) original nanoparticles with a diameter of  $6.0 \text{ nm} \pm 0.6 \text{ nm}$ , b) nanoparticles subsequent to enlargement reaction with a diameter of  $10.5 \text{ nm} \pm 0.5 \text{ nm}$ . The images were taken with the same magnification. Inset: electron diffraction corresponding to image b) indicating the *hcp* arrangement of the nanoparticles due to the sixfold symmetry of the superlattices reflections.

## 2.2.2 Optical Characteristics of Gold Nanoparticles

The optical absorption intensity of Au arises from two contributions, the intraband and interband transitions. The intraband transitions are common to all metals and take place within the broad conduction band, mainly consisting of Au  $6s^1p$  hybridized atomic orbitals. The absorbance resulting from these transitions appears near 250 nm and is quite weak. The second contribution arises from the interband transitions between the  $5d^{10}$  band and the conduction band. The crucial  $d \rightarrow p$  character of this transition causes very intense absorption and is responsible for the brilliant colors of colloidal gold.<sup>[38]</sup> This feature of a broad and strong absorption band, which is absent in bulk spectra, is common to the spectra of many metallic nanoparticles. The giant dipole, or so-called surface plasmon resonance (SPR) band, is assigned to a collective oscillation of electrons in the conduction band, occupying energy states directly above the Fermi energy level, in response to interaction with light. The electron cloud is displaced relatively to the nuclei causing a strong restoring Coulomb attraction. This results in

an oscillation of the electron cloud with a distinct oscillation frequency. The frequency is a function of the density of electrons, the effective electron mass, and the shape as well as the size of the charge distribution. In 1908, Mie's theory expressed substantial progress for classical physics. Gustav Mie presented a solution to Maxwell's equation describing the extinction spectra, *i.e.* the sum of absorption and scattering, of spherical particles independent of their size.<sup>[59]</sup> Still, this theory is of vital significance, as it is the only simple, exact solution to the Maxwell's equation material for particles.<sup>[113,114]</sup>

The SPR band of Au nanoparticles is characterized by its position around 520 nm, while a strong dependency of the intensity on the nanoparticle size was observed (Figure 2.7). The relative spectral intensity decreased linearly with the mass (core size) of the as prepared gold nanoparticles, which is shown in the inset of Figure 2.7. Furthermore, the decreased intensity was accompanied by a broadening of the plasmon bandwidth. According to Mie's theory, the position of the surface plasmon band is dependent on the size only for larger nanoparticles on the one hand, but on the other hand dependent on the ligands, the medium dielectric constant, and the temperature causing a change of the effective local dielectric function surrounding the particles. Therefore, only a slight bathochromic shift of the absorption maximum of 4 nm was observed upon increasing the core size from 4 nm to 17 nm (Figure 2.7), which was in accordance with literature. For instance, Kreibig *et al.* described a slight but distinct bathochromic shift accompanied by an increase in *FWHM* (full width at half maximum) upon decreasing the diameter.<sup>[115]</sup>

Creighton *et al.* calculated the UV-VIS spectra of 10 nm nanoparticles of 52 metallic elements by means of Mie's theory. Generally speaking, there is no strong dependence of the absorption spectrum on the core size of the nanoparticles according to Mie's theory within the 3 - 20 nm diameter range. This arises from the particle size being below the range at which higher-order terms than the dipole term in the Mie summation become significant.<sup>[89]</sup> However, the experimental data showed a significant size dependency. This so-called damping of the surface plasmon resonance is attributed to the reduction of the particle size below the electronic mean-free path of the conduction electrons, which is in the range of the Bohr radius of 17.4 nm for gold. It can be described in terms of a 1/radius dependency caused by enhanced scattering of the free electrons at the particle surface for core sizes below 3 nm.<sup>[38,116]</sup>

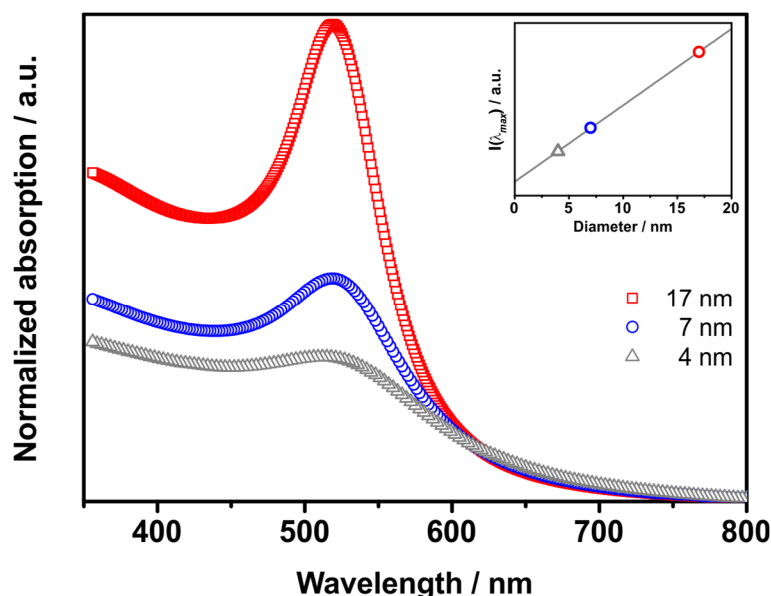


Figure 2.7: UV-VIS spectra of Au nanoparticles of different core diameters, namely 4 nm, 7 nm, and 17 nm, illustrating the strong correlation between spectral intensity and core size. The inset shows the linear dependency of the maximum intensity of the SPR on the core diameter. The spectra were measured in hexane and normalized at 800 nm.

Coinciding with the increase in spectral intensity, the rising slope of the absorption band increased with the core size resulting in a sharper onset of spectral absorption for larger particles. This onset became less distinct for smaller nanoparticles of ca 3 nm, but was also observed in the spectra displayed in Figure 2.7. It is located near 1.7 eV, which is the energy of the interbandgap  $5d \rightarrow 6sp$ , and is evident for the electronic band structure of the nanoparticles owing to quantum-mechanical rules. This metal-to-insulator transition was reported to occur for particle sizes below 20 nm, which are small enough that the size-dependent quantization effect becomes important.<sup>[38]</sup>

### 2.2.3 Formation of Gold Nanoparticles

The formation of the nanoparticles took place immediately upon injection of reduction solution into a precursor solution of tetrachloroauric acid hydrate in tetralin and oleylamine. The reducing solution contained *tert*-butylamine borane complex as the active species. This nucleation could be easily followed due to the drastic color change from the orange precursor solution to the ruby-red nanoparticle dispersion (Figure 2.8).

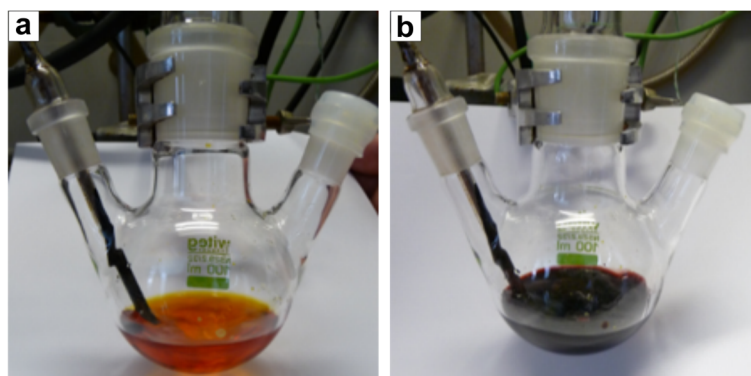


Figure 2.8: Photographs taken from the reaction flask equipped with temperature control and reflux condenser a) prior and b) subsequent to swift injection of the reduction solution.

The synthesis can be explained with assistance of the classical “burst of nucleation” concept. This was originally developed to explain the formation of micron-sized, monodisperse particles, colloidal suspensions, and sulfur hydrosols by LaMer and co-workers in the 1940s.<sup>[71]</sup> One central statement of this model is the importance of the separation of nucleation and growth to ensure monodispersity of the particles. In the case of homogeneous nucleation, there is an energy barrier to be overcome for the spontaneous formation of nuclei, as the system changes from a homogeneous to a heterogeneous phase. This energy barrier consists of two terms: first, the Gibbs free energy of a spheroidal particle with a distinct radius  $r$  bearing the surface free energy  $\gamma$  per unit area, and, second, the energy change  $\Delta G_v$  from the monomers in solution to the unit volume of a bulk crystal.  $\Delta G$  is maximum for the critical radius  $r_c$ , which determines the minimum radius of a nucleus to be stable against re-dissolution, and therefore, able to grow in the solution.

$$\Delta G = 4\pi \cdot r^2 \cdot \gamma + \frac{4}{3}\pi \cdot r^3 \cdot \Delta G_v \quad \frac{d(\Delta G)}{dr} = 0 \quad \rightarrow \quad r_c = \frac{-2\gamma}{\Delta G_v}$$

According to the classical nucleation theory, growth can only occur when the increase in interfacial energy vanishes compared to the decrease in chemical potential.<sup>[109]</sup> Based on the critical radius, the nucleation rate has to be sufficiently high to overcome the re-dissolution rate of the particles, which is the second central statement of LaMer’s as well as of the classical nucleation theory. However, the LaMer model was developed for micron-sized hydrosols, and, therefore, several parameters were assumed to be constant. On the contrary, parameters, such as  $\gamma$  and  $\Delta G_v$ , are highly size-dependent for nanoparticles due to the strong increase in the surface-to-volume ratio. Thus, attention has to be paid to additional driving forces to reduce the surface free energy, for example by reconstruction of the surface,<sup>[60]</sup> formation of “magic number” metal clusters,<sup>[117]</sup> or change of the crystal structure.<sup>[118,119]</sup>

The LaMer plot is commonly used to visualize the effect of the energy barrier with respect to homogeneous nucleation and how it induces the burst of nucleation (Figure 2.9).<sup>[71]</sup> Starting a synthesis, the concentration of the smallest subunit of the emerging crystal, the so-called monomer, increases above even the supersaturation  $S$  of the solution. Within this first stage of

reaction, no precipitation occurs due to the energy barrier to nucleation. In the second stage, the degree of supersaturation is above the critical supersaturation  $S_c$  and, therefore, stable nuclei are spontaneously formed. As a result of the nucleation, the monomer concentration decreases rapidly, below even the concentration needed for further nucleation. Hence, no additional nuclei are formed and the particles are growing only in size within the third stage of the reaction.<sup>[72]</sup> However, very little is known about nuclei present during synthesis due to their small sizes.

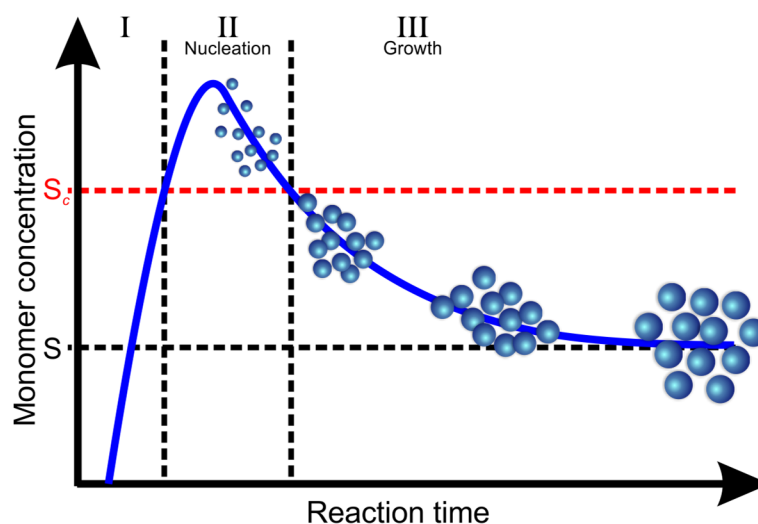


Figure 2.9: LaMer plot showing the monomer concentration as a function of the reaction time and, therefore, illustrating the separation of nucleation and growth. Based on [72,120].

Applying the LaMer model to the performed formation of gold nanoparticles, the burst of nucleation was actuated by swift injection of the reduction agent into the precursor solution containing tetrachloroaurate(III) complexes stabilized by oleylamine (Figure 2.8). The fast reaction consumed the major part of the monomers so that no further nucleation took place. Thus, the system proceeded to the third stage of the LaMer model, namely growth until depletion of reactants.<sup>[106]</sup> The reaction was monitored by reaction snapshots utilizing their surface plasmon resonance as well as TEM. The aliquots taken immediately after injection of the reduction solution until 30 minutes showed large, insoluble aggregates. Therefore, they are not discussed any further with respect to particle size and absorption intensity. Starting at 30 minutes after injection of the reduction solution, aliquots were taken at 15-minutes intervals, and the associated UV-VIS spectra are shown in Figure 2.10. Within the first 90 minutes after the reaction was started, the surface plasmon absorption centered at 512 nm became significantly more distinct. No notable shift of the absorption maximum was observed. This suggested that the particles did not grow significantly in diameter, but the size distribution sharpened, resulting in a more pronounced surface plasmon resonance.

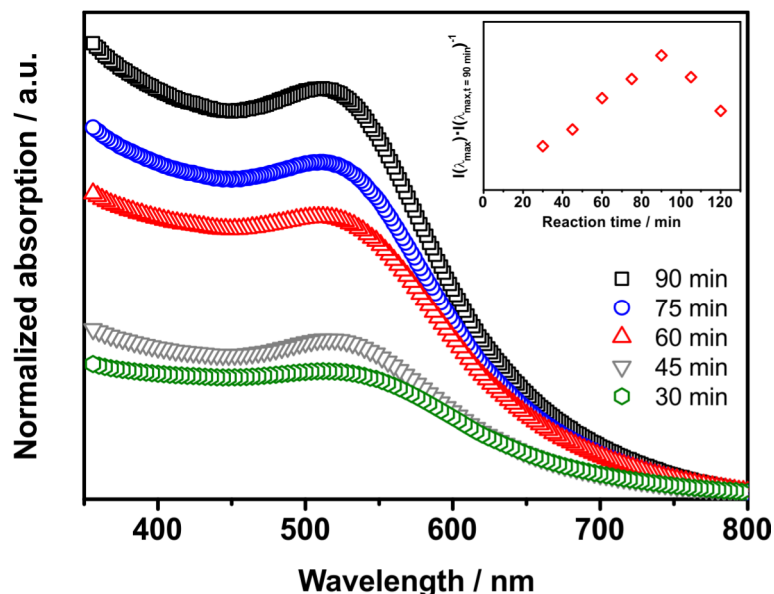


Figure 2.10: UV-VIS spectra of reaction snapshots of the synthesis of Au nanoparticles at room temperature after a reaction time of 30 min, 45 min, 60 min, 75 min, and 90 min. The inset shows the evolution of the spectral intensity as a function of the reaction time. The spectra were measured in hexane and scaled to unity at 800 nm.

In order to study the evolution of the particle size, the reaction snapshots were analyzed by TEM (Figure 2.11). At the early stages of the reaction, *i.e.* after 30 - 45 minutes, the particles were poorly crystalline as indicated by their shape. Furthermore, they showed a broad size distribution ranging from the sub-nanometer range to ca 30 nm (Figure 2.11a - b). Nonetheless, particles of similar sizes already started to order hexagonally upon drying on the TEM grid, so that a sorting according to size took place (Figure 2.11b). According to literature, the reaction is finished after a reaction time of 60 minutes.<sup>[106]</sup> This was displayed by the sharp size distribution, which promoted the formation of self-assembled 3D superlattices (Figure 2.11c). The size distribution was sharpened even more after a reaction time of 90 minutes (Figure 2.11d), as was indicated by the increase in spectral intensity. However, any further prolongation of the reaction time did not translate into continued growth of the particles. This became evident by the decrease in spectral intensity after 105 minutes and 120 minutes (inset of Figure 2.10) as well as by the decreased diameter and broadened size distribution determined by TEM analysis (Figure 2.11e - f).

Within the first 90 minutes of the reaction, the kinetically driven focusing effect actively reduced the size distribution as confirmed by TEM and UV-VIS spectroscopy. This focusing effect was described for the first time by Peng and co-workers for CdSe nanocrystals.<sup>[121]</sup> In general, this process is valid for a high degree of supersaturation and is dominant as long as the growth is diffusion controlled. As soon as the degree of supersaturation decreases even further, Ostwald ripening becomes more prominent.<sup>[72]</sup>

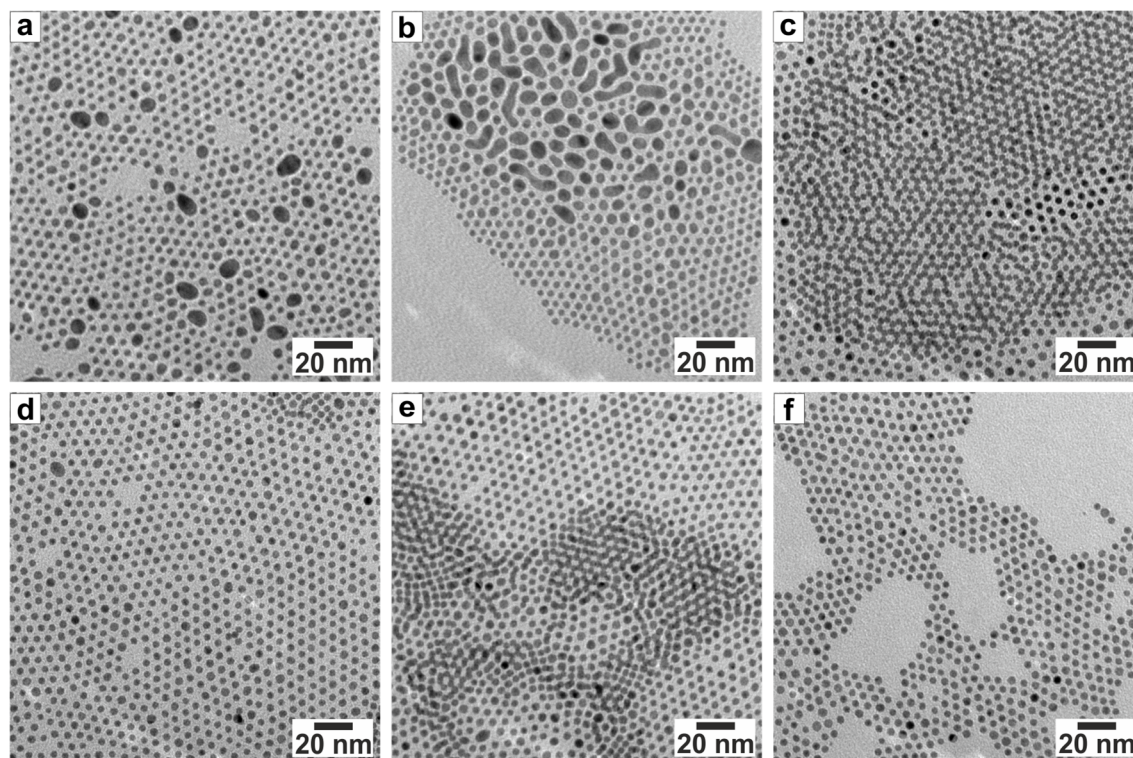


Figure 2.11: TEM micrographs of reaction snapshots of the formation of Au nanoparticles at room temperature showing the temporal evolution. The nanoparticles were purified from the reaction mixture after a) 30 min, b) 45 min, c) 60 min, d) 75 min, e) 90 min, and f) 120 min, respectively, subsequent to injection of the reduction solution.

The comparison of UV-VIS and TEM analysis summarizes the formation of the gold particles (Table 2.1). In addition to the diameter and its standard deviation determined by measuring TEM images, the absorption maximum of the surface plasmon resonance as well as the spectral absorption, normalized to the absorption after 90 minutes, illustrated the evolution.

Table 2.1: Comprehensive analysis of Au snapshots by TEM and UV-VIS spectroscopy. \*The determination of the diameter by analysis of TEM images was not performed for the snapshots taken after 30 min and 45 min, as the samples were too polydisperse to give a meaningful result.

Reaction time	Diameter / nm	$\lambda_{max}$ / nm	$\frac{I(\lambda_{max})}{I(\lambda_{max}(t=90min))}$
30 min	---*	510	0.33
45 min	---*	514	0.40
60 min	$4.0 \pm 0.6$	510	0.69
75 min	$4.4 \pm 0.5$	511	0.82
90 min	$4.4 \pm 0.3$	512	1.00
105 min	$4.1 \pm 0.5$	511	0.84
120 min	$4.1 \pm 0.8$	509	0.59



## 2.2.4 Self-Assembled Superlattices of Gold Nanoparticles

Self-assembly on molecular size-scale, e.g. liposomes<sup>[122]</sup> or vesicles,<sup>[123]</sup> has attracted an enormous research interest. In recent years, it was extended to the assembly of nanoparticles, as the quality of the nanoparticle syntheses was tremendously improved. It reveals an important bottom-up technique to hierarchical structures with orders on different length scales. A key aspect of self-assembly is the organization of nanoparticles into ordered, macroscopic structures, which is determined by either direct interaction or directed by a template or an external field. The resulting structures are often described to be in thermodynamic equilibrium as the ordering displays a minimum in the system's free energy. In fact, this becomes possible due to the large variety of syntheses yielding highly monodisperse nanoparticles.<sup>[124,125]</sup> Nanoparticles are taken as the atoms and molecules of prospective materials.<sup>[126,127]</sup> Thus, one of the new goals in current nanoscience is the development and understanding of the self-assembly of nanoscaled compounds.<sup>[128]</sup> Nanoparticle superlattices behave as isotropic bulk metamaterials, which is of particular interest, as the tunable properties of the nanoparticles can be applied to dictate the characteristics of the colloidal crystal. Ordered colloids or colloidal crystals have been the focus of research for more than 50 years, as they enable the investigation of new collective physical phenomena.<sup>[129,130]</sup> The most prominent example of colloidal crystals are opals, as they are found in nature. Their iridescence is caused by Bragg diffraction of light by 3D arrays of monodisperse SiO<sub>2</sub> particles.<sup>[131]</sup> Further, coupling effects by plasmonic nanoparticles in close proximity have been shown to result in enhanced plasmonic heating,<sup>[132,133]</sup> hot spots for surface enhanced Raman scattering (SERS),<sup>[134,135]</sup> and fluorescence enhancement.<sup>[136,137]</sup> Self-assembled nanostructures enable the fabrication of plasmonic waveguides, focusing lenses, light generators, and optical switches, even though bottom-up self-assembly is rarely applied for industrial use.<sup>[138]</sup>

Independent of their size scale, hydrophobic colloids show an inherent tendency to self-organize, which supplies a general technique for new nanomaterials. Here, a concentration-dependent drying pattern was observed, when a drop of a colloidal solution of the as-prepared monodisperse Au nanoparticles dried on a surface. High-quality, long-range ordering was obtained for oleylamine-functionalized nanoparticles (Figure 2.12a). The interparticle distance was determined to be  $1.6 \text{ nm} \pm 0.5 \text{ nm}$ , which was in good accordance with literature. The same behavior was reported<sup>[132]</sup> by Bigioni *et al.* for low concentrations of gold nanoparticles functionalized with 1-dodecanethiol when the solution was not thoroughly cleaned of excess ligand.<sup>[139]</sup> The surface coating makes the particles softer and more deformable, such that the assembly can be manipulated.<sup>[140]</sup> The interparticle distance is controlled by the van der Waals attraction between the particles and the ligand coating. In addition, the steric repulsion gains in importance, when particles come into too close contact, thus, preventing further interdigitation.<sup>[141]</sup>

If the solution was thoroughly cleaned of excess ligands or the concentration of colloidal particles was significantly increased, no monolayer formation was observed. Bare nanoparticles have a higher surface energy as well as strongly attractive van der Waals forces leading to aggregation in solution.<sup>[140]</sup> The purification was performed by repeated precipitation with methanol, centrifugation, and dissolution in hexane. Consequently, the nanoparticles formed three-dimensional ordered nanoparticle assemblies, so-called superlattices (Figure 2.12b, c). This was reported in the same way for CdSe nanocrystals, resulting in 5 to 50  $\mu\text{m}$  3D quantum dot superlattices.<sup>[107]</sup> Thereby, a concentration-dependent behavior can be discussed in terms of the evaporation rate. The formation of a monolayer is controlled by rapid evaporation arranging the particles close to the air-liquid interface as well as attractive forces in between the particles.<sup>[139]</sup>

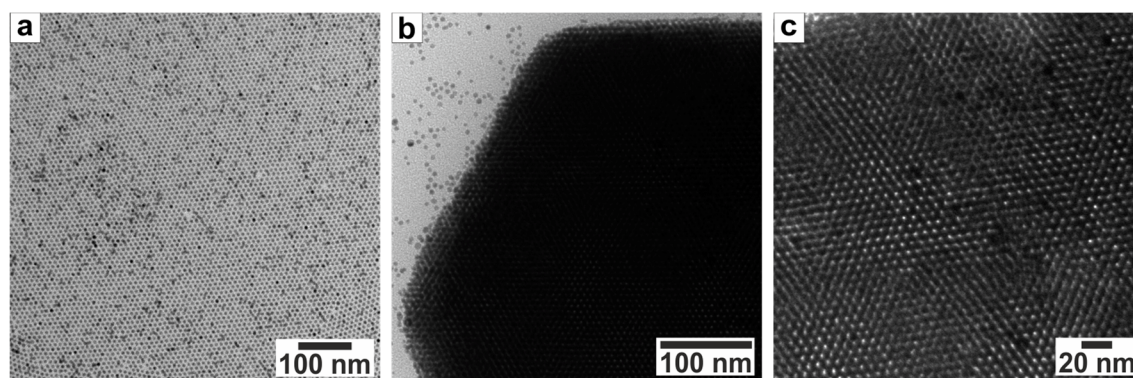


Figure 2.12: TEM images of self-assembled Au nanoparticles: a) high quality, long-range ordered monolayer of  $6.4 \text{ nm} \pm 0.4 \text{ nm}$  Au nanoparticles, b) faceted colloidal crystal, and c) 3D superlattice demonstrating the triangular shape contrast typical for *hcp* ordering.

Common to a large variety of nanoparticle superlattices is the sixfold symmetrical arrangement of the particles. Careful attention must be paid, as this configuration corresponds to either the *fcc*  $(111)_{\text{SL}}$  or the *hcp*  $(0001)_{\text{SL}}$  direction. In order to prove the stacking order, tilting of the TEM specimen to another low index zone axis is essential.<sup>[142]</sup> In previous studies the nanoparticle organization was observed to be affected by several parameters such as core structure or ligand chain length. Hexagonal close-packed nanocrystal superlattices are predominantly found for polycrystalline nanoparticles and when no directional ordering is induced by ligand coatings. Therefore, the superlattices formed by larger, polycrystalline particles synthesized within this work, especially when prepared using the seeding-growth technique, were found to be *hcp* ordered (Figure 2.6). Face-centered cubic structures with long-range translational and orientational ordering is preferred by single-crystalline nanoparticles dictated by bundling and interdigitation of the ligand coating.<sup>[108,141]</sup> Thus, the gold nanoparticles with a core size of ca. 4 nm, which were determined to be mixed single- and polycrystalline, realized both stacking alternatives (Figure 2.13).

The colloidal crystals formed upon stacking monolayers of hexagonally arranged uniform gold nanoparticles finally reached a hexagonal close-packed structure, as can be seen in Figure

2.13a - c. Further, the perfectly ordered A-B stacking of two hexagonal ordered monolayers is enlarged in Figure 2.13d. The triangular phase-contrast, clearly visible in Figure 2.13d and e, is characteristic for *hcp* ordering.<sup>[108]</sup> However, a small area of *fcc* packed nanoparticles showing the (100)<sub>SL</sub>-face was observed in Figure 2.13e as well.

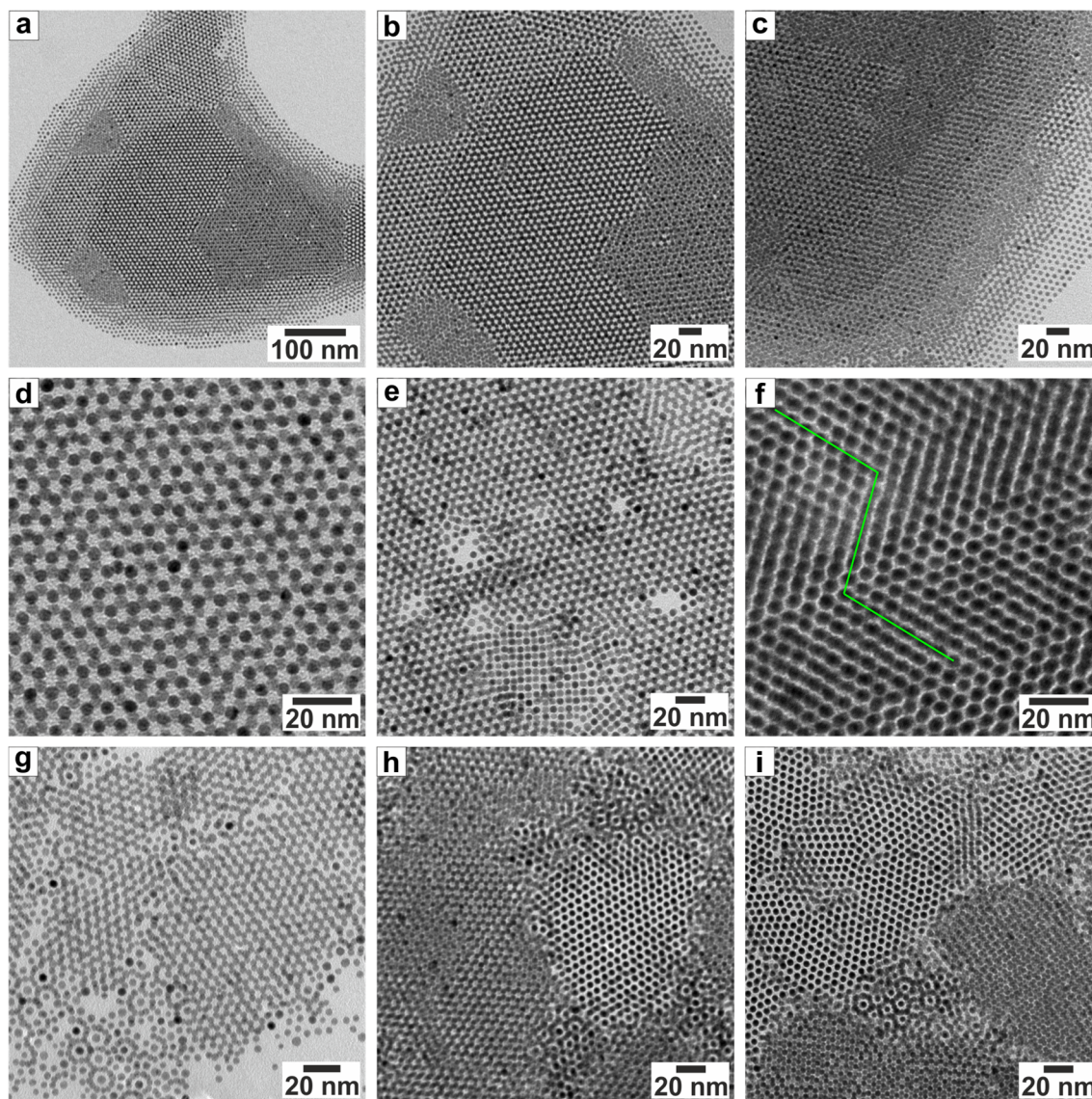


Figure 2.13: TEM images of self-assembled 3D superlattices of assorted samples of oleylamine-functionalized 4 nm Au nanoparticles formed spontaneously upon drying a colloidal solution in hexane on TEM grids.

Aside from perfectly-ordered nanoparticle assemblies, all types of defects known for bulk crystals can be found for superlattices as well.<sup>[142]</sup> For instance, slip planes were observed as forming a perfect angle of  $107^\circ \pm 1^\circ$ , indicated by the green lines in Figure 2.13f. The resulting domains exhibited a twin relationship as was reported for *fcc* packed nanoparticles oriented along the (110)<sub>SL</sub> plane. Moreover, Moiré patterns are not only known in electron diffraction patterns, but can also be obtained in self-assembled nanoparticle superlattices. This “donut ring contrast”<sup>[142]</sup> surrounding the center of rotation emerged due to the rotation of a hexagonal packed layer by  $30^\circ$  and its stacking on another hexagonal packed layer. This was observed for

the stacking of two monolayers (Figure 2.13g) as well as for a higher degree of stacking (Figure 2.13h - i). In the latter case, the Moiré pattern was observed as a delineation separating two differently oriented superlattices from each other, while the major part of the superlattices assumed the (110)<sub>SL</sub> face.

## 2.3 Platinum Nanoparticles

For industrial research, the underlying research interest behind fabrication of Pt nanoparticles was the optimization of the amount and activity of the expensive, but exceptionally well-performing catalyst material.<sup>[70]</sup> The commonly used approach for Pt nanoparticles is the polyol process: Pt nanoparticles are obtained by reduction of hydrogen hexachloroplatinate(IV) in various alcohols in the presence of polyvinylpyrrolidone (PVP) as stabilizing agent at elevated temperatures. This method enables the formation of various morphologies of Pt nanoparticles, ranging from spheres and star-shaped particles to branched multipods and nanowires, which have not been accessible for a long time.<sup>[143]</sup> Although various techniques have been developed, the synthesis of monodisperse, size- and shape-tunable Pt nanoparticles has rarely been reported. Substantial progress was accomplished by Wang *et al.*, as they reported a general approach to size- and shape-controlled Pt nanoparticles by thermal decomposition of an organic-platinum precursor complex in hydrophobic solvents.<sup>[144]</sup>

### 2.3.1 Morphology of Pt Nanoparticles

Platinum nanoparticles were prepared according to an established procedure. Single-crystalline nanoparticles formed upon thermal decomposition of platinum(II) acetylacetonate, where the nucleation was promoted by the hot-injection of Fe(CO)<sub>5</sub> at 190 °C. This was reported to enhance control over the size distribution as well as the morphology of the particles. Furthermore, the temperature, at which the injection took place, was found to determine the morphology of the particles. The particles formed perfect cubes at elevated temperatures, whereby the shape gradually changed to truncated cubes and polyhedra upon decreasing temperature.<sup>[144]</sup>

Here, the obtained Pt nanoparticles showed truncated cubic morphology (Figure 2.14). The size distribution was uniform with a core size of 5.6 nm ± 0.5 nm. Conversely, Wang *et al.* described the formation of 3 nm truncated cubes upon injection at 180 °C, while an increased core diameter was accomplished by lowering the injection temperature to 120 °C.<sup>[144]</sup> Thus, the obtained morphology was in good accordance with literature,<sup>[145]</sup> though the core sizes differed.

The electron diffraction pattern (inset Figure 2.14c) displayed rather diffusive rings, characteristic for nanoparticles.<sup>[146]</sup> HR TEM proved the particles to be single crystalline. In contrast to the twinned structures of Au nanoparticles discussed earlier, these structures are

rarely known for Pt. This is attributed to the elevated internal strain energy corresponding to twinned Pt nanocrystals.<sup>[143,146,147]</sup>

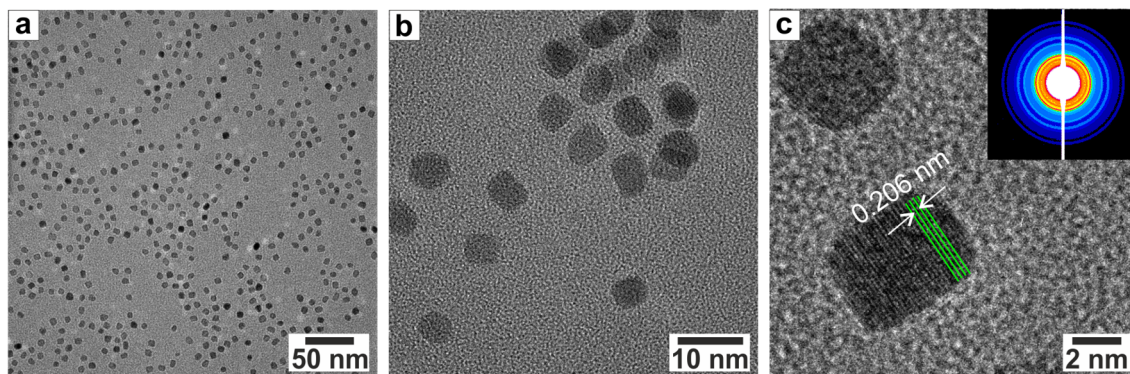


Figure 2.14: HR TEM images of Pt nanoparticles showing their uniform size distribution (a) and the single-crystalline character of the particles (b, c). Inset of c: HR TEM electron diffraction pattern corresponding to c). The FFT image is shown in pseudo-colors (ImageJ, look up table: 16 color). The HR TEM analysis was performed by [REDACTED].

The slow evaporation of the solvent at preparation of the TEM grids resulted in a (100) textured assembly, as can be taken from the dominant (200) peak at  $0.51 \text{ \AA}^{-1}$  (Figure 2.15) as well as the lattice fringes visible in HR TEM images (Figure 2.14c).<sup>[144]</sup> The large rings in electron diffraction covered the reflection of the (220), (311), and (222) planes.<sup>[146]</sup> The distance between two lattice fringes was 0.206 nm, corresponding to (200) spacing of 0.196 nm in *fcc* Pt. The severe conformity of the crystal structure of Pt nanoparticles with bulk Pt suggests a *fcc* structure for Pt nanoparticles as discussed in literature.<sup>[24,144,147]</sup>

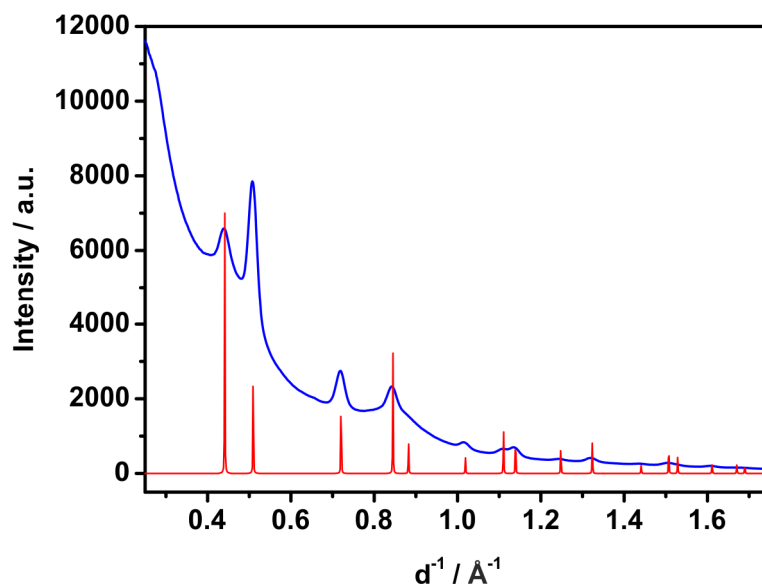


Figure 2.15: Electron diffraction of Pt nanoparticles (blue line) referred to simulated pattern of Pt (red line). The electron diffraction analysis was performed by [REDACTED].

Converse to the observed superlattices of Au nanoparticles (see page 19), monodisperse Pt nanoparticles showed barely any tendency to form hexagonal monolayers, which can be attributed to the morphology of the particles. Instead, a square lattice of truncated nanocubes was observed according to the particles morphology, even though only short ranged

(Figure 2.16). The perfect square lattice is commonly observed for highly faceted Pt nanocubes. As these truncated cubes represent the intermediate morphology between spheroidal and perfect cubes, so that a transition between the hexagonal *fcc* and the quadratic pattern was often observed. This is usually accompanied with the loss of long range order.<sup>[148]</sup>

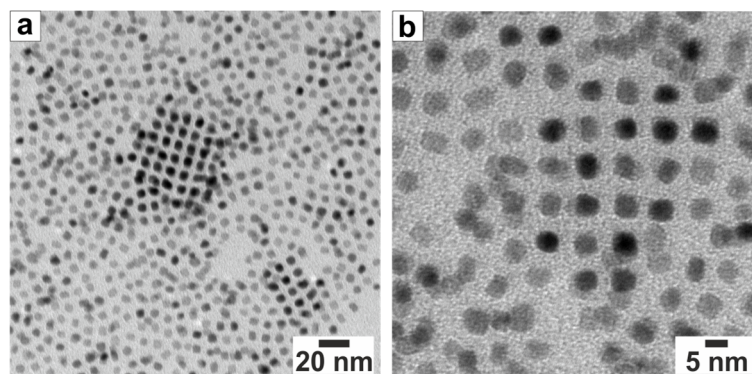


Figure 2.16: TEM images of truncated Pt nanocubes revealing their tendency to square superlattices accompanied with loose hexagonal order, as suggested by their morphology.

### 2.3.2 Optical Properties of Pt Nanoparticles

Even more strikingly different than the crystal structure of Pt nanoparticles as compared to Au is their optical performance. According to dipole calculations utilizing Mie's theory of Creighton and co-workers, spheroidal 10 nm Pt nanoparticles should exhibit a weak absorption band near 200 nm. In addition, the absorption spectra of prolate spheroidal Pt nanoparticles in water were calculated to show a faint longitudinal dipole resonance centered around 400 nm.<sup>[89]</sup> UV-VIS spectra of the as-prepared Pt nanoparticles were only recorded between 300 and 800 nm due to experimental restrictions. Nevertheless, the absorption spectrum revealed the predicted faint shoulder of absorption at ca 400 nm (Figure 2.17). This was attributed to the cubic structure of the Pt nanoparticles, as their morphology was neither spheroidal nor perfectly square.

Furthermore, the spectral intensity of the absorption of Pt was heavily reduced as compared to Au nanoparticles (inset of Figure 2.17). This was reported to be common to more than half of the metallic elements, which show no prominent absorption bands in the range between 200 and 900 nm. The observed absorption features for these elements were attributed to  $5d \rightarrow 6sp$  interband transitions of less free-electrons (compare with optical characteristics of Au nanoparticles, page 12). Caused by their dielectric function at visible wavelengths, the absorption spectrum is rather flat and featureless.<sup>[89]</sup>

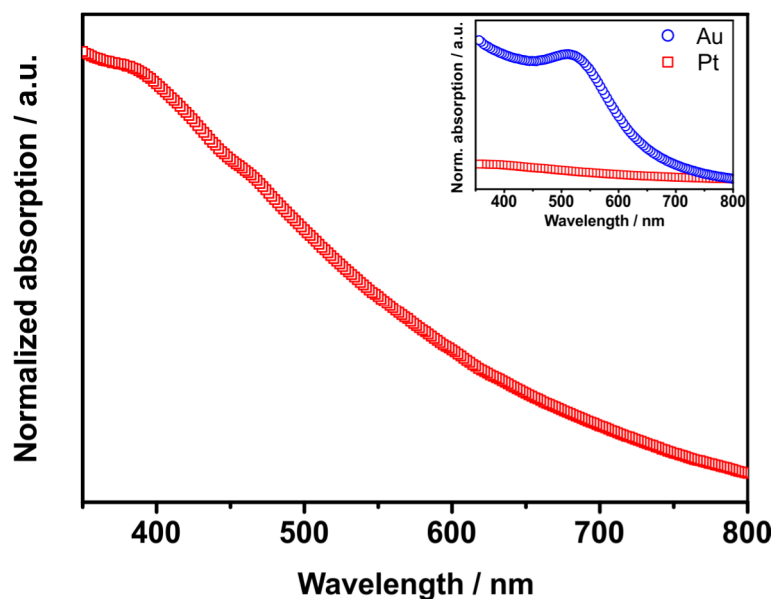


Figure 2.17: UV-VIS spectrum of  $5.6 \text{ nm} \pm 0.5 \text{ nm}$  Pt nanoparticles. Inset: UV-VIS spectrum of Pt nanoparticles as compared to Au nanoparticles of comparable size. The spectra were measured in hexane and normalized at 800 nm.

## 2.4 Gold-Platinum Alloy Nanoparticles

Traditionally, intermetallics and alloys are prepared using metallurgical techniques, which are not suitable for nanoparticle synthesis. Among the solution-based chemical syntheses including co-reduction, thermal decomposition, seeding-growth, galvanic replacement, and noble-metal-induced-reduction, here, the co-reduction technique was chosen for the preparation of  $\text{Au}_x\text{Pt}_{1-x}$  nanoparticles. Wang and co-workers reported a seeding-growth technique starting from Pt nanoparticles. They obtained various morphologies of composite nanoparticles such as pear-like, peanut-like, or clover-like Pt- $\text{Au}_n$  nanoparticles ( $n = 1, 2, 3-4$ ).<sup>[149]</sup> In general, a key issue for bimetallic nanoparticles is their morphology-controlled synthesis, which is even more challenging than for monometallic nanoparticles. Obviously, their structure is complicated and multiform due to the placement of a second element, ranging from core/shell, heterostructure, and intermetallic to alloyed arrangement.<sup>[90]</sup>

### 2.4.1 Synthesis of Gold-Platinum Alloy Nanoparticles

The chemical analogy of gold and platinum was exploited to transfer the previously discussed synthetic procedure of Au to  $\text{Au}_x\text{Pt}_{1-x}$  nanoparticles. This principle of transferring preparation techniques from Au nanoparticles to the  $\text{Au}_x\text{Pt}_{1-x}$  alloy is known in literature for different chemical protocols. Further, the formation of  $\text{Ag}_x\text{Au}_{1-x}$  alloy nanoparticles by reduction utilizing borane complexes similar to Au nanoparticle methods was reported.<sup>[105]</sup> Due to the extraordinary size control in the technique discussed for Au nanoparticles (see page 9), this protocol was transferred to the alloy nanoparticles. Furthermore, the co-reduction process in solution was shown to be very effective regarding the formation of high-quality and size-tunable

nano-alloys.<sup>[90]</sup> Thus, a precursor solution containing a mixture of tetrachloroauric acid and hexachloroplatinate in tetralin and oleylamine was prepared. Subsequently, a reduction solution of *tert*-butylamine borane complex was injected rapidly. The obtained particles were uniform in size (Figure 2.18a) and polycrystalline, as was identified by HR TEM images (Figure 2.18b - c). Similar to Au nanoparticles, fivefold twinning defects were observed, while a reduced tendency toward the formation of twins as compared to Au nanoparticles was observed. This was ascribed to the alloy formation as Pt nanoparticles nucleate preferably in the form of single crystalline nanoparticles due to their high twinning strain (compare page 22).

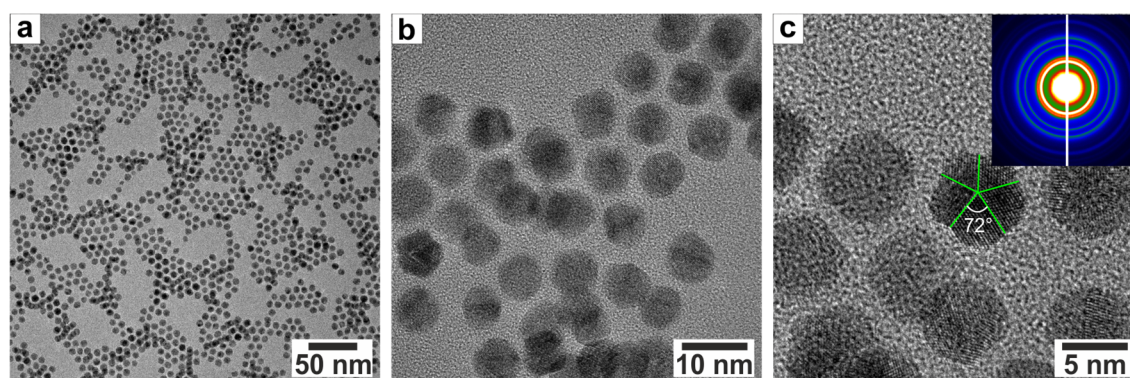


Figure 2.18: HR TEM images of  $Au_xPt_{1-x}$  nanoparticles showing the uniformity of the size distribution (a). The polycrystallinity is evident due to the typical fivefold defects known for Au nanoparticles (b, c). Inset of c): Electron diffraction pattern of corresponding HR TEM image. The FFT image is shown in pseudo-colors (ImageJ, look up table: 16 color). The HR TEM analysis was performed by [REDACTED].

The formation of the nanoparticles was observed by a color change in the precursor solution just as for pure Au nanoparticles, though the color of the colloidal solution was strongly dependent on the ratio of the metal precursors. The more hexachloroplatinate was used, the more obvious was the color change of the colloidal nanoparticle solution from ruby red to dark brown. Nevertheless, the precise size control was successfully transferred to the bimetallic system. As was discussed earlier, the core diameter of the nanoparticles could be increased by seeding-growth, but not only the core size was increased, also the uniformity of the size distribution was enhanced due to the size-focusing effect (Figure 2.19a - b).

Aside from the fivefold twinning of the nanoparticles, the characteristics of Au nanoparticles dominated the formation of self-assembled monolayers and superlattices of  $Au_xPt_{1-x}$  as well (Figure 2.19b - c). This became obvious as the particles formed hexagonally-ordered monolayers in the case of sufficiently sharp size distributions. Increasing the concentration further resulted in the self-assembled 3D superlattices with *hcp* structure as discussed for large, polycrystalline Au nanoparticles.



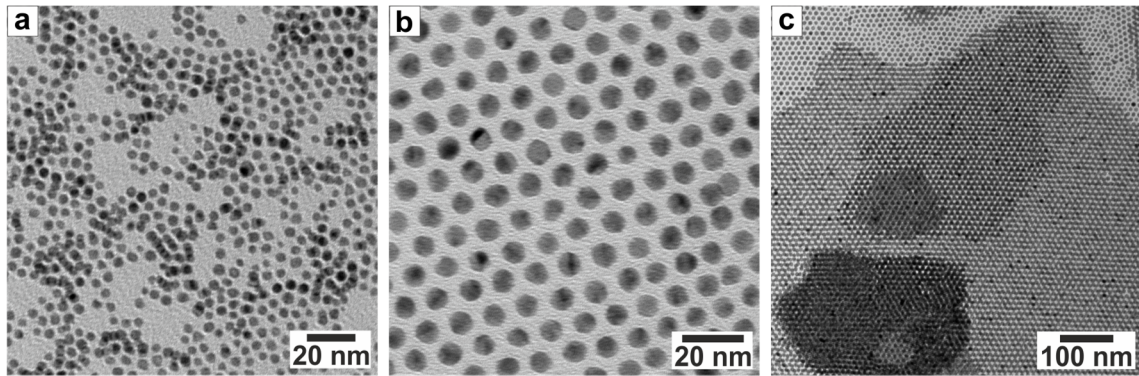


Figure 2.19: TEM images of  $\text{Au}_x\text{Pt}_{1-x}$  nanoparticles displaying the increase in diameter as well as the focusing effect upon seeding growth. a) Primary nanoparticles with a core size of  $4.0 \text{ nm} \pm 0.6 \text{ nm}$ , b) subsequent to enlargement with a core size of  $8.0 \text{ nm} \pm 0.5 \text{ nm}$ ; c) the nanoparticles showed an enhanced tendency to form hexagonally-ordered monolayers and superlattices due to the sharpened size distribution.

## 2.4.2 Compositional Analysis of Gold-Platinum Nanoparticles

A composition-controlled synthesis is of particular importance as the physical and chemical properties of alloy nanoparticles are strongly dependent on the composition aside from the known dependency on the core size. Thus, the composition was adjusted by changing the molar ratio of the two metal precursors. Nevertheless, attention had to be paid as the composition of the final product is not necessarily exactly consistent with the used molar ratio of metal precursor. In order to examine the actual amount of gold and platinum within the nanoparticles, SEM EDS measurements were performed (Figure 2.20).

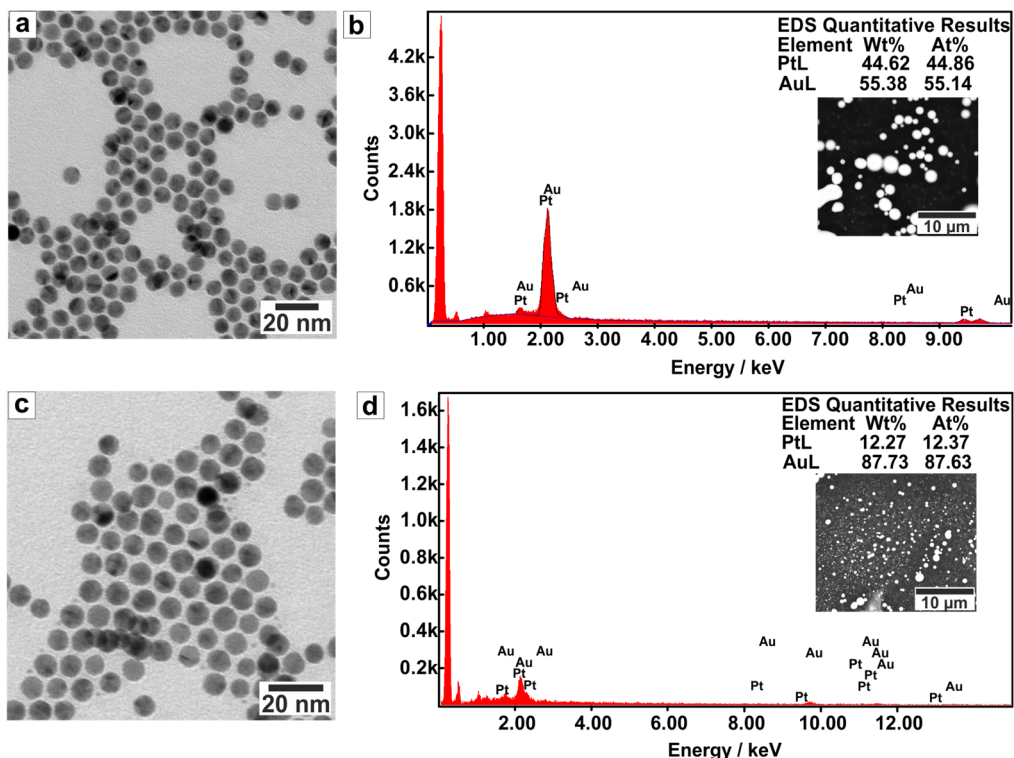


Figure 2.20: TEM images and compositional analysis of  $\text{Au}_x\text{Pt}_{1-x}$  nanoparticles by SEM EDS with corresponding SEM images as insets: a), b)  $\text{Au}_{0.55}\text{Pt}_{0.45}$  and c), d)  $\text{Au}_{0.88}\text{Pt}_{0.12}$ . The SEM EDS measurements and analysis were performed by [REDACTED].

The results of the compositional analysis are shown in Table 2.2 in comparison to the molar ratio of metal precursors applied to two exemplary measurements. It was obvious that tetrachloroauric acid was preferentially reduced, as was expected by its higher redox potential of 1.498 eV for  $\text{Au}^{3+}/\text{Au}$  over 1.180 eV for  $\text{Pt}^{2+}/\text{Pt}$ . Therefore, the content of platinum was significantly decreased as compared to the molar ratio. Nevertheless, upon increasing the molar ratio, a substantial increase in the platinum content was obtained.

Table 2.2: Compositional analysis of  $\text{Au}_x\text{Pt}_{1-x}$  nanoparticles based on the molar ratio of metal precursors used in the synthesis and subsequent SEM EDS analysis.

	Molar ratio of metal precursors	Composition according to SEM EDS
$\text{Au}_{0.88}\text{Pt}_{0.12}$	1.00 : 0.42	1.00 : 0.14
$\text{Au}_{0.55}\text{Pt}_{0.45}$	1.00 : 1.20	1.00 : 0.82

According to LaMer and co-workers, monodisperse particles are obtained upon effective separation of nucleation and growth (see page 14).<sup>[71]</sup> This condition is even more challenging for bimetallic nanoparticles. The nucleation behavior of two different metals varies based on their redox potentials and chemical behavior, as can be seen from the differences in Table 2.2. Thus, the formation of core/shell structures becomes feasible by the successive nucleation of the different precursors. In order to distinguish between an alloy and a core/shell structure within the nanoparticles, HR TEM electron diffraction was applied to  $\text{Au}_{0.55}\text{Pt}_{0.45}$  nanoparticles (Figure 2.21). In the case of a core/shell structure, a peak splitting would be observable due to the formation of separate crystal lattices. As this was not the case, this observation in combination with the reduced tendency of twinning defects can be taken as an indication for alloy nanoparticles. The comparison of the electron diffraction pattern to the one of gold particles showed only slight differences (inset Figure 2.21). As the morphology of the alloy nanoparticles was dominated by the twinning of gold, a preference of the orientation similar to gold particles was observed. The diffraction peak at lowest reciprocal distance, ascribed to the (111) plane, was the most intense. Thus, Au as well as  $\text{Au}_x\text{Pt}_{1-x}$  nanoparticles tended to align with the (111) plane facing the TEM grid. This was unlike the alignment of Pt nanoparticles, where (100) textured orientation was observed (compare with Figure 2.15). As reported in previous studies, the bimetallic nanoparticles showed alloy-like behavior across the whole compositional range, which is in sharp contrast to the miscibility gap of the analogous bulk alloy.<sup>[88]</sup>

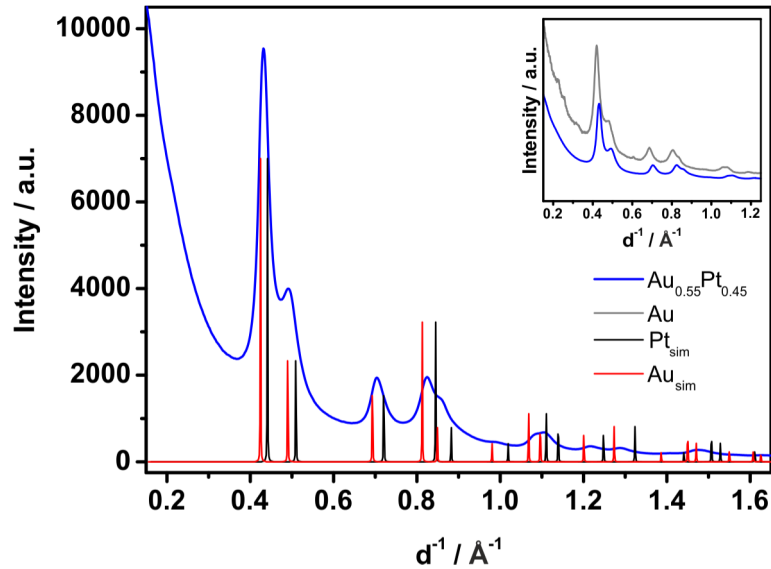


Figure 2.21: Electron diffraction of  $\text{Au}_{0.55}\text{Pt}_{0.45}$  nanoparticles as compared to simulated Au and Pt pattern. Inset: Electron diffraction of Au nanoparticles and  $\text{Au}_{0.55}\text{Pt}_{0.45}$  nanoparticles revealing a slight shift of the diffraction pattern. The electron diffraction analysis was performed by [REDACTED].

### 2.4.3 Optical Properties of Gold-Platinum Alloy Nanoparticles

Alloy nanoparticles are known for their tunability of surface plasmon resonance frequency by the composition of the alloy. This was reported for  $\text{Au}_x\text{Ag}_{1-x}$  alloy nanoparticles by Wang *et al.*, as the maximum of absorption was gradually shifted from 520 nm to 400 nm.<sup>[150]</sup> In the case of  $\text{Au}_x\text{Pt}_{1-x}$  nanoparticles, we observed a different effect of the compositional changes (Figure 2.22). As the content of platinum was increased, the spectral intensity of the absorption maximum was significantly decreased (inset of Figure 2.22).

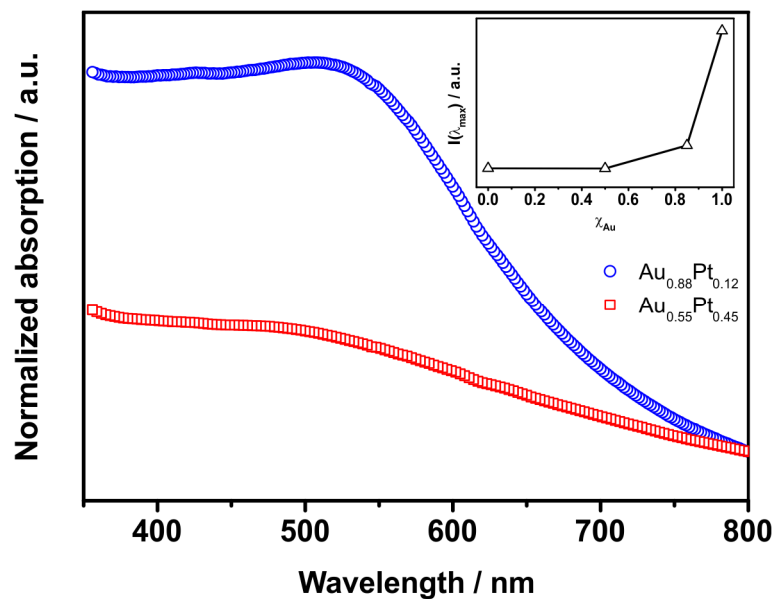


Figure 2.22: UV-VIS spectra of  $\text{Au}_x\text{Pt}_{1-x}$  nanoparticles showing the composition-dependent damping of the surface plasmon resonance. Inset: Spectral intensity at the absorption maximum as a function of the composition of the  $\text{Au}_x\text{Pt}_{1-x}$  alloy nanoparticles. The spectra were measured in hexane and normalized at 800 nm.

This corresponded to the strong blue shift of the surface plasmon resonance for pure Pt nanoparticles. Upon increasing the Pt content, more energy was needed for the excitation of the giant dipole oscillation. Thus, the spectral absorption in the visible range decreased. The results further confirmed that  $\text{Au}_x\text{Pt}_{1-x}$  alloy nanoparticles were obtained, rather than core/shell structured or a mixture of Au and Pt nanoparticles.

## 2.5 Conclusion

In conclusion, we investigated the synthesis of spherical Au nanoparticles by reduction in an aprotic solvent with precise size control in the range between 3 nm and 9 nm, where the particle size increased with decreasing temperature. The mechanism of formation was presented to be in accordance with LaMer's model of homogeneous nucleation, as the separation of nucleation and growth was well defined. In order to obtain larger Au nanoparticles, we developed a seeding-growth technique, which led to monodisperse, high-quality nanoparticles with diameters up to 20 nm. The surface plasmon resonance with its central absorption maximum at ca 520 nm altered the optical properties size-dependently: the spectral intensity was observed to increase with size and coincided with diminution of damping effects. Further, the high quality of Au nanoparticles was demonstrated by the formation of self-assembled superlattices. The amount of excess ligands present in the colloidal solution controlled the preference for 2D hexagonally-ordered layers over 3D self-assembled superlattices (or vice versa) in conjunction with the concentration of nanoparticles.

Further, monodisperse, single-crystalline Pt nanoparticles were obtained by a hot-injection method. In accordance with their truncated cubic shape, square superlattices were predominantly formed with only loose hexagonal arrangements. In comparison to Au nanoparticles, Pt nanoparticles revealed a less intense response to visible light due to the hypsochromic shift of the surface plasmon resonance.

We transferred the synthetic procedure of Au nanoparticles to composition-tunable  $\text{Au}_x\text{Pt}_{1-x}$  alloy nanoparticles, where precise control over size and shape were retained. The characteristics of the alloy nanoparticles were observed to present the synergy of both Au and Pt. This was obvious for the optical properties as well as the structure of the nanoparticles. The alloy nanoparticles showed a reduced twinning tendency as compared to the typical fivefold twinning of Au nanoparticles, which was weakened by the high twinning strain of Pt.

In conclusion, the size- and composition-tunable synthesis of plasmonic nanoparticles was demonstrated, which allowed their sophisticated application as seed particles for the formation of heterodimer nanoparticles in a seed-mediated process.

## 2.6 Experimental Section

**Materials.** All reactions were carried out under argon atmosphere using commercially available reagents without any further purification: Tetrachloroauric(III) acid hydrate (99.9 %-Au,  $\text{HAuCl}_4 \cdot (\text{H}_2\text{O})_x$ ), dihydrogen hexachloroplatinate(IV) (99.9 % metal basis,  $\text{H}_2\text{PtCl}_6$ ), and platinum(II) acetylacetonate (98 %,  $\text{Pt}(\text{acac})_2$ ) were purchased from ABCR. Tetralin (1,2,3,4-tetrahydronaphthalene, anhydrous, 99 %), *tert*-butylamine borane complex (97 %, TBAB), 1-octadecene (technical grade, 90 %), and iron(0) pentacarbonyl (>99.99 % trace metal basis,  $\text{Fe}(\text{CO})_5$ ) were purchased from Sigma Aldrich. 2-Propanol, acetone, ethanol, methanol, heptane, hexane, oleic acid (reagent grade), and oleylamine (80 - 90 %) were purchased from Fisher Scientific.

In order to control the heating rate, self-built heating controllers were used. These were composed of a control unit (KS40, type 9404 407 40001, Philips) and a temperature sensor (type S/S-316RS Components GmbH) connected to a heating mantle (neoLab-Pilz® standard heating mantle, 230 V, 150 W,  $T_{\text{max}} = 450 \text{ }^\circ\text{C}$ ).

**Synthesis of Au NPs.** Monodisperse Au nanoparticles were prepared according to Peng *et al.*<sup>[106]</sup> with some modifications. A precursor solution containing 0.25 mmol  $\text{HAuCl}_4 \cdot (\text{H}_2\text{O})_x$ , 10 mL tetralin, and 10 mL oleylamine was prepared at room temperature and stirred for 15 min under a gentle argon stream. 0.5 mmol TBAB was dispersed in a mixture of 1 mL oleylamine and 1 mL tetralin by ultrasonication (5 min) and quickly added to the precursor solution under vigorous stirring. Stirring was continued for 1 h before the particles were precipitated by addition of methanol and collected by centrifugation (9000 rpm, 10 min). The particles were washed twice using hexane and ethanol:methanol (1:1).

By lowering the reaction temperature to 10 °C, the diameter of the nanoparticles was increased from 4 nm at room temperature to 8 nm.

Further increase in the diameter was obtained by a seeding-growth procedure. A growth solution containing 0.5 mmol  $\text{HAuCl}_4 \cdot (\text{H}_2\text{O})_x$ , 10 mL toluene, and 20 mL oleylamine was prepared at room temperature. Au nanoparticles were dissolved in 10 mL toluene and added to the growth solution under a gentle stream of argon. The reaction mixture was rapidly heated to 111 °C, held at reflux for 2 h, and passively cooled to room temperature by removing the heating mantle. The nanoparticles were precipitated with methanol, collected by centrifugation (9000 rpm, 10 min), and redissolved in hexane. The particles were washed twice using hexane and ethanol:methanol (1:1).

**Synthesis of Pt NPs.** Pt nanoparticles were prepared by thermal decomposition of platinum(II) acetylacetonate according to Wang and co-workers.<sup>[144]</sup> Briefly, 0.1 g  $\text{Pt}(\text{acac})_2$  was dissolved in a mixture containing 10 mL 1-octadecene, 1 mL oleic acid, and 1 mL oleylamine by heating up to 90 °C under a gentle argon stream. Subsequently, the temperature was raised

with a heating rate of 5 °C/min up to 190 °C, where 0.1 mL Fe(CO)<sub>5</sub> dissolved in 1 mL heptane was rapidly added. The reaction mixture was heated to 200 °C, and then cooled to room temperature after 1 h at 200 °C by removing the heating mantle. The nanoparticles were precipitated by 2-propanol, collected by centrifugation (9000 rpm, 10 min), and redissolved in hexane. The nanoparticles were washed twice using hexane and 2-propanol.

**Synthesis of Au<sub>x</sub>Pt<sub>1-x</sub> NPs.** Monodisperse Au<sub>x</sub>Pt<sub>1-x</sub> alloy nanoparticles were prepared by adjusting the synthesis of Au NPs. For Au<sub>0.55</sub>Pt<sub>0.45</sub> nanoparticles, a precursor solution containing 0.125 mmol HAuCl<sub>4</sub>·(H<sub>2</sub>O)<sub>x</sub>, 0.15 mmol H<sub>2</sub>PtCl<sub>6</sub>, 10 mL tetralin, and 10 mL oleylamine was prepared at room temperature and swiftly stirred for 15 min under a gentle argon stream. Subsequently, 0.5 mmol TBAB was dispersed in 1 mL oleylamine and 1 mL tetralin by ultrasonication (5 min) and quickly added to the precursor solution. The reaction was stirred for 1 h at room temperature before precipitating and washing the particles as described for Au nanoparticles.

**Nanoparticle Characterization.** The nanoparticles were characterized employing (high resolution) transmission electron microscopy ((HR) TEM), UV-VIS spectroscopy, high resolution synchrotron powder diffraction, and SEM EDS. Further technical details on employed instruments are elaborated in Chapter 4.4.1.

# 3

## Synthesis of Heterodimer Nanoparticles

This chapter contains parts of an adapted reproduction of *Journal of the American Chemical Society* **2014**, 136, 2473 – 2483,<sup>[54]</sup> reproduced with permission of the American Chemical Society Copyright 2014, and of a manuscript submitted to the *Beilstein Journal of Nanotechnology* linked to the final report of the DFG priority program SPP 1313 “Biological Responses to Nanoscale Particles”.<sup>[151]</sup>

### 3.1 Introduction

In recent years, there has been an increasing interest in design, synthesis, and properties of multifunctional nanoparticles owing to their special structure-property relationship.<sup>[9]</sup> The focus of research was expanded from single-component nanoparticles to hetero-nanoparticles with discrete domains of different materials fused together in a controlled fashion.<sup>[152]</sup> The synthesis of hetero-nanoparticles requires an even higher degree of synthetic control as compared to single-component nanoparticles. As the formation takes place in the “twilight zone” of kinetic and thermodynamic control, a precise balance is needed for the formation of the desired size and shape. On top of this, the evolution is complicated by the interplay of atomic diffusion and exchange, facet-specific reactivity, and the influence of interfacial strain.<sup>[36]</sup> Although, some major problems have been overcome by intelligent design of the synthetic procedure within the last decade,<sup>[36]</sup> the synthesis of well-defined heterodimer nanoparticles, specially designed for applications, is an ongoing endeavor.

Generally, hetero-nanoparticles are obtained by anisotropically-centered sequential growth of another component on one specific crystal plane of the seeding nanoparticle. In this case, it is crucial to suppress homogeneous nucleation of the second or third component, a competitive reaction to heterogeneous nucleation on the preformed or *in situ* formed seeds.

However, controlling synthesis at nanoscale remains challenging, as several aspects contribute to the product quality, which may differ significantly from bulk synthesis. Following classical theory of heterogeneous nucleation, this can be achieved by decreasing the concentration of the precursor below supersaturation, at which point the homogeneous nucleation would be favorable.<sup>[71]</sup> Furthermore, the additional Gibbs free energy term for the adhesive energy at the interface between the seeds and the overgrown particles has to be negative, as given for epitaxial growth.<sup>[37,153]</sup> Aside from that, seed particles often act as catalysts in the reaction, thus, lowering the energy for heterogeneous nucleation. This is caused by a charge transfer between the seeds and the newly nucleated components.<sup>[152]</sup>

An essential condition for the occurrence of heterogeneous nucleation is the matching of the lattice spacing of the components.<sup>[152]</sup> Heteroepitaxy has been used in gas-phase deposition to prepare functional hetero-structures for a long time, but has only recently been transferred to solution phase chemistry.<sup>[70]</sup> However, lattice mismatch is not only responsible for the preference of a hetero-nanostructure, it also controls the product's morphology through the extent of lattice mismatch. Nucleation and epitaxial growth are non-restricted for small differences in lattice constants. For large differences, however, the growth is confined to distinct crystal planes in order to minimize the lattice mismatch, which in turn leads to the formation of anisotropic structures.<sup>[154,155]</sup> At the same time, despite lattice match, it is possible to distinguish between phase-separated hetero-nanostructures and ternary phases, if a sufficient level of molecular control during synthesis can be exerted and the ternary phases exist according to the phase diagrams.<sup>[156–158]</sup>

Amongst the myriads of achievable hetero-nanostructures, dumbbell-like nanoparticles are second to none, as their well-defined morphology enables an even higher control over size- and shape-dependent properties and, thus, more sophisticated applications. The main synthetic routes for obtaining inorganic dumbbell-like heterostructures include heterogeneous nucleation,<sup>[145,159]</sup> asymmetric modification at interfaces,<sup>[160]</sup> and non-epitaxial deposition on the full surface of the first nanoparticle followed by thermal dewetting of the shell into a single domain.<sup>[154]</sup> Nevertheless, dumbbell-shaped heterodimer nanoparticles provide enormous advantages over spherical, desymmetrized nanoparticles due to the combination of intrinsic different surfaces with distinct reactivity. In recent years, non-hydrolytic approaches have been used to overcome the problems appearing in hydrolytic syntheses such as poor crystallinity, polydispersity in size, and little control over the morphology. The studies presented in the literature so far provide evidence of an enormous progress regarding the efficient synthesis of a plethora of pseudobinary metal-metal oxide hetero-nanoparticles<sup>[159,161]</sup> such as Pt@Fe<sub>3</sub>O<sub>4</sub>,<sup>[24]</sup> Pd@Fe<sub>3</sub>O<sub>4</sub>,<sup>[162]</sup> Au@Fe<sub>3</sub>O<sub>4</sub>,<sup>[153,163–166]</sup> Ag@Fe<sub>3</sub>O<sub>4</sub>,<sup>[167]</sup> Cu@Fe<sub>3</sub>O<sub>4</sub>,<sup>[156]</sup> FePt@MnO,<sup>[12]</sup> Au@MnO,<sup>[54,168]</sup> Ni@Fe<sub>2</sub>O<sub>3</sub>,<sup>[158]</sup> and Co@Fe<sub>2</sub>O<sub>3</sub>.<sup>[157]</sup>



Heterodimers with two nanoparticles sharing a common interface are synthesized in a very similar manner to core/shell type hetero-nanoparticles. However, in both cases the heterogeneous nucleation of a second or third component is taking place, limiting these techniques to material combinations where epitaxial growth is possible.<sup>[37,152]</sup> They are obtained via a seed-mediated route either using preformed or *in situ* formed seeds. A key step is the preparation of monodisperse seeding nanoparticles with distinct size and surface functionalization (see Chapter 2). For this purpose, separate preparation of seed particles is superior to a one-pot synthesis. However, the surface functionalization of the seeds is crucial, as it has to be compatible with the subsequent growth conditions. Furthermore, the binding strength can control epitaxial overgrowth of metal oxides on noble metal nanoparticles.<sup>[169]</sup> Aside from many experimental parameters such as temperature, heating profile, concentration, and precursor ratio, the solvent choice is a smart option to control the morphology. Yu *et al.* proposed an electronic transfer between the domains, once nucleation took place. Further heterogeneous nucleation is prevented, as the metal seed becomes electron deficient upon conjugation to an electron deficient metal oxide.<sup>[153]</sup> This is correct for non-polar solvents, but changes upon switching to polar solvents (Figure 3.1). In the majority of cases, they act as  $\pi$ -donors and contribute their electrons to the metal seeds. Thus, the electron deficiency is partially compensated for and additional nucleation is possible.

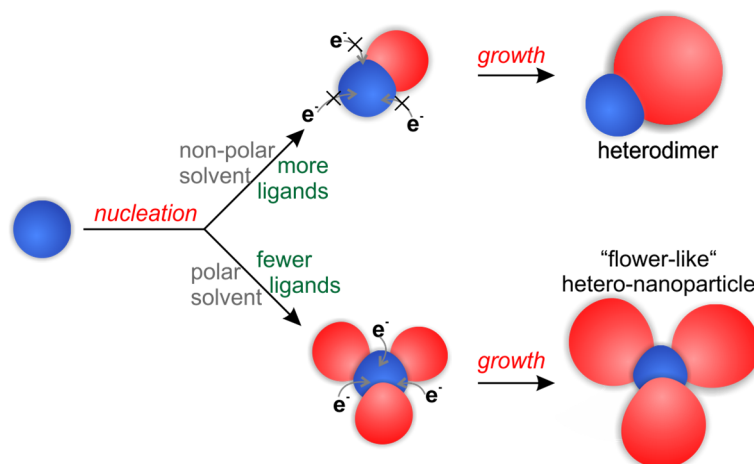


Figure 3.1: Schematic diagram showing the mechanism of formation of heterodimer nanoparticles in a non-polar solvent (top) and "flower-like" hetero-nanoparticles in a polar solvent (bottom).

Inspired by potential applications reported in literature and initial results from our group regarding several hetero-nanoparticle systems,<sup>[12,156–158,168]</sup> we chose Au@MnO and Au@Fe<sub>3</sub>O<sub>4</sub> heterodimer nanoparticles as the central focus of our research. There are three primary aims of this study: first, to establish a synthesis of Au@Fe<sub>3</sub>O<sub>4</sub> as well as Au@MnO heterodimer nanoparticles, which has not yet been reported in the latter case, second, to investigate the differences between the single component nanoparticles and the heterodimers, and, third, to examine the impact of the chemical composition. The epitaxial interaction of two components across a solid state interface is superior to single-component nanoparticles in three aspects:

(i) different functionalities can be included, whereby the sizes and parameters of the individual components are independently optimized; (ii) the intimate contact enhances characteristics and is even able to break natural constraints of single-phase materials; (iii) novel functions emerge, which are not available otherwise. The conjugation of two nanoparticles enables the maintenance of many material properties, which have critical length scales in the order of nanometers. On the other hand, the strong interaction of the two nanoparticles at the nanometer scale modulates physical and chemical characteristics from each individual component. Thus, the first two sections of this chapter will separately examine the synthesis and comprehensive characterization of Au@MnO as well as Au@Fe<sub>3</sub>O<sub>4</sub> heterodimers. It will then go on to analyze the two systems in terms of interaction between the two components across the interface. Therefore, our study contributes to the understanding of the nature of heterodimer nanoparticle interfaces, which is substantial, as they affect many physical and chemical properties. The final section demonstrates the general applicability of the as-described synthetic procedure to various metal nanoparticles, which enables the tailored design of heterodimer nanoparticles for various applications.

### 3.2 Au@MnO Heterodimer Nanoparticles

Gold-containing hetero-nanoparticles have become an active frontier of research based on their intense optical signal, chemical resistance, and their promising materials' characteristics for biomedical applications. For instance, their strong X-ray absorption coefficient makes them an ideal contrast agents for computed X-ray tomography.<sup>[40,41,80]</sup> Furthermore, they are under ongoing investigation for *in vivo* photo-thermal cancer therapy<sup>[16,17,81,82]</sup> and as contrast agents for multi-photon microscopy.<sup>[39]</sup>

Magnetic nanoparticles, on the other hand, constitute a class of nanomaterials that has attracted much research effort for biomedical applications.<sup>[84,85,170]</sup> They are the basis for magnetic nanoparticle-based therapeutics for hyperthermia, drug delivery, and diagnostics.<sup>[19,171,172]</sup> Unlike iron oxide (Fe<sub>3</sub>O<sub>4</sub>) nanoparticles, which are mostly used as T<sub>2</sub> contrast probes by creating hypointensities in magnetic resonance imaging (MRI),<sup>[173]</sup> superparamagnetic manganese oxide (MnO) nanoparticles induce hyperintensities on T<sub>1</sub>-weighted MRI maps, and, therefore, can be diagnostically more informative.<sup>[174]</sup>

Initial results from our group on the combination of these promising materials resulted in Au@MnO "flowerlike" hetero-nanoparticles.<sup>[168]</sup> The lack of morphology control during heterogeneous nucleation translated into multiple MnO domains per Au nanoparticles. Nevertheless, subsequent to selective functionalization of the individual components, their application as multimodal contrast agent was demonstrated based on their enhanced paramagnetic and optical properties. Inspired by these results, we decided to further investigate means to control morphology in order to tap the full potential of this powerful hetero-nanoparticle

system. The formation of heterodimer nanoparticles was desired, as it enabled asymmetric surface functionalization as another point of control, leading to Janus particles with even more elaborated characteristics. The successful synthesis and comprehensive analysis of Au@MnO heterodimer nanoparticles are presented here, whereby the subsequent surface modification and further applications exploiting their intrinsic Janus character will be addressed within the following chapters (see Chapter 4 and Chapter 5).

### 3.2.1 Synthesis of Au@MnO Heterodimer Nanoparticles

Using a typical seed-mediated nucleation and growth technique, Au@MnO nanoparticles were prepared by thermal decomposition of a manganese oxide precursor. Manganese(II) oleate was chosen as precursor based on the strategy of direct employment of a metal-surfactant complex.<sup>[72,175]</sup> Thus, the complex composed of the desired ligand and the metal ion was prepared prior to the proper hetero-nanoparticle synthesis. The thermal decomposition of the metal oleate complex in 1-octadecene without any further additives led to monodisperse MnO nanoparticles.<sup>[176,177]</sup> Oleylamine-functionalized Au nanoparticles, highly uniform in size and shape, were used as seeds (see Chapter 2.2).

Upon adapting the procedure of thermal decomposition of manganese oleate toward the desired heterogeneous nucleation, the first results of the seeding-growth were “flower-like” Au@MnO nanoparticles. That means multiple nucleation of MnO occurred on one Au nanoparticle (Figure 3.2a). Similar results were obtained by Schladt *et al.*, who applied a one-pot-synthetic approach by *in situ* preparation of the Au seeds.<sup>[168]</sup> We selected the step-by-step preparation of Au nanoparticles and their purification prior to the decomposition of the metal oxide precursor to enhance the control over their size and functionalization. Thus, the multiple nucleation of MnO was efficiently suppressed by functionalization of the Au nanoparticles with a long-chain alkanethiol, namely 1-octadecanethiol. Due to the higher binding affinity of thiols for gold, the surface protection of Au was stronger as compared to amines. Thus, heterodimer formation was promoted, as the heterogeneous nucleation remained energetically favored under applied reaction conditions.

Further, in contrast to the preparation of spheroidal MnO nanoparticles, oleic acid as well as oleylamine were necessary as additional ligands to optimize two aspects of the hetero-nanoparticles: first, suppression of free Au nanoparticles was aspired, and, second, the MnO domains required further additives to control their shape. The use of oleic acid as the only ligand led neither to heteroepitaxial growth nor to well-defined MnO nanoparticles. Thus, oleylamine was also added to the reaction mixture. Excessive oleylamine caused free Au nanoparticles to remain in solution, as their surface was passivated by surplus amines. Further, the obtained heterodimer nanoparticles appeared shapeless (Figure 3.2b). On the other hand, strongly aggregated, deformed hetero-nanoparticles were obtained when the amount of additional

ligands was too low (Figure 3.2c). Similarly, this vital synergy of both ligands was also observed for spherical ferrite nanoparticles, as oleic acid or oleylamine alone led to a brown, viscous product or a very low yield of iron oxide nanoparticles, respectively.<sup>[178]</sup>

Here, the optimal molar ratio of oleylamine to oleic acid was determined to be 1:1, and the molar ratio of the manganese oleate precursor to the ligands to be 1:0.3. Regardless of the ratio of gold seeds to manganese oleate, no isolated MnO particles were observed.

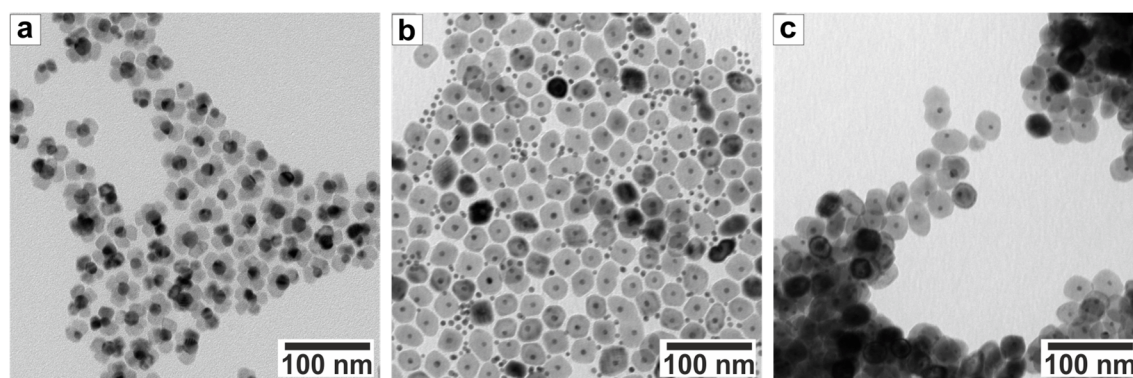


Figure 3.2: TEM images of Au@MnO hetero-nanoparticles showing the impact of various reaction parameters: a) "flower-like" particles were obtained using oleylamine-functionalized Au nanoparticles; b) and c) thiol functionalization of the Au nanoparticles suppressed multiple nucleation of MnO, while the morphology and existence of free Au nanoparticles had to be adjusted by addition and ratio of further stabilizing ligands. Generally, the Au domains appear darker in the images than MnO due to the larger Z-contrast.

The intermediate species of the seeding-growth of Au@MnO heterodimers were characterized by FT-IR spectroscopy. Figure 3.3 displays FT-IR spectra of the two surfactants, oleylamine and oleic acid, the manganese oleate complex, as well as that of the final Au@MnO nanoparticles. As oleic acid acts as a chelating ligand to metal ions, the stretching mode of the carbonyl group at  $1710\text{ cm}^{-1}$  of pure oleic acid was shifted as well as split to two broad bands upon formation of the oleate complex. These were assigned to the asymmetric stretching mode centered at  $1556\text{ cm}^{-1}$  and the symmetric stretching mode at  $ca\ 1423\text{ cm}^{-1}$ . The position and separation are characteristic for the carboxylation coordination mode. A splitting of  $ca\ 145\text{ cm}^{-1}$  has been seen in the case of bidentate coordination.<sup>[177,179]</sup> Moving on to Au@MnO heterodimer nanoparticles, the uniform mode at  $1710\text{ cm}^{-1}$  was again observable with comparable intensity as the split carbonyl stretching modes. In the range of  $1600\text{ cm}^{-1}$  to  $1000\text{ cm}^{-1}$ , the FT-IR spectrum of Au@MnO was dominated by the  $\text{CH}_3$  bending vibration at  $1461\text{ cm}^{-1}$ . Furthermore, the C=C bending mode of oleylamine appeared at  $1634\text{ cm}^{-1}$ , and the N-H stretching mode of oleylamine at  $3320\text{ cm}^{-1}$ .<sup>[178]</sup> These results provide further support for the hypothesis that both ligands were bound to the surface of the Au@MnO heterodimer nanoparticles.

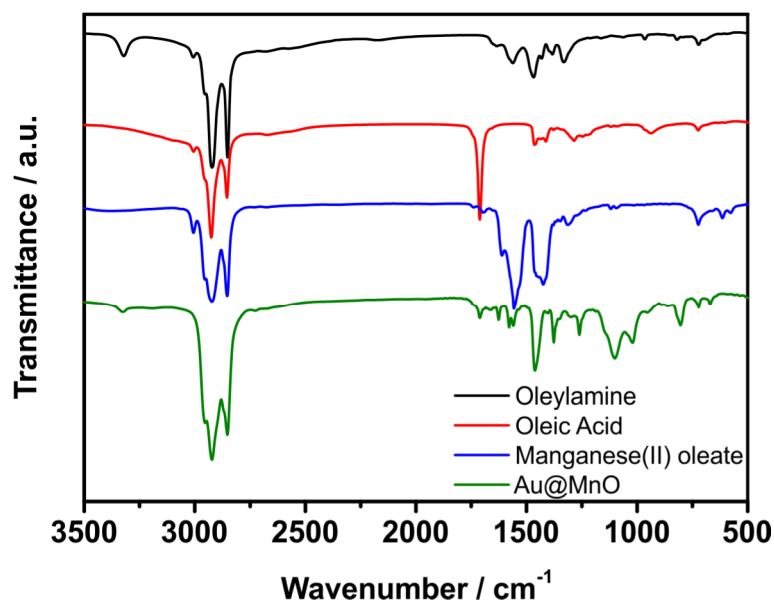


Figure 3.3: FT-IR spectra of oleylamine, oleic acid, manganese(II) oleate, and Au@MnO heterodimer nanoparticles, from top to bottom. The spectra were measured in CHCl<sub>3</sub> solution.

In accordance with the synthesis of spheroidal MnO nanoparticles, 1-octadecene was used as the solvent.<sup>[177]</sup> Changes of the solvent to less polar, *i.e.* electron depleted solvents, or to more polar, electron rich solvents, enhanced neither shape nor size control. This was observed to be the case for diphenyl ether and tri-*n*-octylamine, which were tried amongst other electron donating solvents. They promoted the formation of “flower-like” particles. Once nucleation took place, the electron depletion of the Au domain was compensated for by interaction with the solvent, thus, enabling additional nucleation. For non-polar solvents, *e.g.* heptadecane, solely the formation of heterodimers was observed, and polysized particles were obtained.

The heating rate, the reaction temperature itself, and the reaction time were all examined. First, the heating rate was optimized to 2 °C/min. A faster heating rate resulted in polydisperse nanoparticles due to the inhomogeneous temperature distribution within the reaction flask. Therefore, the conditions of growth were not identical for all nanoparticles, and different processes occurred at the same time. Second, the reaction temperature was screened between 280 °C and 320 °C, but only the reflux temperature of the solvent, 1-octadecene, led to a uniform size distribution. Third, the influence of reaction time was analyzed. Within the first 30 minutes after reaching 320 °C, the MnO domain grew in size and the size distribution became narrower. No change of the heterodimer nanoparticles was observed for a prolonged reaction time up to 90 minutes. However, if the reaction was heated for an even longer period of time, the uniformity of the nanoparticles was lost, as the MnO domains underwent Ostwald ripening. In short, the optimal reaction time was determined to be 30 minutes at 320 °C after applying a heating ramp of 2 °C/min.

The phase composition of the as-prepared Au@MnO heterodimer nanoparticles was investigated by high resolution synchrotron powder diffraction data collected at 11-BM of the Advanced Photon Source (APS) of the Argonne National Laboratory. Figure 3.4 displays quantitative phase analysis by means of Rietveld refinement of room temperature synchrotron data. The reflection profiles were modelled according to the fundamental parameter approach. The positions and relative intensities were in good accordance with expected pattern for *fcc*-type Au and rock-salt-type MnO. The crystallite sizes were determined to 6.4(2) nm for Au and 22.3(7) nm for MnO, while the profile of the Au reflections was broader than of the MnO reflections due to their crystallite sizes. These results corresponded to the domain sizes of  $6.5 \pm 0.3$  nm and  $19.3 \pm 1.8$  nm, respectively, determined by TEM analysis (see Table S2). Unfortunately, the sample was contaminated by a crystalline silicate-type compound, which occurred most likely during sample preparation.

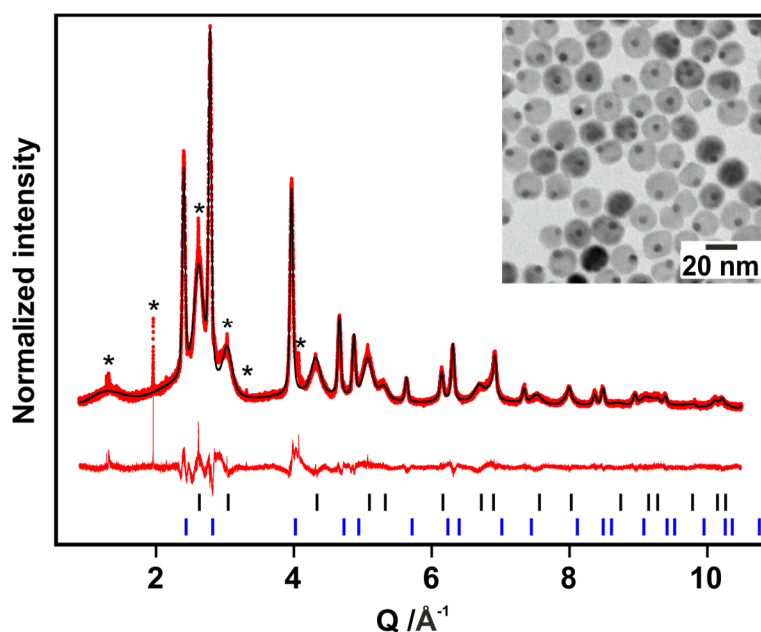


Figure 3.4: Refined synchrotron powder diffraction data for Au@MnO heterodimer nanoparticles (red dots), including profile fit (black solid line), and profile differences (red solid lines). The refined peak positions are indicated by black and blue tick marks for Au (top) and MnO (bottom), respectively. Contaminations are marked by asterisks. The inset displays a corresponding TEM image of Au@MnO heterodimer nanoparticles. The data were refined by [REDACTED].

### 3.2.2 Domain Size Control

Moreover, the facile two-step technique allowed the fine tuning of the metal oxide domain size, which had no impact on the size distribution of the resulting heterodimers. For Au nanoparticles of a given size, the diameter of the MnO domains was varied between 10 nm and 30 nm, depending on the amounts of manganese oxide precursor. To synthesize heterodimer particles with different MnO sizes, the ratio of manganese oleate to gold seeds was varied between 0.2 mmol and 0.4 mmol manganese oleate per 10 mg Au nanoparticles. Representative TEM images of the particles with various domain sizes are shown in Figure 3.5.

However, the synthesis of heterodimer nanoparticles with equally sized domains did not succeed, as larger Au seeds led to multiple heterogeneous nucleation of MnO. In reverse, the diminishment of the MnO domain simply by using less manganese oleate led to polydisperse samples with a high number of remaining Au nanoparticles.

Upon drying colloidal solutions on TEM grids, the self-assembly of heterodimers with small Au domains was determined by the pseudo-spherical shape of the MnO domains. Due to their low polydispersity, below 10 %, the heterodimers formed well-ordered hexagonally close-packed layers (Figure 3.5 d - f). Upon increasing the size ratio  $r_{Au}/r_{MnO}$ , a tendency to a side-on arrangement was observed (Figure 3.5 a - c).

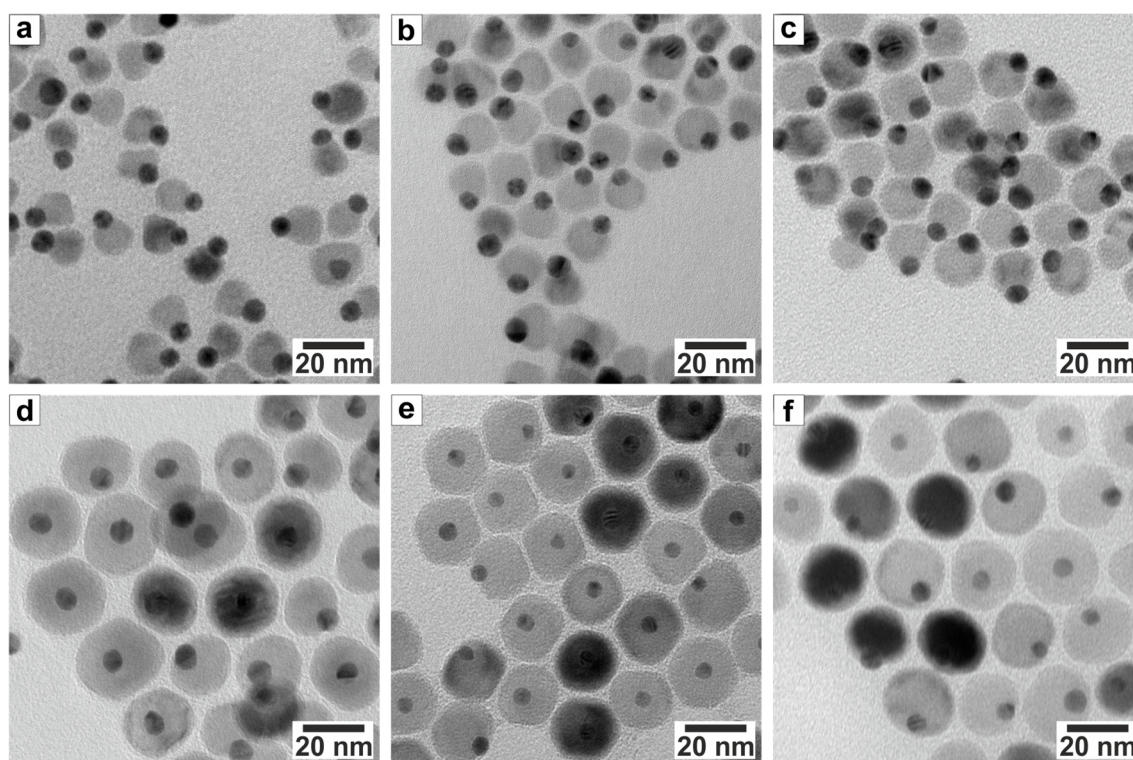


Figure 3.5: TEM images of Au@MnO heterodimers with tunable sizes of Au and MnO domains: a) 7@12 nm, b) 7@15 nm, c) 9@16 nm, d) 8@20 nm, e) 3@20 nm, and f) 4@24 nm. All images were taken with the same magnification.

The sensitivity of Au nanoparticles to changes in the dielectric environment of the surface plasmon resonance (SPR) is well known. For this reason, Au nanoparticles are used as sensors based on the shift of the resonance frequency, for example to surface binding of biomolecules.<sup>[180,181]</sup> Furthermore, the absorption characteristics are modified upon changes in the particle morphology and composition.<sup>[153,163,182]</sup> Consequently, the morphological and compositional change from spheroidal Au nanoparticles to Au@MnO heterodimers was reflected in the optical properties of the particles (Figure 3.6). The heteroepitaxial growth of MnO domains on gold seeds changed the local dielectric function of their surrounding medium, and, therefore, the position of the maximum of the plasmon absorption band (Figure 3.6b).<sup>[113]</sup>

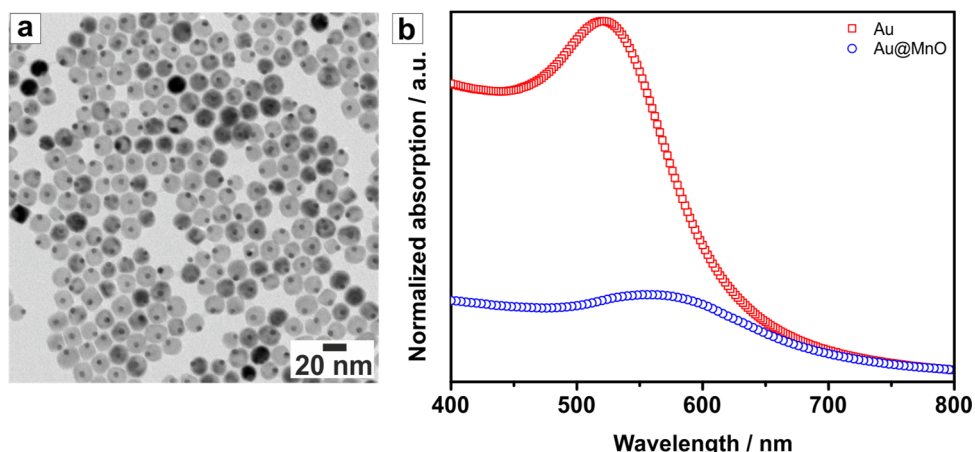


Figure 3.6: a) TEM image of Au@MnO heterodimers, b) UV-VIS spectra of Au seeds as well as sequencing Au@MnO heterodimers. The spectra were measured in hexane and scaled to unity at 800 nm.

The observed shift can be explained by means of classical Mie theory, whereas this model failed to describe the drastic decrease in intensity and broadening of the absorption band. Wei *et al.* ascribed this damping to tunneling of the conduction band electrons of the Au domains into the projected density of states of the metal oxide domain, while investigating a related system. This so-called interface decay channel was attributed to change the relaxation behavior of the SPR electrons, and, thus, the intensity and widths of the absorption band.<sup>[183]</sup>

Consequently, the magnitude of the bathochromic shift was found to be a function of the domain size of the MnO proportion. Figure 3.7 shows the shift by about 30 nm to 70 nm as compared to the absorption of pristine Au nanoparticles. The observed correlation might be explained as an interplay of concomitant factors. A common approach in literature, aside from Mie's theory, associates the observed shift with the core charge.<sup>[152]</sup> The position of the absorption band is directly proportional to the so-called number of free electrons  $N$  following an  $N^{1/2}$  dependency. In other words, excess electronic charge induces hypsochromic shifts, whereas electron deficiency results in bathochromic shifts.<sup>[113]</sup> Here, the reported Au@MnO heterodimers illustrate this relation. As the electron deficient material MnO nucleated heterogeneously on the Au nanoparticles, the induced charge arising from the polarization at the interface was compensated for by the free electrons from the Au nanoparticles. Therefore, the number of free electrons within the plasmonic nanoparticles was reduced causing a bathochromic shift. This reduction of the free electrons was suggested to contribute to the observed shift. However, it was not the only contributing change: for instance, a shift of 50 nm from 520 nm to 570 nm would require a 20% decrease in the total number of free electrons, which was barely reasonable.

For Au@MnO heterodimer nanoparticles, a linear dependency of the absorption maximum and the ratio of domain sizes  $r_{MnO}/r_{Au}$  was obtained (Figure 3.7b). Linear extrapolation of this trend to infinitesimal MnO proportions, showed an offset of ca 20 nm as compared to pristine Au nanoparticles. A similar result was reported by Kelly and co-workers for the gradual



embedding of Ag nanoparticles into mica shells.<sup>[14]</sup> Likewise, the nucleation can be regarded as stepwise embedding of Au into MnO, where not the core/shell architecture but rather the heterodimer morphology was the final structure. This congruousness could be attributed to the refractive index change of the surrounding medium upon decomposition of manganese oleate. In fact, the Drude Model describes the dependency of the resonance frequency from the dielectric constant of the surrounding medium, so that a shift of ca 100 nm is expected per refractive index change. However, this relationship is not accurate for nanoparticles, as neither the interband transitions nor the size of the nanoparticles are considered as two of the main simplifications.<sup>[14]</sup>

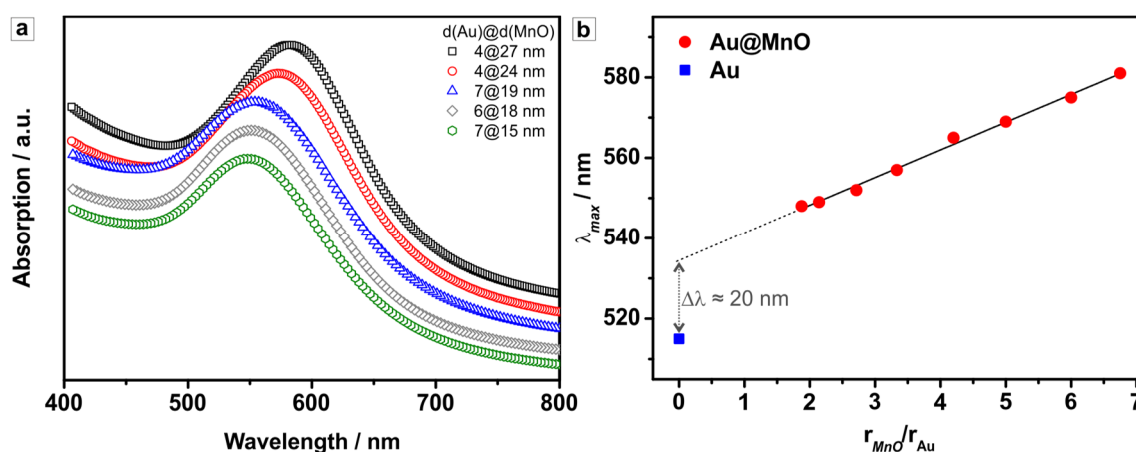


Figure 3.7: UV-VIS spectra of Au@MnO heterodimers as a function of their domain sizes revealed the significant bathochromic shift of the absorption maximum upon increasing the MnO proportion: a) spectra stacked along the y-axis, b) absorption maximum as a function of the domain sizes in comparison to pristine Au nanoparticles showing the linear dependency as well as an offset of ca 20 nm. The corresponding UV-VIS spectra were measured in hexane.

To conclude, several aspects were discussed to contribute to the modification of the optical characteristics of the investigated heterodimer nanoparticles: (i) the dielectric constant of the surrounding medium, (ii) its refractive index, as well as (iii) the net charge of the Au domains. These parameters were dependent on the size of the MnO domain, though the diameter of the Au domain had to be considered as well.

Dynamic light scattering was applied as a complementary characterization technique to TEM. The solution behavior of heterodimer particles Au@MnO as well as the precursor Au nanoparticles was investigated in view of the size distribution, aggregation, and stability in solution (Figure 3.8). Both types of particles were highly monodisperse, as can be seen from the constancy of the apparent diffusion coefficients as a function of the scattering vector  $q^2$  (Figure 3.8a) and the amplitude of the autocorrelation function fits (Figure 3.8b). The hydrodynamic radii were extracted from the Stokes-Einstein equation to  $R_h(\text{Au}) = 6.5 \text{ nm} \pm 0.1 \text{ nm}$  and  $R_h(\text{Au@MnO}) = 14.1 \text{ nm} \pm 0.2 \text{ nm}$ . This was in good accordance with the diameter measured from TEM images, which were  $d(\text{Au}) = 9.3 \text{ nm} \pm 0.5 \text{ nm}$  and  $d(\text{Au@MnO}) = 21.9 \pm 1.5 \text{ nm}$ . The increase in radii from TEM to DLS derived from the ligand shell and the solvation. No correction term was applied to make allowance for the anisotropy of the heterodimers. This

assumption of pseudo-spheroidal particles was reasonable due to the small aspect ratio of  $d(\text{Au@MnO})/d(\text{MnO}) = 1.1$ . These results in combination with TEM data confirmed the precise size control of the domain sizes and the uniformity of the size distribution.

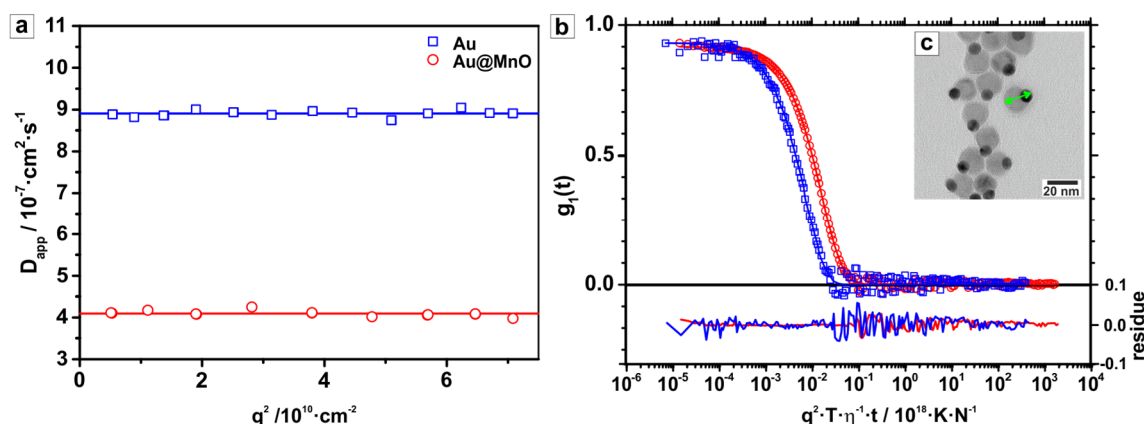


Figure 3.8: Dynamic light scattering results of Au and Au@MnO dispersed in *n*-heptane. a) Apparent diffusion coefficients as a function of scattering vector  $q^2$  in the range of scattering angle  $30^\circ \leq \theta \leq 150^\circ$ , b) universally-scaled and normalized field autocorrelation functions measured at scattering angle  $30^\circ$  together with bi-exponential fitting functions and appendant residues, and c) corresponding TEM image of Au@MnO heterodimer nanoparticles. The diameter of the nanoparticles was measured from TEM images as indicated by the green arrow.

### 3.2.3 Mechanism of Growth

As an *in situ* observation of the nucleation by common techniques remains challenging, aliquots of a typical synthesis of Au@MnO heterodimers were taken to monitor the mechanism. The aliquots were first taken at  $260^\circ\text{C}$ , thus 90 minutes after the heating ramp was started. According to the heating rate of  $2^\circ\text{C}/\text{min}$ , a 5-minute-increment was equal to  $10^\circ\text{C}$ . The reaction snapshots were analyzed without any purification, because the usually applied centrifugation and re-dissolution procedure could have an influence on the composition. As the position as well as the spectral intensity were determined to be directly related to the MnO domain size (see Figure 3.7), UV-VIS spectroscopy was used as a powerful technique to examine the evolution of the heterodimer nanoparticles. Within the first 110 minutes after the start of heating, only a slight decrease in the absorption intensity was observed (see Figure 3.9). Starting at  $310^\circ\text{C}$ , after 115 minutes, the spectral intensity dropped drastically indicating sudden nucleation of the electron deficient material on the Au nanoparticles. For the remaining reaction time of 25 minutes, the absorption intensity varied little. Coinciding with the drop in intensity, the absorption maximum showed a significant bathochromic shift confirming the sudden heterogeneous nucleation.

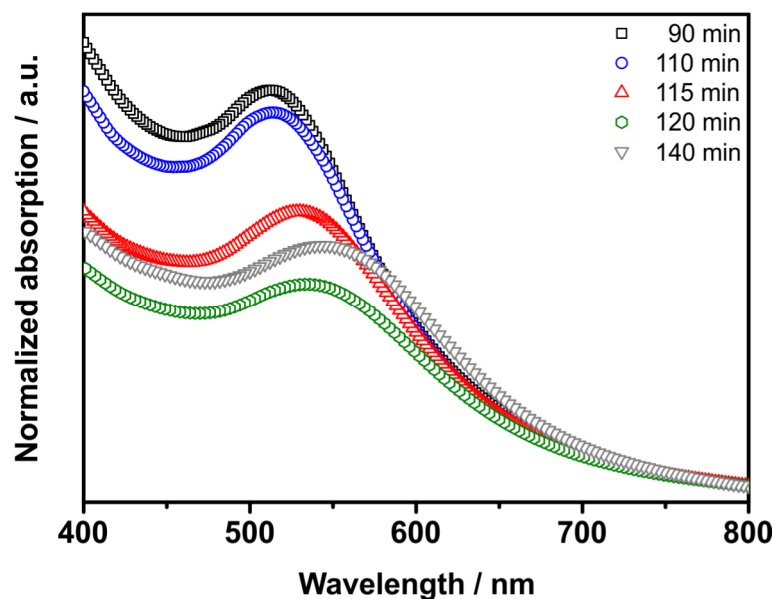


Figure 3.9: UV-VIS spectra of reaction snapshots of a typical Au@MnO synthesis. The spectra were recorded without further purification to retain the composition of the reaction mixture and normalized to absorption at 800 nm.

At first glance, this observation contradicted the nucleation behavior of manganese oleate forming spheroidal MnO nanoparticles. Schladt *et al.* reported the decomposition to have already started at 215 °C forming poorly crystalline particles, which were about 4.5 nm in diameter.<sup>[177]</sup> However, upon closer examination, this discrepancy could be attributed to the differences concerning the nature of nucleation: the formation of MnO nanoparticles occurred as a homogeneous nucleation, whereas Au@MnO nanoparticles formed heterogeneously. Compared to the formation of pure MnO nanoparticles, the concentration of manganese oleate was lowered in order to suppress homogeneous nucleation. Thus, even though the same precursor was used, the reaction kinetics were designed to differ according to the morphology of the nanoparticles.

Further, TEM analysis of the reaction snapshots confirmed the suggestion of sudden nucleation at 310 °C. The temporal evolution is shown in Figure 3.10, where no indication of heterogeneous nucleation was observed up to 300 °C. Then, abrupt nucleation of MnO domains took place at 310 °C, justifying the drastic decrease in spectral intensity. Further temperature increase and prolonged reaction time at reflux temperature of 320 °C sharpened the size distribution, but no further nucleation was observed.

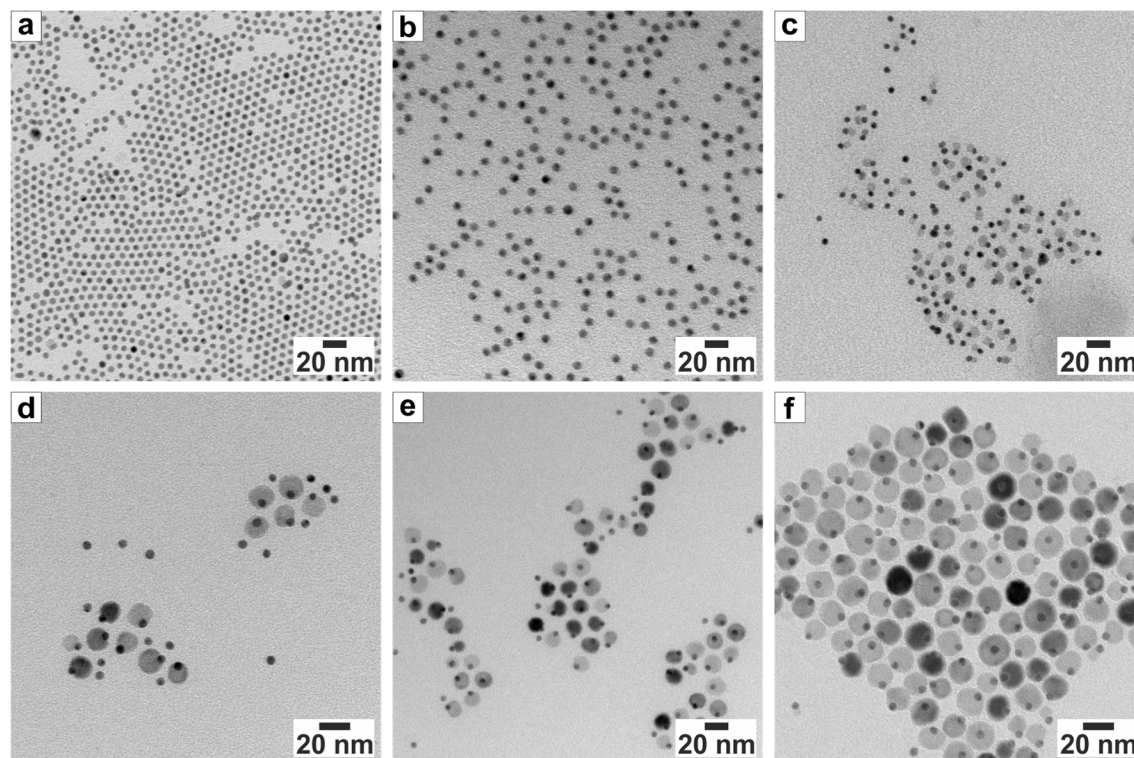


Figure 3.10: TEM images of reaction snapshots of a typical Au@MnO synthesis. The aliquots were taken at a) 260 °C, b) 300 °C, c) 310 °C, while d), e), and f) were all taken at 320 °C. This corresponded to reaction times of a) 90 min, b) 110 min, c) 115 min, d) 120 min, e) 130 min, and f) 140 min. The specimen were prepared without further purification from the reaction mixture.

In conclusion, these findings suggested this synthetic approach to proceed according to the LaMer model for heterogeneous nucleation. The crucial separation of nucleation and growth was achieved by smart design of the reaction conditions. The narrow size distribution of the obtained nanoparticles was ascribed to a single nucleation event at 310 °C. This became evident upon analysis of the UV-VIS spectra in terms of evolution of the absorption maximum and the spectral intensity (Figure 3.11). Both correlations showed a drastic change upon trespassing 310 °C. This offset represented the sudden change in the local dielectric function of the medium surrounding the gold nanoparticles. Subsequent to the nucleation event, the absorption maximum shifted nearly linear with the reaction time, indicating further growth of the MnO domains. Further, the spectral intensity recovered slightly after the nucleation event. In contrast to the absorption wavelength, the absorption remained constant rather than showing a linear behavior. This indicated that the spectral intensity was insensitive to the proportion of electron deficient material, once conjugation took place.

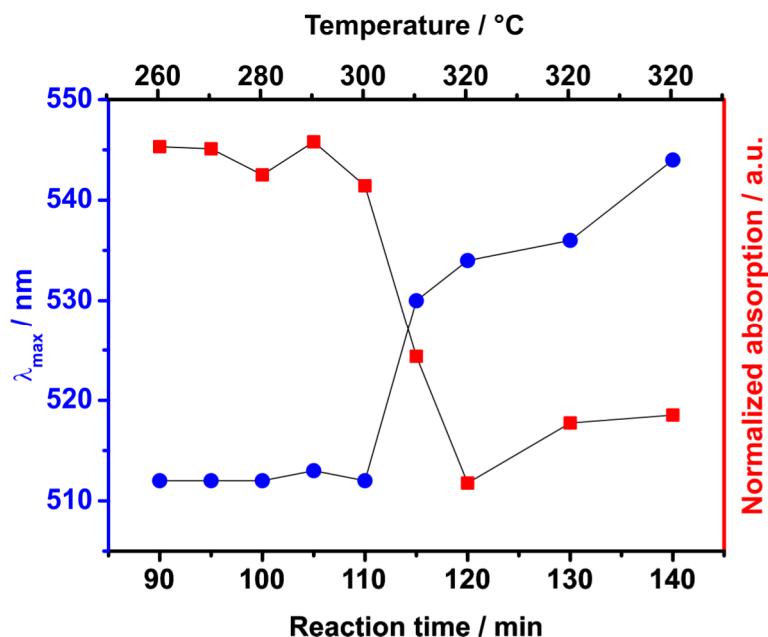


Figure 3.11: Analysis of the UV-VIS spectra of the growth of Au@MnO heterodimers showing the evolution of the position of the absorption maximum  $\lambda_{max}$  and of the spectral intensity as a function of reaction time as well as temperature. The corresponding UV-VIS spectra were measured without further purification of the aliquots.

### 3.2.4 Morphology of Au@MnO Heterodimer Nanoparticles

Upon drying nanoparticle solutions on TEM specimen, Au@MnO particles with smaller MnO domains were observed to lie flat on one side, showing the morphology of the heterodimers (see Figure 3.5). However, particles with larger MnO domains, typically > 20 nm, ordered in a hexagonal fashion with respect to the MnO domains. Thus, TEM EDX line scans were performed in order to clarify the particle morphology of these larger hetero-nanoparticles (Figure 3.12).

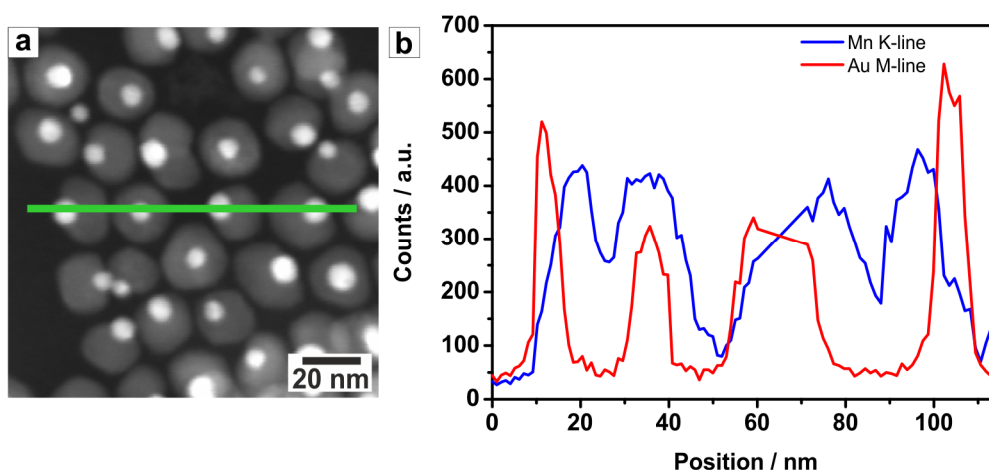


Figure 3.12: a) HAADF STEM image and b) Au and Mn elemental profiles of Au@MnO heterodimer nanoparticles corresponding to the green line in image a). The TEM EDX analysis was performed by [REDACTED].

The spatially resolved element mapping of manganese and gold showed the hetero-nanoparticles to be composed of separate nanoparticles joined together along a common interface. For instance, it became obvious from the elemental profile plot between 30 nm and

50 nm that the supposed core/shell particle was caused by an Au@MnO heterodimer lying upright on the MnO domain.

Further, the anisotropy was confirmed by TEM tomography: the tilting of the  $xy$ -plane revealed the heterodimer character, as the position of the metal domains changed relatively to the MnO domains upon increasing the rotation angle. For instance, this effect was obvious for the nanoparticle highlighted in Figure 3.13.

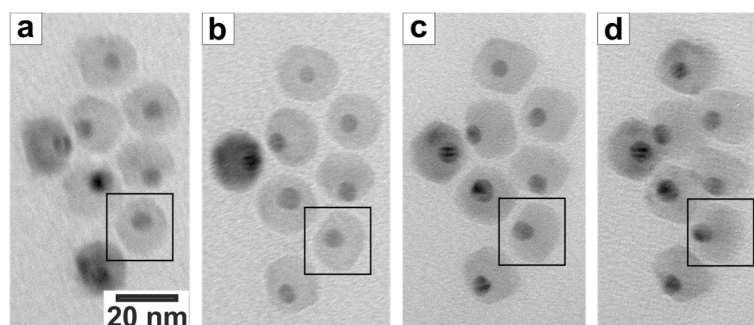


Figure 3.13: TEM tomography of Au@MnO heterodimers with tilting angles of the  $xy$ -plane of a)  $0^\circ$ , b)  $25^\circ$ , c)  $45^\circ$ , and d)  $65^\circ$ . All images were taken with the same magnification.

Moreover, HR TEM analysis showed the MnO domains to be single crystalline, while the Au domains retained the mixed single crystalline and fivefold-twinned structure (Figure 3.14a and b). The lattice constant of MnO was determined to  $4.4 \text{ \AA}$  by electron diffraction, which was in good accordance with bulk manganosite. As shown in Figure 3.14a, the lattice fringes of both particles were clearly visible, which corresponded to atomic planes within each particle. This indicated both domains to be single crystalline. The distance between adjacent planes was determined to  $0.2495 \text{ nm}$ . This coincided perfectly well to be midway between the plane distances of MnO and Au nanoparticles. The interplanar distance of the (111) planes in the cubic rock salt structure of MnO was ascertained to be  $0.256 \text{ nm}$  for  $14 \text{ nm}$  MnO nanoparticles.<sup>[184]</sup> On the other hand, the distance between adjacent (111) planes of *fcc* structured Au nanoparticles was reported to be  $0.24 \text{ nm}$ .<sup>[153]</sup>

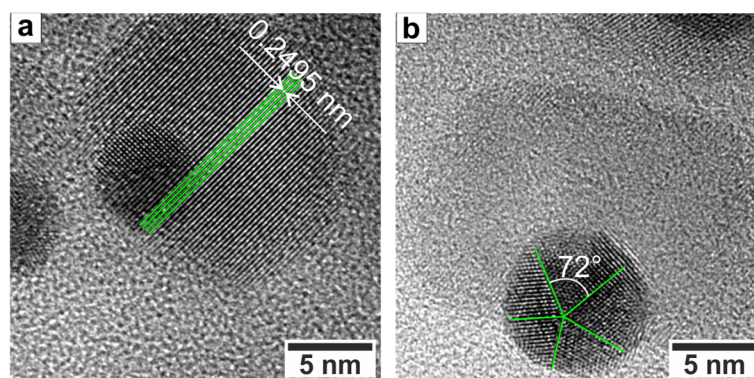


Figure 3.14: HR TEM images of a single Au@MnO heterodimer nanoparticle: a) lattice fringes reveal both domains to be single crystalline, and b) typical image of heterodimer particle indicating the fivefold twinning of the Au domain. The HR TEM measurements were performed by [REDACTED].

### 3.2.5 Magnetic Properties

Detailed examination of spheroidal MnO nanoparticles by Schladt and co-workers showed weak size-dependent superparamagnetic behavior.<sup>[177]</sup> In contrast, bulk MnO is known to be antiferromagnetic with a Néel-temperature of  $T_N = 122$  K. According to Lee *et al.*, the non-compensated surface spins of MnO nanoparticles cause ferromagnetic behavior, while the core remains antiferromagnetic.<sup>[185]</sup> These disordered spins emerge due to the change in metal coordination on the surface.<sup>[186]</sup> As the number of uncompensated surface spins increased with the surface-to-volume ratio, smaller MnO nanoparticles showed a higher blocking temperature and higher magnetization values.<sup>[187]</sup> However, it has conclusively been shown that the communication of the individual components across the interface of hetero-nanoparticles modifies the magnetic properties of hetero-nanoparticles. For instance, an exchange bias effect was observed for FePt@MnO heterodimers, as the spins of the antiferromagnetic MnO domain pinned down the magnetic moments of the ferromagnetic FePt domains.<sup>[12]</sup>

In fact, even the conjugation of magnetic nanoparticles to a diamagnet was reported to influence the magnetic behavior. Comparing the magnetic data of Au@MnO to spheroidal MnO nanoparticles demonstrated the impact of the Au domain. Au@MnO heterodimers showed superparamagnetic behavior as well, but had an 11 K higher blocking temperature of  $T_B = 22$  K (Figure 3.15a). A similar trend was observed for Au@MnO “flower-like”<sup>[168]</sup> as well as for Au@Fe<sub>3</sub>O<sub>4</sub> “dumbbell-like”<sup>[153]</sup> nanoparticles. In literature, these effects are ascribed to thermal fluctuations as well as to surface spin canting of the nanoparticles, which is even more pronounced for hetero-nanoparticles.<sup>[177,188]</sup> Furthermore, the FC and ZFC data (Figure 3.15a) diverged at low temperatures, as it has been reported for several oxide nanoparticles.<sup>[184]</sup> In contrast, the temperature-dependent magnetization measurements showed no indication of the Néel temperature, which was observed as a weak feature for 25 nm MnO nanoparticles.<sup>[177]</sup>

The nanoparticles showed a hysteresis loop below their blocking temperature, where no saturation of the magnetization occurred (Figure 3.15b). This was observed in the same way for pristine MnO nanoparticles.<sup>[184]</sup> Furthermore, the magnetization value of heterodimer nanoparticles of  $M(T = 5\text{ K}) = 4.9$  emu/g was ca 30 % lower than reported for “nanoflowers”.<sup>[168]</sup> This is reasonable as the proportion of MnO was significantly decreased for heterodimers as compared to nanoparticles bearing multiple MnO domains per Au seed. Thus, the coercivity was concurrently lowered to 320 Oe ( $\mu_0H = 0.03$  T). A similar trend was reported for the coercivity of Au@MnO “nanoflowers” in comparison to pristine MnO nanoparticles.<sup>[168]</sup> To conclude, Au@MnO heterodimer nanoparticles exhibited magnetic characteristics, which were in between those of spherical MnO and “flower-like” Au@MnO multimers, and demonstrated a significant impact of the solid state interface.

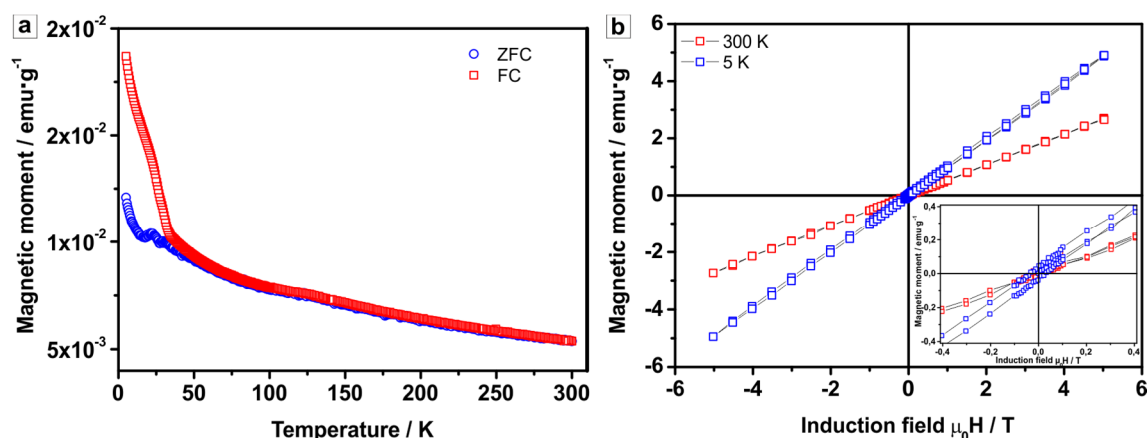


Figure 3.15: Magnetic data of 4@25 nm Au@MnO heterodimer nanoparticles: a) temperature-dependent magnetization curves (ZFC-FC) under an applied field of 100 Oe, b) corresponding magnetic hysteresis loops; the inset enlarges the view of the hysteresis loops. The measurement was performed by [REDACTED].

### 3.3 Au@Fe<sub>3</sub>O<sub>4</sub> Heterodimer Nanoparticles

In recent years, magnetic nanoparticles have attracted much research effort due to their tunable intrinsic magnetic properties. Among a great variety of magnetic nanoparticles, Fe<sub>3</sub>O<sub>4</sub> nanoparticles combine several characteristics that make them ideal for biomedical applications such as a high, tunable magnetic moment,<sup>[189]</sup> large-scale synthesis of monodisperse nanoparticles,<sup>[190]</sup> low cytotoxicity,<sup>[7]</sup> and controlled surface modification.<sup>[191]</sup> Nowadays, superparamagnetic iron oxide nanoparticles, so-called SPIONs, are even clinically used for improving magnetic resonance contrast serving as T<sub>2</sub> contrast agents.<sup>[173]</sup> Initially, the combination with plasmonic Au nanoparticles to form Au@Fe<sub>3</sub>O<sub>4</sub> hetero-nanoparticles was inspired by their use as dual contrast agent for CT and MRI,<sup>[192]</sup> which will be addressed further in Chapter 6. However, they emerged as a powerful nanoparticle system and, therefore, are under investigation concerning their use for catalysis<sup>[11,159]</sup>, drug delivery,<sup>[28]</sup> bimodal bioimaging,<sup>[163,192–194]</sup> and biomedical applications<sup>[181,195]</sup> such as cancer treatment.<sup>[196]</sup>

One of the best-known examples of dumbbell-like hetero-nanoparticles are Au@Fe<sub>3</sub>O<sub>4</sub> heterodimers. We chose Au@Fe<sub>3</sub>O<sub>4</sub> as the reference system for Au@MnO heterodimer nanoparticles for several reasons. On the one hand, the adjacent metal in the periodic system of elements was shown to behave similarly concerning the synthesis of metal oxide nanoparticles. On the other hand, large changes were determined with regard to their properties, especially the magnetic properties and their use as MRI contrast agents. Thus, this study provided an important opportunity to advance understanding of the synthesis, the characteristics, and the communication across the interface of heterodimer nanoparticles as a function of their metal oxide composition.

Here, we describe a procedure that allows precise control over the domain sizes and morphology of Au@Fe<sub>3</sub>O<sub>4</sub> heterodimer nanoparticles. It was developed by adapting the parameters of the preparation of Au@MnO heterodimers. This technique extends and modifies



the methods known in literature, as it differs regarding the metal oxide precursor,<sup>[153]</sup> heating profile, and the amount of additional ligand.<sup>[165]</sup>

### 3.3.1 Synthesis of Au@Fe<sub>3</sub>O<sub>4</sub> Heterodimer Nanoparticles

As there is no ternary Au-Fe-O phase or a gold oxide present under the experimental conditions, there is no need to pay attention to achieve phase-separation when synthesizing Au@Fe<sub>3</sub>O<sub>4</sub> heterodimers, though the morphology control remains a challenge. In 2005, Yu and co-workers demonstrated the formation of Au@Fe<sub>3</sub>O<sub>4</sub> heterodimer nanoparticles for the first time. Both synthetic options, namely the one-pot technique and the seed-mediated growth, were demonstrated.<sup>[153]</sup> The last-named approach became state of the art for the synthesis of Au@Fe<sub>3</sub>O<sub>4</sub> heterodimer nanoparticles, as it was commonly adapted by other groups. We therefore used this procedure as a starting point. However, only poor control over domain size and morphology was obtained when the synthetic protocol was reproduced: The heteronanoparticles were prepared in a seed-mediated synthesis starting with monodisperse oleylamine-functionalized Au nanoparticles (see Chapter 2.2). Heterogeneous nucleation was induced by hot-injection of iron(0) pentacarbonyl Fe(CO)<sub>5</sub> into the seed solution at 120 °C. Nonetheless, several problems occurred, which have not been addressed in literature. Due to the immediate decomposition of Fe(CO)<sub>5</sub> upon injection, multiple nucleation of iron on the seeds took place, no matter which precursor ratio, concentration, or ligand concentration were used. Thus, core/shell type nanoparticles rather than heterodimers were obtained due to subsequent growth of the Fe<sub>3</sub>O<sub>4</sub> domains forming a closed shell (Figure 3.16a). To overcome this problem, thiol-functionalized Au nanoparticles were used to suppress multiple nucleation in analogy to the formation of Au@MnO heterodimer nanoparticles. But this did not facilitate the heterodimer formation. In contrast, it promoted homogeneous nucleation of Fe<sub>3</sub>O<sub>4</sub> due to the passivation of the Au surface. By adjusting the ligand concentration as well as the precursor ratio, the formation of peanut-like particles or heterodimers was facilitated (Figure 3.16b and c, respectively). Moreover, homogeneous nucleation of Fe<sub>3</sub>O<sub>4</sub> occurred for elevated ligand concentrations. As the last choice to optimize this protocol, the addition of long-chain 1,2-alkyldiols, such as 1,2-hexadecanediol or 1,2-tetradecanethiol was tested. In literature, they were associated with an improved formation of heterodimer nanoparticles. Sheng *et al.* proposed a delay in nucleation of Fe<sub>3</sub>O<sub>4</sub> due to the interaction of the intermediate iron species with the adjacent hydroxyl groups, and, thus, a slow-down in reaction kinetics promoting anisotropic growth.<sup>[197]</sup> Conversely, no impact of any long-chain 1,2-alkyldiol independent of their concentrations was observed. Thus, no precise control regarding the formation of Au@Fe<sub>3</sub>O<sub>4</sub> heterodimers was obtained using Fe(CO)<sub>5</sub> as precursor, although it is most commonly employed in literature.

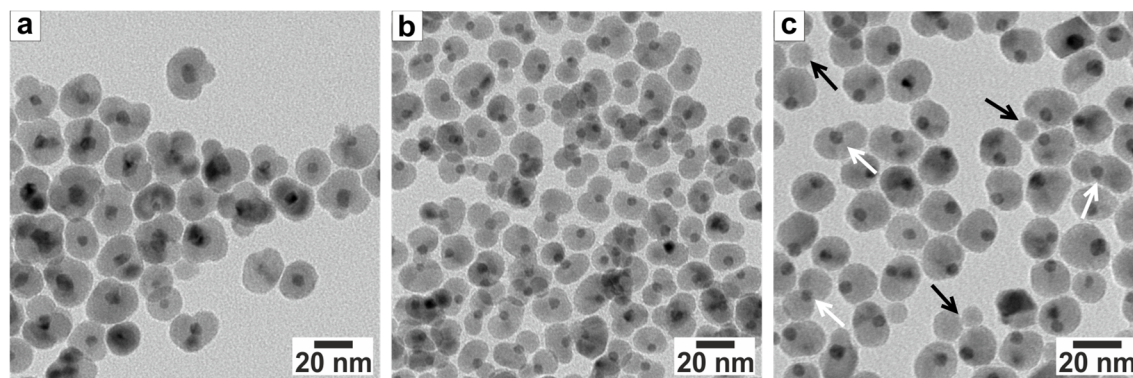


Figure 3.16: TEM images of Au@Fe<sub>3</sub>O<sub>4</sub> nanoparticles, which were prepared using Fe(CO)<sub>5</sub> as the iron oxide precursor. The morphology changed gradually from a) core/shell type hetero-nanoparticles, to b) more peanut-like, and, finally, to c) heterodimer-like nanoparticles, while homogeneous (black arrows) and multiple heterogeneous nucleation (white arrows) of Fe<sub>3</sub>O<sub>4</sub> occurred as well.

Aside from Fe(CO)<sub>5</sub>, various precursors are discussed in literature. For instance, iron(III) acetylacetonate is applied, but only in combination with 1,2-hexadecandiol to slow down the kinetics.<sup>[198]</sup> Furthermore, iron(III) oleate is the second most used, where various heating protocols and compositions of the reaction mixture are reported. In this case, the role of long-chain 1,2-alkyldiols is controversial, whether they are needed to control the morphology<sup>[192]</sup> or not.<sup>[165,199]</sup> Iron(III) oleate was developed to be thermally decomposed in a large scale synthesis of 40 g to yield monodisperse Fe<sub>3</sub>O<sub>4</sub> nanoparticles.<sup>[190]</sup> In contrast to Fe(CO)<sub>5</sub>, it enables precise control over the nucleation process, as its decomposition temperature is substantially higher, at 240 - 280 °C. It is reported to depend on the degree of purification from weakly bound oleic acid.

The chemical protocol of Au@MnO heterodimers was used as the starting point and modified as suggested by Lin and co-workers.<sup>[165]</sup> The reaction parameters were optimized regarding the precursor ratio and heating protocol to obtain monodisperse Au@Fe<sub>3</sub>O<sub>4</sub> heterodimer nanoparticles with precise control over the morphology. Briefly, the synthesis was performed as a seed-mediated nucleation and growth technique in 1-octadecene with oleylamine-functionalized Au nanoparticles as seeds and oleylamine as well as oleic acid as ligands. In other words, multiple nucleation was successfully suppressed by a slow heating rate of 2 °C/min and stabilization by the ligands. As was discussed for Fe(CO)<sub>5</sub> as precursor, thiol-functionalized Au nanoparticles inhibited heterogeneous nucleation, which led to spheroidal Fe<sub>3</sub>O<sub>4</sub> nanoparticles.

The intermediate stages of the growth of Au@Fe<sub>3</sub>O<sub>4</sub> heterodimers were investigated by FT-IR spectroscopy. Spectra of the precursors oleic acid, oleylamine, and iron oleate were analyzed in comparison to Fe<sub>3</sub>O<sub>4</sub> as well as Au@Fe<sub>3</sub>O<sub>4</sub> nanoparticles (Figure 3.17). The spectrum of iron oleate indicated a significant fraction of oleic acid apart from oleate chelating iron ions, which did not correlate to the manganese oleate complex (see page 39). The absorption band of the carbonyl stretching mode of free oleic acid at 1710 cm<sup>-1</sup> was maintained, although additional absorption bands of higher intensity occurred at 1525 cm<sup>-1</sup> and 1425 cm<sup>-1</sup>. This splitting of 100 cm<sup>-1</sup> is characteristic for a bidentate coordination of the carboxyl group.

Bronstein *et al.* observed that this additional amount of oleic acid modifies the decomposition process and acts as a stabilizer during nanoparticle formation.<sup>[179]</sup> Upon thermal decomposition of the iron oleate complex to  $\text{Fe}_3\text{O}_4$  nanoparticles, the vibrational modes of oleic acid changed. First, the absorption due to free oleic acid centered at  $1710\text{ cm}^{-1}$  disappeared, and, second, the splitting of the afore mentioned bands was increased to  $133\text{ cm}^{-1}$ . Thus, the coordination changed most likely to a bridging ligand, as a separation of  $140 - 200\text{ cm}^{-1}$  was found to be characteristic. Moving on to  $\text{Au@Fe}_3\text{O}_4$  heterodimer nanoparticles, the uniform mode at  $1710\text{ cm}^{-1}$  was of moderate intensity and significantly reduced as compared to iron(III) oleate. The absorption band of the carbonyl stretching mode was in between the two split bands observed for spherical  $\text{Fe}_3\text{O}_4$  nanoparticles. The presence of oleylamine bound to the surface of  $\text{Au@Fe}_3\text{O}_4$  heterodimer nanoparticles was confirmed by its broad N-H stretching mode centered at  $3390\text{ cm}^{-1}$ . These results provide further support for the binding of both oleic acid and oleylamine to the surface of  $\text{Au@Fe}_3\text{O}_4$  heterodimer nanoparticles and, thus, their impact on the formation and morphology.

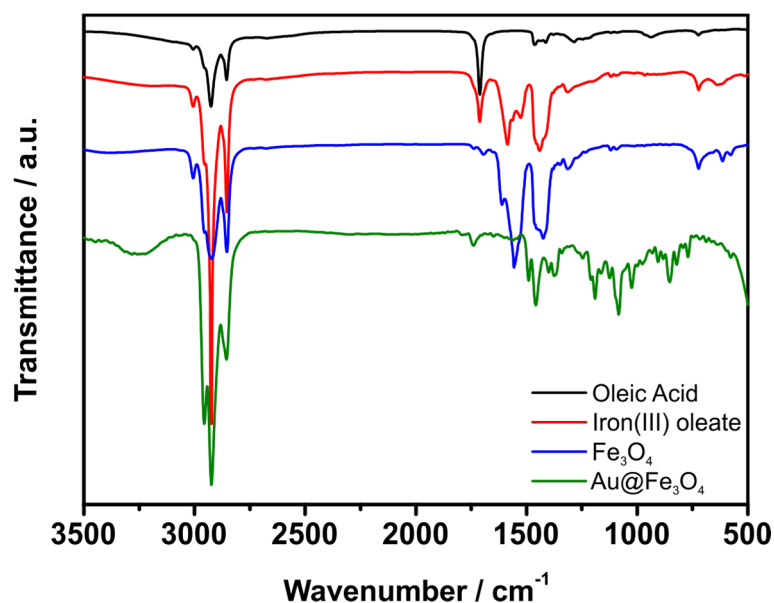


Figure 3.17: FT-IR spectra of oleic acid, iron oleate, spherical  $\text{Fe}_3\text{O}_4$ , and  $\text{Au@Fe}_3\text{O}_4$  heterodimer nanoparticles, from top to bottom. The spectra were measured in  $\text{CHCl}_3$  solution.

High resolution synchrotron data collected at room temperature at the beamline 11-BM at the Advanced Photon Source (APS) of the Argonne National Laboratory were used for quantitative phase analysis of  $\text{Au@Fe}_3\text{O}_4$  nanoparticles by means of Rietveld refinement (Figure 3.18). Reflection profile modelling according to the fundamental parameter approach led to crystallite sizes of  $7.7(1)\text{ nm}$  for the Au domain and  $18.4(1)\text{ nm}$  for the iron oxide domain. This was in good accordance to the domain sizes of  $9@16\text{ nm}$  as determined by TEM analysis, although the crystallite size of the metal oxide domain was slightly larger (see Table S3). The phase composition was approximated to  $\text{Fe}_{0.733(9)}\text{O}$  by refinement of the site occupancy, which corresponded to magnetite as main component. The slightly reduced iron content indicated a

contamination by  $\text{Fe}_2\text{O}_3$ , which could originate from partial oxidation at the surface. Due to the structural resemblance and, thus, the similarity of their diffraction pattern,  $\text{Fe}_3\text{O}_4$  and  $\gamma\text{-Fe}_2\text{O}_3$  are barely distinguishable from each other. Especially for small crystallite sizes, the phase analysis has to be treated with caution.

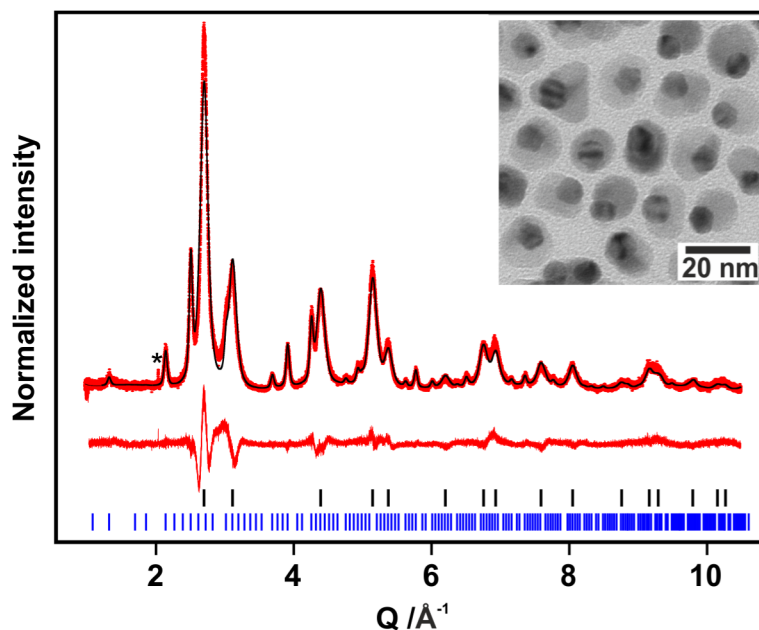


Figure 3.18: Refined synchrotron powder diffraction data of  $\text{Au}@Fe_3O_4$  heterodimer nanoparticles (red dots), including profile (black solid line), and profile difference (red solid line). The refined peak positions are indicated by black and blue tick marks for the Au (top) and  $Fe_3O_4$  (bottom) component, respectively. The inset displays a corresponding TEM image of  $\text{Au}@Fe_3O_4$  heterodimer nanoparticles. Contaminations are marked by an asterisk. The data were refined by [REDACTED].

### 3.3.2 Shape Control

The synthesis of iron(III) oleate was performed as described by Park and co-workers,<sup>[190]</sup> where only sodium oleate with a higher amount of impurities was available. Aside from a spherical morphology, this also resulted in triangular or bi-pyramidal iron oxide domains of  $\text{Au}@Fe_3O_4$  heterodimers. However, precise control of the hetero-nanoparticle morphology was achieved (Figure 3.19a): further purification of the iron(III) oleate complex prior to thermal decomposition enabled the synthesis of  $\text{Au}@Fe_3O_4$  heterodimers with solely spheroidal oxide domains (Figure 3.19b). Similarly, this shaping effect has been observed for single component  $Fe_3O_4$  nanoparticles. The purity of the iron(III) oleate complex is known to be crucial for the obtained morphology of the nanoparticles. In literature, residues of fatty acid salts, such as the precursor sodium oleate, were associated with the formation of cubic  $Fe_3O_4$  instead of spherical nanoparticles. This is discussed in terms of a facet-selective ligand adsorption on the (100) facets, whose growth, thus, is significantly slowed down. Furthermore, bi-pyramidal, twinned  $Fe_3O_4$  nanoparticles have been reported upon addition of sodium oleate and slight adjustment of the reaction parameters by Kovalenko and co-workers.<sup>[200]</sup>

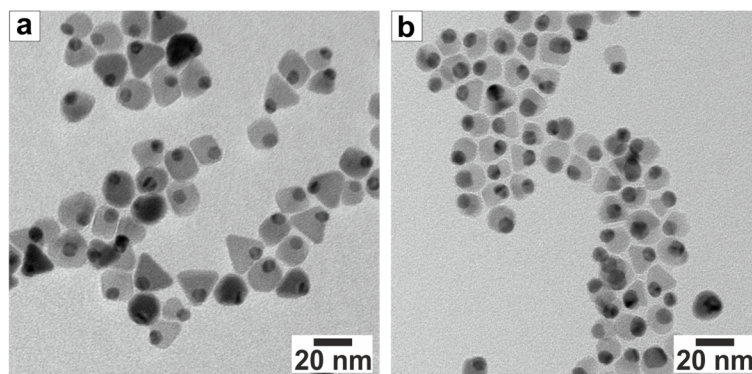


Figure 3.19: TEM images of Au@Fe<sub>3</sub>O<sub>4</sub> heterodimers prepared with iron(III) oleate as iron oxide precursor: a) contamination of iron oleate with sodium oleate led to triangular shaped iron oxide domains, b) thorough purification of the precursor resulted in spheroidal metal oxide domains.

In order to examine the directional relation of the two domains, HR TEM analysis was performed. The central question behind this study was whether the affinity for certain crystal planes is responsible for exclusive formation of heterodimer nanoparticles. However, owing to the fivefold twinning of the Au nanoparticles, no clear statement was possible concerning the anisotropic morphology in relation to lattice match or mismatch of the various crystal facets of gold and iron oxide (Figure 3.20). Furthermore, not all of the Fe<sub>3</sub>O<sub>4</sub> domains were single crystalline, as they partially showed twinning defects (Figure 3.20b). The interplanar distances of adjacent lattice fringes were determined to be 0.482 nm for Fe<sub>3</sub>O<sub>4</sub> and 0.240 nm for Au domains. These spacings corresponded to the (111) facets of the inverse spinel Fe<sub>3</sub>O<sub>4</sub> and *fcc* Au, which are 0.485 nm and 0.24 nm, respectively. Thus, the heteroepitaxial match occurred across the (111) facet of Fe<sub>3</sub>O<sub>4</sub> and twice the (111) facet of Au. In addition to the reported distance of lattice fringes for Au@Fe<sub>3</sub>O<sub>4</sub> (Figure 3.20a - b), an interplanar distance of 0.312 nm was measured for the Fe<sub>3</sub>O<sub>4</sub> domains (Figure 3.20c). This corresponded to the (220) facet of Fe<sub>3</sub>O<sub>4</sub>.<sup>[153,201]</sup>

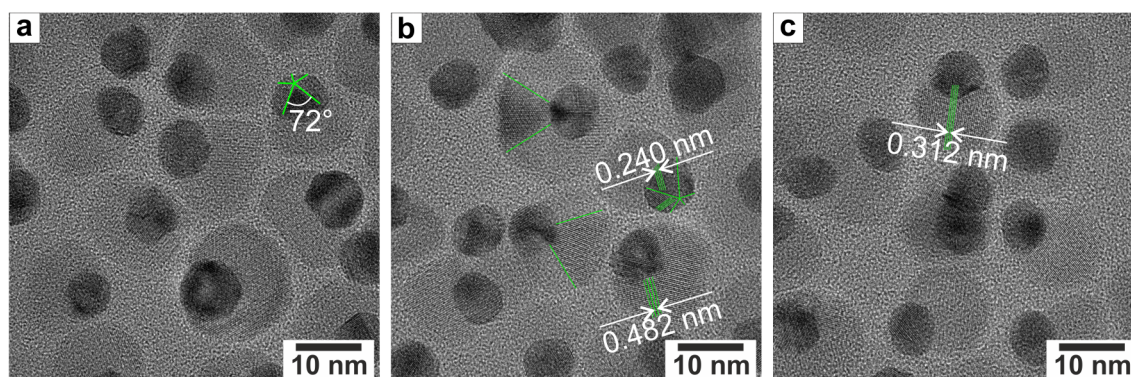


Figure 3.20: HR TEM images of Au@Fe<sub>3</sub>O<sub>4</sub> heterodimers showing the typical fivefold twinning defects of the Au domains (a, b), the twinning defects of Fe<sub>3</sub>O<sub>4</sub> as well as the lattice fringes of Au (b), and Fe<sub>3</sub>O<sub>4</sub> (c). HR TEM analysis was performed by [REDACTED].

Furthermore, the nanoparticles were analyzed by means of dynamic light scattering to investigate the uniformity of the size distribution as well as the colloidal stability. Dynamic light scattering is a powerful technique, as it allows the analysis of size and polydispersity of an

ensemble of nanoparticles in solution. In contrast, TEM displays a very restricted amount of nanoparticles, which also relies critically on the sample preparation.<sup>[202]</sup> Solutions of Au@Fe<sub>3</sub>O<sub>4</sub> heterodimers dissolved in *n*-heptane were compared to those of pristine Au nanoparticles (Figure 3.21). Both samples were highly monodisperse, which was indicated by two observations: first, the apparent diffusion coefficients showed no dependency on the scattering vector  $q^2$  (Figure 3.21a), and, second, the amplitude of the autocorrelation functions decayed single-exponentially (Figure 3.21b). The hydrodynamic radii were extracted from the Stokes-Einstein equation to be  $R_h(\text{Au}) = 6.5 \text{ nm} \pm 0.1 \text{ nm}$  and  $R_h(\text{Au@Fe}_3\text{O}_4) = 12.8 \text{ nm} \pm 0.2 \text{ nm}$ . This was in good accordance with the diameter measured from TEM images, which were  $d(\text{Au}) = 9.3 \text{ nm} \pm 0.5 \text{ nm}$  and  $d(\text{Au@Fe}_3\text{O}_4) = 16.4 \pm 1.1 \text{ nm}$ . The increase in radii from TEM to DLS derived from the ligand shell and the solvation. Furthermore, the rather slight extent of anisotropy was displayed by the aspect ratio of  $d(\text{Au@Fe}_3\text{O}_4)/d(\text{Fe}_3\text{O}_4) = 1.1$ . Consequently, the DLS data were analyzed assuming a pseudo-spherical morphology of the heterodimer nanoparticles. In other words, no correction term was added in order to consider the anisotropy.

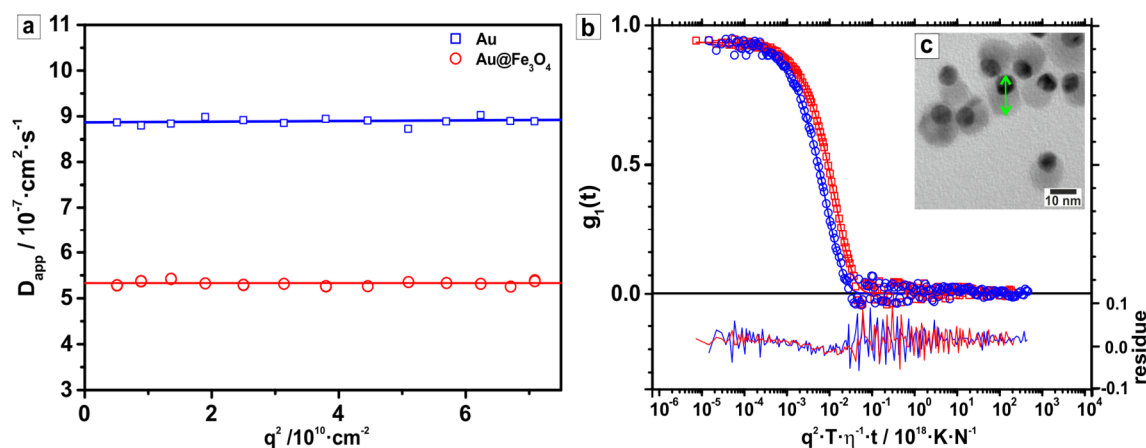


Figure 3.21: Dynamic light scattering results of Au and Au@Fe<sub>3</sub>O<sub>4</sub> dispersed in *n*-heptane. a) Apparent diffusion coefficients as a function of scattering vector  $q^2$  in the range of scattering angle  $30^\circ \leq \theta \leq 150^\circ$ , b) universally-scaled and normalized field autocorrelation functions measured at scattering angle  $30^\circ$  together with bi-exponential fitting functions and residues, and c) corresponding TEM image of Au@Fe<sub>3</sub>O<sub>4</sub> heterodimer nanoparticles. The diameter of the nanoparticles was measured from TEM images as indicated by the green arrow.

In conclusion, the optimization of the Au@Fe<sub>3</sub>O<sub>4</sub> synthesis led to highly monodisperse heterodimer particles using iron(III) oleate as precursor. As there was no indication of any aggregates in DLS measurements, the nanoparticles remained stable in solution after the purification. Therefore, solely this approach was applied for the supplementary analysis and succeeding applications.

### 3.3.3 Domain Size Control

Like the control over domain sizes that was demonstrated for Au@MnO (see Chapter 3.2.2), a precise control was achieved for Au@Fe<sub>3</sub>O<sub>4</sub> as well. The domain sizes were adjusted independently from each other. The size of the Au nanoparticles was controlled by the reaction

temperature as described earlier (see Chapter 2.2.1). For Au nanoparticles of a given size, the diameter of the  $\text{Fe}_3\text{O}_4$  domain was determined to be between 8 and 30 nm depending on the amount of iron oleate. In order to obtain heterodimer nanoparticles with different  $\text{Fe}_3\text{O}_4$  sizes, the ratio of iron oleate to Au seeds was varied between 0.2 mmol to 0.5 mmol oleate per 30 mg Au nanoparticles. The ratio of iron oleate to oleic acid and oleylamine as ligands remained constant. The precise size control obtained in this seed-mediated growth process is displayed by TEM images in Figure 3.22. Upon drying a colloidal solution, the orientation of heterodimer nanoparticles on the TEM grid was dictated by the ratio of the domain sizes of the heterodimers. A tendency for a side-on arrangement was clearly visible for  $\text{Au}@Fe_3O_4$  with large size ratios  $r_{Au}/r_{Fe_3O_4}$  (Figure 3.22a - b). Upon increasing the size of the metal oxide domain, the alignment was dominated by their hexagonal arrangement. An upright orientation led to hexagonal close-packed layers, when the local concentration of nanoparticles was increased (Figure 3.22c).

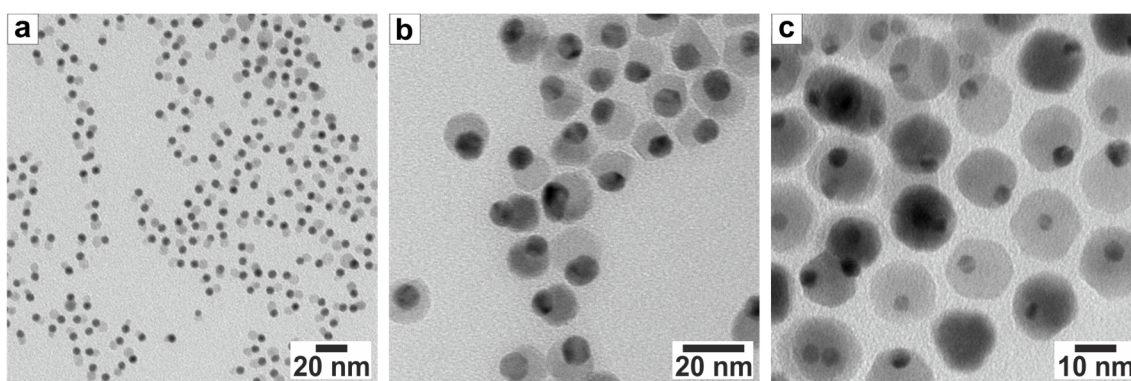


Figure 3.22: TEM images of  $\text{Au}@Fe_3O_4$  heterodimers with different domain sizes of Au and  $Fe_3O_4$  domains: a) 6@8 nm, b) 8@15 nm, and c) 4@17 nm.

The morphological change from Au nanoparticles to  $\text{Au}@Fe_3O_4$  heterodimers was reflected by the optical properties, which were analyzed by UV-VIS spectroscopy (Figure 3.23). Similarly, this was discussed earlier for  $\text{Au}@MnO$  heterodimers (see Chapter 3.2.2). The absorption maximum was red-shifted as compared to pristine Au nanoparticles, whereby the extent was proportional to the domain sizes: the larger the  $Fe_3O_4$  domain, the more pronounced the red shift. This affiliation can be described in terms of the  $N^{1/2}$  dependency of the wavelength of the absorption maximum from the so-called number of free electrons  $N$ .<sup>[113]</sup> From Mie's theory, Shi and co-workers simulated quantitatively the absorption spectrum of  $\text{Au}/Fe_3O_4$  core/shell particles as a function of the proportions. They were able to show that the shift in the maximum is represented by the impact of the change in the local dielectric function surrounding the Au nanoparticles.<sup>[203]</sup> This influence by the dielectric constant is commonly accepted to explain the alternation of the optical properties of  $\text{Au}@Fe_3O_4$  hetero-nanoparticles of various morphologies in literature.<sup>[153,182,183,203]</sup>

However, the influence of the charge state of the Au domains and the interface communication is controversially discussed. The classical Mie theory accounts for the shift of

the absorption band, but does not describe the damping, which was found to also be a function of the domain sizes (Figure 3.23). In literature, this damping has been associated with the electronic interaction of the components across the solid state interface. A feasible approach to explain the broadening of the absorption band as well as the decreased intensity is the so-called interface decay channel. The interface communication of the two components led to tunneling of electrons of the Au domains into the projected density of states of  $\text{Fe}_3\text{O}_4$ . As a consequence, the relaxation time of the SPR electrons was changed, which resulted in the observed damping of the absorption band. Wei *et al.* introduced this model to explain the observations of  $\text{Au}@\text{Fe}_3\text{O}_4$  “flowerlike” nanoparticles.<sup>[183]</sup>

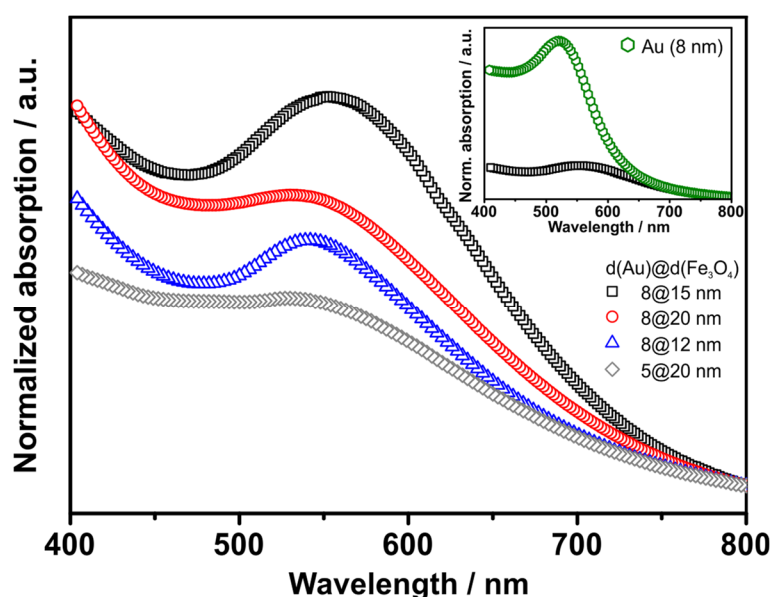


Figure 3.23: UV-VIS spectra of  $\text{Au}@\text{Fe}_3\text{O}_4$  heterodimers with different domain sizes of Au and  $\text{Fe}_3\text{O}_4$ . The inset shows the decreased spectral intensity of  $\text{Au}@\text{Fe}_3\text{O}_4$  in comparison to Au nanoparticles. The spectra were measured in hexane and normalized to unity at 800 nm.

### 3.3.4 Mechanism of Growth

Kwon and co-workers analyzed the formation of spherical  $\text{Fe}_3\text{O}_4$  nanoparticles by thermal decomposition of iron(III) oleate. At 230 °C, a slight decrease in the magnetic moment occurred, indicating some structural changes, although any nanoparticles were detectable below 310 °C. Thus, the existence of polyiron oxo clusters as the intermediate species was suggested, which act as monomers within the classical LaMer model.<sup>[204]</sup> As was demonstrated for  $\text{Au}@\text{MnO}$  as compared to spherical MnO nanoparticles, the reaction kinetics changed drastically for heterogeneous nucleation (see Chapter 3.2.3) so that the mechanism of growth of  $\text{Au}@\text{Fe}_3\text{O}_4$  heterodimers was analyzed via reaction snapshots. Starting at 260 °C, aliquots were taken at an interval of 5 minutes until the reaction temperature of 320 °C was reached. Thereafter, the interval was prolonged to 10 minutes. As the reaction was heated up with a rate of 2 °C/min, 260 °C were reached after 90 minutes. The reaction snapshots were analyzed by UV-VIS and TEM as complementary techniques without any purification.



UV-VIS spectroscopy of the aliquots showed a continuous decrease in the spectral intensity over time (Figure 3.24). This observation corroborated the observation of Kwon *et al.*, as they reported decomposition of the oleate complex starting at 230 °C. Since the formation of Au@Fe<sub>3</sub>O<sub>4</sub> required only heterogeneous nucleation, the energy barrier for Fe<sub>3</sub>O<sub>4</sub> was significantly lower and nucleation occurred below 320 °C. Moreover, the steep slope of intensity as a function of the reaction coordinate suggested a nucleation at the early stages of the reaction. Concurrent with the decline in spectral intensity, the position of the surface plasmon resonance was shifted (Figure 3.24b). The observed overall trend was a bathochromic shift of the absorption maximum from the resonance wavelength of 517 nm of the Au seeds. Nonetheless, the shift was not continuous for the analyzed aliquots. It showed a light maximum at 270 °C. This was ascribed to the decomposition of the iron oleate complex to form polyiron oxo clusters. These uniformly altered the local dielectric function surrounding the Au seeds. As a consequence, the bathochromic shift was more distinct than for the final anisotropic heterodimers. According to expectations, further growth of the oxide domain did not alter the position of the absorption maximum. The decomposition temperature of ca 270 °C coincided with the observation of weakly bound oleic acid in the iron oleate precursor, which was observed by FT-IR spectroscopy (see Figure 3.17).

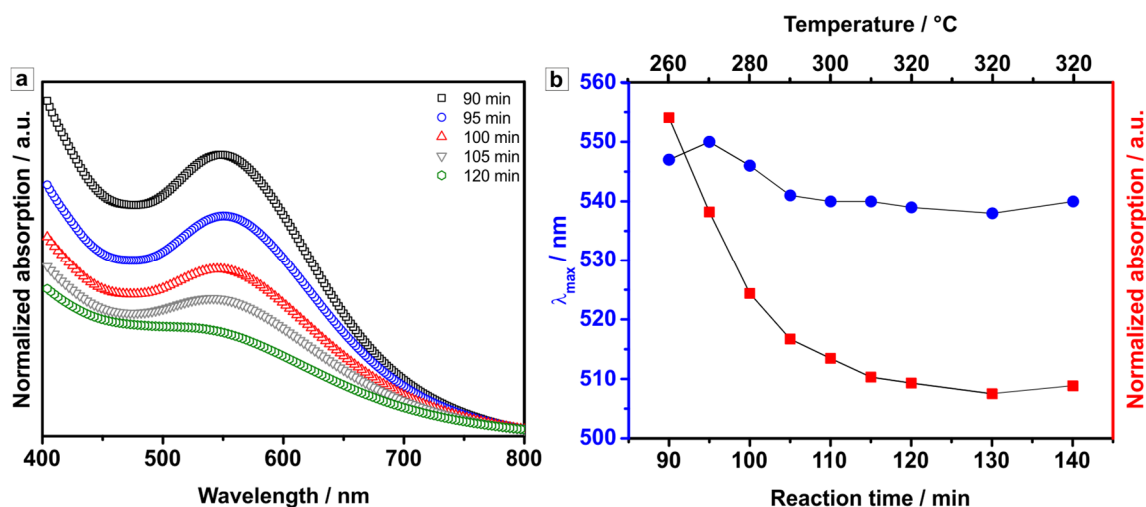


Figure 3.24: a) UV-VIS spectra of reaction snapshots of a typical Au@Fe<sub>3</sub>O<sub>4</sub> synthesis, b) analysis of the UV-VIS spectra showing the evolution of the position of the absorption maximum  $\lambda_{max}$  as well as of the spectral intensity as a function of reaction time and temperature. The corresponding UV-VIS spectra were measured without further purification of the aliquots and normalized to 800 nm.

TEM was used to confirm the relationship of nucleation and growth to optical properties and representative images of the evolution of heterodimer nanoparticles are shown in Figure 3.25. As suggested by UV-VIS spectroscopy, nucleation occurred below 320 °C, more precisely at 270 °C. However, no burst of nucleation was observed, as nucleation did not proceed simultaneously on all Au. Further increasing the reaction temperature led to heterogeneous nucleation on all Au seeds. Prior to the obvious nucleation of Fe<sub>3</sub>O<sub>4</sub> between 270 °C and 280 °C,

an elongation of the Au seeds was visible, though it was dubious whether this can already be viewed as nucleation.

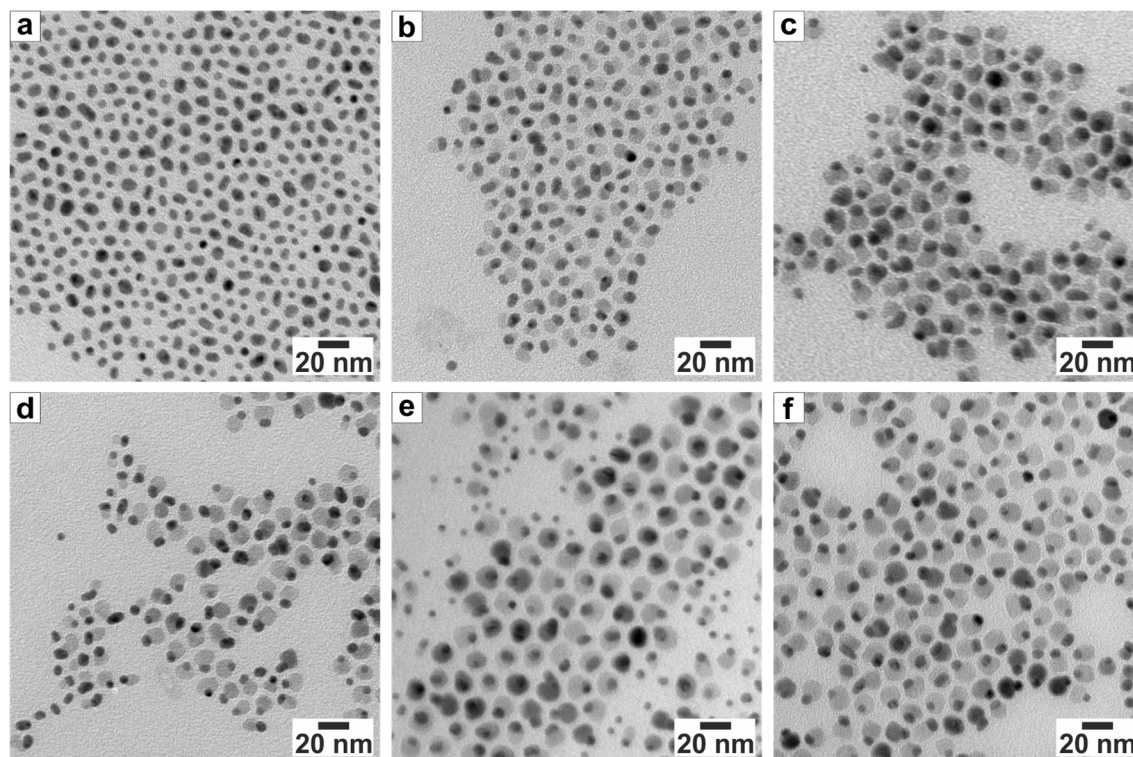


Figure 3.25: TEM images of reaction snapshots of a typical Au@Fe<sub>3</sub>O<sub>4</sub> synthesis. The aliquots were taken at a) 260 °C, b) 280 °C, c) 300 °C, d) 310 °C, and both e) as well as f) at 320 °C. This corresponded to reaction times of a) 90 min, b) 105 min, c) 115 min, d) 120 min, e) 130 min, and f) 140 min. The specimens were prepared without further purification of the reaction mixture.

Technically speaking, this nucleation cannot be described in terms of the LaMer model, as neither a burst of nucleation nor the separation of nucleation and growth was ensured. As was discussed in literature, the homogeneous formation of Fe<sub>3</sub>O<sub>4</sub> nanoparticles was found to be subdivided into two steps: first, the thermal decomposition of the oleate complex, and, second, the nucleation and growth of the nanoparticles. For this system, the homogeneous nucleation was found to be finished after 2 minutes at 320 °C. Subsequently, a narrowing of the size distribution was observed, before Ostwald ripening started to defocus it again.<sup>[204]</sup> Due to the presence of Au seeds in the reaction mixture, the energy of intermediate species required for nucleation was significantly lowered. Therefore, the nucleation started at lower temperatures than for homogeneous nucleation, but continued until the final temperature of the heating rate. However, monodisperse Au@Fe<sub>3</sub>O<sub>4</sub> heterodimer nanoparticles were obtained after refluxing for 20 minutes at 320 °C. This was attributed to a size-focusing effect.<sup>[121]</sup> Further prolongation of the reaction time led to polydisperse hetero-nanoparticles, where multiple Fe<sub>3</sub>O<sub>4</sub> oxide domains per Au seed were observed as well.

### 3.3.5 Magnetic Properties

Interactions across the solid state interface are known to determine the magnetic properties of multicomponent nanoparticles, as has been demonstrated for a plethora of nanoparticles. This ranges from retaining the magnetic properties of Co within Co/CdS<sup>[152]</sup> to significant interaction across the interface for FePt@MnO<sup>[12]</sup> or even further to tunable exchange bias in FeO/Fe<sub>3</sub>O<sub>4</sub> nanoparticles.<sup>[205]</sup> Further, Au/Fe<sub>3</sub>O<sub>4</sub> core/shell nanoparticles were shown to significantly alter the magnetic properties as compared to Fe<sub>3</sub>O<sub>4</sub> nanoparticles.<sup>[203]</sup>

Similar behavior was observed for the as-prepared Au@Fe<sub>3</sub>O<sub>4</sub> heterodimer nanoparticles. The hysteresis loops revealed the nanoparticles to be superparamagnetic at room temperature, but ferrimagnetic at 5 K (Figure 3.26a). The saturation magnetization of 4@20 nm Au@Fe<sub>3</sub>O<sub>4</sub> was 37.0 emu·g<sup>-1</sup>, which was close to the maximum of 39.7 emu·g<sup>-1</sup> for isotropic Fe<sub>3</sub>O<sub>4</sub> nanoparticles of comparable size. The difference was attributed to the small weight percentage of Au nanoparticles. This conformance was reported for 3@14 nm Au@Fe<sub>3</sub>O<sub>4</sub> heterodimers as well.<sup>[153]</sup> In contrast, the coercivity of Au@Fe<sub>3</sub>O<sub>4</sub> was significantly decreased by a factor of 2.2 to 90.6 Oe as compared to Fe<sub>3</sub>O<sub>4</sub> nanoparticles. This can be explained by the synergy of two effects: the thermal agitation of the small particles and an increased surface anisotropy.<sup>[203]</sup> The Fe<sub>3</sub>O<sub>4</sub> domains can be described as core/shell particles composed of a magnetic core and a magnetically disordered shell.<sup>[206–208]</sup> In the case of Au@Fe<sub>3</sub>O<sub>4</sub> heterodimers, the number of nearest neighbors for Fe atoms was decreased at the Au-Fe<sub>3</sub>O<sub>4</sub> interface resulting in a heightened surface anisotropy. Therefore, the interatomic exchange coupling was lowered and the canted spins at the surface saturated only under very high fields.

The superparamagnetic-to-ferrimagnetic transition behavior of Fe<sub>3</sub>O<sub>4</sub> and Au@Fe<sub>3</sub>O<sub>4</sub> nanoparticles was observed in temperature-dependent magnetization curves as well (Figure 3.26b). The magnetization of both systems dropped in the zero-field-cooled ZFC measurement. The run of the curves deviated from the field-cooled-magnetization FC due to the disabled orientation of the magnetic spins along the external field. For Fe<sub>3</sub>O<sub>4</sub>, this deviation occurred sharply at the blocking temperature, as was reported by Park *et al.*<sup>[190]</sup> For Au@Fe<sub>3</sub>O<sub>4</sub>, however, the deviation already started at room temperature, while a significant decrease was observed at the blocking temperature. The blocking temperature for Au@Fe<sub>3</sub>O<sub>4</sub> of  $T_B = 216$  K was substantially higher than for Fe<sub>3</sub>O<sub>4</sub> at  $T_B = 191$  K. This effect is generally observed for magnetic hetero-nanoparticles and was associated with the surface spin canting.<sup>[153]</sup>

Furthermore, both ZFC curves of Au@Fe<sub>3</sub>O<sub>4</sub> and Fe<sub>3</sub>O<sub>4</sub> nanoparticles showed an additional transition at ca 120 K, which was more pronounced for Au@Fe<sub>3</sub>O<sub>4</sub>. This observation coincided with investigations of Au/Fe<sub>3</sub>O<sub>4</sub> core/shell nanoparticles by Walz and co-workers.<sup>[209]</sup> This drop in magnetization was assigned to a Verwey transition, which typically occurs for Fe<sub>3</sub>O<sub>4</sub> near 125 K. It is characterized by an abrupt change in crystallographic structure at the critical

temperature. Consequently, resistivity increases by two orders of magnitude, but further anomalies in related parameters responsible for magnetic or electric interactions are induced. The structural transition is discussed as a change to an orthorhombic symmetry, although no reliable structural model is known.<sup>[207]</sup>

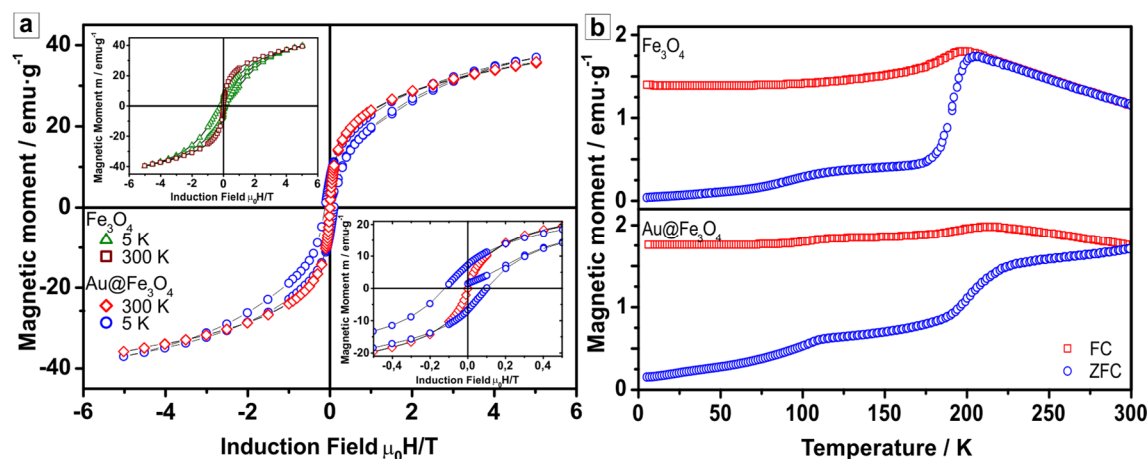


Figure 3.26: Magnetic data of 4@20 nm  $\text{Au@Fe}_3\text{O}_4$  heterodimer nanoparticles in comparison to spheroidal  $\text{Fe}_3\text{O}_4$  nanoparticles: a) temperature-dependent magnetic hysteresis loops, the inset enlarges the view of the hysteresis loops, b) corresponding magnetization curves (ZFC-FC) under an applied field of 100 Oe. The measurements were performed by [redacted].

### 3.4 Schottky Junctions in Heterodimer Nanoparticles

A key aspect of hetero-nanoparticles is their communication across the solid state interface. The most prominent hetero-nanostructures are plasmonic photocatalysts, which combine two synergistic features: a Schottky junction enhancing charge separation and the surface plasmon resonance, which is responsible for strong absorption of visible light and the excitation of charge carriers within the photocatalyst. However, the emergence of a Schottky junction is not limited to plasmonic photocatalysts, but rather is an intrinsic feature of heterodimer nanoparticles.<sup>[14]</sup> To date, there are plenty of examples of interfacial interactions inducing new properties that are not present in the individual components. This is attributed to an electron transfer across the nanometer contact at the interface. Upon direct contact between a metal and a semiconductor metal oxide, electrons tend to diffuse from the Fermi level of the metal to the conduction band of the metal oxide. This results in a downward band bending of the metal oxide, which causes charge accumulation at the interface.<sup>[37]</sup> Nowadays, it is most prominently used to enhance catalytic properties. Regarding catalytic activity, the metal oxide domain acts as a charge reservoir, while the metal domain acts as the active component towards metal-organic reactions. For instance, this enhanced catalytic activity in comparison to the single component nanoparticles was demonstrated for several systems, such as  $\text{Au@TiO}_2$ ,<sup>[13,210–212]</sup>  $\text{Ag@TiO}_2$ ,<sup>[213]</sup>  $\text{Pt@Fe}_3\text{O}_4$ ,<sup>[24]</sup>  $\text{Au@ZnO}$ ,<sup>[13,25]</sup>  $\text{Ni@Fe}_2\text{O}_3$ ,<sup>[158]</sup>  $\text{Ag@Fe}_3\text{O}_4$ ,<sup>[167]</sup> and  $\text{Au@Fe}_3\text{O}_4$ .<sup>[10,11,214]</sup> Besides, an alternation of magnetic or optical properties was observed.<sup>[12,205,215,216]</sup> Due to the well-defined morphology and the tunability of the domain sizes,

heterodimers are an ideal system to analyze not only the properties that are caused by the intrinsic characteristics of the individual components, but also the communication between the two components.<sup>[37]</sup>

At first glance, Au@MnO and Au@Fe<sub>3</sub>O<sub>4</sub> heterodimer nanoparticles, which were introduced within the previous two subchapters, share many characteristics, e.g. synthetic method, optical properties, as well as tunability of their morphology and domain sizes. On closer investigation, Au@MnO and Au@Fe<sub>3</sub>O<sub>4</sub> differ distinctly. For instance, both types of heterodimers were synthesized following a seed-mediated growth process starting from Au seeds. The subsequent functionalization of the Au nanoparticles with a surface-passivating thiol was found to be crucial to obtain Au@MnO heterodimers. In contrast, it inhibited the heterogeneous nucleation of Fe<sub>3</sub>O<sub>4</sub> on the Au seeds. As the Au seeds were polycrystalline, this observation could not be ascribed to preferred nucleation on distinct crystal facets, which showed different affinity or binding strength to the ligands. Furthermore, nucleation was observed on the (111) facet for both systems. On the other hand, drastic changes in the characteristics of the individual components were observed, especially in the alternation of the surface plasmon resonance. This indicated a communication to take place across the interface, which was strongly dependent on the electronic structure of the two components, was taking place. Magnetite is known to be a semi-metal with a small direct band gap of  $\Delta E_{direct} = 0.14$  eV. In contrast, manganosite is a wide band gap semiconductor with an indirect band gap of  $\Delta E_{indirect} = 3.40$  eV, while it is an insulator concerning its direct band gap of  $\Delta E_{direct} = 4.44$  eV. Consequently, communication with the Au domains across the interface was fundamentally changed.

Upon contact of Au and Fe<sub>3</sub>O<sub>4</sub>, the energy levels of the conduction bands, valence bands, as well as the Fermi level equilibrated due to the electron transfer between the two components (Figure 3.27). Therefore, the electron density of the Au nanoparticles was decreased, which was directly reflected during synthesis by the inhibition of multiple nucleation of Fe<sub>3</sub>O<sub>4</sub> on Au seeds.

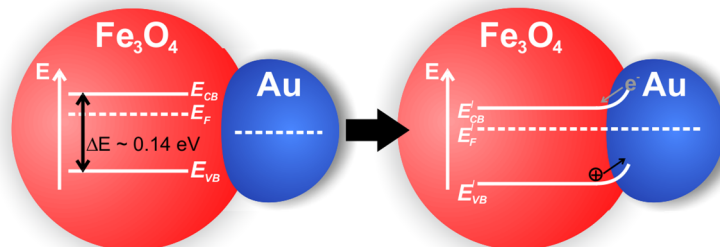


Figure 3.27: Schematic representation of the interface communication of Au and Fe<sub>3</sub>O<sub>4</sub> within the heterodimers; on the left side before equilibration, on the right afterwards.  $E_{CB}$ ,  $E_{VB}$ , and  $E_F$  stand for the energies of the conduction band, valence band, and Fermi level, respectively.

In contrast, no charge equilibration took place upon direct contact of MnO as insulator or indirect semiconductor and Au as metal as the band gap was too large. Therefore, no electron transfer occurred in the case of Au@MnO, and the Au domains retained sufficient electron density for multiple nucleation. However, analysis of the surface plasmon resonance showed a broadening accompanied by a decreased spectral intensity in comparison to Au nanoparticles. This indicated a certain degree of polarization of the conducting electrons of Au toward the electron deficient metal oxide, although no electron transfer occurred. Figure 3.28 displays the direct comparison of the UV-VIS spectra, which were obtained from the kinetic studies at 320 °C after 140 minutes of total reaction time (see Figure 3.9 for Au@MnO and Figure 3.24 for Au@Fe<sub>3</sub>O<sub>4</sub>, respectively). The difference in spectral intensity was substantial, where Au@MnO displayed intermediate behavior in between Au and Au@Fe<sub>3</sub>O<sub>4</sub>. In contrast to the UV-VIS spectra discussed so far, the spectra were normalized to unity at 350 nm instead of 800 nm. This low-energy wavelength was usually chosen as the contribution to the absorption at 800 nm did not alter much upon changing the domain sizes, as long as only spectra of one nanoparticle system were compared. However, for different materials it is distinctly different. In comparison to Au nanoparticles, the heterodimers showed stronger absorption over the whole measuring range and less pronounced absorption maxima. This was strongest for Au@Fe<sub>3</sub>O<sub>4</sub>, which absorbed significantly at 800 nm as well. Thomann and co-workers observed a similar effect for Au@Fe<sub>2</sub>O<sub>3</sub> nanoparticles and ascribed it to the enhanced absorption of visible light by low band gap materials upon conjugation to plasmonic nanoparticles.<sup>[217]</sup>

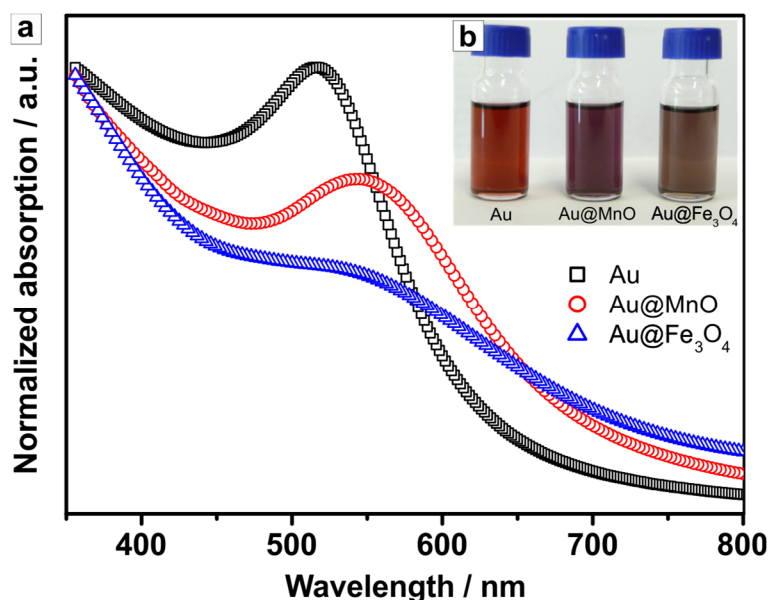


Figure 3.28: Comparison of the optical characteristics of Au nanoparticles, Au@MnO, as well as Au@Fe<sub>3</sub>O<sub>4</sub> heterodimers dissolved in hexane: a) UV-VIS spectra normalized to 350 nm and b) corresponding photograph of nanoparticle solutions.

Furthermore, the differences were clearly visible subsequent to the synthesis as indicated by the colors of the colloidal solutions (Figure 3.28b). Their brilliance decreased upon heterodimer formation. The color of Au@MnO heterodimers as a function of the domain sizes

was a shading of purple. In contrast, the solutions of Au@Fe<sub>3</sub>O<sub>4</sub> were brownish and their color showed only little size dependence.

This result confirmed the suggested correlation between the optical properties of Au@Fe<sub>3</sub>O<sub>4</sub> and two parameters: first, the variation of the local dielectric function, which was common between Au@MnO and Au@Fe<sub>3</sub>O<sub>4</sub>, and, second, the interface decay channel responsible for the electron transfer, which did not take place for Au@MnO. Wei *et al.* were able to explain the red shift of the SPR by classical Mie theory approximating the changes of the local dielectric environment as a combination of the solvent and Fe<sub>3</sub>O<sub>4</sub>.<sup>[183]</sup> The damping remained undeclared by means of Mie's theory, though it was less pronounced for Au@MnO. Therefore, a polarization of the conducting electrons of the Au domains was suggested, which resulted in a slightly modified relaxation behavior. As UV-VIS spectroscopy enabled only statements regarding the steady-state behavior, transient absorption spectroscopy was applied to study the relaxation behavior.

Electron dynamics of free-standing Au nanoparticles in solution have been thoroughly investigated, while drastic changes may appear upon heterodimer formation. They cannot be simply explained by changes in the dielectric medium. Prior studies have noted the importance of transient absorption spectroscopy in order to explain energy relaxation across the interface. However, the results are contradictorily discussed: Korobchevskaya and co-workers discussed the absence of electron transfer across the interface for Au@Fe<sub>2</sub>O<sub>3</sub> heterodimer nanoparticles based on probing the Fe<sub>2</sub>O<sub>3</sub> component.<sup>[218]</sup> However, probing at 800 nm might cause the photo-induced absorption of the excited states, while the absorption of the ground state contributes as well. Further, George *et al.* reported a faster relaxation of Au@Fe<sub>2</sub>O<sub>3</sub> heterodimer nanoparticles investigated by near-infrared transient absorption spectroscopy.<sup>[219]</sup> This was confirmed by significantly faster bleaching dynamics upon probing the gold domain of Au@Fe<sub>2</sub>O<sub>3</sub> using white light, as reported by Comin and co-workers.<sup>[220]</sup> Generally, these reports confirmed the electronic interaction of the two components of a heterodimer. However, the nature of the interface of Au@Fe<sub>2</sub>O<sub>3</sub> and Au@Fe<sub>3</sub>O<sub>4</sub> heterodimer nanoparticles is supposed to vary due to the wide band gap of maghemite of 2.03 eV.

Thus, the fluorescence spectra and decay dynamics of the pristine Au nanoparticles in comparison to Au@Fe<sub>3</sub>O<sub>4</sub> and Au@MnO heterodimers were systematically investigated by time-resolved photoluminescence spectroscopy (TR-PL). The nanoparticles were dissolved in toluene, excited by a femtosecond laser pulse at 400 nm, and the subsequent emission was detected by a Streak Camera setup. The time-integrated fluorescence spectra showed a close resemblance between pristine Au nanoparticles and Au@Fe<sub>3</sub>O<sub>4</sub> heterodimers, which had a maximum of photoluminescence at 481 nm and 475 nm, respectively. This was slightly shifted to 463 nm for Au@MnO. These heterodimers, however, displayed an additional peak at 632 nm (Figure 3.29a).

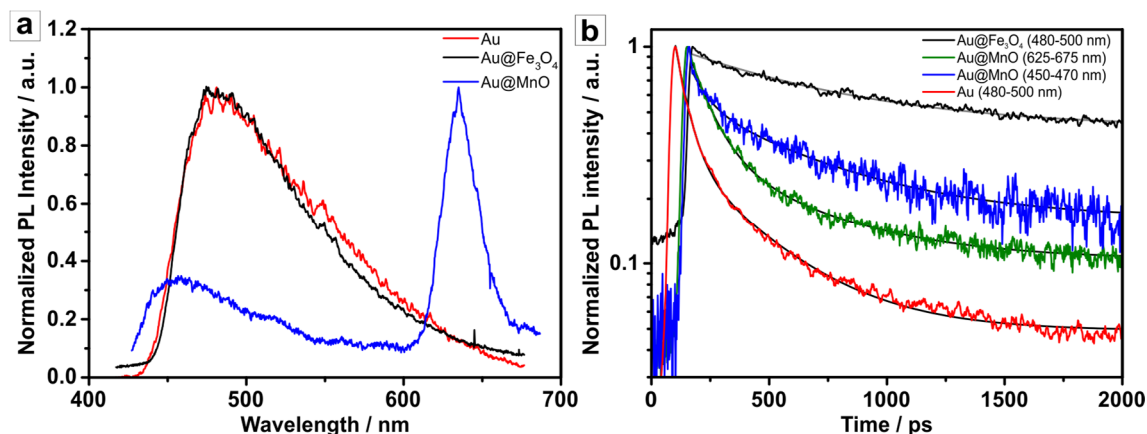


Figure 3.29: (a) Time-integrated emission spectra of pure Au nanoparticles as well as Au@Fe<sub>3</sub>O<sub>4</sub> and Au@MnO heterodimers. The samples were excited at 400 nm by a 100 fs laser pulse. (b) Fluorescence dynamics monitored at the emission peak wavelengths and stretched exponential fits according to the functions displayed in Table 3.1. TR-PL measurements were performed by [REDACTED].

The analysis of the fluorescence dynamics confirmed the suggested prolonged relaxation time for the electrons of the conduction band of Au nanoparticles upon conjugation to Fe<sub>3</sub>O<sub>4</sub> (Figure 3.29b). The fluorescence lifetime of Au@Fe<sub>3</sub>O<sub>4</sub> was increased to more than 2000 ps as compared to  $\tau < 100$  ps for Au nanoparticles. Further, the emission of Au@Fe<sub>3</sub>O<sub>4</sub> was described as stretched-exponential decay with an extremely decreased inverse decay rate of 249 ps as compared to 72 ps for Au nanoparticles. The fluorescence dynamics of Au@MnO affirmed the weak interaction with the electrons of the Au domain, as the inverse decay rates were slowed down to 147 - 187 ps.

Table 3.1: Inverse decay rates  $\tau$  and stretching exponent  $\beta$  obtained from fitting the fluorescence dynamics to a stretched-exponential decay.

Sample	$\tau$ / ps	$\beta$ / ps
Au (480-500 nm)	72	0.55
Au@Fe <sub>3</sub> O <sub>4</sub> (480-500 nm)	249	0.55 (fixed)
Au@MnO (450-470 nm)	187	0.55 (fixed)
Au@MnO (625-645 nm)	147	0.55 (fixed)

In contrast to earlier findings for Au@Fe<sub>2</sub>O<sub>3</sub>, however, a prolongation of relaxation times was observed. A possible explanation of this contrary trend may be the differences between the band gap of maghemite and magnetite. Due to the wide band gap of Fe<sub>2</sub>O<sub>3</sub>, no clear evidence of a charge transfer across the interface was reported. Thus, the alternation of the relaxation behavior was attributed to a spill-out of the gold electrons at the interface.<sup>[218,220]</sup> However, the prolongation observed upon conjugation to the semimetal Fe<sub>3</sub>O<sub>4</sub> suggested an electron transfer. The interfacial communication is subject to ongoing investigation, which includes the



determination of the electronic structure of the domains by angular-resolved X-ray as well as ultraviolet photoelectron spectroscopy in dependency of the chemical composition of the heterodimer nanoparticles.

### 3.5 Variation of Metal Domain

Nowadays, many  $\text{Fe}_3\text{O}_4$ -based heterodimer nanoparticles, which are of particular interest due to their enhanced magnetic and catalytic properties over single-component and other morphologies of  $\text{Fe}_3\text{O}_4$ -based nanoparticles, have been developed. For instance,  $\text{Pt}@\text{Fe}_3\text{O}_4$  nanoparticles were shown to enhance the catalytic activity for oxygen reduction over the individual component nanoparticles.<sup>[24]</sup> However, these approaches utilize  $\text{Fe}(\text{CO})_5$  as iron oxide precursor, which has several disadvantages as discussed earlier (see page 51).

Here, we demonstrated the general applicability of the iron(III) oleate-based synthetic procedure by the substitution of the gold seeds with various metal nanoparticles. This exchange enabled investigation of the impact of the metal domain on the properties of the heterodimer nanoparticles, as only the influence of metal oxide domain was investigated in the previous subchapters. Further, the conjugation of  $\text{Fe}_3\text{O}_4$  to  $\text{Au}_x\text{Pt}_{1-x}$  alloy nanoparticles, which are also in use for their enhanced properties, has not been seen in literature so far. Briefly, the iron oleate based procedure was extended to Pt as well as  $\text{Au}_x\text{Pt}_{1-x}$  nanoparticles. Figure 3.30 shows monodisperse  $\text{Pt}@\text{Fe}_3\text{O}_4$  heterodimer nanoparticles, which were prepared by exchanging only the seed particles and leaving all other reaction parameters unchanged. Therefore, besides the uniformity of the size distribution, the ability to tune the domain sizes was also maintained. Due to their uniform size distribution, a tendency toward a hexagonal arrangement with regard to the  $\text{Fe}_3\text{O}_4$  domains was observed (Figure 3.30a). An increase in the ratio of domain sizes  $r_{\text{Pt}}/r_{\text{Fe}_3\text{O}_4}$  led to a side-on arrangement being preferred (Figure 3.30c).

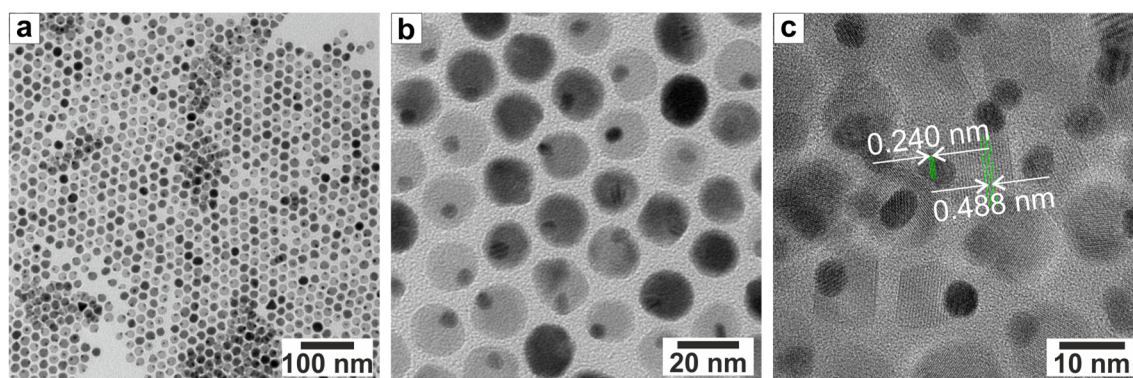


Figure 3.30: TEM images of 4@18 nm  $\text{Pt}@\text{Fe}_3\text{O}_4$  heterodimer nanoparticles showing the hexagonal arrangement of monodisperse particles (a, b), HR TEM micrographs of 6@13 nm  $\text{Pt}@\text{Fe}_3\text{O}_4$  displayed the lattice fringes of the single crystalline domains (c). The HR TEM analysis was performed by [REDACTED].

The truncated cubic Pt nanoparticles (see Chapter 2.3) triggered heteroepitaxial growth of  $\text{Fe}_3\text{O}_4$  domains on their (111) plane, as was measured by HR TEM analysis. As a consequence of the single crystalline seed particles, no twinning defects were observed for

$\text{Fe}_3\text{O}_4$ . The interplanar distances of adjacent lattice fringes were determined to be 0.240 nm for Pt, which was close to the distance in bulk *fcc* Pt of 0.22 nm. As was found for  $\text{Au}@Fe_3O_4$ , the lattice fringes of the (111) plane of  $\text{Fe}_3\text{O}_4$  domains were separated by 0.488 nm, which is in good accordance with literature.<sup>[24]</sup>

Likewise,  $\text{Au}_x\text{Pt}_{1-x}$  alloy nanoparticles were used as seed nanoparticles for heteroepitaxial growth. The obtained  $\text{Au}_x\text{Pt}_{1-x}@Fe_3O_4$  heterodimer nanoparticles were as uniform in size as  $\text{Au}@Fe_3O_4$  or  $\text{Pt}@Fe_3O_4$  nanoparticles, which was shown by HR TEM analysis (Figure 3.31). As the alloy nanoparticles showed fivefold twinning defects similar to Au nanoparticles, the orientational relationship could not be substantiated. Nevertheless, the distances of adjacent lattice fringes of 0.482 nm for  $\text{Fe}_3\text{O}_4$  was found to coincide with the reported data for (111) facets. The interplanar distance of  $\text{Au}_x\text{Pt}_{1-x}$  was marginally increased to 0.249 nm as compared to 0.24 nm for (111)  $\text{Au}$ <sup>[153]</sup> and 0.22 nm for (111) Pt.<sup>[221]</sup>

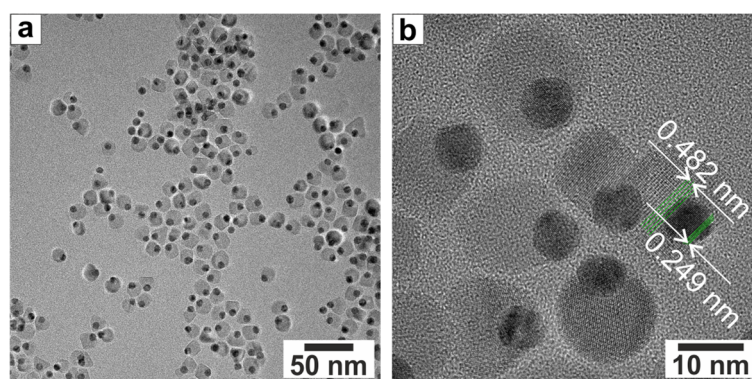


Figure 3.31: HR TEM images of  $\text{Au}_{0.55}\text{Pt}_{0.45}@Fe_3O_4$  heterodimer nanoparticles showing the uniformity of the sample (a) and the lattice fringes of the domains upon enlargement (b). The HR TEM analysis was performed by [REDACTED]

The comparison of the electron diffraction patterns revealed the slight, but distinct variation due to the alloy nanoparticles (Figure 3.32). The pattern of  $\text{Au}_x\text{Pt}_{1-x}@Fe_3O_4$  presented a single peak at  $0.44 \text{ \AA}^{-1}$  for (111)  $\text{Au}_x\text{Pt}_{1-x}$  indicating the maintenance of their alloyed structure. The alloying showed most significant impact on the two strongest reflections of the metal domain, which emerged upon interaction between the (111) and (200) planes. A shift to smaller reciprocal distances was observed, which confirmed the analysis of the HR TEM images. As a consequence, the less intense reflections of  $\text{Fe}_3\text{O}_4$  were not clearly observable, but contributed to the shoulder of the peak at  $0.48 \text{ \AA}^{-1}$ . Furthermore, the ratio of the peak intensities for the peaks correlating to the (111) and (200) planes of  $\text{Fe}_3\text{O}_4$  differed: as was described for pristine Pt nanoparticles in Chapter 2.3, the cubic morphology of Pt nanoparticles triggered a (200) textured assembly upon slow evaporation of the solvent on the TEM grid. This resulted in a pronounced (200) peak. This feature was observed in the same way for  $\text{Pt}@Fe_3O_4$  nanoparticles. In  $\text{Au}_x\text{Pt}_{1-x}@Fe_3O_4$ , however, the properties of the metal domain were dominated by the Au proportion.

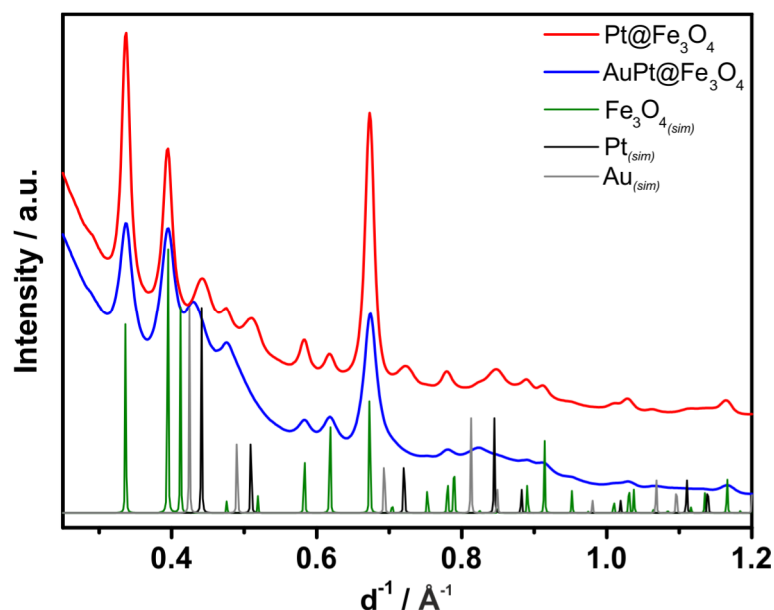


Figure 3.32: Electron diffraction pattern of Pt@Fe<sub>3</sub>O<sub>4</sub> and Au<sub>0.55</sub>Pt<sub>0.45</sub>@Fe<sub>3</sub>O<sub>4</sub> heterodimer nanoparticles referenced to simulated pattern of Fe<sub>3</sub>O<sub>4</sub>, Pt, and Au. The electron diffraction analysis was performed by [REDACTED].

High resolution synchrotron diffraction data were collected at the beamline 11-BM at the Advanced Photon Source (APS) of the Argonne National Laboratory. Figure 3.33 displays the quantitative phase analysis by means of Rietveld refinement of the room temperature synchrotron data of Au<sub>x</sub>Pt<sub>1-x</sub>@Fe<sub>3</sub>O<sub>4</sub> (top) and Pt@Fe<sub>3</sub>O<sub>4</sub> (bottom) nanoparticles. Interestingly, the refined site occupancy and approximated compositions of Fe<sub>0.689(1)</sub>O and Fe<sub>0.665(2)</sub>O for Pt@FeO<sub>y</sub> and Au<sub>x</sub>Pt<sub>1-x</sub>@FeO<sub>y</sub>, respectively, revealed the iron oxide domains to be  $\gamma$ -Fe<sub>2</sub>O<sub>3</sub> (maghemite) rather than Fe<sub>3</sub>O<sub>4</sub> (magnetite). This was in contrast to Au@Fe<sub>3</sub>O<sub>4</sub> nanoparticles, although all heterodimer nanoparticles have been prepared under identical conditions. Nevertheless, attention has to be paid as the diffraction pattern of magnetite and maghemite are closely resembled due to their structural affinity, which becomes even more important for decreasing crystallite sizes. Reflection profiles were modelled according with the fundamental parameter approach. Refined crystallite sizes of the Fe<sub>2</sub>O<sub>3</sub> domains of both samples as well as those of the Pt differ by a factor of 1.4 from the values determined in TEM analysis, which cannot be explained in terms of experimental and computational methods. The crystallite size of Au<sub>x</sub>Pt<sub>1-x</sub> domains was determined to 4.8(1) nm, which was in good accordance to the observed twinning and the domain size of 8.0 ± 0.5 nm in TEM analysis (see Table S3). The chemical composition of Au<sub>x</sub>Pt<sub>1-x</sub> domains was determined to Au<sub>0.73</sub>Pt<sub>0.27</sub> assuming a Vegard's type behavior of the lattice parameter, which was reported by Luo and co-workers.<sup>[88]</sup>

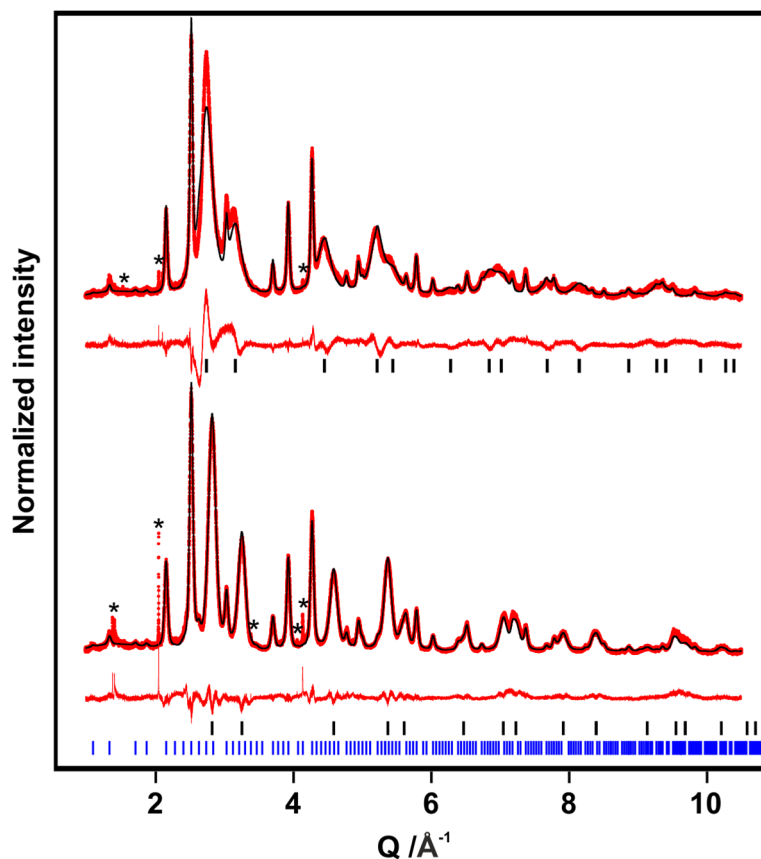


Figure 3.33: Refined synchrotron powder diffraction data for  $\text{Au}_x\text{Pt}_{1-x}@\text{Fe}_2\text{O}_3$  (red dots, top) and  $\text{Pt}@\text{Fe}_2\text{O}_3$  (red dots, bottom), including profile fits (black solid lines), and profile differences (red solid lines). The refined peak positions are indicated by black and blue tick marks for the metal and  $\text{Fe}_2\text{O}_3$  component, respectively. Contaminations are marked by asterisks. The data were refined by [REDACTED].

The quantitative phase analysis of high resolution synchrotron powder diffraction data was further confirmed by the magnetic properties.  $\text{Au}_x\text{Pt}_{1-x}@\text{Fe}_2\text{O}_3$  heterodimer nanoparticles showed superparamagnetic behavior at room temperature, but ferrimagnetic at 5 K (Figure 3.34a). The saturation magnetization was determined to  $52.7 \text{ emu}\cdot\text{g}^{-1}$ , which was significantly higher as compared to  $\text{Au}@\text{Fe}_3\text{O}_4$  heterodimer nanoparticles. On the other hand, it was substantially smaller than  $80 \text{ emu}\cdot\text{g}^{-1}$  for bulk and  $\text{Fe}_2\text{O}_3$  nanoparticles.<sup>[222]</sup> Further, their coercivity was increased to 328 Oe. These results confirmed the iron oxide domain to be composed of  $\text{Fe}_2\text{O}_3$  rather than  $\text{Fe}_3\text{O}_4$ . The determination of the blocking temperature was complicated by the curve shape of FC and ZFC data (Figure 3.34b). The FC and ZFC curves deviated, starting below ca 175 K, whereby an additional feature was observed around 100 K, which might translate to two blocking temperatures.

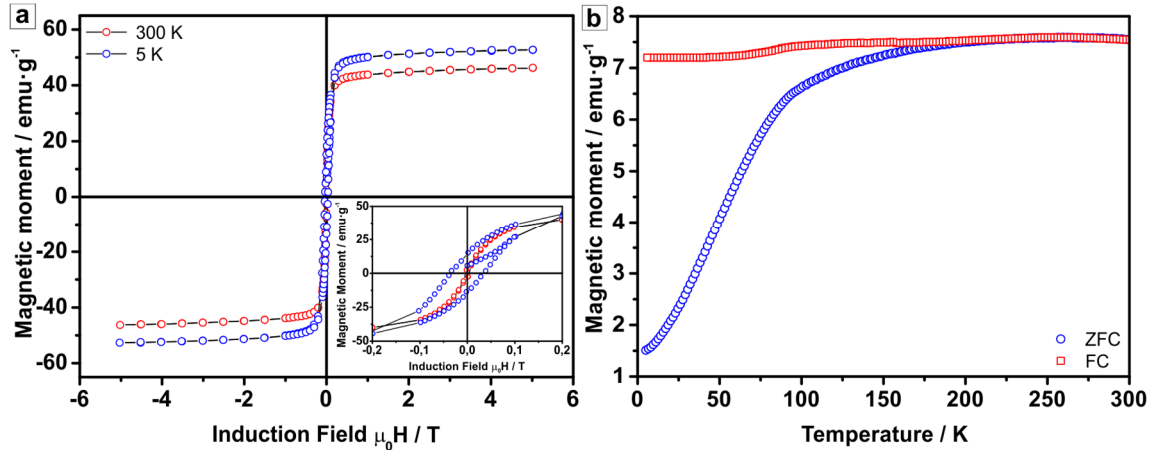


Figure 3.34: Magnetic data of 8@16 nm  $\text{Au}_x\text{Pt}_{1-x}@Fe_2O_3$  heterodimer nanoparticles: a) temperature-dependent magnetic hysteresis loops, b) corresponding magnetization curves (ZFC-FC) under an applied field of 100 Oe. The measurements were performed by [REDACTED].

The application of Au, Pt, and their alloy nanoparticles enabled the chemical tuning of the characteristics of the metal nanoparticle, which was reflected most obviously in the optical properties. The UV-VIS spectra of  $\text{Au}_x\text{Pt}_{1-x}@Fe_2O_3$  clearly showed the superposition of two effects (Figure 3.35): first, the damping, broadening, and shifting of the SPR due to the conjugation to an electron deficient metal oxide, which had been observed before, and, second, the spectral intensity and position of the SPR as a function of the composition of the metal domain. The higher the Pt content, the less pronounced was the absorption in the visible spectrum due to the hypsochromic shift of the absorption maximum as well as the less intense spectral absorption of Pt nanoparticles.

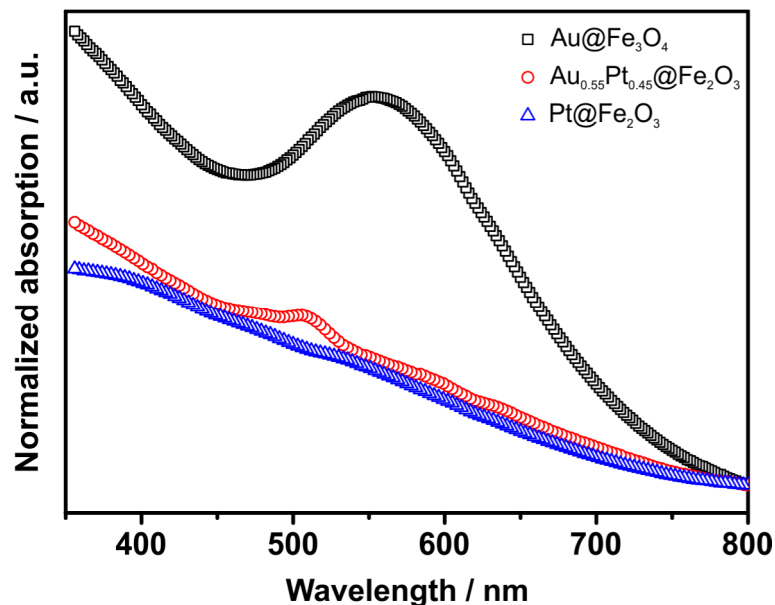


Figure 3.35: UV-VIS spectra of  $\text{Au}_x\text{Pt}_{1-x}@Fe_2O_3$  heterodimer nanoparticles showing the damping and bathochromic shift of the surface plasmon resonance working in opposite direction as a function of the composition of the metal domain. The spectra were measured in hexane and normalized to unity at 800 nm.

### 3.6 Conclusion

In summary, we have developed a facile method to fabricate Au@MnO heterodimer nanoparticles by a seed-mediated nucleation and growth technique with precise control over morphology and domain sizes. The size of the metal oxide domains for a given diameter of Au seeds was varied in the range of 10 nm to 30 nm by adjusting the molar ratio of the precursor. The investigation into the formation revealed the mechanism to comply with LaMer's model of heterogeneous nucleation. Further, dynamic light scattering was employed as a complementary technique and confirmed the impressive uniformity of both, the Au seeds as well as the heterodimer nanoparticles. The morphology was conclusively determined by TEM tomography as well as TEM EDX line scans. Magnetic data as well as optical measurements revealed a significant interaction, as the properties of the heterodimer nanoparticles differed distinctly from the individual components.

Moving on to the next step, we transferred this chemical protocol of heteroepitaxial growth to the related system of Au@Fe<sub>3</sub>O<sub>4</sub> heterodimers, as efforts based upon procedures described in literature did not produce the desired nanoparticles. For both systems, the corresponding metal oleate complex was used as metal oxide precursor, as it enabled control of the decomposition kinetics and obtained nanoparticle morphology. In analogy to Au@MnO, both size and morphology of the individual domains could be controlled by adjustment of the synthetic parameters. The domain sizes were varied in the range of 8 nm to 30 nm. However, the heterodimer systems differed regarding their mechanism of growth: the formation of Au@Fe<sub>3</sub>O<sub>4</sub> showed no indication of a separation of nucleation and growth, although monodisperse heterodimers were obtained anyhow due to a size-focusing effect.

Moreover, the universal applicability of the chemical protocol was confirmed by the exchange of the metal nanoparticles used as seeds to Pt or Au<sub>x</sub>Pt<sub>1-x</sub> alloy nanoparticles. Generally, an extremely high uniformity in size was obtained. Therefore, the comparison of the individual heterodimer systems with regard to their composition was possible. High resolution synchrotron diffraction data were used for quantitative phase analysis confirming the composition of Au@MnO as well as Au@Fe<sub>3</sub>O<sub>4</sub>, while Au<sub>x</sub>Pt<sub>1-x</sub>@Fe<sub>2</sub>O<sub>3</sub> was suggested by Rietveld refinement and corresponding magnetic data.

The intrinsic heteroepitaxial linkage enabled interaction of the individual components across their interface, which was reflected by modulation of the optical, magnetic, and structural characteristics. It revealed distinct differences between Au@MnO and Au@Fe<sub>3</sub>O<sub>4</sub> regarding the synthetic procedure as well as the properties to be altered by the variation of the electronic structure of the metal oxides. The chemically congeneric metal oxides differ significantly concerning their band gap, which regulates the formation of a Schottky junction at the interface of the two components in a heterodimer nanoparticle. For instance, transient absorption spectroscopy was utilized to analyze Au@MnO and Au@Fe<sub>3</sub>O<sub>4</sub> with reference to Au

nanoparticles. We observed prolonged relaxation times for Au partially embedded in metal oxide domains as compared to free-standing Au nanoparticles in solution. This confirmed the interaction across the interface. Taken together, these results suggested an electron transfer between Au domains and the semi-metal  $\text{Fe}_3\text{O}_4$ , while only a polarization occurred at the interface to the insulator MnO.

To summarize the optical characteristics, the surface plasmon resonance was found to be a function of several parameters: i) the electronic structure of the metal oxide controls the extent of interaction of the components, ii) the size of the domains, as well as the size ratio influences the position and the spectral intensity, and iii) the chemical composition of the metal domain is decisive for the native position and intensity of the SPR prior to the consideration of any influences and interactions. In fact, this set of composition- and size-tunable heterodimer nanoparticles enabled the shift of the optical resonance over a range of about 100 nm.

In conclusion, these findings enhanced the understanding of the formation of heterodimer nanoparticles and enabled the ascription of the modulated characteristics to the elementary concept of solid state interfaces. In short, we presented a kind of LEGO schematic as the individual components can be seen as building blocks. Consequently, a variety of heterodimer nanoparticles was established, which exhibits promising characteristics for further applications. It would be interesting to expand this concept to heterodimers composed of materials with electronic structures in between the extreme cases of a semi-metal,  $\text{Fe}_3\text{O}_4$ , and an indirect wide-band gap semiconductor, MnO. This might facilitate the fine-tuning of characteristics, which is of particular interest for catalytic and biomedical implementation.

### 3.7 Experimental Section

**Materials.** All reactions were carried out under argon atmosphere using commercially available reagents without any further purification: Manganese(II) chloride tetrahydrate ( $\text{MnCl}_2 \cdot 4\text{H}_2\text{O}$ , Reagent Plus, > 99 %), iron(III) chloride hexahydrate ( $\text{FeCl}_3 \cdot 6\text{H}_2\text{O}$ , Reagent Plus, 98 %), sodium hydroxide (99 %), sodium oleate (> 82 % fatty acids (as oleic acid) basis), 1-octadecene (technical grade, 90 %), and 1-octadecanethiol (ODT, 98 %) were purchased from Sigma Aldrich. 2-Propanol, acetone, ethanol, heptane, hexane, oleic acid (reagent grade), and oleylamine (80 - 90 %) were purchased from Fisher Scientific.

In order to control the heating rate, self-built heating controllers were used. These were composed of a control unit (KS40, type 9404 407 40001, Philips) and a temperature sensor (type S/S-316RS Components GmbH) connected to a heating mantle (neoLab-Pilz® standard heating mantle, 230 V, 150 W,  $T_{max} = 450\text{ }^\circ\text{C}$ ).

**Ligand Exchange of Au NPs.** The ligand exchange to 1-octadecanethiol was performed by addition of a solution of oleylamine-functionalized Au NPs to 10 mL toluene

containing 3 mmol ODT under argon atmosphere. The solution was stirred at room temperature overnight. The particles were precipitated by addition of methanol, collected by centrifugation (9000 rpm, 10 min), and washed using hexane/ethanol.

**Synthesis of Manganese(II) Oleate.** The chemical protocol was modified from Schladt and co-workers.<sup>[177]</sup> Briefly, 40 mmol  $\text{MnCl}_2 \cdot 4\text{H}_2\text{O}$  and 80 mmol oleic acid were dissolved in 200 mL methanol. A solution of 80 mmol sodium hydroxide (or potassium hydroxide) in 200 mL methanol was added dropwise to the vigorously stirring solution over a period of 2 h. The product precipitated in the form of a deep red, waxy solid. Stirring was continued for 1 h, after which the solvent was discarded. The precipitate was washed repeatedly with water, ethanol, and acetone. The oily residue was dissolved in hexane and washed again with a 1:1 mixture of ethanol:methanol. The solution was stirred over  $\text{MgSO}_4$  overnight before the solvent was removed. The final product was dried in fine vacuum ( $2 \cdot 10^{-2}$  mbar) at 100 °C for 3 h.

**Synthesis of Au@MnO Heterodimers.** Heteroepitaxial growth of manganese oxide on ODT-functionalized gold particles was used for the preparation of monodisperse Au@MnO heterodimers with tunable size of the MnO domains. For 4@25 nm-heterodimers, 0.4 mmol manganese oleate was mixed with 20 mL 1-octadecene containing 6 mmol oleic acid and 6 mmol oleylamine at 80 °C under argon atmosphere. 10 mg ODT-functionalized Au nanoparticles in 1 mL 1-octadecene were added to the mixture, which was degassed at 80 °C for 1 h before being heated slowly up to 320 °C (heating rate: 2 °C/min). The reaction mixture was held at reflux for 30 min before cooling down to room temperature by removing the heating mantle. The particles were washed by repeated precipitation with acetone, centrifugation (9000 rpm, 10 min), and dissolution in hexane.

**Synthesis of Iron(III) Oleate.** The synthetic procedure was adapted from Park *et al.* with some modifications regarding the purification.<sup>[190]</sup> Briefly, 40 mmol  $\text{FeCl}_3 \cdot 6\text{H}_2\text{O}$  and 120 mmol sodium oleate were dissolved in a mixture containing 80 mL ethanol, 60 mL distilled water, and 140 mL hexane. Subsequently, the reaction mixture was heated up to 70 °C and kept at reflux for 4 h. After completion of the reaction, the organic layer was washed repeatedly with distilled water and methanol until no turbidity of the wash solution occurred. In the next step, the solvent was evaporated, and the iron(III) oleate complex was dried under fine vacuum ( $2 \cdot 10^{-2}$  mbar) at 100 °C for 3 h.

**Synthesis of  $\text{Fe}_3\text{O}_4$  Nanoparticles.** The synthesis was adapted from Hatakeyama and co-workers.<sup>[223]</sup> Briefly, 10 mmol iron(III) oleate were dissolved in 50 mL tri-*n*-octylamine at 80 °C under argon atmosphere. Next, the reaction mixture was degassed for 1 h, before heating to 320 °C with a heating rate of 3.3 °C/min. The reaction temperature was maintained for 30 min. After cooling down to room temperature by removing the heating mantle, the particles were washed by precipitation with 2-propanol, centrifugation (9000 rpm, 10 min), and dissolution in hexane until a powdery precipitate was obtained. The particles were re-dissolved in hexane.



**Synthesis of Au@Fe<sub>3</sub>O<sub>4</sub> Heterodimers.** The synthetic protocol was developed in analogy to Au@MnO heterodimers based on reports by Lin *et al.* with modifications concerning the heating program as well as the ligand ratio.<sup>[165]</sup> For 7@20 nm heterodimers, 0.4 mmol iron(III) oleate was dissolved in a mixture composed of 30 mL 1-octadecene, 8 mmol oleylamine, and 6 mmol oleic acid at 80 °C under argon atmosphere. 30 mg oleylamine-functionalized Au nanoparticles were added in 1 mL 1-octadecene. In the next step, the reaction mixture was heated slowly to reflux to 320 °C with a heating rate of 2 °C/min. It was held at reflux for 30 min before cooling down to room temperature by removing the heating mantle. The particles were washed twice by precipitation with 2-propanol, centrifugation (9000 rpm, 10 min), and dissolution in hexane.

Au<sub>x</sub>Pt<sub>1-x</sub>@Fe<sub>2</sub>O<sub>3</sub> and Pt@Fe<sub>2</sub>O<sub>3</sub> were prepared as described for Au@Fe<sub>3</sub>O<sub>4</sub>, except spheroidal Au<sub>x</sub>Pt<sub>1-x</sub> or truncated cubic Pt nanoparticles were added as seeds.

**Nanoparticle Characterization.** The nanoparticles were characterized by means of (high resolution) transmission electron microscopy ((HR) TEM), UV-VIS spectroscopy, dynamic light scattering (DLS), Fourier transformed infrared spectroscopy (FT-IR), time-resolved transient photoluminescence spectroscopy (TR-PL), and high resolution synchrotron powder diffraction. The magnetic properties were investigated with a superconducting quantum interference device (SQUID). Further technical details on employed instruments are elaborated in Chapter 4.4.1.



# 4

## Surface Modification of Heterodimer Nanoparticles

This chapter contains parts of an adapted reproduction of *Journal of the American Chemical Society* **2014**, 136, 2473 – 2483,<sup>[54]</sup> reproduced with permission of the American Chemical Society Copyright 2014, and of a manuscript submitted to the *Beilstein Journal of Nanotechnology* linked to the final report of the DFG priority program SPP 1313 “Biological Responses to Nanoscale Particles”.<sup>[151]</sup>

### 4.1 Introduction

As pointed out in the previous chapter, the synthesis of monodisperse, well-defined hetero-nanostructures requires non-hydrolytic reaction conditions. However, water-soluble, multifunctional nanoparticles are crucial for any biomedical application including sensing biomolecules, interaction with cells, diagnosis of diseases, and intracellular delivery.<sup>[5,7,224]</sup> Therefore, it is necessary to exchange the hydrophobic surface functionalization of the nanoparticles with hydrophilic coatings to secure colloidal stability in an aqueous environment. These coatings are applied in order to provide water-solubility and stabilization against aggregation as well as to introduce chemical functionalities on the surface, which is needed for subsequent linking of various (bio-)chemicals of interest.<sup>[44,225]</sup> In this context, the term “water-soluble” refers to a physically and chemically stable colloidal suspension, in which nanoparticles do not aggregate, flocculate, dissociate, or chemically react.<sup>[226]</sup>

There are several surface modification strategies based on conventional organic ligands, such as ligand exchange to bind bifunctional or multidentate ligands, the formation of amphiphilic bilayers by interdigitation with the original hydrophobic ligand shell, or a cross-linked coating. The ligand exchange is characterized by the substitution of the native surfactant by a bifunctional hydrophilic molecule. They are composed of an anchoring group at one end, which

coordinates to the nanoparticle surface via Lewis-base interactions, and hydrophilic groups at the other end in order to promote water solubility.<sup>[227]</sup> The fundamental problem of functionalization is often the weak interaction between the nanoparticle surfaces and the ligands.<sup>[225]</sup> Further, all these strategies suffer from the assumption that the ligand coating is neither densely packed nor static with regard to ligand exchange when the particle dispersions are diluted in biological media.<sup>[226]</sup> On the other hand, the encapsulation of isotropic nanoparticles in a silica shell has been established. Silica was demonstrated to be superior for several reasons: it is optically transparent, mechanically stable, and fairly biocompatible.<sup>[228]</sup> Most obvious, its extraordinary chemical stability and mature surface chemistry allow facile targeted functionalization.<sup>[48,229]</sup> Furthermore, the silica shell preserves the intrinsic materials' properties such as magnetic or plasmonic characteristics.<sup>[230,231]</sup> It minimizes agglomeration,<sup>[232]</sup> flocculation,<sup>[233]</sup> release of toxic ions from the nanoparticle surface,<sup>[231]</sup> and the direct contact of the core material with cells.<sup>[234]</sup> Due to its higher packing density as compared to an organic ligand coating, it also diminishes the diffusion of water or solvent molecules to the surface of the underlying particle.

In recent years, there has been substantial progress concerning silica encapsulation of nanoparticles.<sup>[48,180,230,235–243]</sup> Most commonly, two preparation techniques are applied, either the Stöber synthesis or the reverse microemulsion technique. Originally, both were developed for the fabrication of monodisperse silica spheres. In 1968, Stöber *et al.* described the synthesis of 50 nm to 2  $\mu\text{m}$  sized uniform  $\text{SiO}_2$  particles by hydrolysis of alkyl silicates and subsequent condensation of silicic acid in aqueous alcoholic solutions.<sup>[244]</sup> This technique was adjusted to the coating of nanoparticles, though it is restricted to rather large, hydrophilic nanoparticles and thick silica shells in the range of 30 to 100 nm.<sup>[180,235,245]</sup> Alternatively, the reverse microemulsion process is used, which can also be combined with a sol-gel process to prepare multifunctional nanocomposites in a one-pot procedure.<sup>[237]</sup> This technique is superior as it can be directly applied to hydrophobic nanoparticles, which are unstable under the conditions of a typical Stöber synthesis. Microemulsions are frequently used as a confined reaction medium, as they are a homogeneous mixture at macro-scale, but exhibit heterogeneous domains at the microscopic level. Generally, they are composed of water, an organic solvent, and a surfactant, which is responsible for the formation of micelles.<sup>[242]</sup> Water-in-oil microemulsions efficiently dissolve inorganic as well as organometallic precursors aside from the nanoparticles. They facilitate the design of silica-coated nanostructures of various size, shape, and functionalization. Further, they allow an even more facile tuning of the silica shell thickness and surface functionality.<sup>[229,239]</sup> Recently, this coating method of pre-synthesized hydrophobic nanoparticles was demonstrated to be suitable for a variety of metal,<sup>[246]</sup> semiconductor,<sup>[247,248]</sup> or magnetic nanoparticles,<sup>[237,249,250]</sup> and enabled their adjustment to different applications, for instance biocompatibility of CdSe/ZnS quantum dots for *in vitro* imaging,<sup>[251,252]</sup> colloidal stability in

aqueous solution for targeted magnetic resonance imaging using MnO or Fe<sub>3</sub>O<sub>4</sub> nanoparticles as core material,<sup>[48,232,243,253]</sup> or FePt@SiO<sub>2</sub> after heat treatment to obtain the compositionally-ordered L1<sub>0</sub> phase.<sup>[230]</sup>

Nanoparticles are frequently used for biomedical imaging. Therefore, their optical response is crucial for *in vitro* or *in vivo* application in order to label cellular proteins and track cells or nanoparticles themselves.<sup>[254]</sup> Multimodal imaging of nanoparticles by combination of intrinsic material properties with *e.g.* fluorophores is the cutting edge technology, as each imaging technique has its assets and drawbacks.<sup>[255]</sup> Further, multi-photon microscopy possesses some advantages over conventional confocal microscopy, such as a reduced fluorescence background because of the relatively low two-photon cross-section of most biomolecules responsible for autofluorescence, less photo-bleaching by selective excitation of the focal volume, and improved depth penetration in scattering samples by using excitation light within the optical transmission window of biological tissues (near-infrared (NIR) spectral range, 700 - 1000 nm).<sup>[256]</sup> Preliminary work on fluorescent silica spheres by incorporation of covalently linked organic dyes into monodisperse, colloidally-stable silica spheres was undertaken by van Blaaderen and co-workers.<sup>[257]</sup> These incorporated dyes are advantageous as compared to their liquid solutions, as the photo-stability and fluorescence yield is increased.<sup>[258]</sup> Further, the dye molecules are isolated from each other, which inhibits energy transfer due to unwanted non-fluorescent aggregates or complexes. This technique enables the visualization of silica-coated nanoparticles, which do not exhibit intrinsic fluorescence.<sup>[235,241,247,248,250]</sup> Further, leakage of the dye from the silica particles is negligible as they are covalently attached in addition to being held by strong electrostatic forces.<sup>[259]</sup>

A crucial aspect of the surface modification for the subsequent binding of biomolecules is the controlled covalent attachment of desired functional groups. For silica, its well-known surface chemistry allows the effective functionalization by co- or subsequent hydrolysis of functional organo-silanes. In this context, amino-silanes are used most prominently, as they enable the conjugation of dyes and biomolecules, such as sugars, antibodies, and peptides.<sup>[48,232]</sup> Moreover, a challenge concerning the design of nanoparticle surfaces for biomedical applications is the balance of an inert surface with active functionalities in order to minimize the aggregation of nanoparticles as well as the nonspecific binding of biomolecules. This difficulty arises from the large surface area with excess functional groups, which are aimed to interact with distinct chemicals, but can also lead to false positive/negative signals in biological studies.<sup>[232]</sup> Previous research has reported a positive impact of poly(ethylene glycol) (PEG) based coatings on the biological performance of nanoparticles. PEG functionalized nanoparticles were demonstrated to suppress protein adsorption, to be highly biocompatible, and, further, to enhance the residence half-life in the bloodstream within *in vivo* studies, as they escaped the opsonization process.<sup>[7,233,260,261]</sup> Aside from commonly used ligand exchange

reaction to conjugate PEG or its derivatives to nanoparticles, PEG can also be covalently attached to the surface. This covalent binding prevents ligand exchange subsequent to incubation with biological media. For instance, this was demonstrated by initial results from our group: highly-soluble, colloidally-stable, and biocompatible MnO@SiO<sub>2</sub>-PEG nanoparticles were obtained by combining the benefits of a chemically-inert silica coating with subsequent PEG functionalization.<sup>[51]</sup>

Generally, colloidal stability of nanoparticles is controlled by van der Waals interactions, electrostatic, solvation, solvophobic, and depletion forces. The most important forces regarding the interaction of SiO<sub>2</sub> nanoparticles in aqueous solution are van der Waals attraction, electrostatic repulsion, and solvation forces, which are described by the Derjaguin-Landau-Verwey-Overbeek (DLVO) theory of colloid science (Figure 4.1).<sup>[262–264]</sup>

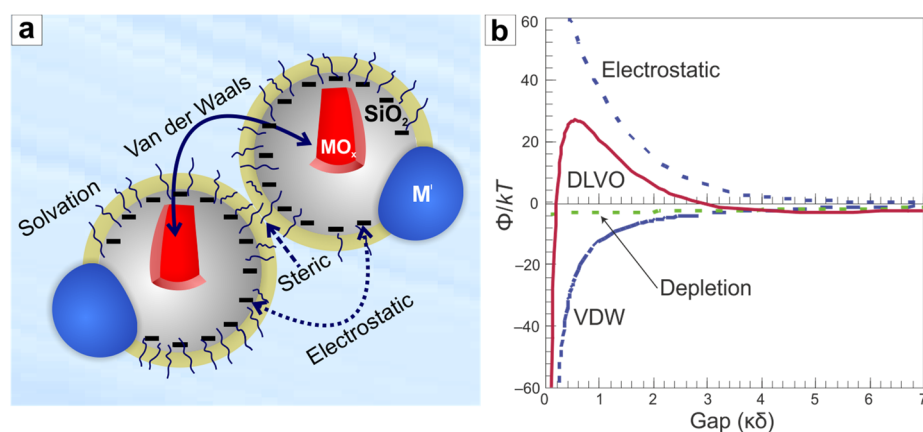


Figure 4.1: Interaction between nanoparticles in aqueous solution: a) schematic illustration of important forces for colloidal stability such as van der Waals, electrostatic, and steric interactions; b) interaction potential  $\Phi$  as a function of the separation distance considering repulsive electrostatic, attractive van der Waals, and depletion forces. a) In the style of and b) reproduced from [265].

According to the DLVO theory, the interaction between nanoparticles can be divided into a repulsive electrostatic force as a consequence of the charged surfaces and an attractive van der Waals (VDW) force due to the solid particle cores. The VDW attraction becomes important for small interparticle distances, as it is caused by electron fluctuations in the core leading to a dipole moment, which may induce aggregation. This comes into account when the hydration shell of charged surfaces in water, the so-called electric double layer, is compressed by a high ionic strength, addition of surfactants, electrolytes, or influenced by changes in the *pH* value. On the other hand, the electrostatic repulsion outranges the VDW attraction. In the case of SiO<sub>2</sub> nanoparticles, the silanol groups at the surface dissociate when in contact with water, such that a negative surface charge emerges. The DLVO theory facilitates predictions of the colloidal stability in dependence of their potential at the hydrodynamic shear plane, the zeta potential  $\zeta$ . For solely electrostatically-stabilized particles, stable colloids are obtained for  $\zeta < -20$  mV, whereby  $-11$  mV  $< \zeta < -20$  mV is on the border of aggregation. Upon additional steric stabilization

this prediction becomes less stringent, as the inhibition of interdigitation of bulky ligands enhances the interparticle distances.<sup>[266]</sup>

Inspired by initial results from our group,<sup>[47,51,168,267]</sup> we present here a facile method for the silica encapsulation of hydrophobic Au@MO<sub>x</sub> heterodimer nanoparticles in order to facilitate water-solubility, stability against aggregation, and tailor-made multifunctionality. Thereby, a precise control over the extent of the silica coating was realized: either only the metal oxide component or the whole particle has been coated with a thin silica layer. This is based on the reduced wetting of the chemically different surfaces, which leaves the noble metal component untouched and available for specific surface functionalization that allows a facile conjugation of biomolecules. Their fluorescence labeling as well as intrinsic two-photon activity makes Au@MO<sub>x</sub>@SiO<sub>2</sub> hetero-nanoparticles not only advantageous for optical bioimaging applications, but also for multimodal detection, which will be addressed in Chapter 6.

## 4.2 Silica Encapsulation of Heterodimer Nanoparticles

The hydrophobic heterodimer nanoparticles were functionalized with silica using the reverse microemulsion technique adapted from spherical nanoparticles. Briefly, a stable water-in-oil emulsion was obtained by mixing cyclohexane, aqueous ammonia, and a non-ionic surfactant. This mixture represents a thermodynamically stable single-phase system with spherical, size-tunable micelles due to the stabilization of the emulsion by a surfactant. Their size was adjusted by the ratio of surfactant to water, which controlled the thickness of the silica coating as well.<sup>[232]</sup> Nowadays, three different non-ionic surfactants are commonly used, Triton<sup>TM</sup> X-100,<sup>[232,268]</sup> Igepal® CO-520,<sup>[230]</sup> and Brij® 97.<sup>[237]</sup> Igepal® CO-520, polyoxyethylene(5)nonyl-phenyl ether, is the only surfactant reported to be used at room temperature with comparably short reaction times. The quality of the resulting silica coating is independent of the non-ionic surfactant used, thus, we chose Igepal® CO-520.

The reaction taking place can be described in terms of a hydrolysis and polymerization of silane monomers, here tetraethoxysilane, TEOS, inside the micelles of the water-in-oil microemulsion.<sup>[48,51,237]</sup> Aqueous ammonia was used for two reasons: water served as reactant and NH<sub>3</sub> as catalyst for the hydrolysis of TEOS. Since water and TEOS are immiscible, the formation of the silica coating took place only at the oil-water interface (Figure 4.2).

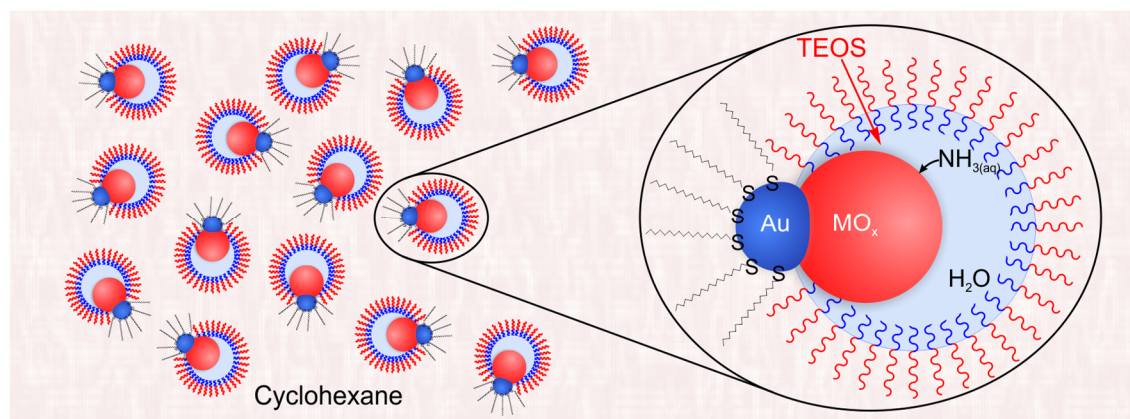


Figure 4.2: Schematic diagram of the silica encapsulation of Au@MO<sub>x</sub> heterodimer nanoparticles using the reverse microemulsion indicating the impact of a long-chain alkane-thiol.

Wu *et al.* suggested a ligand exchange to be the consequence of the interaction of ammonia with the metal oxide surface, which would invert its hydrophobic nature and facilitate the formation of silica on the metal oxide domain.<sup>[166]</sup> Further, due to the different chemical wetting behavior of gold and the metal oxide surface, only the metal domain was encapsulated, leaving the hydrophobic character of the gold domain untouched (Figure 4.3).

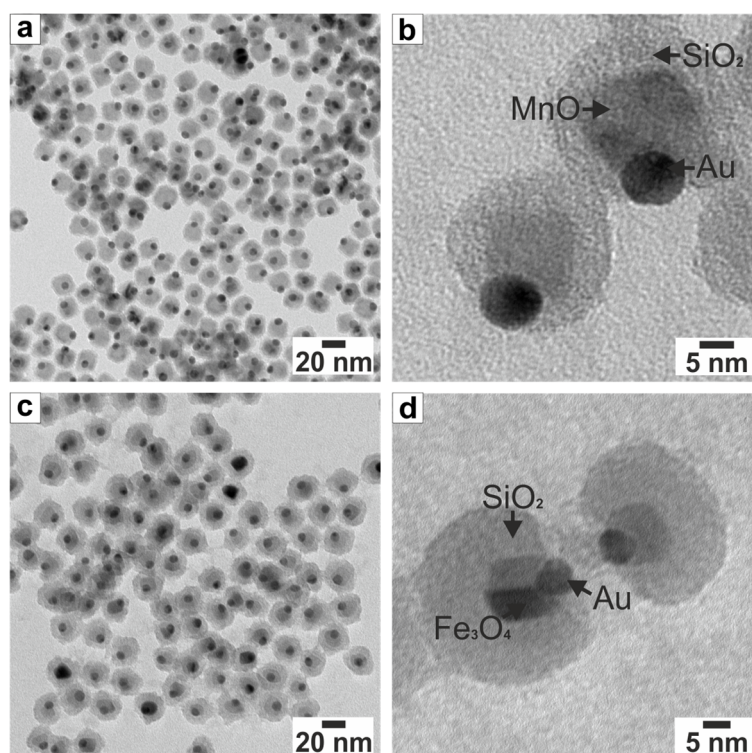


Figure 4.3: TEM micrographs of silica-encapsulated heterodimer nanoparticles: (a, b) Au@MnO@SiO<sub>2</sub> (10@20 nm) and (c, d) Au@Fe<sub>3</sub>O<sub>4</sub>@SiO<sub>2</sub> (9@15 nm).

This selectivity was enhanced by functionalization of the vitreophobic gold domain with a long-chain alkanethiol: it was performed either prior to the growth of manganese oxide or subsequent to the formation of the iron oxide component. The centrality of the thiol functionalization was demonstrated by complete encapsulation of Au@Fe<sub>3</sub>O<sub>4</sub><sup>[166]</sup> and Ag@Fe<sub>3</sub>O<sub>4</sub> nanoparticles with a thin silica shell.<sup>[231]</sup>



Referring to Schladt and co-workers, the stability of silica-coated particles against aggregation due to Coulomb attraction was enhanced by surface modification using a PEG-silane conjugate.<sup>[51]</sup> Likewise, Graf *et al.* demonstrated the colloidal stability of positively charged SiO<sub>2</sub> nanoparticles to scale with the ionic strength of the media, while no indication of aggregation was observed for bare or PEG-coated nanoparticles.<sup>[228]</sup>

The typical thickness of the silica shell of 3 - 5 nm was consistent with the results reported for pure MnO particles.<sup>[51]</sup> Figure 4.4 shows Au@MnO@SiO<sub>2</sub> nanoparticles after the functionalization was completed. Aside from the amount of NH<sub>4</sub>OH, the thickness of the SiO<sub>2</sub> layer was adjusted by simply varying the ratio of nanoparticles to the silica precursor. Thus, it was tuned from ca 4 nm to more than 11 nm, as was demonstrated for spherical FePt nanoparticles.<sup>[230]</sup> However, a crucial shell thickness was also observed, above which the tendency of growing a closed silica shell outweighed the vitreophobic nature of the metal domain. This was true for a shell thickness in the range of or larger than the diameter of the metal oxide domain.

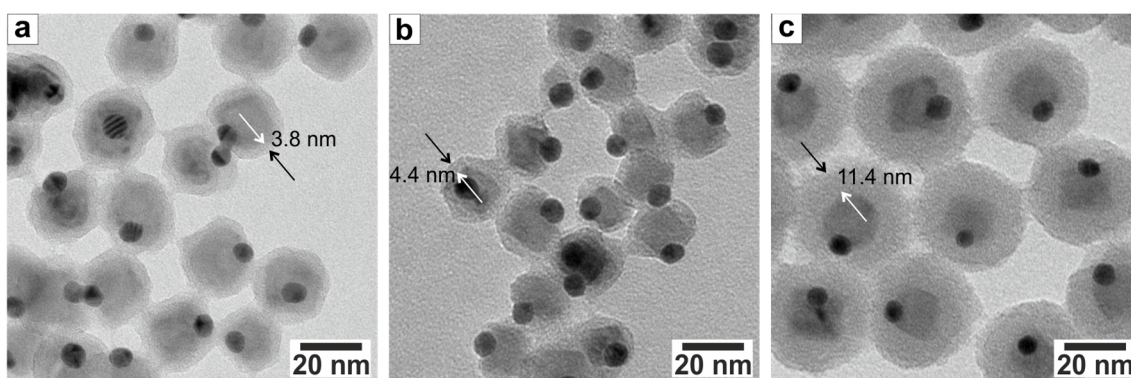


Figure 4.4: TEM images of Au@MnO@SiO<sub>2</sub> heterodimer nanoparticles with increasing thickness of the silica shell from a) 3.8 nm to b) 4.4 and, finally, to c) 11.4 nm. This was obtained by increasing the ratio of tetraethoxysilane to hydrophobic Au@MnO heterodimer nanoparticles from 112  $\mu$ L to 224  $\mu$ L per 10 mg.

High resolution synchrotron powder diffraction data were collected at the beamline 11-BM at the Advanced Photon Source (APS) of the Argonne National Laboratory. Figure 4.5 displays the quantitative phase analysis by means of Rietveld refinement of room temperature synchrotron diffraction data of Au@MnO@SiO<sub>2</sub> Janus particles as compared to hydrophobic Au@MnO heterodimers. Reflection profiles were modelled according to the fundamental parameter approach. The domain sizes of Au@MnO@SiO<sub>2</sub> nanoparticles were 9.0 nm  $\pm$  0.6 nm for the Au domain and 18.8 nm  $\pm$  0.8 nm according to TEM analysis, while the thickness of the silica shell was ca 5 nm. Full profile analysis of the synchrotron data led to a crystallite size for Au of 9.4(3) nm and 6.1(5) nm for MnO, indicating the MnO domains to be composed of multiple crystallites (see Table S2). In comparison to the uncoated particles, the synchrotron data of silica-coated Janus particles exhibited a broad, structureless diffraction maximum at ca  $Q = 1.5 \text{ \AA}^{-1}$ , which indicated the presence of SiO<sub>2</sub> as an amorphous compound.

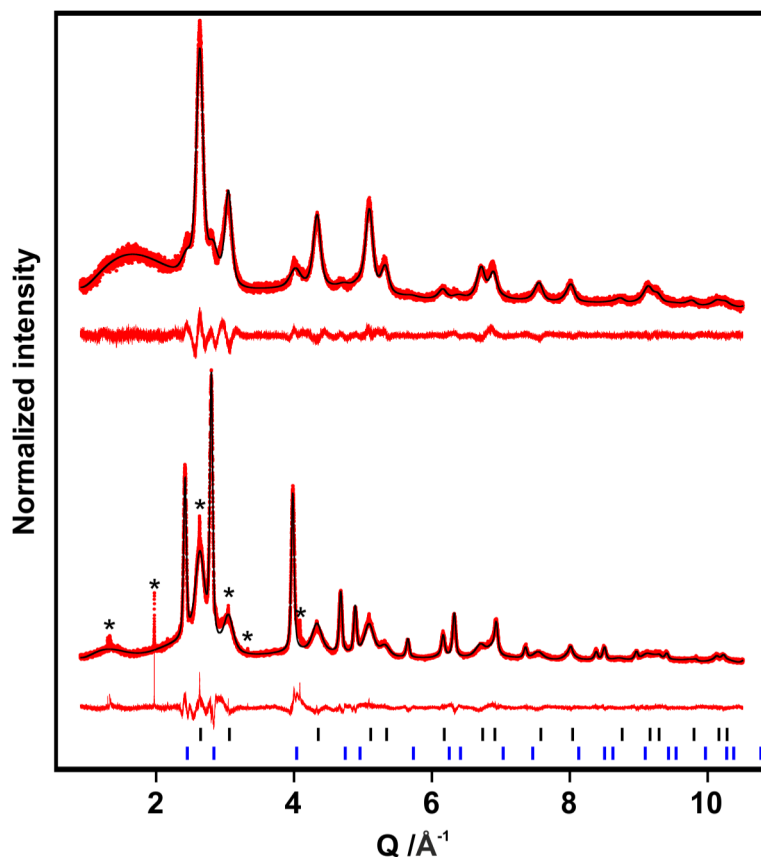


Figure 4.5: Refined synchrotron powder diffraction data for Au@MnO@SiO<sub>2</sub> (top; red dots) and Au@MnO (bottom; red dots), including profile fits (black solid lines), and profile differences (red solid lines). The refined peak positions are indicated by black and blue tick marks for Au (top) and MnO (bottom), respectively. Contaminations are marked by asterisks. The data were refined by [REDACTED].

The formation of the silica shell was monitored by FT-IR spectroscopy. Figure 4.6 displays FT-IR spectra of Au@MnO nanoparticles prior to as well as after the silica encapsulation. The spectrum of oleylamine- and oleic acid-capped Au@MnO nanoparticles showed characteristic vibrational bands at 1377 and 1261 cm<sup>-1</sup>, assigned to the asymmetric and symmetric stretching modes of the carboxylate groups of oleic acid. Further, strong absorption bands at 2850, 2922, and 2958 cm<sup>-1</sup> were assigned to the symmetric and asymmetric stretching modes of the CH<sub>2</sub>- and CH<sub>3</sub>-groups.<sup>[177]</sup> The attachment of the ligand oleylamine was identified by its characteristic N-H stretching mode at 3320 cm<sup>-1</sup> and the C=C bending mode at 1634 cm<sup>-1</sup>. In the spectrum of the Au@MnO@SiO<sub>2</sub> particles, the bands of the carboxylate groups vanished almost completely. A broad, split, and strong band system at 1105 and 1020 cm<sup>-1</sup> appeared instead, which was ascribed to the Si-O-Si asymmetric stretching modes.<sup>[48]</sup> The stretching vibrations due to CH<sub>2</sub>- and CH<sub>3</sub>-groups remained, although less pronounced due to the conjugation of PEG-chains to the surface of the silica shell as well as the ligands of the Au domains.<sup>[51]</sup> Further, the symmetric stretching modes of PEG-chains were measured at 1463 cm<sup>-1</sup> and 1384 cm<sup>-1</sup>.

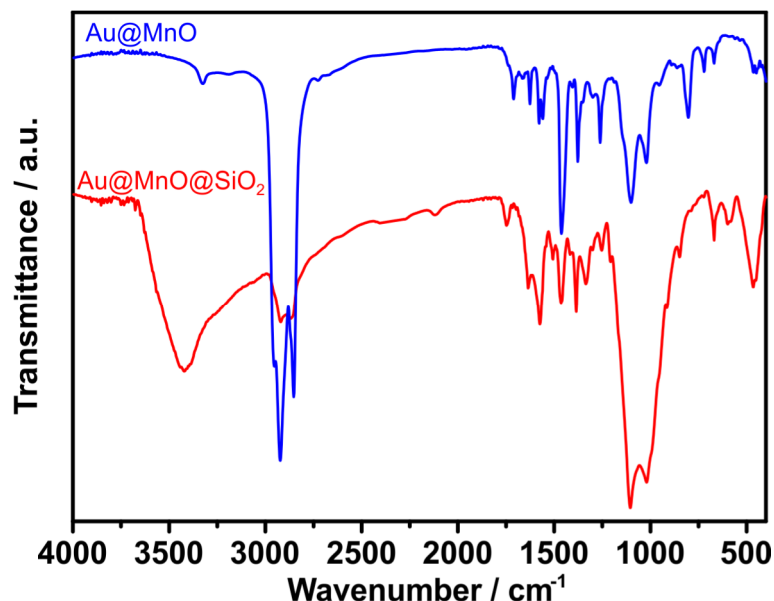


Figure 4.6: FT-IR spectra of Au@MnO and Au@MnO@SiO<sub>2</sub> nanoparticles: the stretching modes of the carboxylic groups disappeared and strong O-Si-O modes emerged due to the encapsulation with silica.

#### 4.2.2 Colloidal Stability of Au@MO<sub>x</sub>@SiO<sub>2</sub> Nanoparticles

Independent of the thickness of the silica shell, the obtained nanoparticles appeared uniform and well separated, although they were orthogonally functionalized. The particles changed their solubility behavior upon encapsulation with silica: the primary hydrophobic particles were transferred from any non-polar solvent to polar solvents, such as acetone, water, or ethanol (Figure 4.7a). However, the colloidal stability of the nanoparticles at all stages of their preparation was not influenced, as confirmed by dynamic light scattering measurements (Figure 4.7b, Figure 4.8).

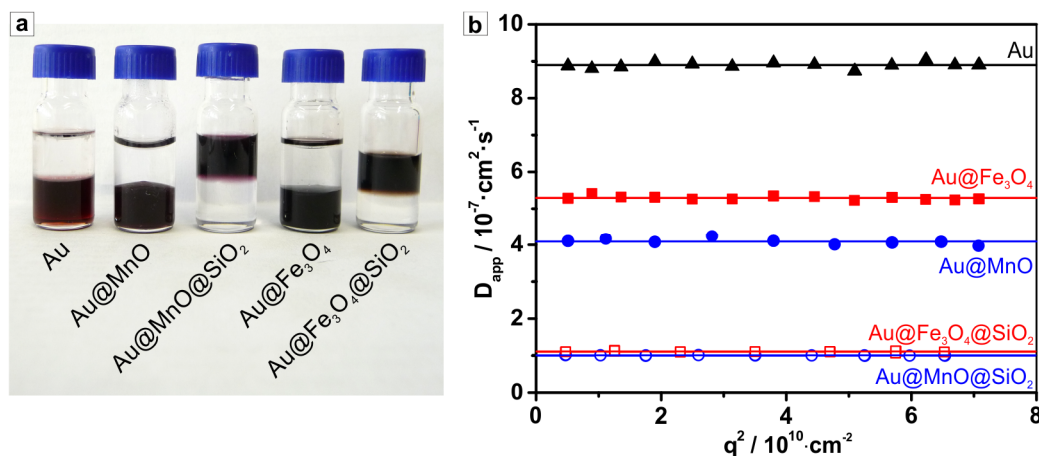


Figure 4.7: a) Photograph of nanoparticles in a two-phase system composed of water (top) and chloroform (bottom), from left to right: Au, Au@MnO, Au@MnO@SiO<sub>2</sub>, Au@Fe<sub>3</sub>O<sub>4</sub>, and Au@Fe<sub>3</sub>O<sub>4</sub>@SiO<sub>2</sub> nanoparticles indicating the reversal of solubility upon silica encapsulation, b) dynamic light scattering results of Au, Au@MnO, and Au@Fe<sub>3</sub>O<sub>4</sub> dispersed in *n*-heptane in comparison to Au@MnO@SiO<sub>2</sub> and Au@Fe<sub>3</sub>O<sub>4</sub>@SiO<sub>2</sub> dispersed in water ( $\lambda = 632.8$  nm,  $T = 293$  K): apparent diffusion coefficients as a function of scattering vector  $q^2$  in the range of scattering angle  $30^\circ \leq \theta \leq 150^\circ$ .

The constancy of the apparent diffusion coefficients as a function of the scattering angle indicated high uniformity of the size distribution of all analyzed nanoparticles, namely spherical Au seeds, hydrophobic Au@MnO and Au@Fe<sub>3</sub>O<sub>4</sub> heterodimers, as well as hydrophilic Au@MnO@SiO<sub>2</sub> and Au@Fe<sub>3</sub>O<sub>4</sub>@SiO<sub>2</sub> nanoparticles. Hydrodynamic radii were obtained using the Stokes-equation and are summarized in Table 4.1. The progressive increase in the hydrodynamic radii of the hydrophobic nanoparticles corresponded to the increase in particles' core diameter determined by TEM. Further, the approximately 7 nm increase in the hydrodynamic radius from hydrophobic to hydrophilic heterodimer nanoparticles was in good accordance with the thickness of the SiO<sub>2</sub> shell detected by TEM of ca 5 - 6 nm and the expected contribution of the hydration shell in aqueous solution. The silica encapsulation of Au@MnO and Au@Fe<sub>3</sub>O<sub>4</sub> differed regarding the wetting of the Au domain. As is indicated by brackets, the silica layer enclosed Au@Fe<sub>3</sub>O<sub>4</sub> completely, as no thiol functionalization was applied beforehand (see also insets of Figure 4.8). However, the colloidal stability and uniformity of the two hydrophilic nanoparticles were indistinguishable.

Table 4.1: Radii of Au and Au@MO<sub>x</sub> as intermediate stages as well as Au@MO<sub>x</sub>@SiO<sub>2</sub> nanoparticles determined by TEM and DLS.

Sample	$R_{TEM} / \text{nm}$	$R_h / \text{nm}$
Au	$4.8 \pm 0.3$	$6.5 \pm 0.5$
Au@MnO	$10.8 \pm 0.8$	$14.1 \pm 0.2$
Au@Fe <sub>3</sub> O <sub>4</sub>	$8.2 \pm 0.6$	$12.8 \pm 0.2$
Au@MnO@SiO <sub>2</sub>	$15.8 \pm 1.0$	$21.6 \pm 0.2$
(Au@Fe <sub>3</sub> O <sub>4</sub> )@SiO <sub>2</sub>	$14.6 \pm 1.0$	$19.5 \pm 0.2$

Further, the amplitude autocorrelation functions measured at a scattering angle of  $\theta = 30^\circ$ , which is most sensitive to aggregates, facilitated bi-exponential fitting for both hydrophobic and hydrophilic nanoparticles. This eliminated conceivable aggregation as a consequence of the orthogonal functionalization of Au@MnO@SiO<sub>2</sub> (Figure 4.8). On the contrary, the selective wetting behavior of SiO<sub>2</sub> on heterodimer nanoparticles would be expected to facilitate self-organization of orthogonally functionalized nanoparticles. Upon closer examination, the lack of self-organization was not contradictory, rather it was attributed to the experimental requirements of dynamic light scattering, namely the great dilution of colloidal dispersions in order to investigate the scattering from single particles instead of interacting ensembles. Thus, the self-aggregation was meant to be suppressed.

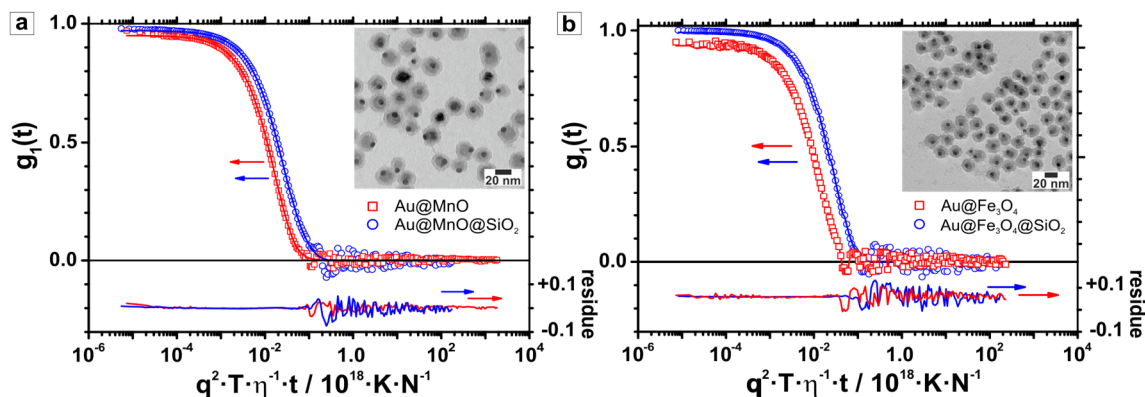


Figure 4.8: Dynamic light scattering results of a) Au@MnO and Au@MnO@SiO<sub>2</sub>, b) Au@Fe<sub>3</sub>O<sub>4</sub> and Au@Fe<sub>3</sub>O<sub>4</sub>@SiO<sub>2</sub> dispersed in *n*-heptane and water, respectively ( $\lambda = 632.8$  nm,  $T = 293$  K, viscosity  $\eta$ : 0.41 cP *n*-heptane, 1.005 cP water): universally-scaled and normalized field autocorrelation functions measured at scattering angle  $30^\circ$  together with bi-exponential fitting function lines and corresponding residues. The inset in each case shows a TEM image of the respective SiO<sub>2</sub>-encapsulated heterodimer nanoparticles.

Aside from the transfer from nonpolar to aqueous solutions, this synthetic route allowed precise control over the surface functionalization and, thus, surface charge. The silica coating of heterodimer nanoparticles was modified by subsequent addition of amino-silanes, such as (3-aminopropyl)triethoxysilane (APTES) to silica-coated nanoparticles in acetone. Zeta potential measurements in highly pure water confirmed the modification of surface functionalization, as the net surface charge was drastically changed. For Au@MnO nanoparticles coated with SiO<sub>2</sub> and subsequent PEG-functionalization, the surface charge at the hydrodynamic shear plane was determined to be  $\zeta = -35$  mV  $\pm$  1.8 mV. The negative charge originated from deprotonated silanol groups -Si-O<sup>-</sup> at the surface. Upon attachment of amino groups, the surface charge was shifted into the positive regime: depending on the molar ratio of amino silane to -Si-O<sup>-</sup> at the surface of Au@MnO@SiO<sub>2</sub>, the zeta potential ranged from  $\zeta = -24$  mV  $\pm$  0.8 mV to  $\zeta = 21$  mV  $\pm$  0.5 mV. This resulted from the co-presence of protonated amine groups -NH<sub>3</sub><sup>+</sup> and deprotonated silanol groups.<sup>[229]</sup> Aside from the shift in the zeta potential, a charge-dependent aggregation was observed: the less negative the surface charge, the more severe the aggregation that was measured became (Figure 4.9). This observation coincided with the prediction from the DLVO theory:  $\zeta > -20$  mV facilitates aggregation, even though the particles were stabilized not only electrostatically, but also by steric hindrance of the PEG ligands.<sup>[262,263]</sup>

The charge-dependent aggregation was attributed to the strong electrostatic attraction of opposite charges on the surface between the particles. However, upon dissolution in buffer, cell media, or blood serum, which exhibit a significantly increased ionic strength, the colloidal stability of even amino-functionalized silica-coated nanoparticles was enhanced. The inset of Figure 4.9a shows a digital photograph of the nanoparticle solutions in water and different concentrations of human blood serum after incubation for 5 days at 22 °C. No indication of aggregation or flocculation was observed.

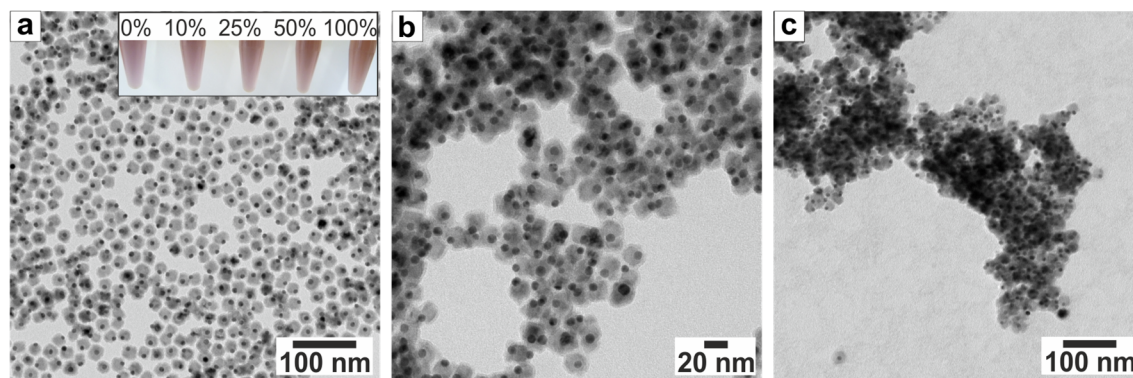


Figure 4.9: TEM images of Au@MnO@SiO<sub>2</sub> nanoparticles with variable surface charge: a) SiO<sub>2</sub>-PEG coating of Au@MnO nanoparticles led to non-aggregated stable nanoparticles with a negative zeta potential of  $\zeta = -35 \text{ mV} \pm 1.8 \text{ mV}$ ; inset: stability of particle solutions in water and increasing amount of human blood serum from left to right after 5 days. Upon attachment of amino groups the surface charge was shifted into the positive regime: b)  $\zeta = -19 \text{ mV} \pm 0.5 \text{ mV}$  and c)  $\zeta = 21 \text{ mV} \pm 0.5 \text{ mV}$ , where the aggregation intensified.

In addition to the colloidal stability, the chemical stability of the nanoparticles was investigated by incubation of Au@MO<sub>x</sub>@SiO<sub>2</sub> nanoparticles with buffer solutions of  $pH = 1 - 10$ . Here, Au@Fe<sub>3</sub>O<sub>4</sub>@SiO<sub>2</sub> nanoparticles were observed to be chemically stable over the whole  $pH$  range investigated. In contrast, Au@MnO@SiO<sub>2</sub> showed comparably fast degradation of the MnO domain upon incubation with buffer solution of low  $pH$ . This was visible *e.g.* in sodium acetate buffer by a color change from purple to red as well as by TEM. Even though the MnO core was etched, the silica shell remained intact and kept its shape so that hollow silica shells, *h*SiO<sub>2</sub>, attached to gold domains emerged (Figure 4.10). Similar behavior was reported by Schladt *et al.* for MnO@SiO<sub>2</sub> nanoparticles.<sup>[51]</sup> A possible explanation for these results may be a certain porosity of the silica coating that permits the flow of protons, which cause the etching of MnO. However, this  $pH$  sensitivity of the MnO domains was used in order to obtain Au@*h*SiO<sub>2</sub> nanoparticles. An application that exploits this instability and the resulting void due to degradation of the MnO domain could be targeted drug loading and transport. As unwanted or non-specific release of drug loading has to be halted, a subsequent coating could be applied and specifically disrupted by photo-thermal treatment exploiting the strong absorption of light by the Au domain.

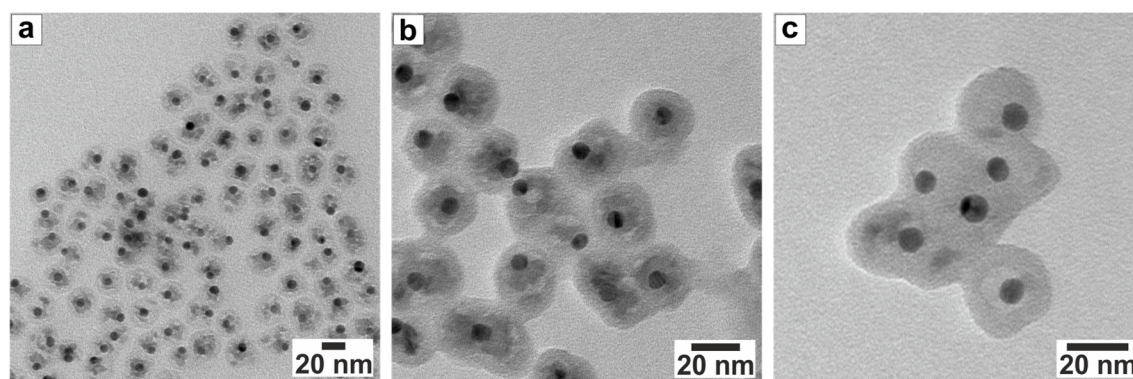


Figure 4.10: TEM images of the degradation of MnO domains in sodium acetate buffer,  $pH = 3.5$ , as a function of the incubation time: a) 1 h, b) 4 h, and c) 24 h.

### 4.2.3 Optical Imaging

Generally, we investigated the individual addressability of both gold and silica surfaces. The SiO<sub>2</sub> shell was labeled by embedding a green fluorescent dye, e.g. FITC or ATTO 495. The dyes were used in their active form as NHS ester or isothiocyanate and coupled to a silane conjugate, (3-aminopropyl)triethoxysilane according to a reported procedure.<sup>[257]</sup> The conjugation product was subsequently added in the SiO<sub>2</sub> synthesis, where the position of the dye, either completely enclosed or at the surface, could be controlled by the moment of addition to the reverse microemulsion.

On the other hand, selective functionalization of the Au domain was achieved by incubating an aqueous solution of Au@MnO@SiO<sub>2</sub> nanoparticles with thiol-modified 24-mers, a customized oligonucleotide. The latter was tagged with the red dye, TexasRed (TR).<sup>[15]</sup> The dye-labeled nanoparticles were analyzed by means of UV-VIS spectroscopy (Figure 4.11). The spectrum of TR-Au@MnO@SiO<sub>2</sub>-FITC was well described by the superposition of the spectra of the single components, which confirmed the orthogonal functionalization as well as the selective addressability.

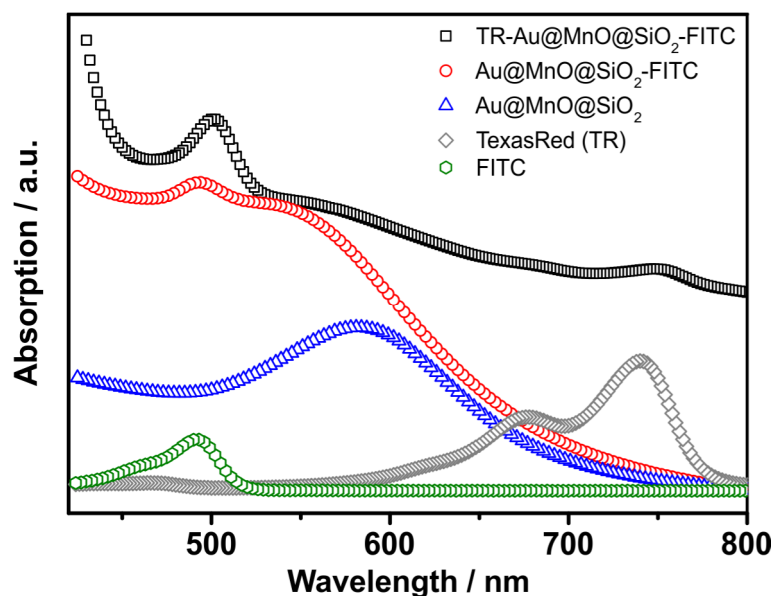


Figure 4.11: UV-VIS spectra of AuMnO@SiO<sub>2</sub>, fluorescent dyes, and dye-labeled Au@MnO@SiO<sub>2</sub> nanoparticles indicating the orthogonal functionalization and individual addressability. The spectra were measured in *n*-hexane or water and stacked along the y-axis.

The functionalized nanoparticles were analyzed using an epi-fluorescence microscope at different emission wavelengths to visualize the green fluorescence of silica-coated MnO domains and the red fluorescence of TexasRed-tagged Au domains (Figure 4.12a - c). The colocalization of the green/red fluorescence signals in Figure 4.12c confirmed the effective labeling with both dyes. This result supported the idea that the heterodimer nanoparticles could be efficient cargo-specific carriers. However, the red signal was not as distinct as the green due to the partial quenching of the dye directly bound to the gold nanoparticles.<sup>[69,269]</sup> Interestingly,

Au@MnO@SiO<sub>2</sub>-ATTO 495 nanoparticles without any red dye present also showed red fluorescence in addition to the expected green fluorescence.

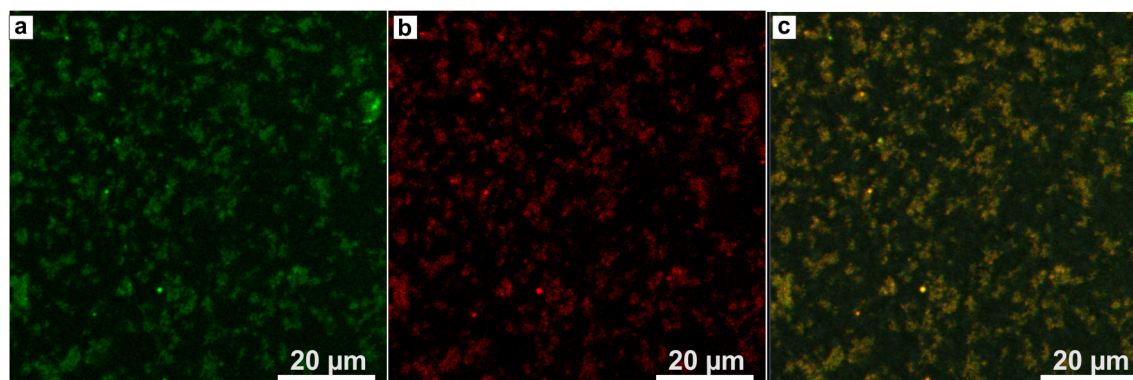


Figure 4.12: Fluorescence images of TexasRed-Au@MnO@SiO<sub>2</sub>-ATTO 495: a) green channel, b) red channel, and c) overlay images. Excitation wavelength  $\lambda_{ex} = 488$  nm. Confocal laser scanning microscopy (CLSM) was measured by [REDACTED].

Furthermore, strong two-photon activity was observed for TR-Au@MnO@SiO<sub>2</sub>-ATTO 495 using an excitation wavelength of 970 nm, where an emission on red, green, and blue channels was detected (Figure 4.13). This excitation wavelength was determined to yield the best emission within the investigated range of 690 nm to 1064 nm. The most striking result to emerge from this data was the emission in the range of 455 - 500 nm, as it could not be attributed to the emission of any dye. Thus, a fluorescence resonance energy transfer process was suggested from the dye incorporated in the silica shell (ATTO 495) to the gold particles. This might also explain the red fluorescence detected without the presence of any red dye.

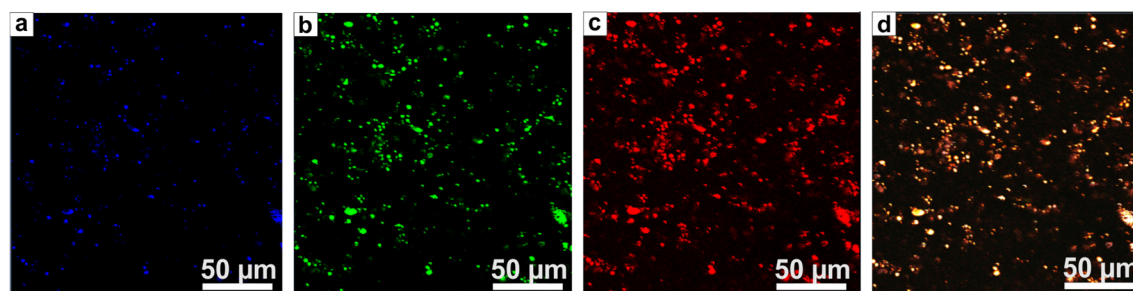


Figure 4.13: Fluorescence images of TexasRed-Au@MnO@SiO<sub>2</sub>-ATTO 495: a), b), and c) fluorescence images showing emission in the blue, green, and red region, respectively, and d) overlay image. Excitation laser wavelength:  $\lambda_{ex} = 970$  nm. Two-photon fluorescence analysis was performed by [REDACTED].

Further, the two-photon stability was studied upon exposure of selected areas of a sample to an intense laser radiation, 10 % of 30 mW, and measurement of the devolution of the emission intensity over time. As a control experiment, a different area of the sample was exposed to half of the laser power for the period of time (Figure 4.14). The control experiment showed a relatively stable emission for 120 s, as the decrease in intensity was 3.5 %, 4.1 %, and 5.5 % for the red, green, and blue region, respectively. On the area that was exposed to higher laser power, an initial decrease of 18 % - 28 % occurred within the first 8 s. Subsequently, the decay conformed to that of the control area. The initial drop revealed the acquired intrinsic



fluorescence to be directly related to the nanoparticle functionalization and not a reflection or refraction effect. Furthermore, even without any attached dye, the particles showed two-photon activity in the green region. This clearly attributed the Au domain of the heterodimer nanoparticles to be the origin of the two-photon activity, which superimposes with the two-photon activity in the case of an encapsulated dye.

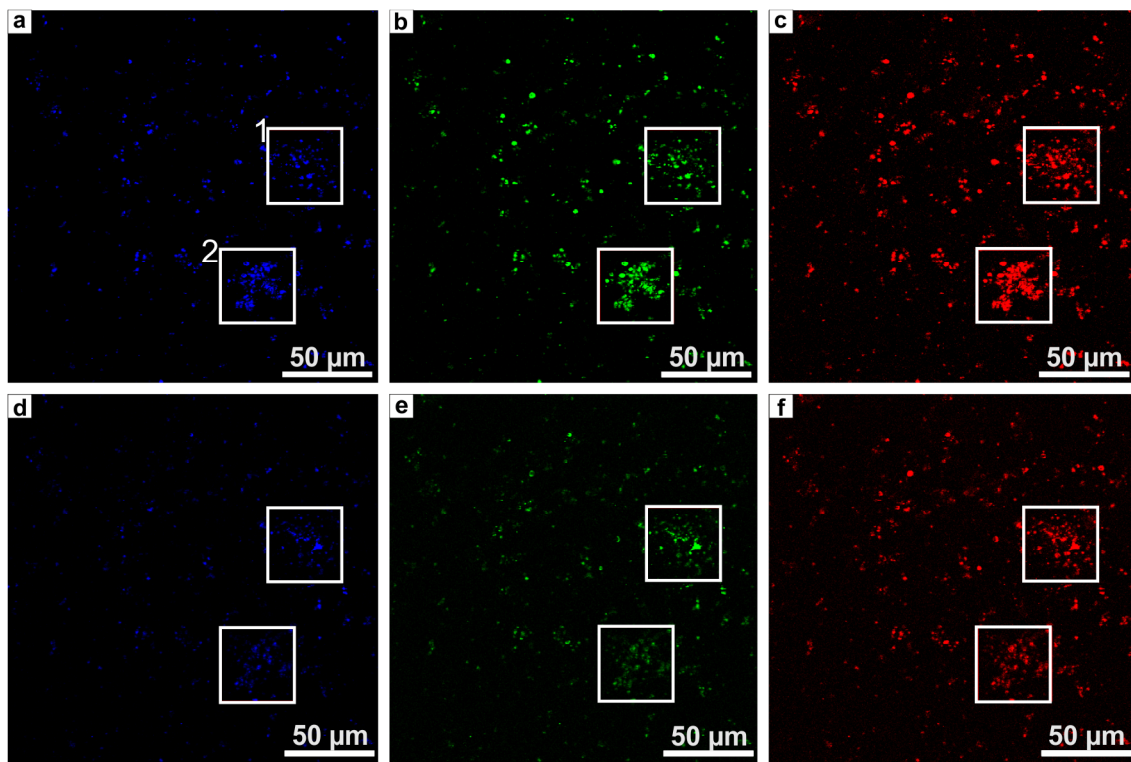


Figure 4.14: Two-photon stability measurements of blue, green, and red regions of TR-Au@MnO@SiO<sub>2</sub>-ATTO 495 nanoparticles: a) - c) prior to bleaching experiments, d) - f) selected areas were exposed to a laser  $\lambda_{ex} = 970$  nm with 5 % (area 1, control experiments) or 10 % (area 2, bleaching experiments) of 30 mW laser power for 120 s. The bleaching experiments were performed by [REDACTED].

In order to understand the emergence of the described effect of unexpected emission in the red region, time-resolved photoluminescence (TR-PL) spectroscopy was applied. The fluorescence spectra and decay dynamics of the dye ATTO 495, the nanoparticles incorporating ATTO 495, and the pristine Au nanoparticles were systematically investigated. Aqueous solutions of the nanoparticles were excited by a femtosecond laser pulse at 400 nm, and the subsequent emission was detected by a Streak Camera setup. Pristine ATTO 495 showed single-exponential fluorescence dynamics (Figure 4.15) with an inverse decay rate of 1.04 ns as specified by the supplier. In contrast, the emission of Au nanoparticles did not decay mono-exponentially, but could be described by a stretched-exponential fitting function. A decay lifetime of 72 ps and a stretching exponent of 0.55 were obtained from the stretched exponential fit to the data. The necessity of a stretching exponent indicated a distribution of fluorescence lifetimes of the emitting species, which was attributed to the differences in size of Au nanoparticles, despite their monodispersity ( $\sigma \leq 5\%$ ). Attaching ATTO 495 to the surface of a SiO<sub>2</sub>-coated MnO nanoparticle changed the excited state dynamics of the dye from a single-exponential to

a bi-exponential decay. Fixing the longer decay component to the value found for pristine ATTO 495 resulted in a value for the shorter-lived decay component of 134 ps, as a consequence of the metal oxide-dye interaction. Thus, the fluorescence of ATTO 495 was partially quenched when incorporated into the silica shell of MnO@SiO<sub>2</sub>. The emission dynamics observed for Au@MnO@SiO<sub>2</sub>-ATTO 495 nanoparticles could be described by a simple superposition of the dynamics observed for the pristine Au nanoparticles and the MnO@SiO<sub>2</sub>-ATTO 495 nanoparticles.

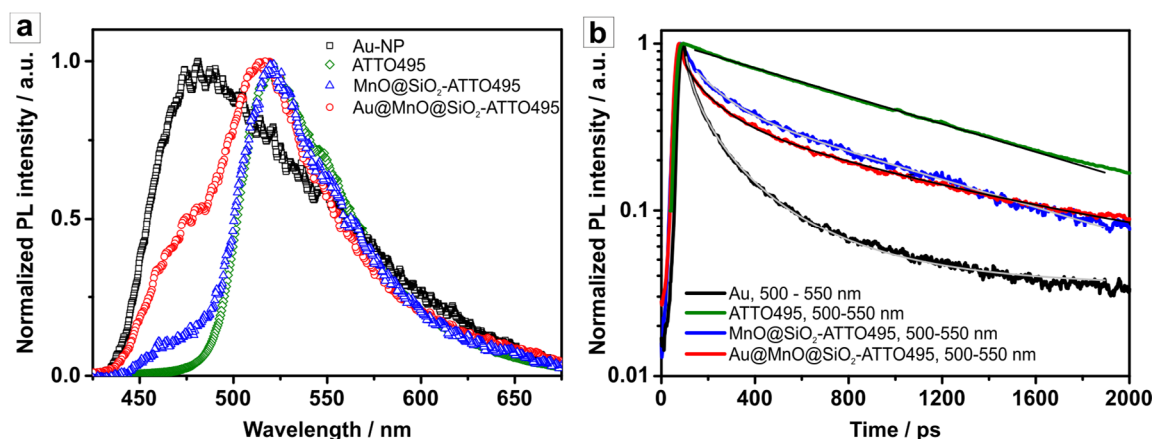


Figure 4.15: a) Time-integrated emission spectra of pristine Au nanoparticles, pure ATTO 495, MnO@SiO<sub>2</sub>-ATTO 495, and Au@MnO@SiO<sub>2</sub>-ATTO 495 nanoparticles. The samples were excited at 400 nm by a 100 fs laser pulse. b) Fluorescence dynamics monitored at the emission peak wavelength and fits according to the function displayed in Table 4.2. The TR-PL measurements were performed by [redacted].

In fact, fixing the decay constants to the values obtained for the latter two yielded a fit that accurately described the emission dynamics of the Janus particles, which is summarized in Table 4.2. Consequently, there is no indication for any electronic interaction between the dye molecules (ATTO 495) attached to the MnO@SiO<sub>2</sub> nanoparticles and the Au moiety within the same Janus particle. However, the TR-PL measurements revealed the continuation of the emission of ATTO 495 up to 650 nm, which explained the observation of red fluorescence without any red dye (see page 90).

Table 4.2: Inverse decay rates  $\tau_1$  and  $\tau_2$  obtained from fitting the fluorescence dynamics to a single-exponential (ATTO 495), a stretched-exponential (Au nanoparticles), a bi-exponential (MnO@SiO<sub>2</sub>-ATTO 495), and a combination of a bi-exponential and a stretched-exponential function (Au@MnO@SiO<sub>2</sub>-ATTO 495).

Sample	$\tau_1$ / ps	$\tau_2$ / ps	$\beta$ / s
ATTO 495	1040	---	---
Au	72	---	0.55
MnO@SiO <sub>2</sub> -ATTO 495	134	1040 (fixed)	---
Au@MnO@SiO <sub>2</sub> -ATTO 495	134 (fixed) 72 (fixed)	1040 (fixed)	0.55 (fixed)

### 4.3 Conclusion

To conclude, we demonstrated the selective silica coating of heterodimer nanoparticles dependent on their surface functionalization: previous thiol functionalization of the gold domain resulted in solely encapsulating the metal oxide domain with a thin silica layer, leaving the vitreophobic gold domain untouched. Without any thiol present, the hydrophobic heterodimers were completely covered by silica. Independent of the extent of the silica encapsulation, the obtained Au@MO<sub>x</sub>@SiO<sub>2</sub> nanoparticles were colloidally stable in water, buffer solutions, and serum, showing no indication of aggregation. The net surface potential at the shear plane  $\zeta$  was observed to be crucial to the colloidal stability, as  $\zeta > -20$  mV led to aggregation and flocculation. This coincided with the DLVO theory, although the stabilization was not solely provided by electrostatic repulsion. In addition, steric hindrance was exploited, as the silica layer was terminated with a PEG-modified organo-silane. However, the composition of the metal oxide domains was decisive for the chemical stability, where a distinct difference was observed for MnO and Fe<sub>3</sub>O<sub>4</sub>. Au@Fe<sub>3</sub>O<sub>4</sub>@SiO<sub>2</sub> nanoparticles did not change after incubation with various buffer solutions in the range of  $1 < pH < 10$ . In contrast, *pH* sensitive Mn<sup>2+</sup>-leaching was observed for Au@MnO@SiO<sub>2</sub> nanoparticles, leading to hollow SiO<sub>2</sub> shells attached to Au domains at low *pH* values. A prospective application of these nanoparticles that exploits the resulting void due to the degradation of MnO could be as drug loading and delivery system.

The potential use of Au@MnO@SiO<sub>2</sub> as Janus-type particles was then explored by selective surface functionalization, taking advantage of the affinity of the individual components for different functional molecules. Time-resolved fluorescence spectroscopy in combination with confocal laser scanning microscopy revealed the silica-coated Au@MnO@SiO<sub>2</sub> heterodimers to be highly two-photon active based on the intrinsic properties of the Au domain. This feature makes them highly attractive for multimodal imaging. The comprehensive techniques revealed no indication of an electronic interaction between the dye molecules incorporated in the silica shell surrounding the MnO domains and the attached Au domains. In addition, fluorescence quenching was observed when dye molecules were directly bound to the Au domains.

Overall, the selective silica coating of the metal oxide domain was demonstrated to be a highly effective technique to convert hydrophobic heterodimer nanoparticles into multifunctional, water-soluble, dye-labeled nanoparticles, which present an alternative to current bioimaging nanoparticle-platforms. Undoubtedly, subsequent selective surface functionalization of the individual domains remains possible, which is crucial for the prospective application of the heterodimers as Janus-type particles.

## 4.4 Experimental Section

**Materials.** All reactions were carried out under argon atmosphere and using commercially available reagents without any further purification: 1-Octadecanethiol (ODT, 98 %), polyoxyethylene(5)nonylphenyl ether (Igepal® CO-520), ammonium hydroxide (NH<sub>4</sub>OH, 25 % aqueous solution), (3-aminopropyl)triethoxysilane (APTES, > 99 %), tetraethoxysilane (TEOS, > 99 %), fluorescein 5(6)-isothiocyanate (FITC), and anhydrous *N,N*-dimethylformamide (DMF, 99.8 %) were purchased from Sigma Aldrich. 2-methoxy-(polyethyleneoxy)-propyl-trimethoxysilane (PEG-silane, *n* = 9 - 12, 90 %) was purchased from ABCR, ATTO 495 NHS-ester from ATTO-tec. Acetone, cyclohexane, hexane, hydrochloric acid (HCl, ≥ 37 %, analytical grade), and nitric acid (HNO<sub>3</sub>, ≥ 65 %, analytical grade) were purchased from Fisher Scientific.

**Thiol Functionalization of Au@Fe<sub>3</sub>O<sub>4</sub> Heterodimer NPs.** The ligand exchange of the Au domain to 1-octadecanethiol was performed by addition of ca 50 mg Au@Fe<sub>3</sub>O<sub>4</sub> heterodimer nanoparticles to 10 mL hexane containing 50 mg ODT under argon atmosphere. The solution was stirred at room temperature overnight. The particles were precipitated by addition of methanol, collected by centrifugation (9000 rpm, 10 min), and washed using hexane/ethanol.

**Synthesis of APTS-Dye Conjugate.** APTES-dye conjugates were prepared using either FITC or ATTO 495 NHS-ester according to a reported procedure.<sup>[51]</sup> Briefly, ca 2 μmol dye were dissolved in 1 mL of dry DMF. Subsequent to the addition of 100 μmol (23.5 μL) APTES, the mixture was shaken for 4 h at 20 °C under exclusion of light.

**Silica Encapsulation of Au@MO<sub>x</sub> Heterodimer NPs.** The metal oxide domains of hydrophobic Au@MO<sub>x</sub> heterodimers were encapsulated with SiO<sub>2</sub> adapting the reverse microemulsion technique as reported for single-component nanoparticles.<sup>[51]</sup> Briefly, 2.0 g Igepal® CO-520 was dissolved in 35 mL cyclohexane and degassed for 15 min under vigorous stirring using a gentle stream of argon. Roughly 10 mg heterodimer nanoparticles in 1 mL cyclohexane were added, and the degassing procedure was continued for another 15 min. Subsequently, 200 μL aqueous NH<sub>4</sub>OH were added dropwise to induce micelle formation. After 5 min, 112 μL TEOS and 100 μL APTES-dye conjugate were added, and the reaction was then stirred overnight under exclusion of light. Further functionalization of the shell was achieved by addition of 130 μL PEG-silane, which led to complete precipitation within 2 hours. The nanoparticles were collected by centrifugation (5000 rpm, 5 min) and washed by dissolution in acetone and precipitation with hexane until a powdery precipitate was obtained.

**Surface Modification of Au@MO<sub>x</sub>@SiO<sub>2</sub> NPs.** In order to control the zeta potential and the addressability of the nanoparticles for tailor-made surface modification, amino groups were introduced onto the surface of the silica encapsulated nanoparticles.<sup>[51]</sup> Subsequent to the silica encapsulation, the nanoparticles were dissolved in 20 mL of acetone. The amino groups were introduced by addition of 150 μL (0.64 mmol) APTES and 150 μL NH<sub>4</sub>OH. The mixture was

stirred under argon atmosphere for another 4 h. The product particles were precipitated using hexane, collected by centrifugation (5000 rpm, 5 min), and re-dissolved in acetone. The nanoparticles were washed several times using hexane/acetone. The obtained particles were easily soluble in acetone, ethanol, DMF/DMSO, and various aqueous media.

**Nanoparticle Characterization.** The nanoparticles were analyzed by means of transmission electron microscopy (TEM), Fourier transformed infrared spectroscopy (FT-IR), UV-VIS spectroscopy, atomic absorption spectroscopy (AAS), dynamic light scattering (DLS), time-resolved photoluminescence spectroscopy (TR-PL), confocal laser scanning microscopy (CLSM), and high resolution synchrotron powder diffraction.

#### 4.4.1 Instrumental Details

**Transmission Electron Microscopy.** Low resolution TEM data were measured using a Philips EM420 microscope equipped with a LaB<sub>6</sub> cathode with an acceleration voltage of 120 kV, a slow-scan CCD camera (1k · 1k), and a spacial resolution of 3.3 nm. Samples for (HR) TEM were prepared by dropping a dilute solution of nanoparticles in the appropriate solvent (hexane, acetone, or water) onto a carbon coated 300mesh copper grid (Science Services, Germany).

**High Resolution Transmission Electron Microscopy.** HR TEM data were obtained using a TECNAI F30 TEM equipped with a field emission gun operating at 300 kV. The images were recorded onto a GATAN US4000 CCD camera with a spatial resolution of 0.1 nm. A built-in Si/Li-detector from Oxford Instruments was used for energy dispersive X-ray (EDX) line scans.

**Scanning Electron Microscopy.** The SEM images were taken using an FEI Nova NanoSEM630 equipped with an Everhart-Thornley detector (ETD) and a low-voltage high-contrast detector (vCD) in high vacuum mode. The acceleration voltage was chosen to be between 15 kV and 30 kV. The samples were attached on an aluminum stub using adhesive conductive carbon tape. For energy dispersive X-ray-spectroscopy (EDX) a built-in EDAX-Genesis detector was used.

**UV-VIS Spectroscopy.** UV-VIS spectra were recorded in the range between 300 nm and 800 nm by a Varian Cary 500 UV-VIS/NIR-spectrometer using 1 mL Hellma® QS-suprasil® quartz absorption cuvettes with a thickness of 10 mm.

**Dynamic Light Scattering.** DLS measurements were performed using a Uniphase He/Ne Laser ( $\lambda = 632.8$  nm, 22 mW), a ALV-SP125 Goniometer, an ALV/High QE Avalanche photodiode with fiber optical detection, an ALV 5000/E/PCi-correlator, and a Lauda RC-6 thermostat unit. Angular-dependent measurements were carried out in the range  $30^\circ \leq \theta \leq 150^\circ$ . For data evaluation, experimental intensity correlation functions were transformed into

amplitude correlation functions applying the Siegert relation, extended to include negative values after baseline subtraction by calculation  $g_1(t) = \text{SIGN}(G_2(t)) \cdot \text{SQRT}(\text{ABS}((G_2(t)-A)/A))$ .  $g_1(t)$  was evaluated by fitting a bi-exponential function  $g_1(t) = a \cdot \exp(-t/b) + c \cdot \exp(-t/d)$  to take polydispersity into account. Average apparent diffusion coefficients  $D_{app}$  were determined according to  $q^2 \cdot D_{app} = (a \cdot b^{-1} + c \cdot d^{-1}) / (a + c)$ . The obtained data were extrapolated to  $D_{app}(q=0)$ . Hydrodynamic radii were then extracted from the Stokes-Einstein equation.

For DLS measurements, sample concentrations were in the range of  $5 < c < 100$  mg/L. Low salt concentrations ( $10^{-5}$  M NaBr) were added in order to prevent fast/slow mode splitting in DLS due to Coulomb interaction of the silica-coated particles in water. All samples were filtered into dust free cylindrical scattering cells (Hellma, Suprasil, 2 cm diameter) using syringe filters (Millipore LCR 450 nm *n*-heptane solutions, PALL GHP 200 nm aqueous solutions). Filtration losses were checked to be well below 10 %.

**Fourier Transformed Infrared Spectroscopy.** FT-IR spectra were measured on a Bruker Tensor 27 spectrometer in the range of  $4000 \text{ cm}^{-1}$  to  $400 \text{ cm}^{-1}$ . The samples were dissolved in  $\text{CHCl}_3$  or prepared in the form of a KBr pellet.

**Superconducting Quantum Interference Device-Magnetometry.** Magnetic measurements of powders by means of superconducting quantum interference were performed using a Quantum Design MPMS-XL. The ZFC, as well as FC analysis, was conducted with an applied field of 100 Oe.

**High Resolution Synchrotron Powder Diffraction.** High resolution synchrotron powder diffraction data were collected at the beamline 11-BM at the Advanced Photon Source (APS), Argonne National Laboratory using a calibrated average wavelength of  $0.413715 \text{ \AA}$ . Discrete detectors covering an angular range from  $-6^\circ$  to  $16^\circ$   $2\theta$  are scanned over a  $34^\circ$   $2\theta$  range, with data points collected every  $0.001^\circ$   $2\theta$  and a scan speed of  $0.1^\circ/\text{s}$ . The samples were mounted in Kapton tubes with  $0.4 \text{ mm}$  radii. The 11-BM instrument uses X-ray optics with two platinum-stripped mirrors and a double-crystal Si(111) monochromator, where the second crystal has an adjustable sagittal bend.<sup>[270]</sup> Ion chambers monitor incident flux. A vertical Huber 480 goniometer, equipped with a Heidenhain encoder, positions an analyzer system comprised of twelve perfect Si(111) analyzers and twelve Oxford-Danfysik  $\text{LaCl}_3$  scintillators, with a spacing of  $2^\circ$   $2\theta$ .<sup>[271]</sup> Analyzer orientation can be adjusted individually on two axes. A three-axis translation stage holds the sample mounting and allows it to be spun, typically at  $\sim 5400 \text{ rpm}$  (90 Hz). A Mitsubishi robotic arm is used to mount and dismount samples on the diffractometer.<sup>[272]</sup> An Oxford Cryosystems Cryostream Plus device allows sample temperatures to be controlled to 295 K. The diffractometer is controlled via EPICS.<sup>[273]</sup> Data are collected while continually scanning the diffractometer  $2\theta$  arm. A mixture of NIST standard reference materials, Si (SRM 640c) and  $\text{Al}_2\text{O}_3$  (SRM 676) is used to calibrate the instrument, where the Si lattice constant determines the wavelength for each detector. Corrections are applied for detector

sensitivity,  $2\theta$  offset, small differences in wavelength between detectors, and the source intensity, as noted by the ion chamber before merging the data into a single set of intensities evenly spaced in  $2\theta$ .

Rietveld refinements of all diffraction data were performed with TOPAS Academic V5<sup>[274]</sup> applying the fundamental parameter approach.

**Time-Resolved Fluorescence Spectroscopy.** Transient emission spectra on a picosecond timescale were taken with a Streak Camera System (Hamamatsu C4742). The excitation wavelength was 400 nm provided by the frequency-doubled output of a Coherent MIRA Ti:Sapphire laser system.

**Confocal Laser Scanning Microscopy and Two-Photon Analysis.** Two-photon analysis was carried out using a Zeiss LSM 710 NLO microscope equipped with Non Descanned Detectors (NDDs) and a Coherent Chameleon Ultra II Ti:Sapphire Laser. For image acquisition a LD C-Apochromat 40x/1.1 W Korr M27 objective was used and the samples were excited at 970 nm. 12 % laser power 30 mW was used for imaging while 10 % laser power was used for bleaching experiments (for 120 s) with 5 % laser power as reference. The emitted fluorescence was passed through 455 - 500 nm, 500 - 550 nm, and 610 - 656 nm band pass filters to NDDs. All data were acquired and processed using the Zen 2009 software (Carl Zeiss, Germany).

**Atomic Absorption Spectroscopy.** The manganese or iron concentration of aqueous nanoparticles solutions was determined by AAS using a Perkin-Elmer 5100 ZL spectrometer, as the respective lighting sources were missing. For sample preparation, aliquots of a volume of 50  $\mu$ L were treated with 1 mL aqua regia (3:1 HCl:HNO<sub>3</sub>) at 90 °C for 10 minutes followed by adjusting the *pH* value using NH<sub>4</sub>OH and filling up to 5 mL using a measuring flask.

**Zeta Potential.** Zeta potential measurements were carried out in highly pure water using a Malvern Instruments Zetasizer Nano-ZS, where ten runs of triplicates at 25 °C were recorded.

# Part II



# 5

## Harnessing the Janus Character of Heterodimer Nanoparticles

This chapter contains parts of an adapted reproduction of *Journal of the American Chemical Society* **2014**, 136, 2473 – 2483,<sup>[54]</sup> reproduced with permission of the American Chemical Society Copyright 2014, and of a manuscript submitted to the *Beilstein Journal of Nanotechnology* linked to the final report of the DFG priority program SPP 1313 “Biological Responses to Nanoscale Particles”.<sup>[151]</sup>

### 5.1 Introduction

In 1991, Pierre-Gilles de Gennes was one of the first to point out the significance and potential of Janus particles in his Nobel lecture “Soft Matter”.<sup>[21]</sup> Eponym for this class of heteronanoparticles is the two-faced Roman god Janus, the god of beginning and ending, doors, and gates.<sup>[275]</sup> Janus particles can be purely inorganic, purely organic, or hybrid-type inorganic-organic. Hence, they combine two or more components, which are distinct in chemistry, properties, and morphology. Such particles exhibit many intriguing properties, including amphiphilic,<sup>[192]</sup> magnetic,<sup>[276]</sup> optical,<sup>[277,278]</sup> and catalytic characteristics,<sup>[24]</sup> therefore opening a wide range of potential applications as catalysts,<sup>[211,279,280]</sup> in drug delivery,<sup>[28]</sup> and biomedical imaging.<sup>[281,282]</sup> Janus particles are outstanding among the heteronanoparticles owing to their asymmetry as an additional design module. Moreover, they are able to combine even very different chemical and physical properties within a single particle. In de Gennes’ vision, Janus particles would enable the fabrication of a “breathable skin”, a film with large interstices that allows chemical exchange between two phases.

Initiated by de Gennes’ lecture, huge research effort was put into the design of Janus structures, though the first Janus particles were already synthesized by Casagrande and co-workers in the early 1980s.<sup>[283]</sup> Their approach to “Janus pearls” was the deposition and

immobilization of particles onto a surface and subsequent functionalization of the exposed surface by a metal (Figure 5.1a). A major drawback is that the method is restricted to small amounts of nanoparticles and cannot easily be scaled up. Nevertheless, the method is still used because of its simplicity and has been extended to liquid-liquid interfaces of Pickering emulsions to obtain spatial control over functionalization.<sup>[284]</sup> A classic example for the directed functionalization of isotropic silica particles is the adsorption of nanoparticles on a solidified wax-water interface, where they are selectively exposed to silane vapor. This principle can be applied to create amphiphilic or dipolar Janus particles.<sup>[285]</sup> The effectiveness of this selective functionalization technique was shown by Perro and co-workers by applying a Pickering emulsion of wax-in-water to obtain a large amount of Janus silica particles with a diameter under 100 nm (Figure 5.1c).<sup>[286]</sup>

Nevertheless, dumbbell-shaped nanoparticles provide enormous advantages over spherical, desymmetrized nanoparticles because of their combination of intrinsically different surfaces with distinct reactivity (Figure 5.1d). The design of hetero-structured Janus particles began with organic Janus particles composed out of two different polymers forming an amphiphilic particle. Nie *et al.* reported a microfluidic method for fast continuous synthesis of Janus particles, as well as three-phase particles, with narrow size distribution by emulsification of monomer liquids and *in situ* photo-initiated polymerization of multiphase droplets (Figure 5.1e).<sup>[287]</sup> Another approach to polymer-based particles with two distinct phases is provided by the simultaneous electro-hydrodynamic jetting of polymer solutions under the influence of an electrical field (Figure 5.1f).<sup>[288]</sup>

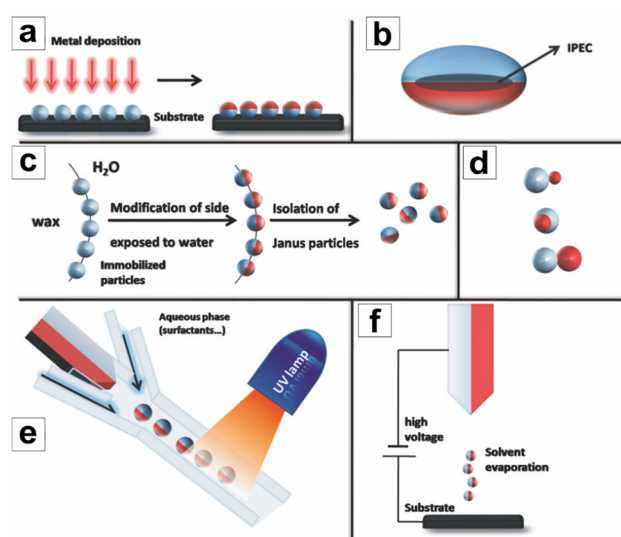


Figure 5.1: Summary of synthetic routes towards organic Janus particles. (a) Directed functionalization after immobilization, (b) ellipsoidal complex core-coacervate micelle with an interpolyelectrolyte complex (IPEC), (c) classical Pickering emulsion technique, (d) different topologies of Janus particles: snowman-, acorn-, and dumbbell-like nanoparticles (top to bottom), (e) microfluidic photo-polymerization system, and (f) electro-spinning technique with a bi-phasic nozzle. Reproduced from [31].

Here, we used inorganic dumbbell-like heterodimer nanoparticles, which were prepared as described earlier (see Chapter 3), as they are superior to their organic analogues in the

design of highly desired multifunctional nanoparticles. The Janus character was introduced exploiting the different chemical characteristics of the two domains, namely metal and metal oxide. More precisely, two synthetic routes were applied: first, the selective ligand exchange of the hydrophobic ligands of either the metal or the metal oxide domain to a  $\alpha,\omega$ -bifunctional PEG-ligand, and, second, the silica encapsulation of the metal oxide domain with optional subsequent conjugation to PEG-ligands, leaving the metal domain untouched (Figure 5.2).

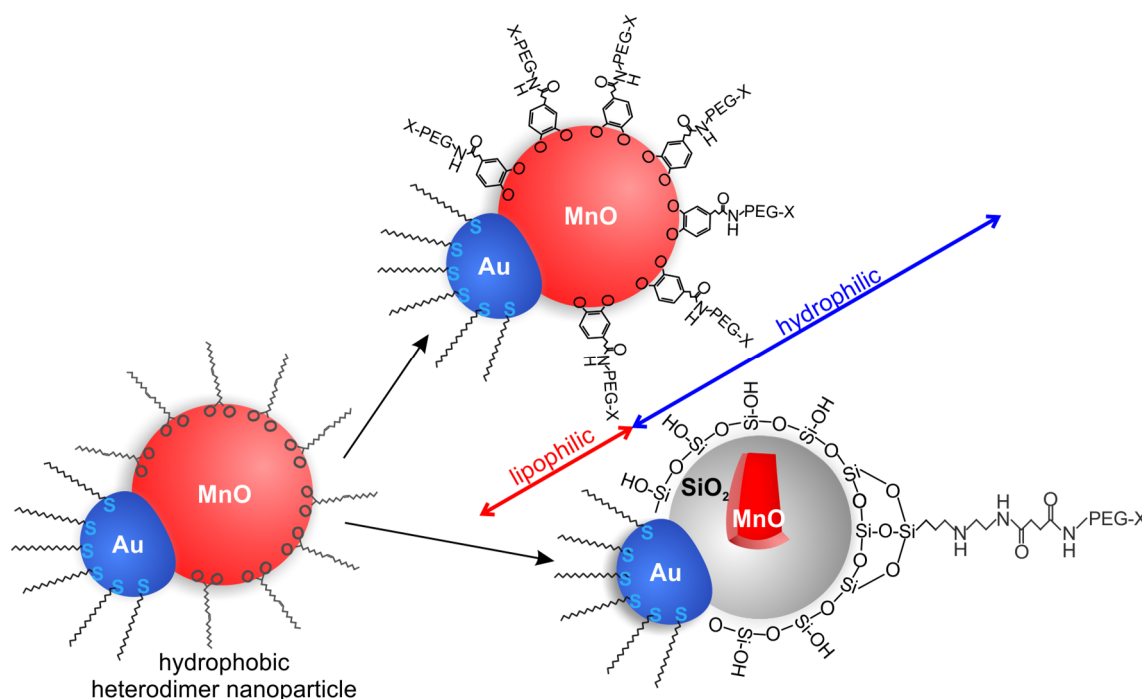


Figure 5.2: Synthetic routes toward inorganic Au@MnO Janus particles used within the scope of this work: the hydrophobic heterodimer nanoparticles, coated with 1-octadecanethiol and oleic acid, were transformed into Janus particles either by ligand exchange (top) or by selective silica encapsulation (bottom).

Based on their detergent-like morphology, Janus particles may also find use as surfactants,<sup>[26,289,290]</sup> water-repellent coatings,<sup>[27]</sup> or building blocks for supramolecular structures,<sup>[126,291]</sup> as soon as the formation process and the interparticle forces are understood. Thus, the present study of the Janus character has been divided into two parts. The first part deals with the assembly of orthogonal functionalized heterodimer nanoparticles, both on pseudo-molecular scale as well as at air-water and oil-water interfaces. Inspired by the structural analogy to the building blocks of natural lipid bilayers and the importance for biomedical applications, the impact of Janus particles on artificial membranes is analyzed within the second part.

## 5.2 Assembly of Janus Particles

Janus particles are interesting for a variety of reasons, one of them being their self-organization into complex and well-defined assemblies.<sup>[32]</sup> The advanced surface-active properties of particles with a segregated corona are superior to particles with a uniform

wettability. Moreover, the theme of self-assembled Janus building blocks is inspired by nature, where it is most commonly present in the form of organic materials such as lipids or proteins, for instance a class of fungal proteins called hydrophobins. In nature, self-assembled architectures formed by amphiphilic molecules are often hierarchically organized and composed of smaller units, e.g. micelles and bilayers. In many cases, the final micrometer-sized structures have been observed to result of a higher level aggregation process involving smaller units. Recently, Hirsemann *et al.* demonstrated the native Janus character of the natural mineral kaolinite  $[Al_2Si_2O_5(OH)_4]$ , which is a dioctahedral layered silicate found in the form of anisometric platelets with large aspects ratios (Figure 5.3). Due to the hydrophilic nature of both surfaces, the Janus character remains hidden until the octahedral (OS) and tetrahedral surfaces (TS) are selectively modified by cation exchange and covalent grafting of catechol ligands. Up to now, large technical applications of Janus particles are restricted by the lack of accessibility. Therefore, polymer-modified kaolinite provides the enormous advantage of being an abundant, ubiquitous, and inexpensive mineral, which can be used as a superior Pickering emulsifier.<sup>[292,293]</sup>

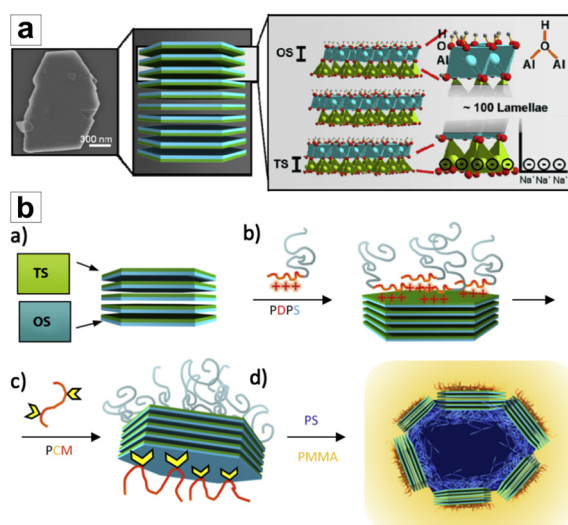


Figure 5.3: a) SEM top view image of a typical kaolinite platelet (left), schematic picture of kaolinite platelets (center), and crystal structure of three kaolinite lamellae with the specific chemical functions at the basal TS and OS (right). (b) Schematic picture of a) pristine kaolinite, b) modified with PDPS on the tetrahedral surface (TS), c) further modified with PCM on the opposite octahedral surface (OS), and d) embedding of the final hybrid particle at the interface in a PS-PMMA blend. Reproduced from [293].

More than 100 years ago, Ramsden and Pickering inhibited the coalescence of the emulsion drops of two immiscible liquids by adding micron-sized particles.<sup>[294,295]</sup> The stable fluid-fluid interfaces within these so-called Pickering emulsions emerge upon self-assembly of colloidal particles. This is ascribed to the high desorption energy of the particles from the interface as well as to the decrease of total free energy.<sup>[296]</sup> However, this amount of energy is much larger for micron-sized particles than for nanoparticles, for which it is in the range of the thermal energy. Thus, nanoparticles are able to reach their equilibrium structure at interfaces due to continuous particle exchange. Aside from the particle size and the interaction between

particles and phases, the interfacial tension, which is controlled by the wettability of the particle surface, is crucial. It is described by the contact angle of the particle and the interface. In general, the less wetting liquid is found to be the dispersed phase. Janus particles exhibit two contact angles, as they are both surface active as well as amphiphilic. Thus, they unify the characteristics of a typical molecular surfactant with the Pickering effect.<sup>[297]</sup> According to Binks and co-workers, the maximum amphiphilicity is realized by an upright orientation of a Janus particle with equivalent polar and nonpolar regions, each of them completely wetted by the appropriate solvent. Further, they predicted that the surface activity of Janus particles is up to three times higher at an oil-water interface than that of uniform particles, which leads to a strengthened adsorption at the interface.<sup>[298]</sup> Recently, Glaser *et al.* confirmed Binks' theoretical prediction by showing that Au@Fe<sub>3</sub>O<sub>4</sub> Janus particles lead to a significant reduction of the oil-water interfacial tension as compared to similar uniform particles (Figure 5.4). Furthermore, the interfacial activity was enhanced by increasing the amphiphilic character using long alkyl chain thiols.<sup>[299]</sup>

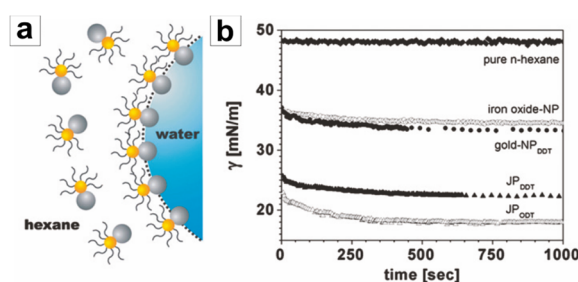


Figure 5.4: a) Schematic representation of surface activity of Au@Fe<sub>3</sub>O<sub>4</sub> Janus particles self-assembled at the hexane-water interface. Here, the hydrophobic Au domains are represented in yellow, while hydrophilic Fe<sub>3</sub>O<sub>4</sub> domains are depicted in gray. b) Interfacial tension vs time measured by pendant drop tensiometry for different homogeneous nanoparticles and Au@Fe<sub>3</sub>O<sub>4</sub> Janus particles, where the Au domain was functionalized using either 1-dodecanethiol (DDT) or 1-octadecanethiol (ODT). Reproduced from [299].

### 5.2.1 Molecular Assembly of Janus Particles

The current interest in the self-assembly properties of amphiphilic compounds brought out a new class of block-copolymers known as “superamphiphiles” or “giant amphiphiles”.<sup>[300]</sup> Examples are block-copolymers derived from polystyrene and polyacrylic acid, which were found to self-assemble into a variety of architectures. They followed principally the same assembly rules, namely the Israelachvili rules,<sup>[301]</sup> as those observed for their low molecular weight counterparts.<sup>[302]</sup> Amphiphilicity as a self-assembling principle can also be applied to inorganic particles to provide a new and simple route for a controlled self-assembly of such particles into one-, two-, and three-dimensional structures.

If each component of an inorganic Janus particle is thought of as an artificial atom, the construction of artificial molecules is an important and complementary activity to the construction of artificial solids. The two components of a Janus particle can be taken as pseudo-atoms. This allows the introduction of concepts of molecular chemistry to understand and control

the interactions between functionalized nanoparticles. Wei *et al.* demonstrated this analogy between nanoscale and molecular synthesis and transferred the important concepts of bond strength and steric hindrance to primitive colloid molecules.<sup>[164]</sup>

Likewise, we utilized Au@MnO heterodimer nanoparticles to investigate their applicability as molecular building blocks (Figure 5.5a). Following Wei *et al.*, who studied the impact of the molecular structures of linking dithiols, we chose 1,4-benzenedimethanethiol as the molecular linker between the nanoparticles. It was found to bridge nanoparticles most efficiently due to its distinct length and flexibility. On the other hand, this flexibility had to be restricted in order to prevent divalent adsorption onto a single particle.<sup>[164]</sup> We investigated the concepts of bond strength and steric hindrance by variation of the domain sizes of the heterodimer nanoparticles as well as the concentration of the linking dithiol. For a given concentration of 1,4-benzenedimethanethiol, the impact of the relative domain sizes of the metal and the metal oxide component was clearly observable: large metal oxide domains introduced steric hindrance and strain at nanoscale, such that barely any colloid molecules were formed, independent of the concentration of the linking dithiol (Figure 5.5b). Decreasing the size of the unreactive metal oxide domain, the fraction of colloid molecules went up and the number of nanoparticles in these molecules simultaneously increased up to 3 (Figure 5.5d). Further, the fraction of dimeric colloid molecules was dominant for low concentrations of the linking dithiol (Figure 5.5c).

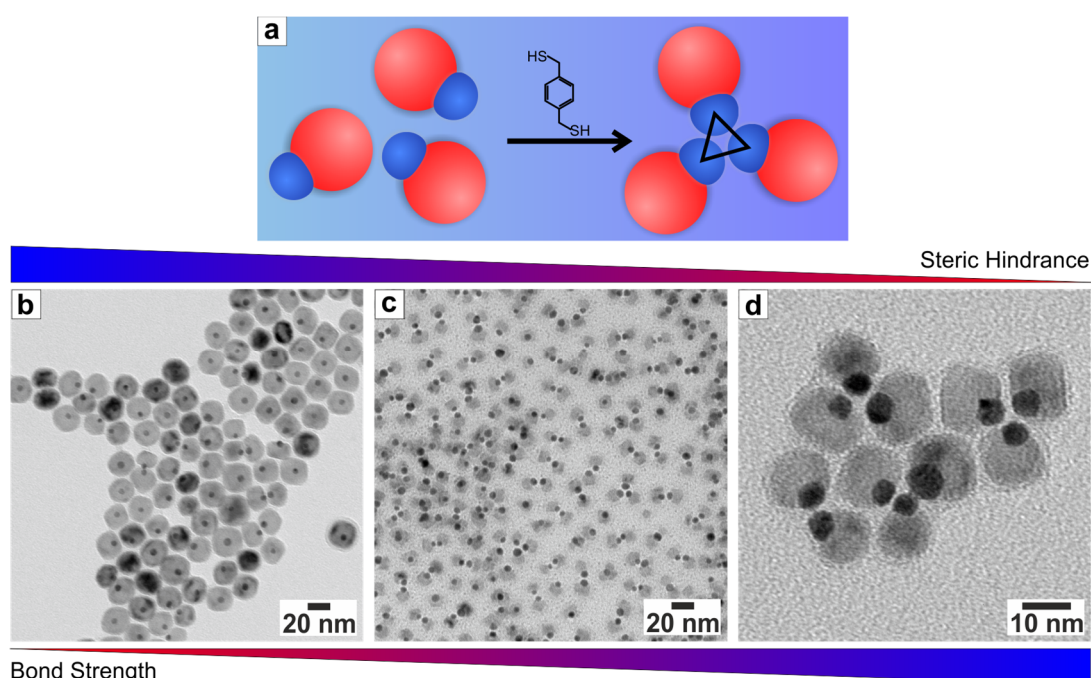


Figure 5.5: a) Scheme of heterodimer nanoparticles and 1,4-benzenedimethanethiol used to link three individual particles into a trimeric colloid molecule; b) - d) TEM images of colloid molecules obtained for different domain sizes of Au@MnO nanoparticles displaying the influence of steric hindrance and bond strength: b) for 3@20 nm Au@MnO ( $r_{Au}/r_{MnO} = 0.15$ ) nanoparticles at a dithiol concentration of 0.16  $\mu\text{M}$  barely any molecules were detected; increasing the domain size ratio to  $r_{Au}/r_{MnO} = 0.31$  (4@13 nm Au@MnO) led to quantitative formation of colloid molecules composed of c) 2 or d) 3 heterodimer nanoparticles when the dithiol concentration was simultaneously raised to 3.1  $\mu\text{M}$  in the latter case.

As a consequence of the strong affinity of thiols for gold, any dissociation of the colloid molecules was noted. However, it was not possible to prepare suspensions consisting of the same colloid molecules, *i.e.* the same number of building blocks. Overall, these reactions were observed to progress with high selectivity and yields following analogous trends to metal-ligand complexes introduced for phosphorus ligands in organometallic chemistry by Tolman.<sup>[303]</sup> The impact of steric hindrance for large metal oxide domains confirmed Binks' prediction of the Janus character to be strongest for dumbbell-like particles with domains of the same size. Thus, heterodimer nanoparticles with large domain size ratios  $r_{Au}/r_{MnO}$  were used for the following investigations. However, it was not possible to study Au@MO<sub>x</sub> Janus particles with identical domain sizes due to restrictions, which emerged during their fabrication (see Chapter 3.2.2).

### 5.2.2 Assembly of Janus Particles at Interfaces

Aside from their structural and chemical similarity to typical surfactants, Janus particles resemble their molecular counterparts in many aspects, as they self-assemble at interfaces as well as in bulk media. However, the enhanced topological control, irrespective of their amphiphilicity, allows superior governance of their surface activity. In reverse, the defined surface chemistry of inorganic dumbbell-like hetero-nanoparticles leads to distinct tuning of the Janus character.

In order to investigate the surface activity of the heterodimer nanoparticles, we applied an orthogonal functionalization, which was based on the attachment of a PEG-ligand via a specific anchoring group to one of the two domains. Besides the well-known thiol-chemistry for Au, catechols have been established as a binding moiety for a large number of metal oxide nanoparticles. This results from their stable coordination to the oxide surface creating a five-membered ring.<sup>[304–307]</sup> The catechol anchoring group attached via an amide coupling to any surfactant is commonly referred to as “dopa” due to its similarity to the amino acid *L*-dopa, although neither *L*-dopa nor dopamine are used as a building block. Here, we used a typical DCC/NHS-amide coupling of a terminal amino group of a  $\alpha,\omega$ -bifunctional PEG to 3,4-dihydroxyhydrocinnamic acid in order to obtain a PEG-based ligand with a catechol anchoring group. The hydrophobic ligands of the respective other domain remained untouched. Thus, amphiphilic particles with precise control over their functionalization were obtained.

The inset of Figure 5.6 displays a surface-pressure area isotherm cycle of ODT-Au@MnO-Dopa-PEG<sub>500</sub>-NH<sub>2</sub> measured using a Langmuir trough. Here, the surface area was repeatedly compressed until a pressure of 5 mN/m was reached and then fully expanded afterwards, while the surface area had to be compressed to a greater extent for each additional cycle. Due to a larger proportion of the 4@23 nm Au@MnO heterodimer nanoparticles being hydrophilic, the preferential complete wetting of the particle by the aqueous phase dominated over the amphiphilic character. Thus, the particles submerged in the bulk phase as soon as the

surface pressure was slightly increased. Several improvements were made in order to strengthen the stability of the particles at the interface. According to the prediction of Binks and co-workers, heterodimer particles having two domains of the same size would be favorable.<sup>[298]</sup> As the synthetic control over the morphology becomes even more challenging for same-sized domains, 7@15nm Au@MnO heterodimers were used. Further, the functionalization was reversed by using a thiol-conjugated PEG, leaving the hydrophobic ligands of the MnO domain untouched. Figure 5.6 shows the enhanced surface activity of these Janus particles, where a dependency on the chain length of the PEG ligands was observable. For high molecular weights, the surface pressure was strikingly increased. This might be a consequence of the stronger interaction of particles at the interface upon compression of the surface area, as the interdigitation of ligands started earlier. Further, the water solubility of PEG ligands is known to be roughly inversely proportional to their chain length.<sup>[260]</sup> Thus, these Janus particles, functionalized with high molecular weight PEG ligands, constitute intermediate amphiphilicity, which has been reported to form most stable monolayers.<sup>[308]</sup> Park *et al.* discussed two contributions to the interaction of Janus particles at oil-water interfaces: Janus particles attract each other via capillary interactions as a consequence of their intrinsic heterogeneity, whereas the repulsive forces originate from charged domains.<sup>[309]</sup> The capillary interactions were reported to depend on the interface distortion and, thus, the shape and wetting of the particles, but to be rather independent of the materials' characteristics.<sup>[310]</sup> The repulsion is caused by the asymmetric distribution of counterions at the surface, leading to repulsive forces between the dipoles of adjacent particles.<sup>[308]</sup>

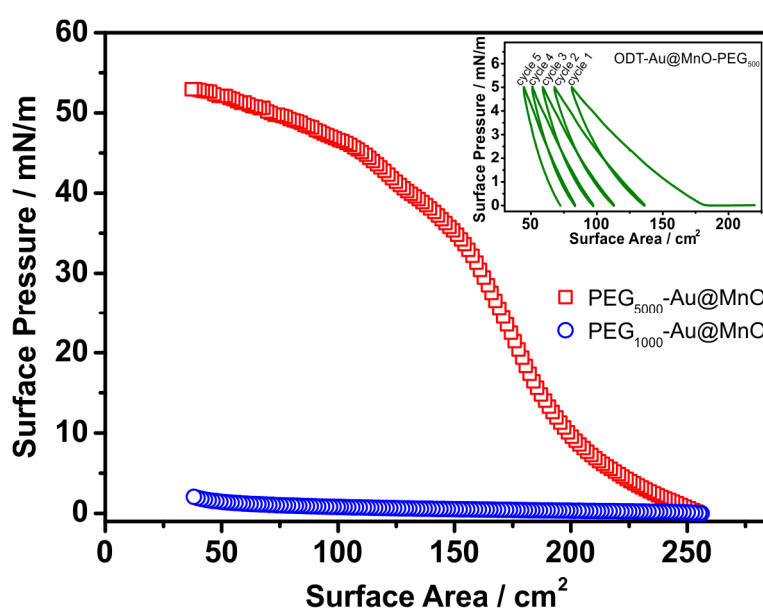


Figure 5.6: Surface-pressure area isotherms of amphiphilic Au@MnO Janus particles with differing molecular weight, *i.e.* chain length of the hydrophilic PEG ligands attached to the Au domain. Inset: Isotherm cycle of Au@MnO Janus particles functionalized with a catechol-PEG on the MnO domain revealing the preferential complete wetting of the aqueous phase. The measurements were performed by [REDACTED].



The shape of the isotherm of PEG<sub>5000</sub>-Au@MnO Janus particles suggested a progressive compression of close-packed domains with diminishing void spaces at increasing surface pressure, as reported by Guo *et al.* for monodisperse  $\gamma$ -Fe<sub>2</sub>O<sub>3</sub> nanoparticles.<sup>[311]</sup> In order to identify the orientation and packing, the Langmuir-Blodgett technique was used to transfer the particle film from the air-water interface to AFM or TEM specimen.<sup>[312,313]</sup> Subsequent analysis revealed no clear conclusion, as the film was only barely transferred to the substrates. It could not necessarily be assumed that the particles remained in their original orientation, as the interaction with the substrates might also have had an impact. For this reason, the self-assembly of Janus particles was additionally studied at oil-water interfaces, which could be analyzed more easily by TEM. Thereby, the two possible orientations of amphiphiles were realized, as indicated in Figure 5.7.

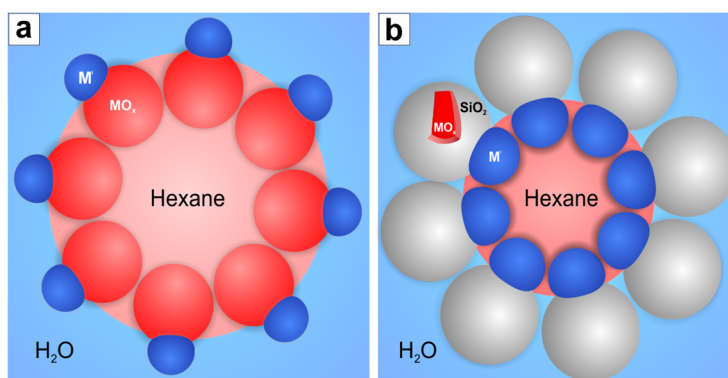


Figure 5.7: Self-assembly of Janus particles at liquid interfaces depending on their functionalization; a) the functionalization of the metal domain was changed to a hydrophilic coating, while the metal oxide component remained hydrophobic; b) reverse orientation caused by the hydrophilic silica coating of the metal oxide domain, leaving the hydrophobic metal domain untouched.

In the first step, Au@MnO Janus particles modified with a thiol-conjugated PEG dissolved in water were incubated with a small amount of toluene, and the resulting two-phase mixture was analyzed by TEM (Figure 5.8). After drying the sample on a TEM specimen, a micelle-like orientation was observed. Thereby, the orientation of the Janus particles fulfilled the expectations: the hydrophilic Au domains protruded into the aqueous phase, the hydrophobic MnO domains were included within the micelle. Further, the contact angle of the Janus particles was estimated from TEM images to be 90°. This has been reported to be the most stable configuration of Janus particles, as it maximizes the detachment energy. However, in order to exclude the micelle-like structures as an artifact caused by the drying process, cryo-TEM measurements were performed (Figure 5.8b). The process of sample preparation for these amphiphilic particles was challenging, as they self-assembled at both air-water as well as water-oil interfaces. Prior to injection in liquid ethane, the specimen was blotted with filter paper to remove excess water, which stripped off a sensible fraction of Janus particles at the same time. Nevertheless, micelles of variable sizes were observed, thus confirming the self-assembly behavior to be an intrinsic characteristic of the Janus particle and not a drying artifact.

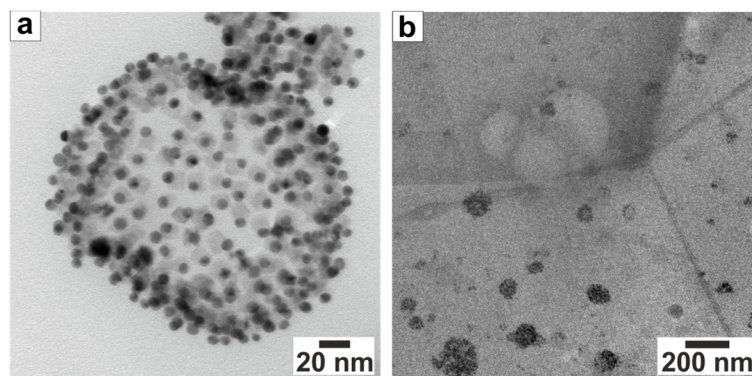


Figure 5.8: Self-assembled PEG-functionalized Au@MnO Janus particles at an oil-water interface: a) TEM as well as b) cryo-TEM image of PEG<sub>5000</sub>-Au@MnO in water. The cryo-TEM measurements were performed by [REDACTED].

As was pointed out in the previous chapter, the stability of Au@MnO@SiO<sub>2</sub> heterodimer particles was strongly dependent on the *pH* value. This became even more pronounced when the protecting silica shell was replaced by a PEG-coating of the Au domain. These particles were not stable regarding dissolution of the MnO domain in aqueous solution. On the other hand, Au@Fe<sub>3</sub>O<sub>4</sub>@SiO<sub>2</sub> nanoparticles were demonstrated to be stable, such that these were used for further self-assembly experiments. The selective wetting behavior of 1-octadecanethiol-functionalized Au@Fe<sub>3</sub>O<sub>4</sub> heterodimer nanoparticles was exploited to obtain Janus particles, bearing a silica shell only around the metal oxide domain. Their amphiphilic character was reversed as compared to PEG-Au@MnO, which was reflected in the orientation of the particles in micelles (Figure 5.7). In contrast to the particles discussed earlier, the metal oxide domain, as the major component of Au@Fe<sub>3</sub>O<sub>4</sub>@SiO<sub>2</sub>, was hydrophilic, so that the particles were dissolved in water for the bulk phase. The Janus particles self-assembled at the oil-water interface, with the hydrophobic Au domain projecting into the toluene droplets (Figure 5.9).

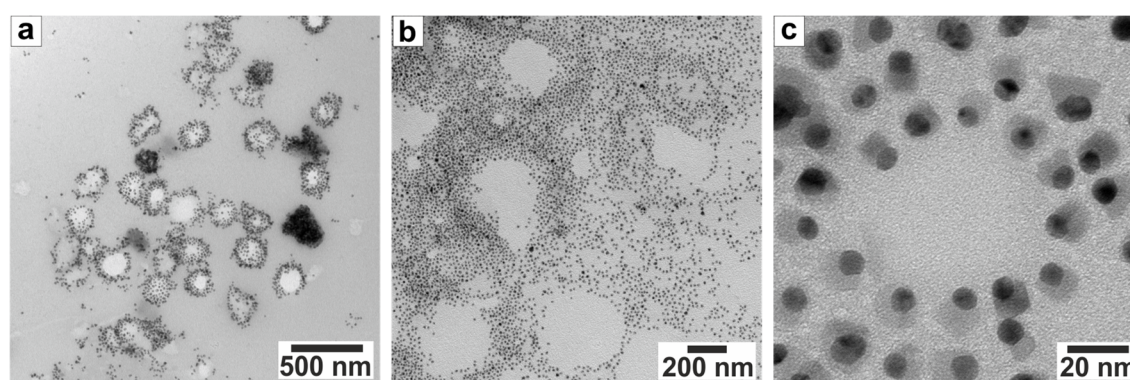


Figure 5.9: TEM images of amphiphilic ODT-Au@Fe<sub>3</sub>O<sub>4</sub>@SiO<sub>2</sub> Janus particles stabilizing toluene droplets in water.

Overall, the as-prepared inorganic Janus particles were demonstrated to be a powerful tool for tuning the self-assembly at interfaces, even though the interparticle forces are not completely understood. Our investigations showed spontaneous arrangement of Janus particles, which is not observed for homogeneous particles.

## 5.3 Interaction Between Janus Particles and Artificial Membranes

This project was done in collaboration with [REDACTED] and [REDACTED], Georg-August-University Göttingen. Material synthesis and chemical characterization were conducted at the Johannes Gutenberg-University Mainz. Here, only a small excerpt of the comprehensive study concerning the interaction of Janus particles with membranes is presented in order to demonstrate the impact of the chemical structure. Further details on the interaction were reported by [REDACTED].<sup>[314]</sup>

### 5.3.1 Introduction

A fundamental understanding of the interactions of nanoparticles with cell membranes is crucial in order to master the cellular uptake, drug or gene delivery, and cytotoxic effects. The size, shape, and functionalization of nanoparticles is an important feature concerning their uptake into cells and, thus, their cytotoxicity.<sup>[315]</sup> Regarding isotropic nanoparticles, it has been shown that they are taken up into the cell via endocytotic pathways, such as pinocytosis, receptor-mediated endocytosis, or phagocytosis.<sup>[316,317]</sup> In addition to these common uptake pathways, the direct interaction of Janus particles with membranes is of great importance due to their amphiphilic character, which is similar to the natural structure of lipids.<sup>[318]</sup> Up to now, there are several calculations concerning the interaction of Janus particles and artificial membranes, which are schematically presented in Figure 5.10. Using coarse-grained simulations, Reynwar *et al.* were able to demonstrate long-ranged interactions between Janus particles placed onto a membrane. Once a minimal local bending occurred, two particles attract each other due to energy minimization of the deformed lipid bilayer when the local curvature induced by a single-particle overlaps with a second indentation. The resulting pair of Janus particles is trapped in a membrane tubule, attracting more and more particles, which eventually may lead to the formation of small, separate vesicles inside the membranes. This uptake can be described as a passive, artificial endocytosis, as it is purely caused by the particles themselves.<sup>[52]</sup> A similar mechanism seems to be involved in the uptake of Shiga toxin proteins into cells.<sup>[319]</sup>

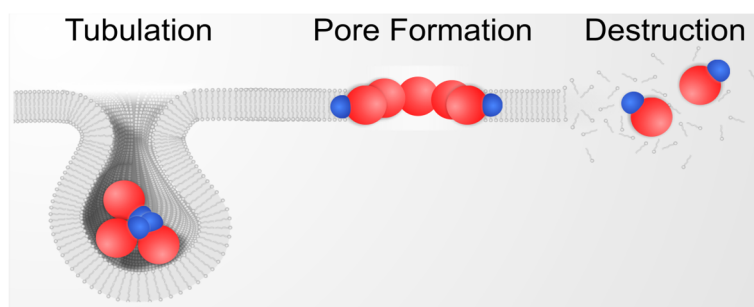


Figure 5.10: Simulations of the interaction of membranes and Janus particles predict either the formation of tubes or the opening of pores, while the amphiphilic particles could also disrupt the bilayer structure due to detergent-like behavior. Adapted from [REDACTED].<sup>[314]</sup>

Moreover, Alexeev and co-workers reported coarse-grained simulations on the interaction of Janus beads and membranes, revealing the formation of controllable pores. Upon membrane rupture, the Janus particles were shown to diffuse to the edges, forming a stable pore. This pore is sensitive to small changes in the membrane tension and, thus, opens readily, allowing transport through the membrane.<sup>[53]</sup> Further, based on their amphiphilic, detergent-like functionalization, Janus particles could destruct the bilayer integrity, which would cause severe cytotoxic effects.<sup>[320]</sup> Nevertheless, there has been no experimental evidence for any proposed Janus particle-membrane interaction to be more likely.

### 5.3.2 Interaction of Janus Particles with GUVs

As model system for the interaction of Janus particles with membranes, we chose giant unilamellar vesicles (GUVs), which were obtained by electroformation. These GUVs were composed out of the natural lipid 1,2-dioleoyl-*sn*-glycero-3-phosphatidylcholine (DOPC) and contained 0.5 % TexasRed® 1,2-hexadecanoyl-*sn*-glycero-phosphoethanolamine (TR-DHPE) as fluorescent dye in order to visualize the GUVs using a fluorescence microscope. Additionally, the impact of Janus character was investigated by varying their surface functionalization as compared to spherical control particles. We chose a PEG with a low molecular weight in order to obtain strong amphiphilic Janus particles, in which neither of the ligands of the two domains dominated over the other. The functionalization of the Au domain remained untouched. The time-resolved incubation of GUVs with ODT-Au@MnO-Dopa-PEG<sub>500</sub>-OMe Janus particles in comparison to spherical MnO-Dopa-PEG<sub>500</sub>-OMe nanoparticles revealed significant impact of the Janus character. Using an epi-fluorescence microscope, first indications of tubulation inside the GUVs were visible directly after addition, but only for vesicles incubated with Janus particles (Figure 5.11d - f). These tubes became more pronounced over time and, finally, smaller vesicles appeared inside the GUVs. Interestingly, these smaller vesicles were exclusively observed within the upper half of the GUVs (Figure 5.11f). This was attributed to the difference in densities of the surrounding medium (glucose) and the medium in GUVs (sucrose). Consequently, this observation confirmed that the smaller vesicles contained media with lower density, which is only possible if they have been taken up from the outside. The spherical nanoparticles did not show any impact on the GUVs over the investigated time of 30 minutes (Figure 5.11a - c).

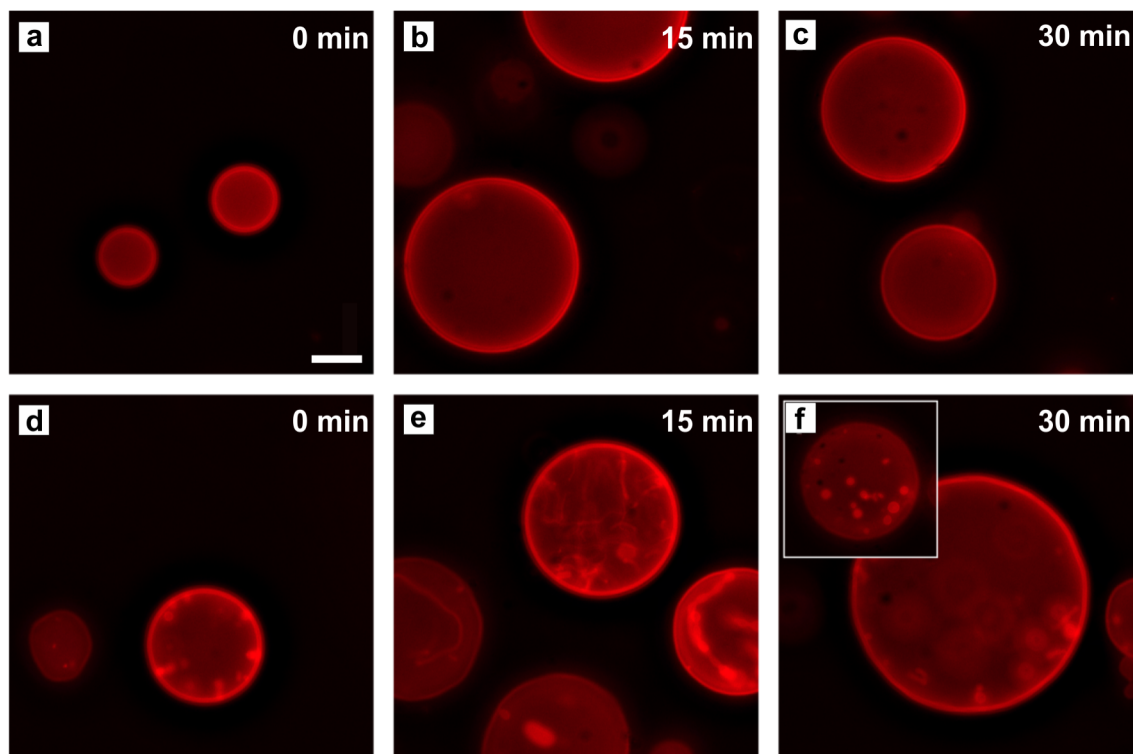


Figure 5.11: Evolution of interaction of Janus particles with GUVs over time, whereby incubation was started at 0 min. Epi-fluorescence images of DOPC/TR-DHPE GUVs in the equatorial plane treated with  $1 \mu\text{g Mn}^{2+}/\text{mL}$  of a) - c) MnO-Dopa-PEG<sub>500</sub>-OMe nanoparticles and d) - f) ODT-Au@MnO-Dopa-PEG<sub>500</sub>-OMe. The inset of f) displays the upper half of the GUV shown in f). Scale bar:  $20 \mu\text{m}$ . The measurements were performed by [REDACTED].

The nanoparticle solutions were hypoosmolar in comparison to the medium inside the GUVs, so that the resulting membrane tension prevented thermal membrane undulations from being responsible for the observed effects. The interaction with Janus particles induced severe membrane deformations and vesiculation, though it was not strong enough to result in membrane wrapping of single particles, as was predicted by simulations of Ding and co-workers.<sup>[318]</sup> This contradiction might originate from the repulsive forces between the hydrophobic Au domain and the polar membrane. However, Reynwar *et al.* proposed cooperative interactions of Janus particles with membranes.<sup>[52]</sup> The evolution of interaction of Janus particles with GUVs over time was found to comply extremely well with this simulation, although the procedure of particle interaction and, thus, cooperative effects could not be visualized, as the particles were invisible to the experiments. The attachment of fluorophores to the PEG-coating altered the interactions with the membranes, so that no comparable effects were observed.

Aside from solely PEG-functionalized nanoparticles, silica-coated Janus particles were analyzed concerning their interaction with artificial membranes. As the tubulation and vesiculation after treatment with Janus particles might represent an additional entry route into living cells, the activity of silica-coated Janus particles was of peculiar importance, as these were designed for biomedical applications. Due to the facile surface chemistry of  $\text{SiO}_2$ , the conjugation to various PEG ligands was possible via an amide coupling to an activated amino-

silane (Figure 5.12).<sup>[321]</sup> For this purpose,  $\alpha,\omega$ -bifunctional PEGs were used with either two terminal amino groups or a terminal amino and a methoxy group.

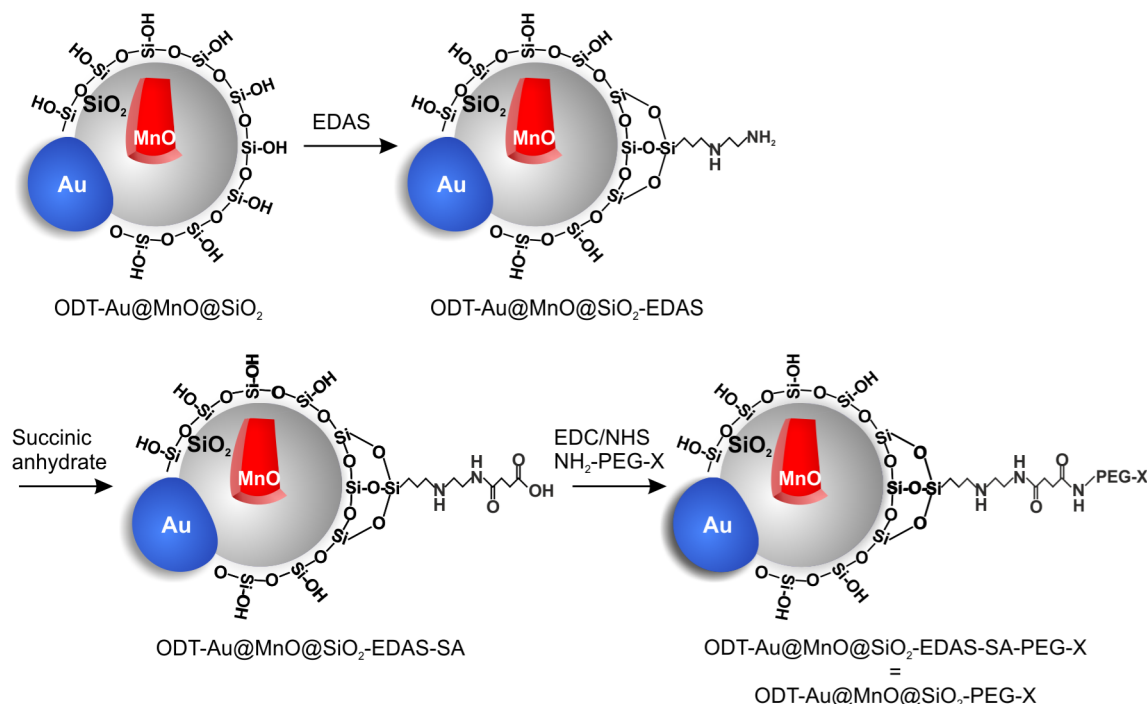


Figure 5.12: Synthetic procedure for fabrication of PEG-conjugated  $\text{SiO}_2$ -coated Janus particles, whereby the terminal group of the PEG chain was  $X = \text{OMe}$  or  $\text{NH}_2$ . The functionalization of the Au domain remained untouched, *i.e.* 1-octadecanethiol was bound to the surface.

The PEG-conjugated silica-coated Janus particles were analyzed in comparison to spherical MnO particles, which bore identical functionalization to the oxide component of the Janus particles, by means of dynamic light scattering (Figure 5.13). The Janus character had a large impact on the behavior in solution, which was evident due to the significant shift in the autocorrelation functions and the decreased correlation at larger lag times.

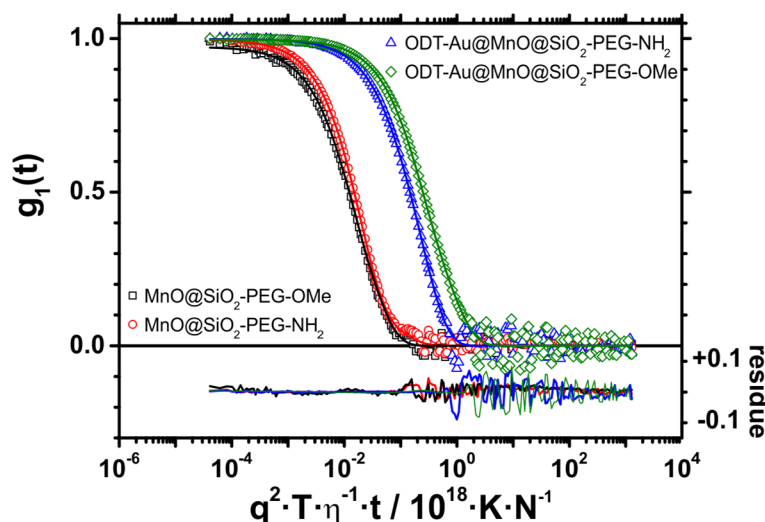


Figure 5.13: Dynamic light scattering results of PEG-conjugated spherical  $\text{MnO@SiO}_2$  as well as  $\text{ODT-Au@MnO@SiO}_2$  Janus particles dispersed in water: universally-scaled and normalized autocorrelation functions measured at scattering angle  $\theta = 90^\circ$  together with bi-exponential fitting function lines and corresponding residues ( $\lambda = 632.8 \text{ nm}$ ,  $T = 293 \text{ K}$ ,  $\eta = 1.005 \text{ cP}$ ).

The hydrodynamic radii (Table 5.1) confirmed the observation regarding the autocorrelation functions, namely a significant increase in the radius for the Janus particles. In contrast, the sizes of the spherical counterparts were in good accordance with TEM measurements. Thus, the Janus particles formed aggregates in aqueous solution due to their orthogonal functionalization, which are presumably of micellar shape as discussed earlier.

The strength of interaction between a monolayer of DOPC and the nanoparticles was analyzed using surface plasmon resonance (SPR) spectroscopy in order to determine whether the nanoparticles could have an effect on the membranes of GUVs. Concentration-dependent measurements of the SPR signal allowed determination of the dissociation constant  $K_D$  of the monolayer of small unilamellar vesicles (SUVs) and the nanoparticles with different functionalization and morphology. Langmuir adsorption kinetics were used for fitting the obtained equilibrium data, which are summarized in Table 5.1 together with the consequent Gibbs free energy  $\Delta G^\circ$  and the corresponding data obtained from TEM and DLS characterization.

Table 5.1: Characterization of PEG-functionalized silica-coated spherical and Janus particles.  $R_{TEM}$  denotes the radii of the nanoparticle cores and domains of Janus particles obtained from TEM. The hydrodynamic radius  $R_h$  was obtained from the apparent diffusion coefficients as a function of the scattering vector  $q^2$  in the range of the scattering angle  $30^\circ \leq \theta \leq 120^\circ$ .  $K_D$  is the dissociation constant between the particles and SUVs obtained from SPR measurements fitting the data with a Langmuir adsorption isotherm.  $\Delta G^\circ$  was calculated using the relationship to the dissociation constant  $\Delta G^\circ = R \cdot T \cdot \ln(K_D \cdot c_0^{-1})$ . The SPR measurements and subsequent analysis were performed [redacted]. \*The determination of the dissociation constant of MnO@SiO<sub>2</sub>-PEG<sub>500</sub>-NH<sub>2</sub> nanoparticles was not reasonable, as the signal intensity of the SPR measurements could only be explained by superposition with a buffer effect.

	$R_{TEM} / \text{nm}$	$R_h / \text{nm}$	$K_D / \mu\text{g/mL}$	$\Delta G^\circ / \text{kJ/mol}$
ODT- Au@MnO@SiO <sub>2</sub> - PEG <sub>500</sub> -OMe	Au: $5.0 \pm 0.2$ MnO: $10.0 \pm 1.0$	$202 \pm 6$	$10 \pm 7$	-50
MnO@SiO <sub>2</sub> - PEG <sub>500</sub> -OMe	$10.4 \pm 0.9$	$12 \pm 0.1$	$138 \pm 34$	-45
ODT- Au@MnO@SiO <sub>2</sub> - PEG <sub>500</sub> -NH <sub>2</sub>	Au: $5.0 \pm 0.2$ MnO: $10.0 \pm 1.0$	$127 \pm 2$	$90 \pm 86$	-46
MnO@SiO <sub>2</sub> - PEG <sub>500</sub> -NH <sub>2</sub>	$10.4 \pm 0.9$	$15 \pm 0.1$	---*	---

The adsorption of all tested nanoparticles to DOPC monolayers prepared on the SPR chip led to an increase in the measured SPR signal in a concentration-dependent manner, whereby the binding to the lipids was completely reversible. However, the concentration-dependent adsorption measurements did not reach the saturation, so the calculated dissociation constants only represent a rough estimation. Interestingly, the spherical MnO@SiO<sub>2</sub>-PEG<sub>500</sub>-OMe nanoparticles showed a weaker binding to the DOPC lipids than the Janus particles bearing the same functionalization of the MnO domain. Further, the terminal

amino group of the PEG ligand weakened the binding of the Janus particles to the membrane, so that the dissociation constant was in between that of the PEG<sub>500</sub>-OMe functionalized Janus particles and the spherical analogues. Based on the relationship between the dissociation constant and the Gibbs free energy  $\Delta G^\circ$ , the binding energy of the nanoparticles to the DOPC membranes was determined. The obtained values were 45 - 50 kJ/mol. In this context, Reynwar *et al.* calculated the binding energy per particle, which is necessary to form a spherical vesicle from a flat membrane, to be of the order of  $500 k_B T$ .<sup>[52]</sup> As the binding energies of all tested nanoparticles was roughly  $20 k_B T$  ( $50 \text{ kJ/mol} / (N_A \cdot k_B \cdot T)$ ), no vesiculation induced by a single particle was expected.

Following the physical characterization of the interaction between DOPC and the nanoparticles, GUV experiments were performed and analyzed by confocal laser scanning microscopy. In addition to the staining of the vesicles with TexasRed®, the outer medium was dyed using pyranine, so that uptake of the surrounding medium into GUVs could be followed. The corresponding images of the time-dependent incubation of GUVs with ODT-Au@MnO@SiO<sub>2</sub>-PEG<sub>500</sub>-OMe Janus particles are displayed in Figure 5.14. Starting as early as 15 minutes after addition of the particles, small tubular structures appeared at the membrane. Over time, these membrane tubes grew larger in size and were observable throughout the complete vesicle after 60 minutes. The corresponding image in the pyranine channel also showed little uptake of outer medium into the tubular structure, as indicated by red circles, as well as no leakage of the dye into the interior of the vesicle. Nevertheless, in contrast to previous experiments using ODT-Au@MnO-Dopa-PEG<sub>500</sub>-OMe, no vesicles were found. Most likely, this resulted from the weaker interaction of the lipid bilayer and the Janus particles. The introduction of an intermediate silica shell increased the hydrophilicity of the MnO domain, which became dominant over the hydrophobic Au domain. The vesicle shown after 30 minutes was moving, which caused the ellipsoidal appearance in orthogonal view. Osmotic shrinking could not be responsible for the observed effects, as the GUVs retained their spherical shape throughout the whole experiment.



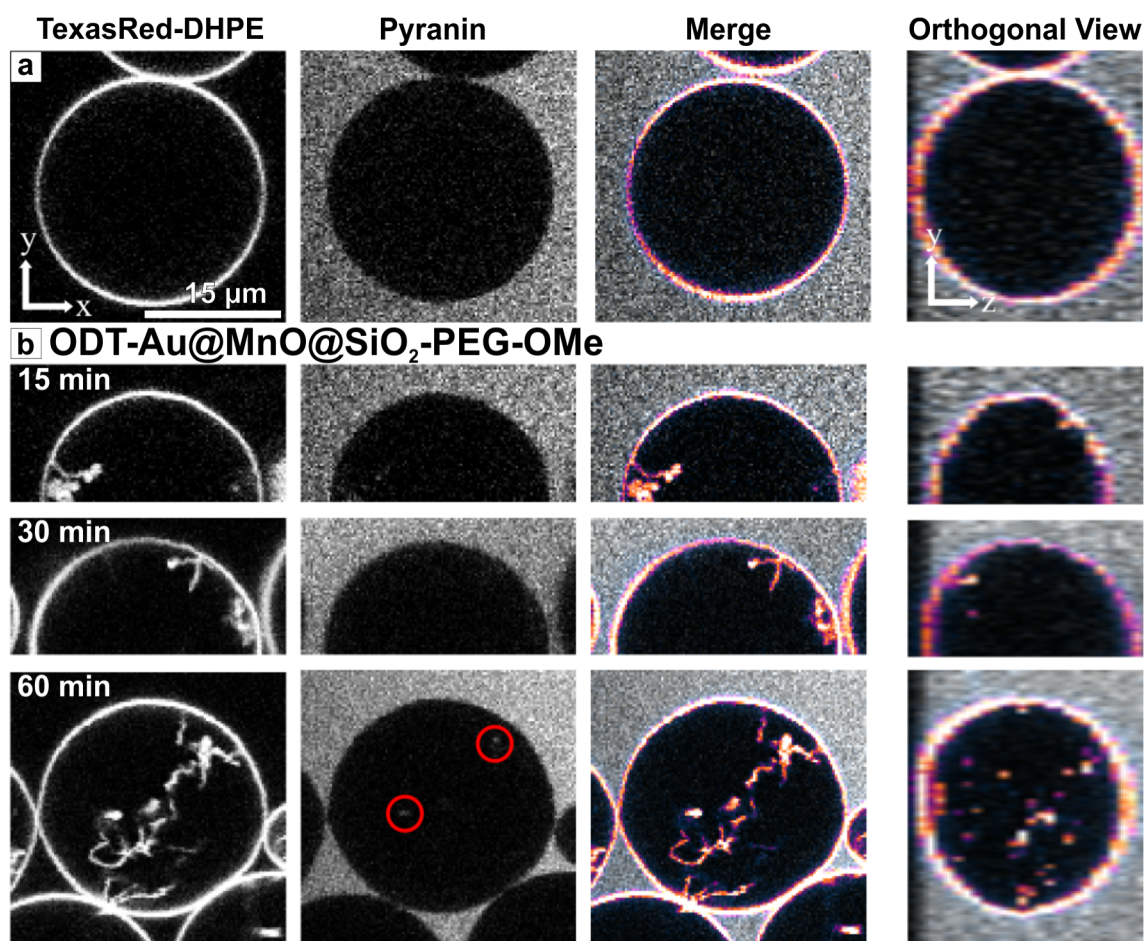


Figure 5.14: CLSM images of DOPC/TR-DHPE GUVs: a) untreated vesicles and b) GUVs treated with  $5 \mu\text{g Mn}^{2+}/\text{mL}$  ODT-Au@MnO@SiO<sub>2</sub>-PEG<sub>500</sub>-OMe Janus particles. The solution contained 2 mM pyranine. The images of single channels are displayed in grey scale, TR-DHPE is shown in pseudo-colors in the merged images. GUVs are shown in both directions, the equatorial and the meridian plane (orthogonal view). The experiments were performed by [REDACTED].

In comparison to spherical nanoparticles, the Janus particles led to a higher number of vesicles showing tubulations. Starting with only 10 % after 5 minutes, the proportion of vesicles with tubular structures increased exponentially up to 74 % after 50 minutes for ODT-Au@MnO@SiO<sub>2</sub>-PEG<sub>500</sub>-OMe Janus particles. For the spherical analogue, 9 and 43 % of the vesicles showed an effect after 5 and 50 minutes, respectively. Janus particles bearing a terminal amino group induced tubulation in nearly 100 % of the vesicles as early as 10 minutes after addition. As expected from the similar change in Gibbs free energy, the induced effects on GUVs were comparable. However, no tubulation or vesiculation was observed for any tested nanoparticles when an increase in osmotic pressure was applied to create tension of the membrane. This might be an effect of the weak amphiphilicity and their low binding strength to the lipid bilayer.

## 5.4 Conclusion

To conclude, we prepared inorganic Janus particles starting from hydrophobic heterodimer nanoparticles either by directed ligand exchange or silica encapsulation of the metal oxide domain, leaving the respective domain untouched. The selectivity during surface modification reactions was ensured due to the distinct surface chemistry of each domain. Thus, specific anchoring groups were exploited, e.g. thiols for Au domains and catechols or silica for the metal oxide components.

We demonstrated the use of heterodimer nanoparticles as building blocks for composite materials of lower symmetry when coupled with a crosslinking dithiol, here 1,4-benzenedimethanehol. The concepts of steric hindrance and bond strength, known from metal-organic complexes, were transferred to these pseudo-molecules. Thus, the formation of colloid molecules composed of two, three, or more heterodimer nanoparticles was realized, dependent on the ratio of domain sizes as well as the concentration of the crosslinking dithiol.

Further, we studied the self-assembly behavior of Janus particles at the air-water interface using a Langmuir-Blodgett trough as well as in solvent mixtures by (cryo-)TEM. In measurements of pressure-surface area cycles of 4@23 nm ODT-Au@MnO-Dopa-PEG<sub>500</sub>-NH<sub>2</sub>, the nanoparticles submerged into the bulk water phase, as their hydrophilic proportion dominated over their amphiphilic character. Thus, the ratio of domain sizes was increased in addition to a reversal of the amphiphilic character, so that the smaller Au domains became hydrophilic. These changes enabled the formation of Langmuir-films, although it remained challenging to clarify the orientation of the Janus particles within these films. However, the analysis of the Janus particles in solvent mixture clearly showed the expected upright orientation at the interface. This remained true upon reversal of the Janus character.

Finally, we analyzed the interaction of Janus particles with DOPC lipid bilayers serving as a model system for the impact on cellular membranes. These experiments demonstrated the ability of Janus particles to induce membrane tubulation under isoosmotic conditions, which displays a passive, artificial endocytotic uptake pathway. Further, ODT-Au@MnO-Dopa-PEG<sub>500</sub>-OMe Janus particles were taken up in vesicles, whereas spherical MnO nanoparticles showed no effect. The surface of the Janus particles was modified by an intermediate SiO<sub>2</sub> shell in order to investigate nanoparticles suitable for biomedical applications. In SPR experiments, the dissociation constants and binding strength of these nanoparticles were determined to be able to cause tubulation, but no vesiculation, in tension free membranes. This was confirmed by time-resolved CLSM analysis of GUVs incubated with nanoparticles. Here, Janus particles induced the formation of membrane tubes in 74 % to 100 % of the GUVs, though spherical MnO nanoparticles induced in only up to 43 %. From these experiments, it was inferred that the introduction of the SiO<sub>2</sub> shell changed the Janus character and consequently the interaction with the lipid bilayer. Presumably, the overall hydrophilic character of the Janus particles

became more pronounced, leading to less marked amphiphilic interaction with the membranes. Further, an increase of the membrane tension was applied. However, no effect was observed for nanoparticles added to membranes under tension. Consequently, it remains unclear whether the formation of membrane tubes or vesicles may serve as an additional uptake pathway in living cells. This has to be analyzed by cytotoxicity studies, as an increased uptake would be reflected by a higher cytotoxicity. In addition, no indication of pore formation or disruption of the lipid membrane due to interaction with Janus particles was observed. Overall, this is one of the first studies showing experimental evidence for Janus particles being able to induce tubular structures and vesicles in tension free membranes dependent on their amphiphilic functionalization.

## 5.5 Experimental Section

**Materials.** All reactions were carried out under argon atmosphere using commercially available reagents without any further purification: 1,4-Benzenedimethanethiol (98 %), 3,4-dihydroxyhydrocinnamic acid (98 %), ammonium hydroxide (NH<sub>4</sub>OH, 25 % aqueous solution), 1-hydroxybenzotriazole (HOBt, 98 %, 12 % water), *N,N'*-dicyclohexylcarbodiimide (DCC, 99 %), *N*-hydroxysuccinimide (NHS, 97 %), succinic anhydride (>99 %), polyethyleneglycol-methyletherthiol-1000 (HS-PEG<sub>1000</sub>-OMe), *O*-[2-(3-mercaptopropionylamino)ethyl]-*O'*-methylpolyethylene glycol-5000 (HS-PEG<sub>5000</sub>-OMe), anhydrous *N,N*-dimethylformamide (DMF, 99.8 %), *O,O'*-bis(2-aminopropyl)-polypropylene glycol-block-polyethylene glycol-block-polypropylene glycol-500 (NH<sub>2</sub>-PEG<sub>500</sub>-NH<sub>2</sub>), and *O*-(2-aminopropyl)-*O'*-(2-methoxypropyl)-polypropylene glycol-500 (NH<sub>2</sub>-PEG<sub>500</sub>-OMe) were purchased from Sigma Aldrich. [3-(2-aminoethylamino)]-propyltrimethoxysilane (EDAS, 97 %), 2-methoxy-(polyethyleneoxy)-propyltrimethoxysilane (PEG-silane, *n* = 9 - 12, 90 %) were purchased from ABCR. 1-Ethyl-3-(3-dimethylaminopropyl)carbodiimide (EDC, >99 %) was purchased from ProteoChem. 1,2-dioleoyl-*sn*-glycerol-3-phosphatidylcholine (DOPC) was purchased from Avanti Polar Lipids. TexasRed® 1,2-dihexadecanoyl-*sn*-glycero-3-phosphoethanolamine (TR-DHPE) was purchased from Life Technologies. Acetone, chloroform, diethyl ether, hexane, magnesium sulfate, and toluene were purchased from Fisher Scientific.

**Synthesis of Dopa<sub>500</sub>-PEG-OMe.** The conjugation of the catechol anchoring group to a PEG-derivative was performed following Schladt and co-workers.<sup>[168]</sup> Briefly, 5 mmol 3,4-dihydroxyhydrocinnamic acid and 5.1 mmol HOBt were dissolved in 10 mL DMF and stirred at room temperature for 10 min under a gentle stream of argon. Next, 5.1 mmol DCC dissolved in 10 mL DMF were added. Stirring was continued for 10 min, after which 5.1 mmol NHS in 10 mL DMF were added dropwise over a period of 30 min. The precipitate was removed by centrifugation (9000 rpm, 15 min) after stirring at room temperature for 2 h, and the supernatant

was transferred to a dropping funnel. It was then added dropwise to a solution of 5 mmol  $\text{NH}_2\text{-PEG}_{500}\text{-OMe}$  and stirred under argon atmosphere overnight. After removal of the precipitate by centrifugation (9000 rpm, 15 min), the solvent was removed, and the residue was dissolved in 2 mL DMF. The product was precipitated by dropwise addition into 40 mL ice-cooled diethyl ether. The supernatant was discarded and the product was washed twice with 40 mL ice-cooled diethyl ether. Then, the residue was dissolved in 50 mL  $\text{CHCl}_3$ , washed twice with saturated aqueous NaCl solution and ultrapure water. Finally, the solution was dried over  $\text{MgSO}_4$ , filtered, and the solvent was completely removed by rotary evaporation and fine vacuum at the Schlenk line.

**Ligand Exchange of the MnO Domain of Au@MnO NPs.** 300 mg Dopa- $\text{PEG}_{500}\text{-OMe}$  were dissolved in 15 mL  $\text{CHCl}_3$  at 50 °C under argon atmosphere. Next, 10 mg hydrophobic Au@MnO heterodimer nanoparticles were dissolved in 15 mL  $\text{CHCl}_3$  and added dropwise over a period of 1 h. The solution was stirred at 50 °C overnight. It was reduced to a volume of ca 4 mL. Under vigorous stirring, equal volumes of ultrapure water and hexane were added (30 mL). After stirring for 2 h, the organic phase was washed twice with water, and the combined aqueous phases were concentrated. The resulting concentration of nanoparticles was determined by the  $\text{Mn}^{2+}$  concentration using AAS.

**Ligand Exchange of the Au Domain of Au@MnO NPs.** In order to obtain Janus particles, the Au domain of hydrophobic Au@MnO heterodimer nanoparticles was functionalized using HS- $\text{PEG}_{1000}\text{-OMe}$  or HS- $\text{PEG}_{5000}\text{-OMe}$ . For this purpose, 10 mg Au@MnO nanoparticles were dissolved in 10 mL  $\text{CHCl}_3$  and added slowly to 20 mg HS- $\text{PEG}_{5000}\text{-OMe}$  in 20 mL  $\text{CHCl}_3$ . The solution was stirred under argon atmosphere overnight and concentrated to a volume of 5 mL.

**PEG-Functionalization of Au@MnO@SiO<sub>2</sub> NPs.** The surface modification of silica-encapsulated Au@MnO Janus particles was performed referring to Li and co-workers.<sup>[321]</sup> Subsequent to the encapsulation of 10 mg of Au@MnO nanoparticles, 100  $\mu\text{L}$   $\text{NH}_4\text{OH}$ , 350  $\mu\text{L}$  EDAS, and 75  $\mu\text{L}$  PEG-silane were added to the nanoparticle solution in 10 mL acetone. The reaction mixture was stirred at room temperature for 4 h under argon atmosphere. Subsequently, the nanoparticles were precipitated by addition of hexane, centrifuged (5000 rpm, 5 min), and washed twice with acetone/hexane. Next, the nanoparticles were dissolved in 10 mL DMF and 0.2 mmol succinic anhydride were added. The solution was stirred overnight. Finally, 0.50 mg NHS and 0.25 mmol EDC were dissolved in 1 mL DMF and added to the reaction mixture. After stirring for 2 h, 0.1 g  $\text{NH}_2\text{-PEG}_{500}\text{-X}$  ( $\text{X} = \text{NH}_2, \text{OMe}$ ) was added. The reaction was stirred overnight, concentrated, and transferred to water. The product was dialyzed against water for 3 days (cellulose bag, MWCO = 3,500). The final concentration of nanoparticles was determined by the  $\text{Mn}^{2+}$  concentration using AAS. MnO@SiO<sub>2</sub>-PEG-X nanoparticles were prepared as described, except MnO@SiO<sub>2</sub> nanoparticles were used.

**Production of Small Unilamellar Vesicles (SUVs).** SUVs composed out of DOPC were prepared by dissolution of the lipid in chloroform, transfer to TrisHCl buffer, and sonication for 30 min subsequent to filtration through a porous 0.2  $\mu\text{m}$  filter. For experimental details see [314].

**Production of Giant Unilamellar Vesicles (GUVs).** GUVs were prepared by electroformation of a DOPC/TR-DHPE solution (99.5/0.5) in  $\text{CHCl}_3$  applied to an ITO-covered glass slide. After drying the lipid film in vacuum, the reaction chamber was filled with 100 mM sucrose in deionized water for Dopa-PEG-functionalized particles or 2 mM TrisHCl buffer, *pH* 7 for  $\text{SiO}_2$ -PEG-coated particles. The formation was performed for 2 h at a peak-to-peak voltage of 1.6 V and 12 Hz or 2.3 V and 70 Hz, respectively, for the different sets of nanoparticles. For experimental details see [314].

**Nanoparticle Characterization.** The nanoparticles were characterized by TEM, DLS, and AAS as described in Chapter 4.4.1.

In cooperation with [REDACTED], the surface activity was measured using a NIMA 611 Langmuir-Blodgett trough. The surface pressure was monitored using the Wilhelmy plate method. All measurements were performed at room temperature. Water was used as continuous phase, and  $\text{CHCl}_3$  as the ambient phase, in which the nanoparticles were dispersed. 1.5 mg (46.5  $\mu\text{L}$ ) Janus particles dissolved in  $\text{CHCl}_3$  were spread out on the surface of the aqueous phase by using a micro syringe. The surface pressure approached an equilibrium after ca 15 min subsequent to the initial increase upon application of the Janus particle solution. During this time,  $\text{CHCl}_3$  evaporated and the Janus particles self-assembled at the air-water interface. Then, the surface area was compressed starting at 250  $\text{cm}^2$  down to 35  $\text{cm}^2$  measuring isotherms or until a surface pressure of 5 mN/m was reached for isotherm cycles.

Further, cryo-TEM measurements were performed in cooperation with [REDACTED] at University Bayreuth. TEM images of nanoparticles in solution were taken under nitrogen cooling using a Zeiss EM922 Omega microscope (Carl Zeiss Microscopy GmbH) and a Zeiss cryo-Box (Carl Zeiss SMT GmbH) for sample preparation.

The interaction of Janus particles with artificial membranes was analyzed in cooperation with [REDACTED] by means of confocal laser scanning and epi-fluorescence microscopy as well as surface plasmon resonance spectroscopy (SPR). For details on the experimental procedure and data analysis see [314]. SPR experiments were carried out using a Reichelt SR7000DC-SPR setup. GUVs incubated with nanoparticle solutions were analyzed using either a Zeiss LSM 710 confocal laser scanning microscope equipped with an Argon Laser or an Olympus IX81 epi-fluorescence microscope.









# 6

## Janus Particles for Multimodal Bioimaging

This chapter contains parts of an adapted reproduction of *Journal of the American Chemical Society* **2014**, 136, 2473 – 2483,<sup>[54]</sup> reproduced with permission of the American Chemical Society Copyright 2014, and of a manuscript submitted to the *Beilstein Journal of Nanotechnology* linked to the final report of the DFG priority program SPP 1313 “Biological Responses to Nanoscale Particles”.<sup>[151]</sup>

### 6.1 Introduction

In recent years, there has been an increasing interest in the large variety of bioimaging techniques not only for scientific research, but also for clinical diagnostics. Here, ultrasound, computed X-ray tomography (CT), magnetic resonance imaging (MRI), and positron emission tomography (PET) are commonly used on their own or in combination. Nowadays, this combination of comprehensive imaging techniques in diagnostics enables a faster, more accurate, and less physically demanding prognosis. All methods rely on the exposition of a sample or patient and its response to energy, *i.e.* sonic, X-rays, magnetic fields, or positrons, and where they differ distinctly in terms of spatial and temporal resolution, imaging depths, anatomical and molecular details, radiation load, as well as exposure times and damage.<sup>[322]</sup> Common to these methods is their improvement of the signal-to-noise ratio, their sensitivity, and resolution upon application of contrast agents, though each of them has its own requirements for the ideal contrast agent. Taken together, these developments have heightened scientific interest and clinical need for multimodal contrast agents, as they would be able to enhance safety and reduce adverse effects by limiting the amount and dose of different contrast agents, improve patient care, and at the same time lower costs.

Gold nanoparticles have been widely used for biomedical applications due to their extraordinary optical properties relying on the surface plasmon resonance (SPR). Their potential was demonstrated for instance in simultaneous cell-imaging and photothermal therapy,<sup>[16,20,79,81,82,323]</sup> multi-photon microscopy,<sup>[39,256]</sup> and colorimetric sensing of adsorbed biomolecules.<sup>[65,66,324]</sup> Moreover, they are emerging as next generation contrast agents for computed X-ray tomography (CT).<sup>[40–44,80]</sup>

CT uses the X-ray absorption of the (human) body to obtain detailed images, which easily visualize a sharp contrast of electron-dense bones to soft tissue. However, due to the absence of natural contrast in different soft tissues, contrast agents are inevitably required to enhance or lower the density of the targeted structure as compared to the surrounding tissue. For instance, the vascular systems are imaged by CT, where blood vessels as fine as 100  $\mu\text{m}$  could be distinguished upon application of a contrast agent (Figure 6.1a and b).<sup>[40]</sup> The attenuation of X-rays can be described by the Lambert-Beer law,  $I = I_0 \cdot e^{-\kappa x}$ , where  $I$  and  $I_0$  are the intensities of the incidental and resulting beam, and  $x$  is the effective length through which the radiation passes. The absorption coefficient  $\kappa$  of the medium is defined as  $\kappa = \mu \cdot \rho^{-1}$ . As it is inversely proportional to its electron density  $\rho$ , X-ray attenuation can be enhanced by increasing the density of the medium. The X-ray mass attenuation coefficient  $\mu$  itself is an intrinsic elemental characteristic, but strongly dependent on the X-ray energy.<sup>[44]</sup> The basic requirements for an excellent CT contrast agent are manifold, as it has to be i) biocompatible, ii) cost effective, iii) small in size, and iv) long-term colloiddally stable within the body. However, its high contrast efficiency combined with long circulation times is inevitable.<sup>[43]</sup> Water-soluble iodinated molecules based on 1,3,5-triodobenzene are commonly applied as clinical CT contrast agents, although they are not optimal candidates due their low contrast efficiency and substantial adverse effects. Initial studies have demonstrated Au nanoparticles to be superior to iodine-based contrast agents, not only for their low cytotoxicity, unique SPR, and tailored surface chemistry, enabling e.g. passive tumor targeting, but also because Au exhibits a 2.7-fold higher X-ray absorption coefficient of 5.16 at 100 KeV. Preliminary work on size and concentration of Au nanoparticles affecting X-ray attenuation in comparison to the commonly applied iodine-based contrast agent, Omnipaque<sup>TM</sup>, was undertaken by Xu and co-workers.<sup>[325]</sup> Their analysis showed a high impact of small Au nanoparticles of a diameter of 4 nm and 20 nm, since the attenuation depends on the target area. Further, at elevated concentrations above 0.1 mol/L, the attenuation effect increased significantly as compared to Omnipaque<sup>TM</sup>. However, Au nanoparticles as CT contrast agents are still in their infancy, while comprehensive research on their blood circulation characteristics, biological toxicity, and specificity for targeting e.g. tumors, including first *in vivo* applications are under current investigation.<sup>[43]</sup>

On the other hand, tremendous advances in nanotechnology have introduced magnetic nanoparticles as MRI contrast agents. Magnetic resonance imaging is one of the most powerful

diagnosis techniques in current medicine and gives detailed images of soft tissue with extraordinarily high resolution when contrast agents are applied.<sup>[46]</sup> The underlying physical concept is nuclear magnetic resonance combined with the spin relaxation of protons in an external, powerful magnetic field. After excitation by a transverse radio-frequent (RF) pulse, the MR image is recorded from the relaxation process of the protons to their aligned orientation. There are two independent relaxation pathways: the longitudinal or  $T_1$  relaxation and the transverse or  $T_2$  relaxation. Longitudinal relaxation describes the process of equilibration of the initial magnetization after excitation, which takes place as an energy transfer from the proton spins to its surrounding medium. The chemical differences in the surrounding medium are responsible for distinct relaxation behavior and, thus,  $T_1$  contrast of MR images. The second pathway, the transverse relaxation, can be described as a spin dephasing process, which is the randomization of the transverse component of the magnetization of excited spins with identical phase, immediately after the RF pulse. The  $T_2$  contrast originates from differences in the magnetic field experienced by the protons due to local magnetic field gradients, which affect the rate of the dephasing process. In summary, contrast enhancement in MRI emerges from the interaction of the contrast agent and adjacent water protons. This process is strongly dependent on several parameters, such as proton density, their chemical surrounding, and magnetic pulse sequences.<sup>[45,46,326]</sup>

Magnetic nanoparticles with well-defined magnetic properties are promising candidates for enhancing the sensitivity in  $T_2$ -weighted MRI analysis, which has been under investigation for more than two decades. Since then, iron oxide nanoparticle-based therapeutics have been approved for clinical use, for instance for bowel (Lumirem®, Gastromark®) and liver/spleen (Endorem®, Feridex®) imaging, while Combidex® is at the late-stage clinical trials for its use in detecting lymph node metastases.<sup>[45]</sup> Magnetic nanoparticles exhibit a high magnetic susceptibility and are superior to paramagnetic complexes, as their magnetization is dependent on the number of magnetic ions.<sup>[46]</sup> Superparamagnetic iron oxide nanoparticles are used as  $T_2$  contrast agents, as their high magnetic moment in the presence of an external field disturbs the relaxation process of surrounding water protons. The introduced field inhomogeneity facilitates the dephasing of spins, which equals a shortening of the spin-spin relaxation time  $T_2$ . The images therefore show a decreased signal intensity, so that these contrast agents are commonly referred to as  $T_2$ -negative agents.

Nevertheless,  $T_2$  contrast agents suffer from several disadvantages, as the signal-decreasing effect results in a darkening of the image, which can lead to artifacts. Moreover, they distort the magnetic field, known as susceptibility artifact or “blooming effect”. For this reason,  $T_1$  contrast agents are more commonly used in clinical diagnostics. The presence of paramagnetic ions shortens the longitudinal relaxation, as they withdraw excess energy after proton excitation. They are referred to as  $T_1$ -positive contrast agents, as they increase the signal

intensity. Metal ions with a large number of unpaired electrons have been shown to be eminently suitable for this purpose, whereby  $\text{Gd}^{3+}$  complexes are state of the art for clinical diagnostics. Despite their lower number of unpaired electrons and magnetic moments,  $\text{Mn}^{2+}$ ,  $\text{Fe}^{3+}$ , and  $\text{Co}^{2+}$  could be alternatively used. The evolution of contrast enhancing therapeutics dates back to 1973, when  $\text{Mn}^{2+}$  in the form of aqueous  $\text{MnSO}_4$  solutions was the first contrast agent proposed for MRI.<sup>[327–329]</sup> Unfortunately, manganese-enhanced MRI (MEMRI) using  $\text{MnCl}_2$  solutions is restricted to animal studies, as  $\text{Mn}^{2+}$  ions cause hepatic failure and have cardiac toxicity.<sup>[46]</sup> However, MEMRI has attracted much research attention, since superparamagnetic  $\text{MnO}$  nanoparticles have been demonstrated as non-toxic  $T_1$  contrast agents.<sup>[47,51,174,330,331]</sup> Most recently, ultra-small  $\text{Fe}_3\text{O}_4$  nanoparticles have come into the focus of research as  $T_1$  as well as dual contrast agent for MRI. Their small magnetic moment, together with an enhanced biocompatibility as compared to clinically used  $\text{Gd}^{3+}$  agents, enabled *in vivo* application for  $T_1$  as well as  $T_2$  signal enhancement (Figure 6.1c and d).<sup>[332]</sup>

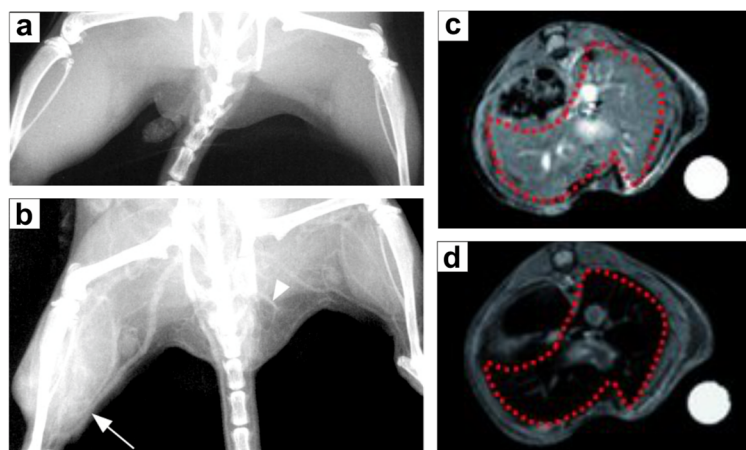


Figure 6.1: Left: *in vivo* X-ray images of mouse hind legs a) before injection and b) 2 min post tail injection of Au nanoparticles. The arrow points to leg with tumor and increased vascularity. Reproduced from [40]. Right: *in vivo* c)  $T_1$ -weighted and d)  $T_2$ -weighted image of mouse liver (selected area) using ultra-small  $\text{Fe}_3\text{O}_4$  nanoparticles as dual contrast agent for MRI. Reproduced from [332].

Following the demand for multimodal contrast agents, we investigated the potential of inorganic Janus particles for multimodal bioimaging applications. Initial results from our group demonstrated the potential of  $\text{Au@MnO}$  “flowerlike” hetero-nanoparticles for simultaneous optical and magnetic imaging.<sup>[168]</sup> Recently,  $\text{Au@Fe}_3\text{O}_4$  hetero-nanoparticles have been developed for multimodal imaging, including combinations of optical and MRI,<sup>[281,282,333]</sup> MRI and CT,<sup>[192,333,334]</sup> as well as optical, MRI, and PET.<sup>[335]</sup> In the study presented here, Au was chosen as material for the metal domain due to its promising performance as a CT contrast agent, while the magnetic metal oxide domain, responsible for contrast enhancement in MRI, was composed of either  $\text{MnO}$  or  $\text{Fe}_3\text{O}_4$ .

On top of the qualification of the individual materials of Janus particles as contrast agents, careful attention has to be paid to their dose needed to obtain optimal imaging results. Preliminary work on Au nanoparticles as CT contrast agents was undertaken by Hainfeld and

co-workers.<sup>[40]</sup> They reported the first use of Au nanoparticles, with a concentration of 10 mg per mL blood, applying them to mice to overcome fundamental restrictions of commonly used iodine-based X-ray contrast agents, such as short imaging times, occasional renal toxicity, poor contrast in large patients, and the need for catheterization in many cases. Further, AuroVist™, a pre-clinical blood-pool X-ray contrast agent based on Au nanoparticles, is tested *in vivo* on mice in the range of 0.07 – 0.7 g/kg mouse. However, commercially available MRI contrast agents based on iron oxide nanoparticles are already used in concentrations as little as 0.56 mg/kg for *in vivo* diagnostics in humans.<sup>[336,337]</sup> Recently, Zhu *et al.* applied Au@Fe<sub>3</sub>O<sub>4</sub> heterodimer nanoparticles for simultaneous *in vivo* MRI and CT imaging of a rabbit model and were able to resolve the rabbit ventricle by CT imaging.<sup>[338]</sup> They observed a saturation of the T<sub>2</sub> contrast effect at a concentration of 0.12 mM Fe, whereas Au concentrations up to 0.2 M showed a continuous increase in signal intensity without saturation.

Overall, efficient application of Janus particles as a dual contrast agent for simultaneous magnetic resonance imaging and computed X-ray tomography requires a higher load of the noble metal for X-ray attenuation as compared to the metal oxide responsible for the more sensitive magnetic resonance imaging. Herein, we describe the synthetic tailoring and comprehensive characterization of Janus particles together with initial results on their qualification as contrast agents in noninvasive bioimaging using CT and MRI phantom experiments. The well-defined morphology of the heterodimer nanoparticles enabled not only the precise control over their properties responsible for optical, magnetic resonance, and computed X-ray tomography imaging, but also facilitated a promising platform for selective surface functionalization and, thus, the combination of targeted imaging, drug delivery, and therapy.<sup>[5,254,255]</sup>

## 6.2 Tailoring Janus Particles for Bioimaging Applications

In order to optimize the domain proportions of Janus particles for simultaneous imaging, we needed to adjust the domain sizes of the small metal and the larger metal oxide component in heterodimer nanoparticles. As discussed earlier, the size of the Au seeds used for hetero-epitaxial growth of the metal oxide was limited to ca 10 nm (see Chapter 3.2.2). Larger seeds led to multiple nucleation of the metal oxide, which was counterproductive regarding the required higher proportion of the noble metal. We chose *de novo* a seeding-growth technique in order to enlarge the metal domains subsequent to the formation of hydrophobic heterodimer nanoparticles. Initially, Wang *et al.* described this overgrowth of Au on Au@Fe<sub>3</sub>O<sub>4</sub> heterodimer nanoparticles.<sup>[155]</sup> Then, Buck and co-workers transferred it to colloidal hybrid particles using Pt@Fe<sub>3</sub>O<sub>4</sub> as seed particles and a variety of metals such as Au, Ag, Ni, or Pd as the third component.<sup>[145]</sup> Here, we report the synthesis of Au@Au@MnO hetero-nanoparticles for the first time and relate it to Au@Au@Fe<sub>3</sub>O<sub>4</sub> particles for their subsequent use in biomedical imaging.

Briefly, the heterodimer nanoparticles were injected into a solution of tetrachloroauric(III) acid in 1-octadene and oleylamine at 90 °C and held at this temperature for 30 minutes. Independent of the chemical composition of the metal oxide, chemo-selective deposition of Au was observed on the Au domain. As described in literature, the overgrowth occurred *de novo* as a nucleation and epitaxial growth of Au on the Au@Fe<sub>3</sub>O<sub>4</sub> heterodimer nanoparticles, resulting in a trimeric structure (Figure 6.2).

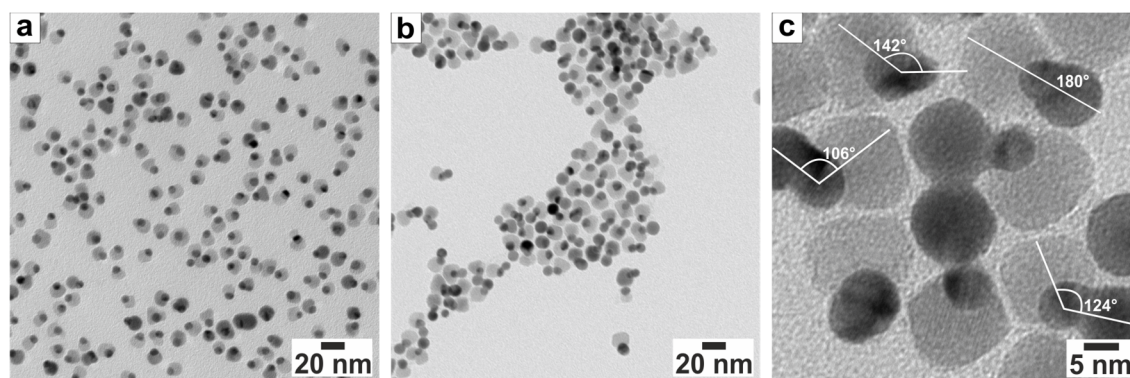


Figure 6.2: TEM images of Au@Au@Fe<sub>3</sub>O<sub>4</sub> hetero-nanoparticles obtained by Au overgrowth: a) 9@15 nm Au@Fe<sub>3</sub>O<sub>4</sub> heterodimer nanoparticles used as seeds, b) - c) Au@Au@Fe<sub>3</sub>O<sub>4</sub> heterotrimer nanoparticles, where the angles in between Au and Fe<sub>3</sub>O<sub>4</sub> heterotrimer nanoparticles indicated a preferred bent morphology.

Interestingly, a preference for a bent over a linear morphology was observed (Figure 6.2c). Similar behavior was found in literature for Au@Pt@Fe<sub>3</sub>O<sub>4</sub> heterotrimer nanoparticles, where the bent morphology was ascribed to the favorable nucleation at high-energy corner sites of Pt domains.<sup>[145]</sup> When comparing Au@Fe<sub>3</sub>O<sub>4</sub> to Pt@Fe<sub>3</sub>O<sub>4</sub>, however, there was a distinct difference in the structure of the metal domains, as Pt preferentially forms single crystalline nanoparticles, while Au is known for its tendency toward twinning (see Chapter 2.3.1). Therefore, the bent morphology of Au@Au@Fe<sub>3</sub>O<sub>4</sub> could not be attributed to specific corner sites of the Au domain, but rather to nucleation at high energy surface defects. Further, nucleation on distinct corners of pre-existing Au domains was expected to result in a constant bending angle of the Fe<sub>3</sub>O<sub>4</sub> and the newly nucleated Au domains, which was not observed to be the case.

The changes in morphology by increasing the Au proportion of the nanoparticles altered the optical characteristics. Figure 6.3a shows the comparison of the UV-VIS spectra of Au@Au@Fe<sub>3</sub>O<sub>4</sub> heterotrimers and Au@Fe<sub>3</sub>O<sub>4</sub> seed particles. The nucleation of Au on the pre-existing Au domain led to rod-like behavior of both Au domains taken together: an additional absorption band emerged at low energy of ca 710 nm, which could be ascribed to a longitudinal dipole oscillation. Further, the absorption at 526 nm was observed even more pronounced than for Au@Fe<sub>3</sub>O<sub>4</sub> heterodimer nanoparticles. As there was no direct contact of the second Au domain to Fe<sub>3</sub>O<sub>4</sub>, their optical properties, *i.e.* the position of the absorption band at higher energy and its spectral intensity, closely resembled those of pure Au nanoparticles. The low energy absorption band indicated strong interactions, such as electron translocation across the

interface of the two Au domains, which enabled the facile tuning of optical properties by variation of the metals used for subsequent overgrowth. When Ag instead of Au was used for the second metal domain, an additional absorption band at ca 410 nm was observed. The absorption band due to the Au domain was not altered, although the dielectric constant of its surrounding medium was changed (Figure 6.3b). The broad absorption of the Ag domains was due to their polydispersity (see inset of Figure 6.3b). In summation, the optical response of  $\text{Ag@Au@Fe}_3\text{O}_4$  could be described as superposition of those of  $\text{Au@Fe}_3\text{O}_4$  and Ag nanoparticles. This observation revealed barely any electronic interaction across the interface, but further confirmed the longitudinal dipole oscillation as being responsible for the low energy absorption band in the case of  $\text{Au@Au@Fe}_3\text{O}_4$ .

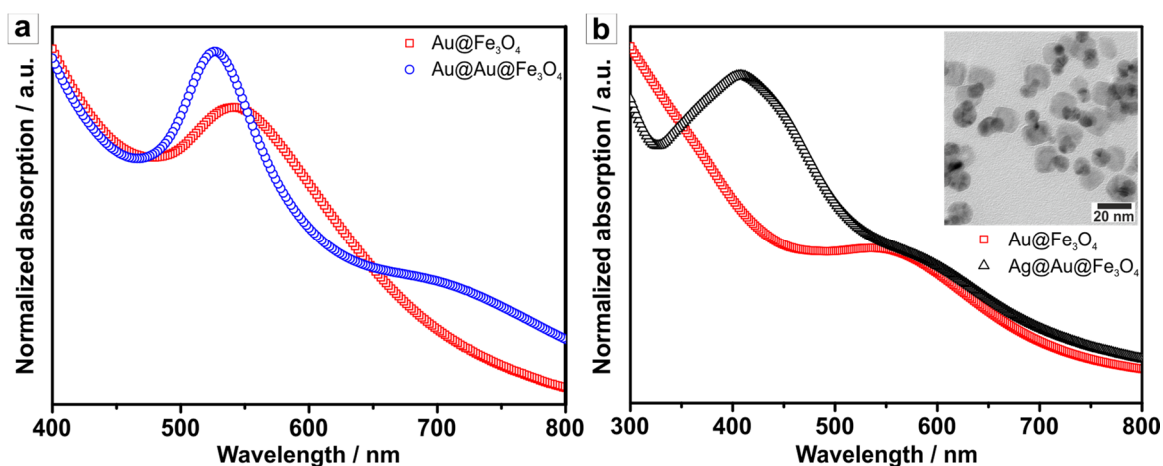


Figure 6.3: UV-VIS spectra of a)  $\text{Au@Au@Fe}_3\text{O}_4$  hetero-nanoparticles as compared to  $\text{Au@Fe}_3\text{O}_4$  seed particles and b)  $\text{Ag@Au@Fe}_3\text{O}_4$  heterotrimer nanoparticles with reference to  $\text{Au@Fe}_3\text{O}_4$ . The inset shows a TEM image of the corresponding  $\text{Ag@Au@Fe}_3\text{O}_4$  nanoparticles. The spectra were measured in hexane and normalized at 350 nm.

In general, the formation of anisotropic hetero-nanoparticles is explained in terms of lattice mismatch and preferential nucleation on distinct crystal planes.<sup>[92]</sup> Here, the nucleation of Au on  $\text{Au@Fe}_3\text{O}_4$  heterodimers is epitaxial and, thus, conformal growth leading to an increased size of the Au domains would be expected. Wang *et al.* proposed a distribution of stress and strain across the seeding heterodimer nanoparticles, which was ascribed to be responsible for the preference for additional nucleation. The formation of heterodimer nanoparticles induces lattice distortion in both components. This distortion is most significant directly at the interface of the domains and dissipates with increasing distance. Thus, the epitaxial growth of Au takes place at the far end of the Au domain, where the strain energy is smallest.<sup>[155]</sup> For multiply-twinned Au domains in  $\text{Au@Fe}_3\text{O}_4$  heterodimer nanoparticles, this concept is ambiguous, as the lattice distortion must not to be the same for all crystallites, since only one of them is in direct contact with the metal oxide domain. Nevertheless, it contributes to a qualitative understanding.

Interestingly, the overgrowth of Au on  $\text{Au@MnO}$  heterodimer nanoparticles led to  $\text{Au@MnO}$  heterodimer nanoparticles with larger Au domains (Figure 6.4), which was originally expected for epitaxial deposition of Au on  $\text{Au@Fe}_3\text{O}_4$  as well. The Au domain size was enlarged

up to 15 nm, depending on the ratio of heterodimer seed particles and Au precursor. This was significant, as the formation of heterodimer nanoparticles with Au domain sizes above 10 nm was not realizable before.

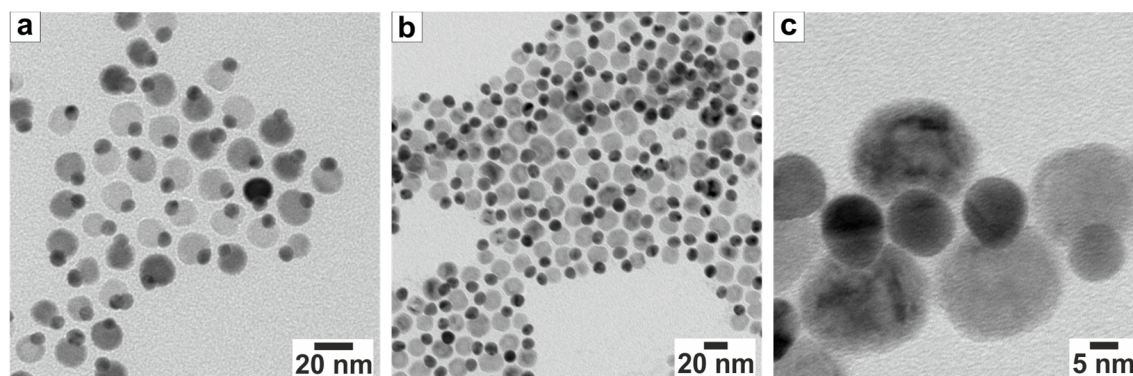


Figure 6.4: Representative TEM images showing a) 8@23 nm Au@MnO seeds and b) - c) 12@23 nm Au@Au@MnO hetero-nanoparticles subsequent to Au overgrowth.

However, the size of the Au domains could only be increased to a certain extent, as further enlargement led to the disruption of the hetero-nanoparticles along the Au-MnO interface (Figure 6.5a). Here, we observed incipient cracking for prolonged reaction times or higher amounts of tetrachloroauric(III) acid (Figure 6.5b). It resulted in an extraction of the Au domains, leaving behind dented MnO nanoparticles (Figure 6.5c).

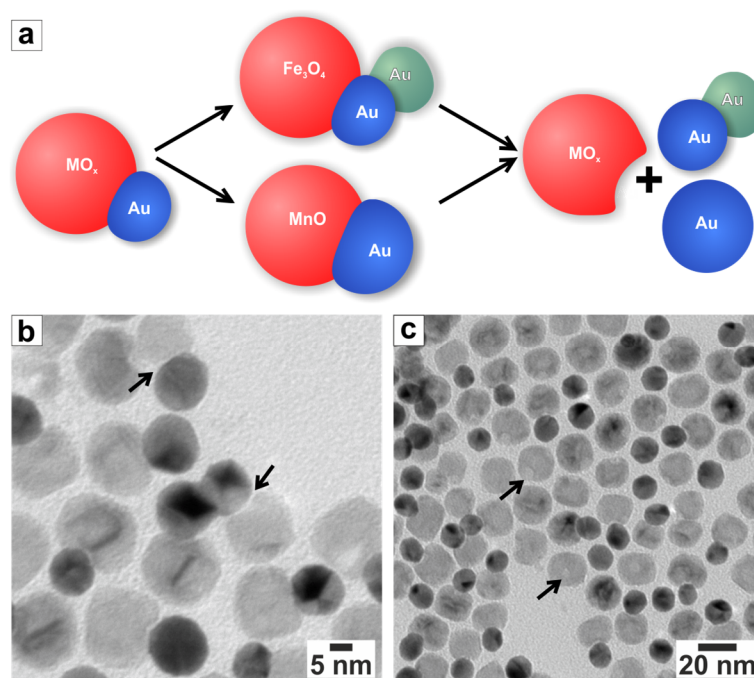


Figure 6.5: a) Schematic illustration of Au overgrowth on Au@MO<sub>x</sub> heterodimer nanoparticles: first, Au@Au@Fe<sub>3</sub>O<sub>4</sub> heterotrimers or Au@Au@MnO heterodimers with enlarged Au domains are formed; second, detachment of the Au domains takes place leaving behind dented metal oxide domains. Corresponding TEM images of Au@Au@MnO hetero-nanoparticles: b) arrows point to the incipient cracking at the domain interfaces, and c) progressive extraction of Au domains resulted in dented MnO nanoparticles as indicated by the arrows.

Similar behavior was observed for Au@Au@Fe<sub>3</sub>O<sub>4</sub> nanoparticles. Thereby, the size of the Au domain was suggested to be restricted by the increase in cohesive stress until it



outweighs the failure strength of the interface. Wang *et al.* reported the failure strength to depend on the initial Au domain size, as it has a high impact on the spatial distribution and the magnitude of strain energy within the heterodimer nanoparticles.<sup>[155]</sup>

As was observed for Au@Au@Fe<sub>3</sub>O<sub>4</sub> heterodimer nanoparticles, the enlargement of the Au domain within Au@MnO nanoparticles resulted in a hypsochromic shift of the absorption maximum of ca 15 nm to 529 nm. Further, its spectral intensity was increased (Figure 6.6). This shows that the electronic properties of the enlarged Au domains of Au@Au@MnO nanoparticles were less influenced by the electron-deficient MnO domain than in heterodimer nanoparticles: the damping of the surface plasmon and the prorated reduction in the number of free electrons became less distinct for larger Au nanoparticles. This observation was confirmed by reaction snapshots taken after 5 minutes subsequent to the injection of the heterodimer nanoparticles. The absorption band was already shifted to higher energies and increased in intensity. Reaction times up to 30 minutes amplified these effects, while further prolongation led to the described disruption of the hetero-nanoparticles and, thus, the strong surface plasmon resonance of pure Au nanoparticles centered at ca 520 nm.

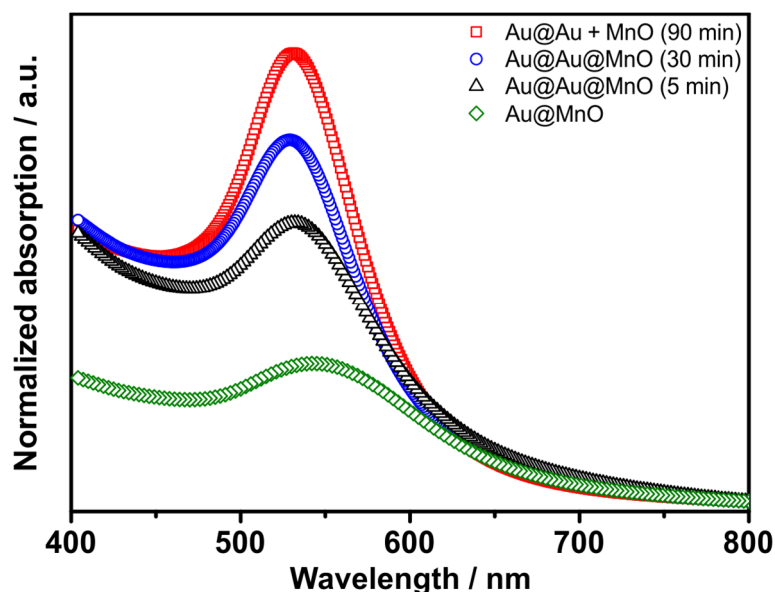


Figure 6.6: UV-VIS spectra of Au@Au@MnO hetero-nanoparticles after 5, 30, and 90 min reaction time in comparison to Au@MnO seed particles. The spectra were measured in hexane and scaled to unity at 800 nm.

DLS measurements confirmed the intactness as well as the monodispersity of Au@Au@MnO nanoparticles suggested by TEM images (Figure 6.7). The autocorrelation function measured at small scattering angles showed no indication of any larger aggregates. Further, the apparent Diffusion coefficient was determined to be independent of the scattering vector  $q^2$ . The hydrodynamic radius was determined to be  $R_h(\text{Au@Au@MnO}) = 17.4 \pm 0.1$  nm, which displayed an increase in radius of ca 3 nm as compared to Au@MnO heterodimer nanoparticles. This was in good accordance with TEM measurements, where an increase in diameter of the Au domain of ca 4 nm was observed. The enlargement of the Au domains

amplified the anisotropy and aspect ratio of the hetero-nanoparticles, which diminished the accuracy of the approximation of a pseudo-spherical morphology while analyzing DLS data.

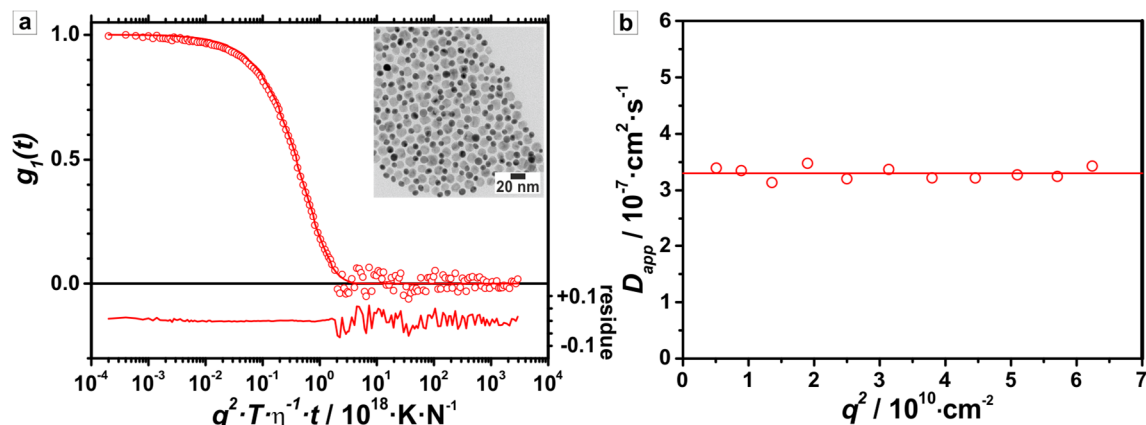


Figure 6.7: Dynamic light scattering results of Au@Au@MnO dispersed in *n*-heptane ( $\lambda = 632.8$  nm,  $T = 293$  K, viscosity  $\eta$ : 0.410 cP *n*-heptane): a) universally-scaled and normalized field autocorrelation function measured at scattering angle  $\theta = 30^\circ$  together with bi-exponential fitting function line and residuum. Inset: corresponding TEM image; b) apparent diffusion coefficients as a function of scattering vector  $q^2$  in the range of scattering angle  $30^\circ \leq \theta \leq 150^\circ$ .

Moreover, the growth of a third domain and the enlargement, respectively, did not alter the behavior of the hetero-nanoparticles regarding subsequent surface modification, such as silica encapsulation. Interestingly, no additional thiol functionalization was necessary in order to passivate the Au surface. The silica shell formed exclusively on the metal oxide domain, leaving the hydrophobic Au domain untouched, as was discussed in Chapter 4.2. In fact, the amphiphilicity of Au@Au@MnO@SiO<sub>2</sub> Janus particles was increased due to the larger hydrophobic portion, which was readily observable in TEM analysis (Figure 6.8): the Au domains congregated whenever the local concentration of nanoparticles was sufficiently high. On the other hand, the Janus character was small enough, such that the individual particles were easily soluble in polar media, e.g. water, acetone, ethanol, DMF, or DMSO. This was crucial as unwanted aggregation reduces the imaging precision due to changes in nanoparticle characteristics, and might cause thrombosis as an adverse effect.<sup>[325,339]</sup>

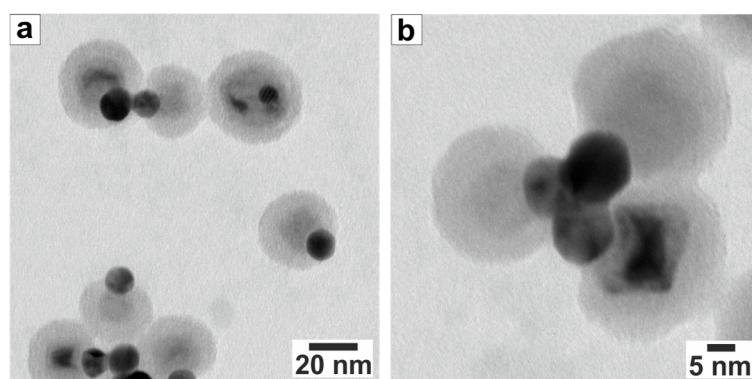


Figure 6.8: TEM images of amphiphilic Au@Au@MnO@SiO<sub>2</sub> hetero-nanoparticles. The enlargement of the Au domains facilitated the Janus character, as was qualitatively observed by assembly upon drying colloidal solutions on the TEM grids.

In conclusion, the subsequent overgrowth of Au on Au@MO<sub>x</sub> heterodimer nanoparticles was established as an important technique to enhance the control over the domain proportions. Hereby, either heterotrimer nanoparticles due to separate nucleation or heterodimer nanoparticles with enlarged Au domain were obtained. This step was crucial for the potential use of Janus particles as multimodal contrast agents. The enlargement of the Au domains can further facilitate the subsequent binding *e.g.* of thiol-conjugated biomolecules, as the steric hindrance due to the bulky metal oxide domains was reduced with an increase in the surface area of the Au domains.

### 6.3 Janus Particles as CT Contrast Agents

Generally, X-ray attenuation is caused by interaction of the photons with the traversed matter, which includes coherent scattering, Compton scattering, and the photoelectron effect. As the contributions to X-ray attenuation of Compton scattering and coherent scattering are negligible at reasonable X-ray energies, the photoelectron effect determines the characteristics of a material. It increases with the atomic number and is strongest at the K-shell binding energy for a given substance.<sup>[43]</sup>

Here, we investigated the X-ray attenuation of Au-containing Janus particles, dependent on their chemical composition, as compared to spherical metal oxide nanoparticles without any noble metal present. Table 6.1 displays the X-ray mass attenuation constants, characteristic for the elements used, as a function of the photon energy. To date, pre-clinical studies are performed using variable energies ranging from 44 keV up to 100 keV.<sup>[43,44,340]</sup> The attenuation is highest at the K-edge of each element and 60 keV is listed, as we performed radio density measurements at 65 keV. The measurements were conducted using a microCT imaging device, where iodine-based contrast agents are usually analyzed. Therefore, this energy was used, as it is slightly higher than the K-edge of iodine.

Table 6.1: X-ray mass attenuation constants  $\mu/\rho$  dependent on the photon energy  $E$ .<sup>[341]</sup>

Material	Z	$\mu/\rho$ / cm <sup>2</sup> ·g <sup>-1</sup> $E = 60$ keV	$\mu/\rho$ / cm <sup>2</sup> ·g <sup>-1</sup> $E = \text{K-edge}$	$\mu/\rho$ / cm <sup>2</sup> ·g <sup>-1</sup> $E = 100$ keV
Au	79	4.528	8.904 $E = 80.72$ keV	5.158
Pt	78	4.339	9.301 $E = 78.34$ keV	4.993
Fe	26	1.205	8.176 $E = 30.00$ keV	0.372
Mn	25	1.060	7.141 $E = 30.00$ keV	0.337
H <sub>2</sub> O	---	0.206	---	0.171

In fact, a signal amplification can be obtained by choosing an X-ray source with an output energy just above the K-edge energy, independent of size and concentration of the contrast agents. This is attributed to the ionization of surface electrons, which results in resonance absorption from atoms in the medium.<sup>[342]</sup> Yusa *et al.* evaluated numerically the impact of the X-ray energy on the effectiveness of Au nanoparticles as CT contrast agents and reported a significantly improved imaging capability for X-ray energies above 80.7 keV.<sup>[343]</sup>

Figure 6.9 summarizes initial results on the X-ray attenuation of aqueous solutions of Janus particles, grouped together according to the chemical composition of the metal oxide domains. The color-coded CT phantom images of MnO-based nanoparticles (Figure 6.9a and b), together with the CT values (Figure 6.9d) revealed a gradual increase in X-ray attenuation with concentration of the same type of nanoparticles. This became even more pronounced for sequential enlargement of the Au domain, as was realized in Au@Au@MnO nanoparticles. The signal amplification was strongest for Au@Au@MnO nanoparticles due to the highest amount of Au. Further, Figure 6.9c and e show the corresponding data of Fe<sub>3</sub>O<sub>4</sub>-containing nanoparticles. Similarly, the introduction and progressive enlargement of noble metal domains significantly increased the X-ray attenuation as compared to pure Fe<sub>3</sub>O<sub>4</sub>@SiO<sub>2</sub> nanoparticles.

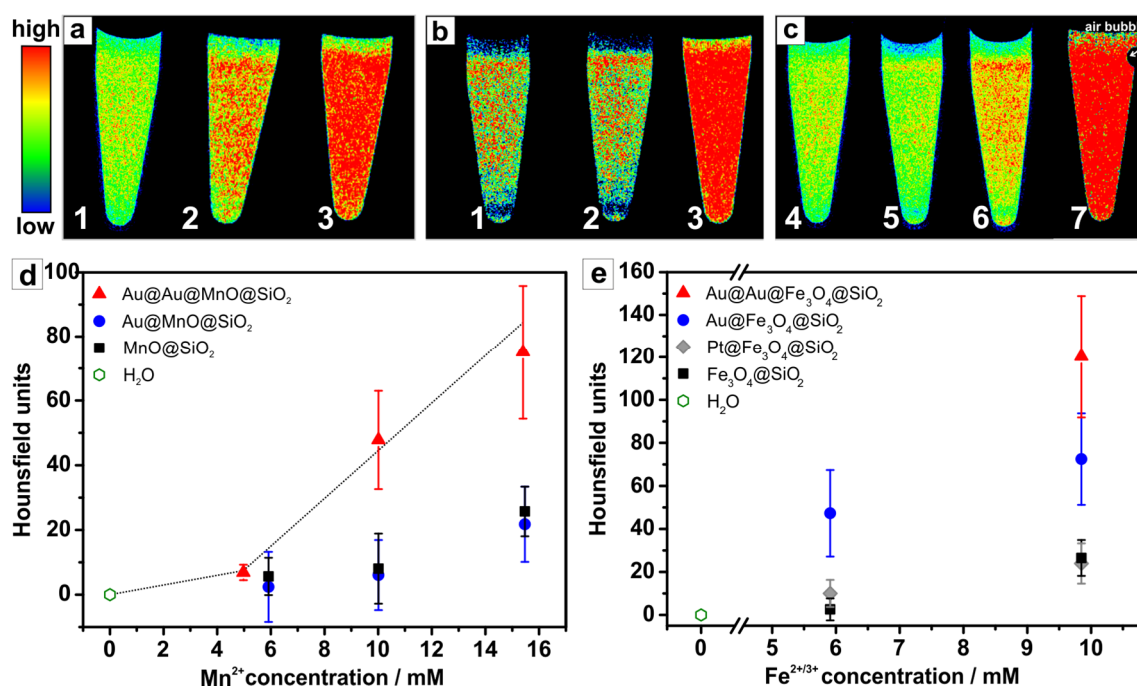


Figure 6.9: X-ray attenuation of hetero-nanoparticles: a) - c) color-coded CT phantom images of aqueous solutions with a concentration of a) 10.0 mM Mn<sup>2+</sup> and b) 15.5 mM Mn<sup>2+</sup> with (1) MnO@SiO<sub>2</sub>, (2) Au@MnO@SiO<sub>2</sub>, and (3) Au@Au@MnO@SiO<sub>2</sub>; c) 10.0 mM Fe<sup>2+/3+</sup> with (4) Fe<sub>3</sub>O<sub>4</sub>@SiO<sub>2</sub>, (5) Pt@Fe<sub>3</sub>O<sub>4</sub>@SiO<sub>2</sub>, (6) Au@Fe<sub>3</sub>O<sub>4</sub>@SiO<sub>2</sub>, and (7) Au@Au@Fe<sub>3</sub>O<sub>4</sub>@SiO<sub>2</sub> nanoparticles; d) - e) CT values of hetero-nanoparticles as a function of the concentration of the metal oxide. The nanoparticle concentrations were determined with respect to Fe<sup>2+/3+</sup> and Mn<sup>2+</sup> instead of the Au or Pt due to technical restrictions. Radio density measurements were performed for 29 s at 65 keV by [redacted] and [redacted].

Table 6.2 correlates the CT values with the corresponding metal domain sizes. Interestingly, there was a notable difference for MnO-based and Fe<sub>3</sub>O<sub>4</sub>-based nanoparticles. Concerning the comparison of MnO@SiO<sub>2</sub> and Au@MnO@SiO<sub>2</sub>, no effect was observed due

to the introduction of a Au domain, independent of the nanoparticle concentration. However, the enlargement of the diameter of the Au domain by a factor of 1.5 led to a 7.8-fold increase in the CT signal for a concentration of 10.0 mM  $\text{Mn}^{2+}$ , while an elevated concentration of 15.5 mM  $\text{Mn}^{2+}$  caused only an enhancement by a factor of 3.5. The observed concentration-dependent signal amplification suggested a threshold concentration of Au required for their use as CT contrast agents, as indicated by the trendline in Figure 6.9d for  $\text{Au@Au@MnO@SiO}_2$  nanoparticles. Likewise, this was described by Yusa *et al.*, as no effects were observable for Au nanoparticle solutions with mass percentages below 0.1%.<sup>[343]</sup> Moving on to  $\text{Fe}_3\text{O}_4$ -based nanoparticles, this trend was also observed: the introduction of small Pt domains did not alter the CT values as compared to pure  $\text{Fe}_3\text{O}_4@SiO_2$  nanoparticles. However, the enlargement of the metal domain to roughly 9 nm caused a 3-fold increase in signal intensity. This became even more evident for  $\text{Au@Au@Fe}_3\text{O}_4$  heterotrimer nanoparticles bearing additional Au domains of comparable size, which showed a 4.8-fold rise.

Table 6.2: Size-, concentration-, and composition-dependent X-ray attenuation of hetero-nanoparticles. The concentrations of aqueous nanoparticle solutions were determined by Mn or Fe AAS and are given as the molar concentrations of  $\text{Mn}^{2+}$  or  $\text{Fe}^{2+/3+}$ , respectively. The radio density measurements were performed by [REDACTED] and [REDACTED].

	$D_{TEM} / \text{nm}$	Hounsfield unit $c = 10.0 \text{ mM}$	Hounsfield unit $c = 15.5 \text{ mM}$
$\text{MnO@SiO}_2$	$20.3 \pm 1.4$	$8.1 \pm 5.8$	$25.7 \pm 7.6$
$\text{Au@MnO@SiO}_2$	Au: $8.3 \pm 0.7$ MnO: $18.3 \pm 1.6$	$6.1 \pm 10.8$	$21.7 \pm 11.6$
$\text{Au@Au@MnO@SiO}_2$	Au: $13.0 \pm 0.9$ MnO: $18.3 \pm 1.6$	$47.8 \pm 15.2$	$75.1 \pm 20.7$
$\text{Fe}_3\text{O}_4@SiO_2$	$15.9 \pm 0.7$	$26.5 \pm 8.3$	---
$\text{Pt@Fe}_3\text{O}_4@SiO_2$	Pt: $5.6 \pm 0.5$ $\text{Fe}_3\text{O}_4$ : $12.9 \pm 1.6$	$25.1 \pm 5.4$	---
$\text{Au@Fe}_3\text{O}_4@SiO_2$	Au: $8.9 \pm 0.4$ $\text{Fe}_3\text{O}_4$ : $14.6 \pm 1.9$	$72.5 \pm 21.3$	---
$\text{Au@Au@Fe}_3\text{O}_4@SiO_2$	Au: $9.1 \pm 1.3$ , $8.9 \pm 0.4$ $\text{Fe}_3\text{O}_4$ : $14.6 \pm 1.9$	$120.3 \pm 28.5$	---

Surprisingly, the comparison of CT values of  $\text{Au@MnO@SiO}_2$  and  $\text{Au@Fe}_3\text{O}_4@SiO_2$  showed a 12-fold higher X-ray attenuation for the  $\text{Fe}_3\text{O}_4$ -containing Janus particles, although the Au domain sizes and the concentration of nanoparticles were the same. As the  $\text{Fe}_3\text{O}_4$  domains were slightly smaller than the MnO domains, the effective number of nanoparticles was larger for a given molar concentration of Fe or Mn, respectively, and the mass percentage of Au was slightly increased. However, the magnitude of X-ray attenuation could not only be attributed to the threshold concentration effect. Further, the impact of the metal oxide itself was expected to cause similar attenuation for both, MnO and  $\text{Fe}_3\text{O}_4$ , as the X-ray mass attenuation coefficients

differ by a factor of only 1.1. These results suggested an impact of the solid state interface on the electronic structure of the metal domain, which was observed to be an intrinsic characteristic of heterodimer nanoparticles (see Chapter 3.4). The electronic communication across the interface led to the formation of a Schottky junction for Au@Fe<sub>3</sub>O<sub>4</sub>, as Fe<sub>3</sub>O<sub>4</sub> is a semi-metal, whereas MnO, as wide band gap semiconductor, only caused a polarization of the conducting electrons. For this reason, the electronic structure of the Au domain was changed upon conjugation to Fe<sub>3</sub>O<sub>4</sub>, which might also alter the X-ray attenuation. However, this hypothesis has not been discussed in literature before, but similar effects have been described. Recently, Au@Fe<sub>3</sub>O<sub>4</sub> hetero-nanoparticles were reported to show significantly stronger X-ray attenuation than pure Au nanoparticles: an increase of ca 200 HU was observed at an Au concentration of 100 mM.<sup>[192,333,334]</sup> The authors solely attributed this effect to the additional metal oxide component, although the strength of signal amplification was significantly above the expected contribution of the less X-ray attenuating Fe<sub>3</sub>O<sub>4</sub>. Thus, this study might also suggest an additional contribution of the electronic interaction of the domains.

As was pointed out in the introduction to this chapter, a high contrast efficiency is inevitable, where a minimum signal amplification of 200 HU is required for clinical use. The Janus particles showed a distinct increase in X-ray attenuation, though the requirements for clinical applications disclose the need of further investigations. The X-ray attenuation can be increased by adjusting the X-ray energy to slightly above that of the K-edge, increasing the concentration, and altering the relative composition of the Janus particles, which is the subject of ongoing research.

## 6.4 Janus Particles as MRI Contrast Agents

In order to establish Janus particles as contrast agents for multimodal imaging techniques, their potential for signal enhancement in MRI was investigated. Recent reports on MnO nanoparticles as T<sub>1</sub> contrast agents revealed a strong dependency of the measured relaxivities on their structure, size, and surface functionalization.<sup>[174]</sup> Here, isotropic MnO@SiO<sub>2</sub> were analyzed in comparison to Au@MnO@SiO<sub>2</sub> nanoparticles using a clinical whole-body MRI scanner. Figure 6.10a displays their T<sub>1</sub>-weighted images, where the signal intensity was observed to increase with the concentrations for both types of nanoparticles. Interestingly, it was even stronger for Janus particles subsequent to enlargement of the Au domain, although little impact of the diamagnetic metal was expected. This effect was also observed for Au@Fe<sub>3</sub>O<sub>4</sub>@SiO<sub>2</sub> Janus particles as compared to Fe<sub>3</sub>O<sub>4</sub>@SiO<sub>2</sub> nanoparticles. Fe<sub>3</sub>O<sub>4</sub> nanoparticles have been introduced in literature for their potential use as T<sub>2</sub> contrast agents, though recent reports highlighted the potential application of ultra-small Fe<sub>3</sub>O<sub>4</sub> nanoparticles as T<sub>1</sub> contrast agents.<sup>[206,332]</sup> The T<sub>1</sub>-weighted images of Fe<sub>3</sub>O<sub>4</sub>-based nanoparticles in Figure 6.10b

clearly showed a concentration-dependent signal enhancement, which was again more pronounced for Janus particles.

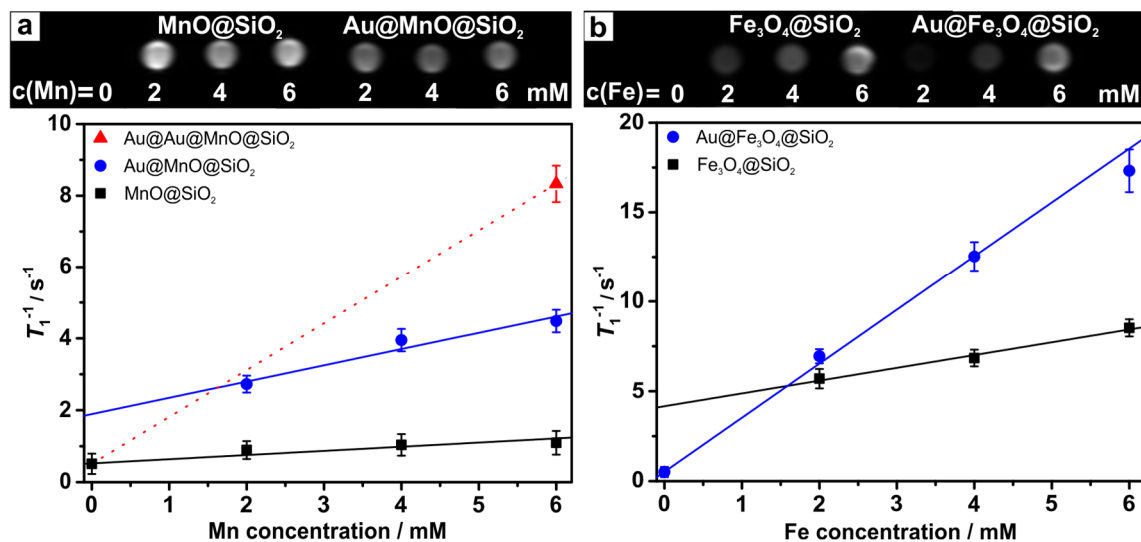


Figure 6.10: T<sub>1</sub>-weighted phantom MR images of aqueous solutions of a) MnO@SiO<sub>2</sub> and Au@MnO@SiO<sub>2</sub> and b) Fe<sub>3</sub>O<sub>4</sub>@SiO<sub>2</sub> and Au@Fe<sub>3</sub>O<sub>4</sub>@SiO<sub>2</sub> nanoparticles with increasing concentrations operated in a 3.0 T MR system (top) and corresponding T<sub>1</sub> relaxivity plots (bottom). The measurements were performed by [REDACTED].

Table 6.3 summarizes the magnetic resonance properties with the relaxivities being defined as  $r_1 = 1/T_1$ . The relaxivity  $r_1$  of MnO@SiO<sub>2</sub> nanoparticles was determined to be 0.12 mM<sup>-1</sup>s<sup>-1</sup>. This was in good accordance with the relaxation properties of 20 nm MnO reported by Na and co-workers.<sup>[174]</sup> As was observed from T<sub>1</sub>-weighted images, the relaxivity of Au@MnO@SiO<sub>2</sub> Janus particles was substantially higher. This effect became even more pronounced for Au@Fe<sub>3</sub>O<sub>4</sub>@SiO<sub>2</sub> Janus particles. The relaxivity of Au@Fe<sub>3</sub>O<sub>4</sub> heterodimer nanoparticles was determined to 3.01 mM<sup>-1</sup>s<sup>-1</sup>, which was consistent with earlier reports by Xu and co-workers.<sup>[163]</sup> Thus, the surface spin canting due to the interfacial contact with a diamagnetic metal domain was suggested to have a positive impact on the aptitude of Janus particles in MRI. Previous results from our group on Au@MnO flowerlike hetero-nanoparticles showed a lower relaxivity of 0.224 mM<sup>-1</sup>s<sup>-1</sup>, which suggested an increase in the relaxivity upon enhancement of the Au/MnO proportion.<sup>[168]</sup> Likewise, this was reported for Au@Fe<sub>3</sub>O<sub>4</sub> nanoparticles, where an increase in the size of the Au domain led to an increase in  $r_1$  and reduction in  $r_2$ .<sup>[163]</sup>

Kim *et al.* demonstrated the potential use of Fe<sub>3</sub>O<sub>4</sub> nanoparticles with a diameter of 3 nm as T<sub>1</sub> contrast agents due to their near-complete spin canting reducing the magnetization. Similarly, the substantially increased relaxivity  $r_1$  observed for Au@Fe<sub>3</sub>O<sub>4</sub>@SiO<sub>2</sub>, as compared to Fe<sub>3</sub>O<sub>4</sub>@SiO<sub>2</sub> of comparable Fe<sub>3</sub>O<sub>4</sub>-domain size, was ascribed to the spin canting. As the Fe<sub>3</sub>O<sub>4</sub> domains were not single crystalline (see Chapter 3.3), this effect was suggested to be caused by the interplay of small crystallite sizes and surface spin canting arising from a junction effect due to the interface to the Au domain.

Table 6.3: Comparison of magnetic resonance properties of silica-coated Janus particles to spheroidal metal oxide nanoparticles.

	$D_{TEM}(MO_x) / \text{nm}$	$D_{TEM}(Au) / \text{nm}$	$r_1 / \text{mM}^{-1}\text{s}^{-1}$
MnO@SiO <sub>2</sub>	20.3 ± 1.4	---	0.12 ± 0.02
Au@MnO@SiO <sub>2</sub>	18.3 ± 1.6	8.3 ± 0.7	0.45 ± 0.09
Fe <sub>3</sub> O <sub>4</sub> @SiO <sub>2</sub>	15.9 ± 0.7	---	0.71 ± 0.08
Au@Fe <sub>3</sub> O <sub>4</sub> @SiO <sub>2</sub>	14.6 ± 1.9	8.9 ± 1.9	3.01 ± 0.12

Despite their acceleration of  $T_1$  relaxation, Fe<sub>3</sub>O<sub>4</sub>-based nanoparticles are basically inapplicable as  $T_1$  contrast agents, as their strong magnetic moment causes inhomogeneities of the magnetic field and leads to high  $r_2$  values. However, an ideal  $T_1$  contrast agent exhibits a small  $r_2/r_1$  ratio, which equates to a large paramagnetic property with negligible magnetic anisotropy.<sup>[46]</sup> As was described by the model of Koenig and Keller, the spin-spin relaxation depends on the magnetic moment of the nanoparticles  $\mu$  and their diameter  $D$ , which can be expressed as  $1/T_2 \propto \mu^2 \cdot D^{-1}$ .<sup>[344,345]</sup> Thus, nanoparticles with a large magnetization are suggested to be efficient  $T_2$  contrast agents. Magnetic measurements of hydrophobic Au@MnO heterodimer nanoparticles revealed a slight decrease in the magnetic moment as compared to spherical MnO nanoparticles (see Chapter 3.2.5),<sup>[177]</sup> while the magnetic moment of Au@Fe<sub>3</sub>O<sub>4</sub> heterodimer nanoparticles was close to that of isotropic Fe<sub>3</sub>O<sub>4</sub> nanoparticles (see Chapter 3.3.5). Based on the magnetic data of hydrophobic heterodimer nanoparticles, the transverse relaxation times of Janus particles are suggested to resemble those of isotropic metal oxide nanoparticles. However, investigation of the impact of Janus particles on transverse relaxation is a focus of current research, as several studies described a dependency on the morphology.<sup>[333]</sup>

## 6.5 Conclusion

Here, we demonstrated progressive overgrowth of Au on pre-formed Au@MO<sub>x</sub> heterodimer nanoparticles to enable precise control over the domain proportions of Janus particles, which was found to be restricted to Au nanoparticles smaller than 10 nm in the case of the seeding-growth technique described earlier. The additional nucleation of gold occurred chemo-selectively on the metal domains of the heterodimers: no deposition was observed on the metal oxide domains, independent of their chemical composition. However, the progressive overgrowth enlarged the Au domains in the case of Au@MnO, while it led to separate Au domains on Au@Fe<sub>3</sub>O<sub>4</sub>, forming Au@Au@Fe<sub>3</sub>O<sub>4</sub> heterotrimer nanoparticles. This effect might



be attributed to the distinct electronic interactions across the solid state interface within these heterodimer nanoparticles. The formation of a Schottky barrier in Au@Fe<sub>3</sub>O<sub>4</sub> heterodimers causes the equilibrium of electronic states and withdraws excess energy from the Au domains. As a consequence of this passivation, the formation of separate Au domains was preferred over uniform enlargement of the preformed metal domains. In fact, this enlargement was observed for Au@MnO heterodimer nanoparticles, as the interfacial communication was restricted by the wide band gap of MnO.

Independent of the morphology of the hetero-nanoparticles, the enlarged Au domain was demonstrated to significantly amplify the X-ray attenuation. Hereby, a threshold effect was observed, as small Au domains did not alter the signal of spherical MO<sub>x</sub>@SiO<sub>2</sub> nanoparticles. The comparison of Au@Fe<sub>3</sub>O<sub>4</sub>@SiO<sub>2</sub> and Au@MnO@SiO<sub>2</sub> also suggested an impact of the interfacial communication, and, thus, the electronic structure on X-ray attenuation: the signal amplification was significantly higher for Fe<sub>3</sub>O<sub>4</sub>-based Janus particles, despite negligible differences in the X-ray attenuation of iron and manganese. This is a topic of ongoing research utilizing Mößbauer spectroscopy and photoelectron spectroscopy in order to analyze the electronic structure of heterodimer nanoparticles in more detail.

Moreover, by virtue of the intrinsic materials' characteristics of the metal oxide domains, Janus particles were exploited as contrast agents for magnetic resonance imaging. Here, an acceleration of longitudinal relaxation processes was observed with increasing concentrations of Au@MO<sub>x</sub>@SiO<sub>2</sub> Janus particles, as compared to spherical metal oxide nanoparticles. The increase in  $r_1$  indicated a junction effect in the dumbbell-structure, which allows facile tuning of the relaxation times by adjustment of the domain sizes. These initial results make Au@MnO@SiO<sub>2</sub> Janus particles suitable as T<sub>1</sub> MRI contrast agents, as we were able to demonstrate their positive contrast ability, in addition to their facile surface functionalization and efficient labeling for simultaneous optical imaging (see Chapter 4) or attachment of biomarkers. Further, the large magnetic moment of Au@Fe<sub>3</sub>O<sub>4</sub>@SiO<sub>2</sub> Janus particles in combination with data reported in literature suggests them to be used as T<sub>2</sub> contrast agents, which is under current investigation.

To sum up, Janus particles are promising candidates with great potential in biomedical imaging. Janus particles are superior to traditional spherical nanoparticles for targeted imaging purposes, as they provide two surfaces, which can be independently modified for the ease of simultaneous diagnosis and therapy. This will be beneficial for the reduction of nanoparticles entering the body and, thus, the certainty of adverse effects, a key point of interest in research on nanoparticles for bioimaging applications. As not only the relation of size, shape, and surface functionalization to imaging effects is of particular importance, but also with pharmacokinetic properties, this will be addressed in the next chapter.

## 6.6 Experimental Section

**Materials.** All reactions were carried out under argon atmosphere and using commercially available reagents without any further purification: Tetrachloroauric(III) acid hydrate (99.9%-Au,  $\text{HAuCl}_4 \cdot (\text{H}_2\text{O})_x$ ) was purchased from ABCR. 1-Octadecene (technical grade, 90 %) was purchased from Sigma Aldrich. Anhydrous silver(I) acetate (99 %,  $\text{Ag}(\text{OAc})$ ) was purchased from Alfa Aesar. 2-Propanol, acetone, ethanol, heptane, hexane, methanol, oleylamine (80 - 90 %), oleic acid (reagent grade), and toluene were purchased from Fisher Scientific.

**Synthesis of Au@Au@MO<sub>x</sub> NPs.** The synthetic procedure was adapted from Buck *et al.* with some modifications regarding the heating protocol.<sup>[145]</sup> Briefly, 0.03 mmol  $\text{HAuCl}_4 \cdot (\text{H}_2\text{O})_x$  was dissolved in 6 mL 1-octadecene and 0.2 mL oleylamine by heating to a temperature of 60 °C (oil bath) using a gently stream of argon. The reaction flask was sealed with a rubber septum, and the temperature was further raised to 90 °C. Next, 10 mg Au@MO<sub>x</sub> heterodimer nanoparticles, dissolved in 1 mL hexane, were rapidly added via a syringe. The temperature was held at 90 °C for 30 min before cooling down to room temperature by removing the oil bath. The particles were washed by repeated precipitation with 2-propanol, centrifugation (9000 rpm, 10 min), and dissolution in hexane.

**Synthesis of Ag@Au@Fe<sub>3</sub>O<sub>4</sub> Heterotrimer NPs.** The synthesis was performed following an adapted procedure of Buck and co-workers.<sup>[145]</sup> In short, 0.075 mmol  $\text{Ag}(\text{OAc})$  were dissolved in 10 mL toluene and 0.74 mL oleylamine at room temperature under argon atmosphere. Then, 9 - 11 mg Au@Fe<sub>3</sub>O<sub>4</sub> heterodimer nanoparticles were added, and the reaction mixture was heated up to 105 °C, where it was held for 3 h. After cooling down by removal of the oil bath, the nanoparticles were precipitated by addition of ethanol, separated by centrifugation (9000 rpm, 10 min), and dissolved in hexane.

**Silica Encapsulation of Au@Au@MO<sub>x</sub> NPs.** The silica encapsulation of heteronanoparticles was performed as described for Au@MO<sub>x</sub> heterodimer nanoparticles, except Au@Au@MO<sub>x</sub> were used without any further surface functionalization (see Chapter 4.4).

**Nanoparticle Characterization.** The nanoparticles were analyzed by means of TEM, UV-VIS spectroscopy, AAS, and DLS as described in Chapter 4.4.1.

Further, they were tested for their use as contrast agents for computed X-ray tomography (CT) in cooperation with [REDACTED]. Radio density measurements of heteronanoparticles were performed using a 29 s and 65 keV protocol by microCT imaging (TomoScope Synergy Twin, CT Imaging). Imalytics Research Software (Philips Technology) was applied for determination of the Hounsfield units (HU).

Magnetic resonance imaging (MRI) was recorded in collaboration with [REDACTED]. The magnetic resonance imaging (MRI) properties of aqueous solutions of Janus particles with different  $\text{Mn}^{2+}$  and  $\text{Fe}^{2+/3+}$  concentrations, respectively, determined by AAS were performed on a clinical 3.0 Tesla scanner (Magnetom Trio, Siemens Medical Solutions, Erlangen, Germany) by means of a  $T_1$  measurement using a spoiled gradient echo (SGRE) with variable repetition time.



# 7

## The Two Faces of Janus Particles for Biomedical Applications

This chapter contains parts of an adapted reproduction of *Journal of the American Chemical Society* **2014**, 136, 2473 – 2483<sup>[54]</sup> and *Biomaterials* **2014**, 35, 6986 – 6997,<sup>[346]</sup> reproduced with permission of the American Chemical Society Copyright 2014 and Elsevier Copyright 2014, and of two manuscripts submitted to the *Beilstein Journal of Nanotechnology* linked to the final report of the DFG priority program SPP 1313 “Biological Responses to Nanoscale Particles”.<sup>[151,347]</sup>

### 7.1 Introduction

Inorganic Janus particles are highly versatile nanomaterials with great potential in biomedical application as *theranostic* agents.<sup>[28,163,199,333,338]</sup> Furthermore, hetero-nanoparticles are in focus of much research due to their exceptional chemical and catalytic reactivity.<sup>[10,24,37]</sup> However, on closer investigations, these applications already insinuate a fundamental problem of nanoparticles for biomedicine: the enhanced reactivity of nanoparticles, which is desirable for catalytic applications, is inextricably linked to unintended, harmful effects in biological systems.<sup>[348]</sup> Recent advances in knowledge and the wide field of potential applications make it necessary to identify general principles of interaction between nanoparticle design, including shape, surface, charge, and composition, and the resulting effects on internalization and cell metabolism.

The analysis of the solid-liquid interface is a key challenge in bio-nano-research, as it is subjected to dynamic changes. When nanoparticles come into contact with body fluids, a variety of serum components binds to the surface of the nanoparticles, and the composition of this so-called protein corona determines the fate of the nanoparticles in the organism.<sup>[349–351]</sup> Hence, specific or non-specific membrane interactions, receptor-mediated binding, and membrane

wrapping occur upon interaction of cells with nanoparticles. Further, the formation of a protein corona might induce structural and functional changes, oxidant injury and transfer of free energy to biomolecules, or damage the mitochondrial and lysosomal activity. Thus, the whole cell would be damaged due to a decreased ATP level.<sup>[265]</sup> Conversely, the coating of nanoparticles with proteins was demonstrated to cause conformational changes, exposure of new epitopes, and altered functions. The various effects resulting from dynamic interactions at the nano-bio interface are displayed in Figure 7.1. The formation of the protein corona is a dynamic process starting with spontaneous protein accumulation on the nanoparticles' surface. The initial corona is composed of highly abundant proteins, which are then replaced by proteins showing a higher affinity for the nanoparticles' surface in a process known as the Vroman's effect.<sup>[352]</sup> Continuous substitution of adsorbed proteins leads to a "hard corona" of barely exchanging, tightly bound proteins and an outer, weakly adsorbed "soft corona".<sup>[353–355]</sup> The typical lifetime of the hard protein corona was determined to be several hours. This duration is sufficiently long for many biological phenomena.<sup>[350,356]</sup> Beyond dispute, the protein corona plays a substantial role in shaping the surface functionalities for distinct applications, as the addressed cells will interact with the protein corona rather than a previously introduced synthetic surface coating. Furthermore, the corona was ascribed to be important for the *in vivo* organ distribution and clearance from circulation. Up to now, the formation and the composition of the protein corona are far from being understood, but their importance is obvious for any further application of nanoparticles in *theranostics*.<sup>[349]</sup>

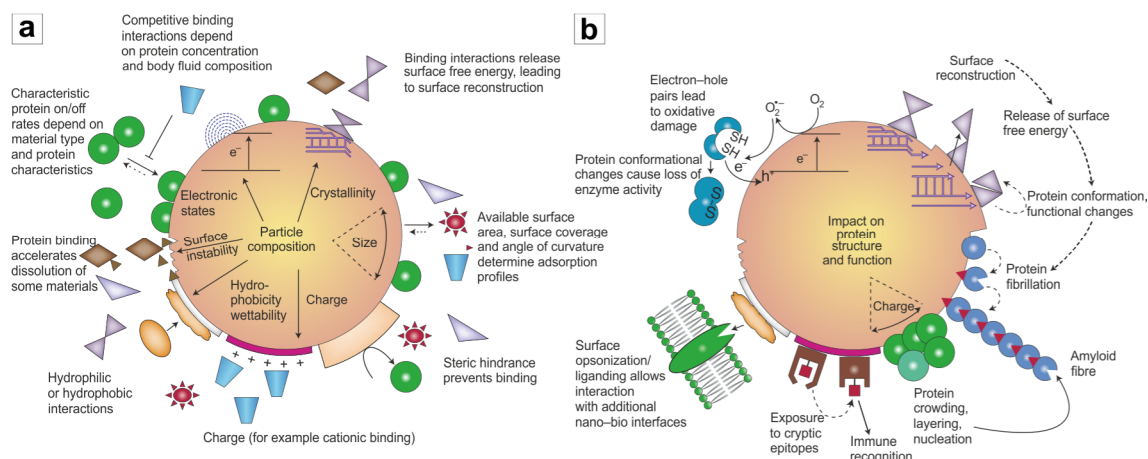


Figure 7.1: Effects of the protein corona surrounding a nanoparticle. The corona forms immediately upon first contact with biological medium, though the composition changes continuously. On the one hand, it determines the fate of a nanoparticle, and on the other hand, it can cause severe effects on the interactive proteins. a) The intrinsic particle characteristics contribute to the constitution and formation of the corona, b) while interaction with proteins can also affect the protein structure and function, leading to a potential contribution to disease pathogenesis. Adopted from Nel and co-workers.<sup>[265]</sup>

The large surface of nanoparticles enhances their contact area with the surrounding medium over that of bulk material of the same mass, leading to increased chemical reactivity. This activity, desired for catalytic applications, evolves into unintended, harmful reactivity *in vivo*, which is the subject of an emerging research area, known as nano-toxicology.

Aside from using supported metal nanoparticles as catalysts, Kotov suggested their use as protein mimics. Nanoparticles resemble in their size, charge, as well as shape and, thus, the interactions with the surrounding medium, proteins, and cells are suggested to be closely related. Current research focuses on the molecular engineering of the nanoparticle surface to realize functions known to be crucial for the operation of proteins. Furthermore, a variety of nanoparticles has been demonstrated to exhibit enzyme-like behavior. Not only the core material, but also the surface functionalization was shown to enable the use as enzyme mimics, or so-called nanozymes.<sup>[357]</sup> Moreover, the formation of hetero-nanoparticles is a well-known alternative for synthetic tuning of catalytic properties, interfacial activation, and enhanced performance as reported amongst others for Ag@Fe<sub>3</sub>O<sub>4</sub>,<sup>[167,358]</sup> Au@Fe<sub>3</sub>O<sub>4</sub>,<sup>[11,214]</sup> Pt@Fe<sub>3</sub>O<sub>4</sub>,<sup>[24]</sup> Pd@Fe<sub>3</sub>O<sub>4</sub>,<sup>[162]</sup> Ni@Fe<sub>2</sub>O<sub>3</sub>,<sup>[158]</sup> Au@TiO<sub>2</sub>,<sup>[210]</sup> and Au@ZnO.<sup>[25]</sup>

Janus nanoparticles are interesting candidates in view of the increased demand for nanoparticles with multiple imaging capabilities<sup>[193–195,231]</sup> (see Chapter 6) and their distinct features, allowing the combination of imaging and therapeutic applications.<sup>[28,196,359]</sup> Considering that spherical MnO and Fe<sub>3</sub>O<sub>4</sub> nanoparticles have been successfully used *in vivo* after intravenous applications for imaging purposes,<sup>[46,336,360]</sup> asymmetric Janus particles made up of the same materials are predicted to exhibit a similar biocompatibility in living organisms. However, detailed data on their cytotoxicity in human cells are missing. So far, experiments assessing the impact of heterodimer nanoparticles on cells after only a short exposure were reported.<sup>[54,163]</sup>

Within the scope of this work, we investigated the interactions of Janus particles composed of Au, Pt, MnO, and Fe<sub>3</sub>O<sub>4</sub> with biological media and their biocompatibility against the background of their enzyme-like catalytic activity. To the best of our knowledge, this study represents the first analysis of the protein corona of Janus particles incubated with human blood plasma. Label-free liquid chromatography mass spectrometry enabled the quantitative analysis of its composition. Janus particles were tested regarding their activity as enzyme mimics, in this particular case for peroxidase reactions, in order to understand the chemical processes involved in biological responses. These results will help to distinguish between the intrinsic and extrinsic effects of nanoparticles on biological systems, and thus, to design nanoparticles with optimized properties concerning chemical stability and biocompatibility. *In vitro* experiments on human cancer as well as endothelial cells were performed, comparing Janus particles of different surface functionalization, domain size, and composition to their spherical counterparts. The multifactorial approach presented in this study can be taken as the first step toward unraveling the complexity of Janus particles at the nano-bio interface.

## 7.2 Protein Corona of Janus Particles

This project was done in collaboration with [REDACTED] and [REDACTED], University Hospital, Johannes Gutenberg University, Mainz. Material synthesis and chemical characterization were performed at the Johannes Gutenberg University, Mainz.

The majority of biomedical nanoparticle applications requires intravenous injection. That is why we analyzed the protein corona of nanoparticles when incubated with human blood plasma. Interactions of nanoparticles with cells will be distinctly influenced by the protein corona surrounding nanoparticles. The composition of the protein corona is in turn dependent on the intrinsic characteristics of the nanoparticles, such that it can be considered a fingerprint of the nanoparticles.<sup>[354]</sup> Therefore, nanoparticles differing with respect to their core materials, morphology, and surface functionalization were incubated for different time intervals with blood plasma. After extensive washing to remove loosely attached proteins, the so-called soft corona, and subsequent elution of the hard protein corona from the nanoparticles, trypsin was used for proteolysis. Label-free liquid chromatography mass spectrometry (LC-MS) enabled the not only qualitative, but also sensitive quantitative analysis of the hard protein corona. By doing so, 96 proteins were reliably detected and quantified. The results were confirmed by measuring three technical replicates, which showed a high correlation coefficient ( $R^2 \geq 0.99$ ). Figure 7.2 displays the compositional analysis of the hard protein corona of isotropic  $\text{Fe}_3\text{O}_4@ \text{SiO}_2$  and  $\text{MnO}@ \text{SiO}_2$  nanoparticles as well as anisotropic  $\text{Au}@ \text{MnO}@ \text{SiO}_2$  Janus particles. The analysis of the protein corona of nanoparticles revealed that the binding profiles did not reflect the relative protein concentrations of the plasma. Irrespective of the core material and particle morphology, a significant enrichment with lipoproteins and proteins involved in coagulation as compared to plasma levels was measured. In contrast, the analysis revealed a lower level of tissue leakage proteins, a group of proteins with potential disease-relevant functions.

Aside from these qualitative trends independent of the particle characteristics, the actual percentage composition was dependent on (i) core materials of isotropic nanoparticles, (ii) the particle morphology, and (iii) the incubation time. Interestingly, there was a significant and unexpected difference in the composition of the protein corona of isotropic silica-encapsulated  $\text{MnO}$  and  $\text{Fe}_3\text{O}_4$  nanoparticles. Compared to the protein amount in plasma, both  $\text{Fe}_3\text{O}_4@ \text{SiO}_2$  and  $\text{MnO}@ \text{SiO}_2$  particles showed an enrichment with immunoglobulins in their protein corona, which was even more pronounced for  $\text{Fe}_3\text{O}_4@ \text{SiO}_2$  nanoparticles. Further, the low affinity for acute phase response proteins, which were present in high amounts in the plasma, was observed to be a common feature. However, the percentage composition of the corona differed concerning complement binding proteins, coagulation, and lipoproteins. Recently, it was found that small variations in size and surface functionalization of silica particles are sufficient to drastically change the affinity for peptides when studying the protein corona.<sup>[361–363]</sup> This



suggests that slight structural differences of the silica shell of MnO and Fe<sub>3</sub>O<sub>4</sub> nanoparticles due to the underlying nanoparticles led to significant changes in protein interaction. Further investigations are underway to confirm these observations.

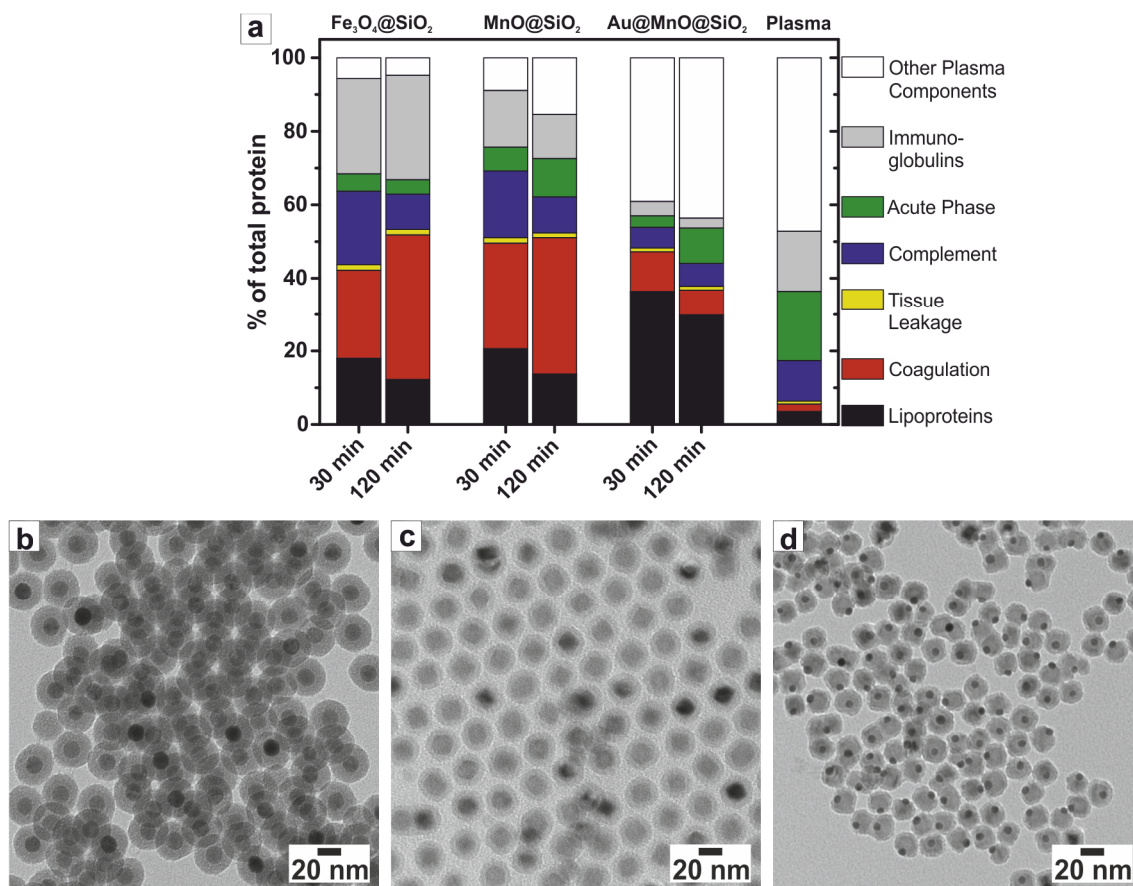


Figure 7.2: a) Label-free LC-MS analysis of the hard protein corona of Fe<sub>3</sub>O<sub>4</sub>@SiO<sub>2</sub>, MnO@SiO<sub>2</sub>, and Au@MnO@SiO<sub>2</sub> nanoparticles showing a dependence on composition, morphology, and also incubation time. The measurements were performed by [redacted]. b) - d) Corresponding TEM images of Fe<sub>3</sub>O<sub>4</sub>@SiO<sub>2</sub> (16.1 ± 0.9 nm), MnO@SiO<sub>2</sub> (19.2 ± 1.6 nm), and Au@MnO@SiO<sub>2</sub> (8.6 ± 0.6 @ 19.0 ± 1.9 nm), respectively.

Introducing another variable, the anisotropy of Janus particles, further increased the complexity of the protein corona. The amphiphilic Janus character was reflected in a specific protein adsorption pattern: it showed a distinct enrichment with lipoproteins and other plasma components as compared to the isotropic analogues. This was ascribed to the affinity of the 1-octadecanethiol-capped Au-domains of the Janus particles for proteins with increased hydrophobicity. Likewise, Cedervall and co-workers observed the preferential binding of apolipoproteins and serum albumin to hydrophobic nanoparticles.<sup>[364]</sup>

Aside from the core material or the morphology of the nanoparticles, incubation time was observed to be a crucial parameter for the composition of the protein corona.<sup>[355,365]</sup> This reflected the dynamic nature of the protein corona and suggested continuous changes to be a result of the adjustment of the equilibrium between protein adsorption and desorption for distinct binding constants and affinities. For instance, the percentage composition of the protein corona of Au@MnO@SiO<sub>2</sub> Janus particles showed barely any changes for proteins involved in

complement activation and tissue leakage after 30 minutes and 2 hours, whereas lipoproteins and acute phase response proteins were significantly enriched. As a consequence thereof, the proportion of bound lipoproteins, immunoglobulins, and proteins involved in coagulation was decreased.

These initial results implied an enormous complexity of the mechanism to be behind the formation and composition of the protein corona. This became even more obvious for Janus particles, which are of particular interest for biomedical applications. That is why further investigations on the early stages of the formation of the protein corona are the subject of our current research. The interplay of colloidal chemistry and biological interfaces constitutes a collective process, whose importance has been acknowledged for many years, even though it is still a long way from being understood.

### 7.3 Janus Particles as Enzyme Mimics

Recently, Au nanoparticles have been demonstrated to exhibit enzyme-like activity based on the catalytic activity of the functional groups attached to their surface. Tailored functionalization enabled their use in replacing enzymes such as nuclease,<sup>[366,367]</sup> esterase,<sup>[368]</sup> or silicatein.<sup>[369]</sup> For instance, the separate functionalization of Au nanoparticles with hydrogen-bonding and nucleophilic patches recreated the active site of silicatein.<sup>[369]</sup> In contrast to the catalytic activity of attached functional groups, Au nanoparticles themselves have been observed to reveal extraordinary catalytic characteristics, which are not observed for bulk material.<sup>[370]</sup> The intrinsic catalytic activity was ascribed to the Au core, which was evidenced by mimicking glucose oxidase,<sup>[371–373]</sup> catalase,<sup>[374]</sup> superoxide dismutase,<sup>[374]</sup> and peroxidase.<sup>[375,376]</sup>

Since the discovery of Fenton's reagent in 1876,<sup>[377,378]</sup> which is just a solution containing  $\text{Fe}^{2+}/\text{Fe}^{3+}$  ions, iron has been known for its peroxidase-like activity. Moreover,  $\text{Fe}_3\text{O}_4$  nanoparticles are subject to ongoing research, as they revealed a higher activity than horseradish peroxidase, a natural enzyme frequently used for these studies. Here, the co-presence of  $\text{Fe}^{2+}$  and  $\text{Fe}^{3+}$  at their surface was found to be vital.<sup>[379]</sup> Aside from  $\text{Fe}_3\text{O}_4$ , many nanoparticles composed of redox-active transition metal oxides including  $\text{V}_2\text{O}_5$ ,  $\text{Fe}_2\text{O}_3$ , and  $\text{MnO}$  were demonstrated to possess intrinsic peroxidase-like activity. Peroxidases are an important class of enzymes, as they catalyze the oxidation of any substrate while reducing peroxides, in most cases hydrogen peroxide. Common to many natural peroxidases is a heme prosthetic group, where  $\text{Fe}^{3+}$  usually acts as the co-factor, even though manganese- and vanadium-based enzymes have also been reported.<sup>[348]</sup> Several substrates have been established in order to colorimetrically analyze peroxidase-like enzyme mimics of nanoparticles including 2,2'-azino-bis(3-ethylbenzothiazoline-6-sulfonic acid) (ABTS), diazaminobenzene (DAB), *o*-phenylenediamine (OPD), and 3,3',5,5'-tetramethylbenzidine (TMB), which was chosen for this study. The

progressive oxidation of TMB by hydrogen peroxide takes place as a two-step electron transfer reaction. TMB is advantageous for analysis, as not only the formation of the yellow diimine, but also the blue intermediate charge-transfer complex can be monitored by UV-VIS spectroscopy (Figure 7.3). The charge-transfer complex is composed of the parent diamine and the emerging diimine and exists in fast equilibrium with the radical cation.<sup>[380]</sup> Its absorption is commonly measured to determine the oxidation of TMB, as it is the first oxidation product and, thus, more sensitive than the formation of the completely oxidized diimine.

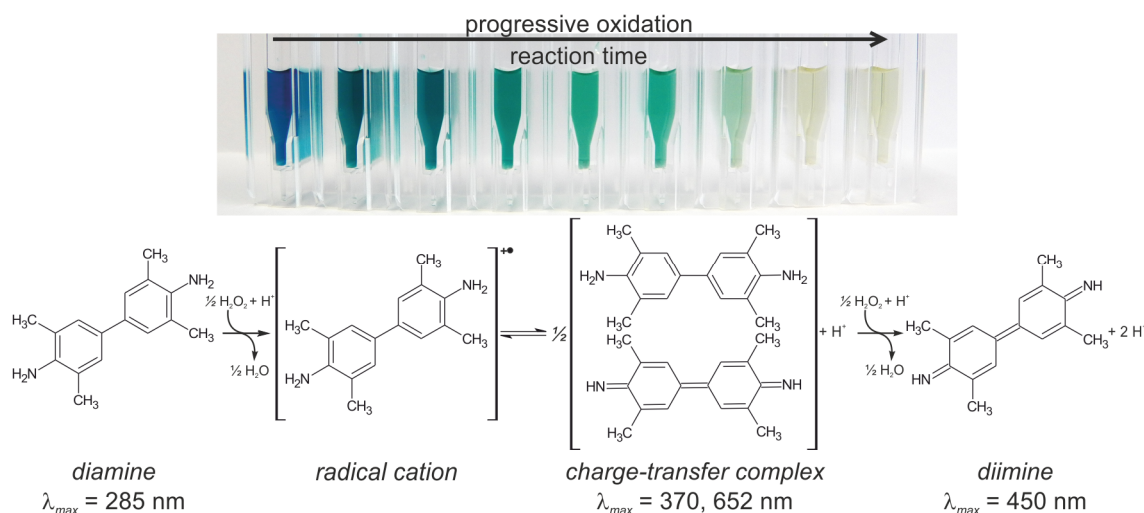


Figure 7.3: Picture of progressively oxidized 3,3',5,5'-tetramethylbenzidine (top) and corresponding reaction scheme (bottom). The first colored product is the blue charge-transfer complex, which is in fast equilibrium with the radical cation; complete oxidation by  $\text{H}_2\text{O}_2$  leads to the yellow diimine.<sup>[380]</sup>

### 7.3.1 Peroxidase-Like Activity of $\text{M}@\text{Fe}_3\text{O}_4$ Janus Particles

Recently, Gao *et al.* reported a comprehensive study of the peroxidase-like activity of  $\text{Fe}_3\text{O}_4$  nanoparticles. The reaction parameters were optimized with regard to  $pH$ , substrate concentration,  $\text{H}_2\text{O}_2$  concentration, and temperature.<sup>[379]</sup> According to this investigation, the peroxidase-like activity of Janus particles was analyzed in order to conceive the impact of the co-presence and interaction of two inextricably linked catalytically-active materials. First, the chemical stability was analyzed, as the degradation of transition metal oxide nanoparticles releases redox-active ions, which are known to exhibit peroxidase-like activity themselves. As discussed earlier (see Chapter 4.2.2),  $\text{Au}@\text{Fe}_3\text{O}_4@\text{SiO}_2$  were observed to be chemically stable over a wide  $pH$  range, as detected by TEM. Here, we confirmed the stability of the investigated nanoparticles by incubation with the substrate, TMB, at  $pH = 3.7$ . Figure 7.4a displays the stability of  $\text{Fe}_3\text{O}_4@\text{SiO}_2$  as well as  $\text{Au}@\text{Fe}_3\text{O}_4@\text{SiO}_2$ , as indicated by the constancy of the absorption observed at 652 nm over a period of 10 minutes. In the case of degradation of the nanoparticles, the release of  $\text{Fe}^{2+}/\text{Fe}^{3+}$  ions would have caused a peroxidase-like activity, resulting in an increased absorption. Upon addition of hydrogen peroxide as substrate, the nanoparticles showed a significantly increased oxidation of TMB. In fact, a ca 15-fold higher

concentration of  $\text{H}_2\text{O}_2$  was needed for the maximal reactivity of  $\text{Fe}_3\text{O}_4@\text{SiO}_2$  as compared to  $\text{Au}@\text{Fe}_3\text{O}_4@\text{SiO}_2$  nanoparticles. As a first result, this already indicated an enormous impact of the Janus character on the activity, which might be due to the intrinsic peroxidase-like activity of Au nanoparticles or the interfacial activation of at least one of the two components. The reaction in the absence of nanoparticles was negligible (Figure 7.4b).

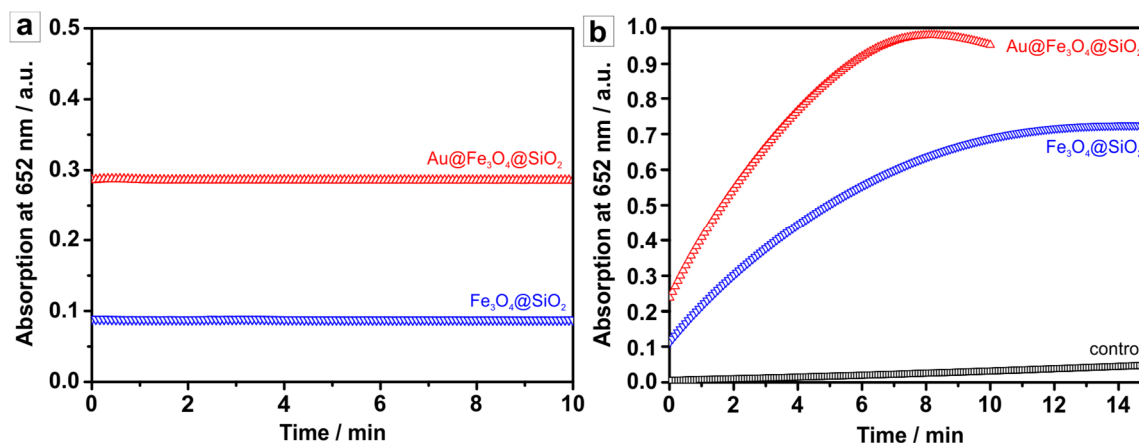


Figure 7.4: Absorption measurements revealing the catalytic activity to not be caused by degradation of nanoparticles. a) The nanoparticles were stable in acetate buffer over a range of 10 min; b)  $\text{Au}@\text{Fe}_3\text{O}_4@\text{SiO}_2$  Janus particles showed a higher peroxidase-like activity than spherical  $\text{Fe}_3\text{O}_4@\text{SiO}_2$  nanoparticles under the same conditions. The oxidation of TMB by  $\text{H}_2\text{O}_2$  without nanoparticles was negligible. Here, 100  $\mu\text{M}$  TMB and 20  $\mu\text{g}$  nanoparticles were dissolved in 1 mL acetate buffer,  $\text{pH} = 3.7$ ; for activity measurements, the concentration of  $\text{H}_2\text{O}_2$  was 500 mM for  $\text{Fe}_3\text{O}_4@\text{SiO}_2$  and 28.5 mM for  $\text{Au}@\text{Fe}_3\text{O}_4@\text{SiO}_2$ . The measurements were performed by [REDACTED].

Further, the reactions were monitored by scanning kinetics. Figure 7.5a shows the temporal evolution of the oxidation products of TMB catalyzed by  $\text{Fe}_3\text{O}_4@\text{SiO}_2$  nanoparticles, whereby the spectral intensity increased gradually for the charge-transfer complex, measured at 370 nm and 652 nm as well as for the diimine at 450 nm. This indicated an equilibrium of the partially and completely oxidized species. The higher sensitivity afforded by measuring the absorption at 652 nm became obvious when comparing its significantly higher spectral intensity to the absorption band at 450 nm. In contrast, the oxidation in the presence of  $\text{Au}@\text{Fe}_3\text{O}_4@\text{SiO}_2$  nanoparticles with a decreased amount of  $\text{H}_2\text{O}_2$  showed only an increase in spectral intensity for all three products within the first 2 minutes (Figure 7.5b). Subsequently, the absorption of the diimine at 450 nm increased further at the expense of the intermediate complex. This confirmed the initial observation of an accelerated reaction of the Janus particles, as they promoted the complete oxidation of TMB, even at significantly lower  $\text{H}_2\text{O}_2$  concentrations.

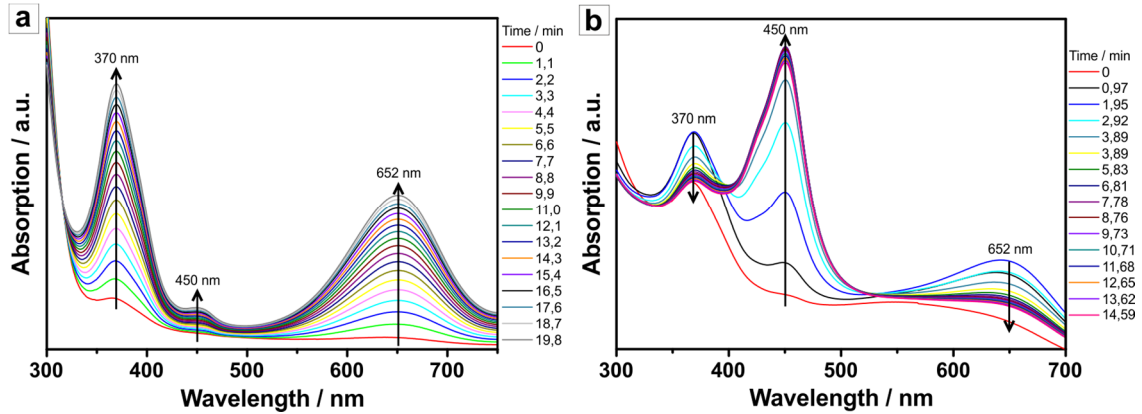


Figure 7.5: Time-resolved UV-VIS spectra of the oxidation of TMB in the presence of  $\text{H}_2\text{O}_2$  and  $\text{Fe}_3\text{O}_4$ -based nanoparticles. The reaction mixture contained  $100 \mu\text{M}$  TMB,  $525 \text{ mM}$   $\text{H}_2\text{O}_2$ , and  $20 \mu\text{g}$  nanoparticles in  $1 \text{ mL}$  acetate buffer,  $\text{pH} = 3.7$ . a) Arrows indicate the increased absorption of all three observable species induced by  $\text{Fe}_3\text{O}_4@SiO_2$  nanoparticles; b) for  $Au@Fe_3O_4@SiO_2$  Janus particles, only the peak at  $450 \text{ nm}$  increased continuously over time, whereas the absorption bands at  $370 \text{ nm}$  and  $652 \text{ nm}$  started to decrease again after  $2 \text{ min}$ . The measurements were performed by [REDACTED].

In order to determine the mechanism of catalysis, the activity was measured as a function of the substrate concentration. With lower TMB concentrations, the substrate was used up and converted on to the final oxidized diimine product, which was observable by the color of the solution: high concentrations of TMB, above  $200 \mu\text{M}$ , turned blue, midrange concentrations ranging from  $75 \mu\text{M}$  to  $150 \mu\text{M}$  were green, while lower concentrations became yellow. The green color emerged due to the co-presence of the blue charge-transfer complex and the yellow product. Figure 7.6 displays the reaction velocity as a function of the concentration of TMB. Hereby, especially for low concentrations in the presence of  $Au@Fe_3O_4@SiO_2$ , the absorption declined after an initial increase. This was due to the fast oxidation to the completely oxidized diimine, such that the intermediate complex was only present within the first minutes, as was already seen in Figure 7.5b.

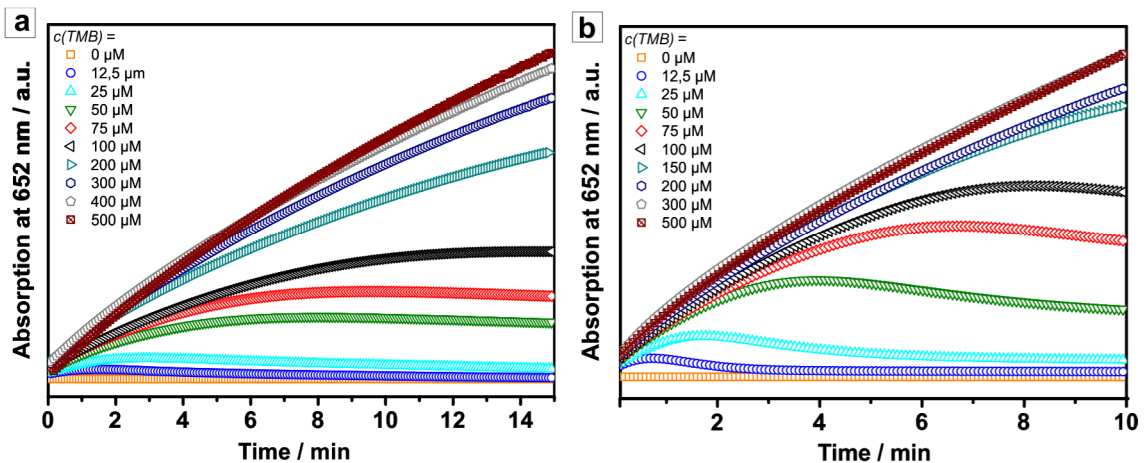


Figure 7.6: The reaction velocity as a function of the substrate concentration was monitored by UV-VIS spectroscopy. a)  $20 \mu\text{g}$   $Fe_3O_4@SiO_2$  dispersed in  $1 \text{ mL}$  acetate buffer,  $\text{pH} = 3.7$ ,  $500 \text{ mM}$   $\text{H}_2\text{O}_2$  and b)  $20 \mu\text{g}$   $Au@Fe_3O_4@SiO_2$  dispersed in  $1 \text{ mL}$  acetate buffer,  $\text{pH} = 3.7$ ,  $28.5 \text{ mM}$   $\text{H}_2\text{O}_2$  were used. The measurements were performed by [REDACTED].

The reaction velocity was calculated from the slope of the curves within the first 30 seconds of each measurement shown in Figure 7.6, and is displayed in Figure 7.7a as

function of the TMB concentration and in Figure 7.7b as a Lineweaver-Burk plot. Both types of nanoparticles, spherical and Janus particles, showed Michaelis-Menten behavior in the tested range of  $\text{H}_2\text{O}_2$  and TMB. The data were fitted according to this model to obtain the kinetic parameters displayed in Table 7.1. This analysis confirmed the higher activity of  $\text{Au@Fe}_3\text{O}_4\text{@SiO}_2$  nanoparticles as compared to  $\text{Fe}_3\text{O}_4\text{@SiO}_2$ .

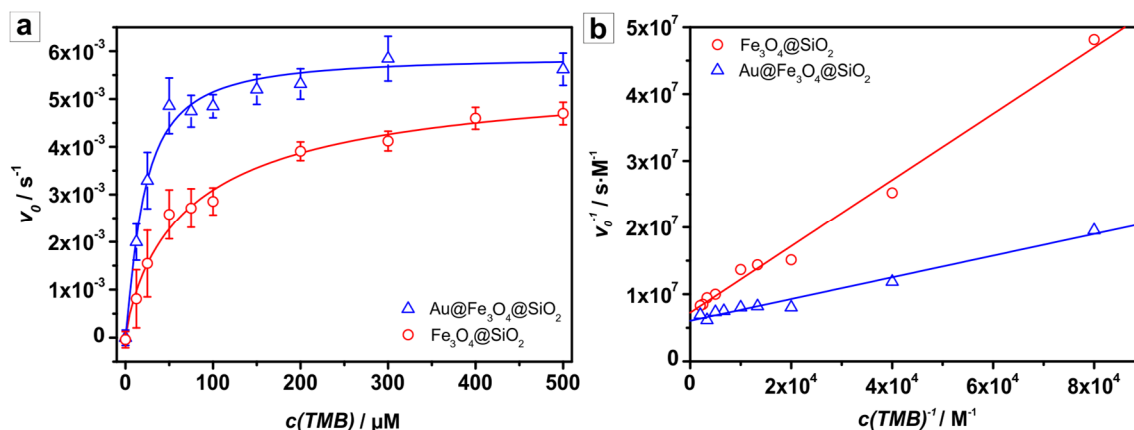


Figure 7.7: Steady-state kinetic assay of  $\text{Au@Fe}_3\text{O}_4\text{@SiO}_2$  and  $\text{Fe}_3\text{O}_4\text{@SiO}_2$  nanoparticles. a) Hill plot and b) Lineweaver-Burk plot of the activity at a fixed concentration of  $\text{Fe}_3\text{O}_4\text{@SiO}_2$  and  $\text{Au@Fe}_3\text{O}_4\text{@SiO}_2$  nanoparticles with varying substrate concentration. The concentration of  $\text{H}_2\text{O}_2$  was 500 mM for  $\text{Fe}_3\text{O}_4\text{@SiO}_2$  and 28.5 mM for  $\text{Au@Fe}_3\text{O}_4\text{@SiO}_2$ . The measurements were performed by [REDACTED].

Moreover, in comparison to literature data on  $\text{Fe}_3\text{O}_4$  nanoparticles, the apparent Michaelis constants  $K_m$  of both types of nanoparticles were lower, actually by a factor of ca 3.7 for  $\text{Au@Fe}_3\text{O}_4\text{@SiO}_2$  Janus particles. Thus, these nanoparticles showed the highest affinity to TMB, as  $K_m$  is the substrate concentration at which the reaction reaches half of the maximum reaction velocity  $v_{max}$ . The maximum reaction velocity was significantly increased in comparison to literature data, but on the same order of magnitude for the tested nanoparticles.<sup>[379]</sup> Wang *et al.* reported the impact of surface charge on the affinity of Au nanoparticles to peroxidase substrates.<sup>[375]</sup> For the silica-coated nanoparticles, a negative surface charge was determined (see Chapter 4.2.2), caused by the presence of deprotonated  $-\text{Si-O}^-$  groups. As TMB is positively charged at the standard reaction conditions, the negatively charged nanoparticles were electrostatically attracted to the reaction substrate TMB, which was reflected by the high affinity. However, the comparison to literature data could not be completed, as Gao *et al.* specified neither the size nor the surface modification of the  $\text{Fe}_3\text{O}_4$  nanoparticles used for their pioneering work of nanoparticles as peroxidase mimics.<sup>[379]</sup> *Prima facie*, the activity of  $\text{Fe}_3\text{O}_4\text{@SiO}_2$  was unexpectedly high, as the  $\text{SiO}_2$  shell inhibited direct contact of the peroxidase substrate TMB and the  $\text{Fe}_3\text{O}_4$  core. However, as the amorphous silica shell is porous to a certain degree, the interaction with the surrounding medium is not as efficiently inhibited as estimated from the core/shell structure.

Table 7.1: Comparison of the steady-state kinetic parameter of  $\text{Fe}_3\text{O}_4@\text{SiO}_2$  and  $\text{Au}@\text{Fe}_3\text{O}_4@\text{SiO}_2$  nanoparticles and literature data of  $\text{Fe}_3\text{O}_4$  nanoparticles.<sup>[379]</sup>  $K_m$  is the Michaelis constant and  $v_{max}$  the maximal reaction velocity.

	Substrate	$K_m / \text{mM}$	$v_{max} / \text{M}\cdot\text{s}^{-1}$
$\text{Fe}_3\text{O}_4$ <sup>[379]</sup>	TMB	0.098	$3.44 \cdot 10^{-8}$
$\text{Fe}_3\text{O}_4@\text{SiO}_2$	TMB	0.071	$1.43 \cdot 10^{-7}$
$\text{Au}@\text{Fe}_3\text{O}_4@\text{SiO}_2$	TMB	0.027	$1.67 \cdot 10^{-7}$

Several reports highlight synergistic effects for the enhanced catalytic activity of heterodimers as compared to single component nanoparticles. Recently,  $\text{PtPd}@\text{Fe}_3\text{O}_4$  heterodimer nanoparticles were demonstrated to have an even higher peroxidase activity than horseradish peroxidase, a natural enzyme frequently used in these studies.<sup>[381]</sup> However, the obtained data for  $\text{Au}@\text{Fe}_3\text{O}_4@\text{SiO}_2$  heterodimer nanoparticles also showed a stronger affinity and higher reaction velocity than was reported for  $\text{PtPd}@\text{Fe}_3\text{O}_4$  nanoparticles. Thus, we examined the impact of the chemical composition as well as the size of the metal domain of  $\text{Fe}_3\text{O}_4$ -based heterodimer nanoparticles. Figure 7.8a displays pictures of initial results of TMB tests. An increased activity of heterodimer nanoparticles as compared to  $\text{Fe}_3\text{O}_4@\text{SiO}_2$  nanoparticles was evident for all investigated chemical compositions. It was apparent from the color of the reaction mixture after 5 minutes of incubation that  $\text{AuPt}@\text{Fe}_3\text{O}_4@\text{SiO}_2$  heterodimer nanoparticles showed the highest affinity and reaction velocity. The green color indicated the co-presence of the yellow diimine, the final reaction product, and the blue intermediate charge-transfer complex. This was confirmed by scanning kinetic measurements, where the absorption was maximal after 2.5 minutes and decreased again afterwards due to the progressive oxidation. More precisely, distinct differences were observed upon variation of the metal domain (Figure 7.8b and c). Aside from the increase in activity for AuPt domains over Au, the enlargement of the metal domain was beneficial with reference to  $\text{Au}@\text{Fe}_3\text{O}_4$  nanoparticles. This was ascribed to a larger metal surface area being able to contribute to the heterogeneous catalysis. Surprisingly, the reaction velocity of  $\text{Au}@\text{AuPt}@\text{Fe}_3\text{O}_4$  nanoparticles was lowered as compared to  $\text{AuPt}@\text{Fe}_3\text{O}_4$  heterodimers.

Here,  $\text{M}@\text{Fe}_3\text{O}_4@\text{SiO}_2$  ( $\text{M} = \text{Au}, \text{AuPt}, \text{Au}@\text{Au}, \text{Au}@\text{AuPt}$ ) hetero-nanoparticles were demonstrated to possess a significantly higher affinity for TMB as peroxidase substrate and a higher catalytic activity than spherical  $\text{Fe}_3\text{O}_4@\text{SiO}_2$  nanoparticles and the natural enzyme, horseradish peroxidase. However, this obvious enhancement could be caused by independent contributions, which are (i) the interfacial communication between the domains and (ii) the presence of metal nanoparticles. These are known for their intrinsic peroxidase-like activity, which was demonstrated to be highly dependent on the surface functionalization.<sup>[374–376]</sup>

Therefore, a differentiation between the two possible contributions could not be provided by peroxidase-like activity tests of individual Au nanoparticles. As the surface of the Au domains within Janus particles was hydrophobic, a ligand exchange would have been necessary in order to perform the tests in aqueous solution, which could have an even higher impact on the activity of the Au particles. For this reason, a comparison to kinetic parameter of Au nanoparticles reported in literature is of relatively little informative value. Nevertheless, a dependence of the catalytic activity on the composition as well as the size of the metal domain was observed. The enlargement of the Au domain of Au@Au@Fe<sub>3</sub>O<sub>4</sub> in comparison to Au@Fe<sub>3</sub>O<sub>4</sub> nanoparticles increased the catalytic activity due to the larger surface area of the Au domain. Furthermore, the exchange of the Au domain with an alloy AuPt nanoparticle boosted the reaction velocity, which had already been observed in the context of heterogeneous catalysis, for instance electro-catalysis,<sup>[93]</sup> CO oxidation,<sup>[150]</sup> and methanol oxidation.<sup>[382]</sup> These results regarding peroxidase-like activity of Au@AuPt@Fe<sub>3</sub>O<sub>4</sub> hetero-nanoparticles showed the competition of interdependent parameters: a higher affinity for TMB than Au@Au@Fe<sub>3</sub>O<sub>4</sub> was determined to be a result of the alloy domain, though their activity was lower than that of AuPt@Fe<sub>3</sub>O<sub>4</sub> heterodimer nanoparticles, as the surface of the more active AuPt nanoparticles was partially covered by the second metal domain.

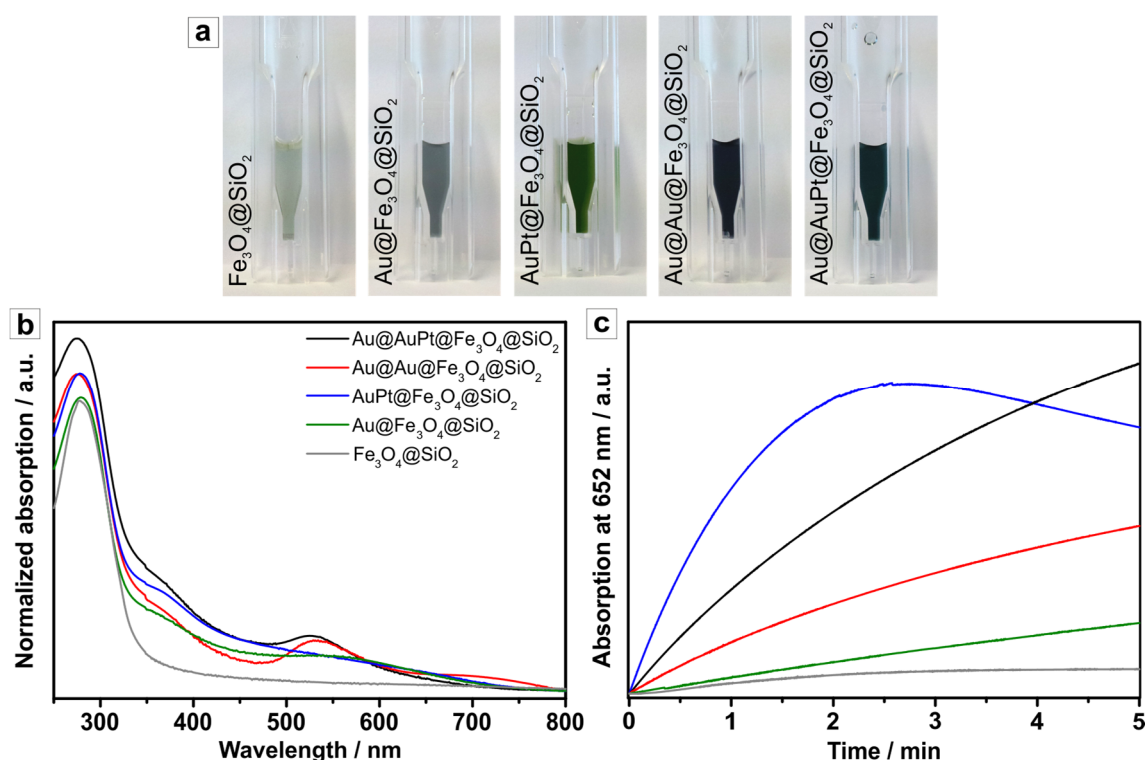


Figure 7.8: Comparison of peroxidase-like activity of Fe<sub>3</sub>O<sub>4</sub>@SiO<sub>2</sub>-based nanoparticles with different chemical compositions. a) Pictures taken from reaction mixtures and b) corresponding UV-VIS spectra of reaction mixtures 5 min after the incubation of 100  $\mu$ M TMB, 5 mM H<sub>2</sub>O<sub>2</sub>, and 10  $\mu$ g nanoparticles in 0.5 mL acetate buffer, pH = 3.7; c) attendant scans of the peroxidase-like activity over a period of 5 min. The study was performed by [REDACTED].



To conclude, we demonstrated the catalytic activity to depend on (i) the morphology, (ii) chemical composition, as well as (iii) size of the metal domain. Therefore, an interplay of the intrinsic catalytic activity and the interfacial activation of at least one of the two domains is suggested to be responsible for the significantly enhanced reactivity of  $\text{Fe}_3\text{O}_4$ -based Janus particles, while this aspect is subject to further investigation.

### 7.3.2 Peroxidase-Like Activity of $\text{M@MnO}$ Janus Particles

In contrast to the peroxidase-like activity of  $\text{Au@Fe}_3\text{O}_4\text{@SiO}_2$  and related nanoparticles, which was caused by the intrinsic activity of the nanoparticle cores, a different mechanism had to be considered in the case of MnO-containing Janus or nanoparticles. As was discussed in Chapter 4,  $\text{Au@MnO@SiO}_2$  nanoparticles were prone to comparably fast degradation at low  $\text{pH}$ . This is of significant importance for biomedical applications as similar conditions are found in intracellular compartments, such as lysosomes or autophagosomes. Upon incubation of  $\text{Au@MnO@SiO}_2$  Janus particles with TMB in acetate buffer in the absence of  $\text{H}_2\text{O}_2$ , an immediate reaction was observed. The solution turned dark blue due to the formation of the partially oxidized charge-transfer complex (Figure 7.9a).

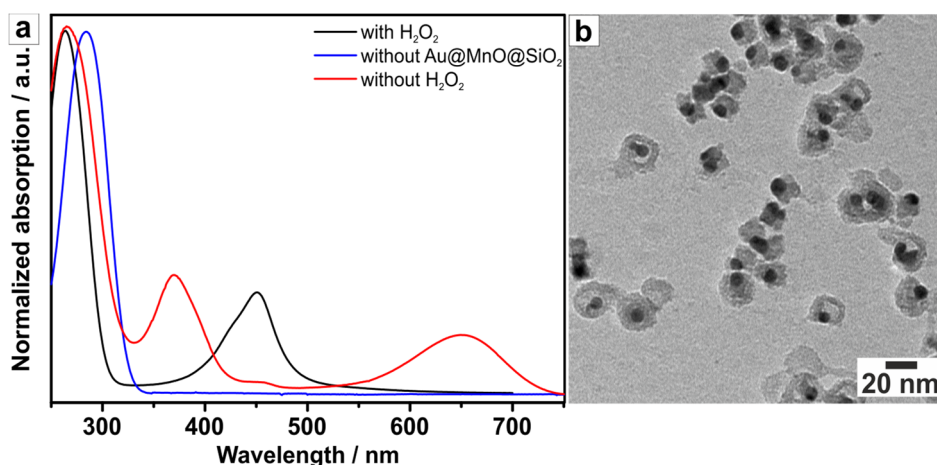


Figure 7.9: a) UV-VIS spectra of  $5 \mu\text{g}$   $\text{Au@MnO@SiO}_2$  nanoparticles incubated with  $50 \mu\text{M}$  TMB w/o  $1 \text{ mM}$   $\text{H}_2\text{O}_2$  in  $1 \text{ mL}$  acetate buffer,  $\text{pH} = 3.7$ , and a control reaction without nanoparticles; b) corresponding TEM image of  $\text{Au@MnO@SiO}_2$  Janus particles incubated with TMB in absence of  $\text{H}_2\text{O}_2$ . The UV-VIS spectra were measured by [REDACTED].

In the presence of  $\text{H}_2\text{O}_2$ , the solution turned yellow without any temporary appearance of the blue intermediate, which was reflected by the single absorption band at  $450 \text{ nm}$  instead of the triplet at  $370 \text{ nm}$ ,  $450 \text{ nm}$ , and  $652 \text{ nm}$ . The reaction could not be slowed down by increasing  $\text{pH}$  or adjusting the substrate concentration, so that the determination of steady-state kinetics was not possible. TEM revealed the reaction conditions to induce the degradation of the MnO domains (Figure 7.9b). Thus, the observed effects were due  $\text{Mn}^{2+}$  ions, which are known to cause peroxidase-like reactions.

Surprisingly, the order of substrate addition was crucial for the reaction findings. The prompt oxidation was hindered when the nanoparticles were incubated with  $\text{H}_2\text{O}_2$  prior to the

addition of TMB. This suggested a reaction of  $Mn^{2+}$  with  $H_2O_2$ . This became even more pronounced for hetero-nanoparticles, whose metal domain has been enlarged by subsequent overgrowth of Au (Figure 7.10a). For  $Au@Au@MnO@SiO_2$  particles, the UV-VIS spectra recorded 5 minutes subsequent to the incubation confirmed the initial observation: in the absence of  $H_2O_2$  a significant amount of the completely oxidized diimine was formed, which was suppressed otherwise (Figure 7.10b). Moreover,  $Au@AuPt@MnO@SiO_2$  nanoparticles showed any oxidation of TMB at all in the presence of  $H_2O_2$  (Figure 7.10c).

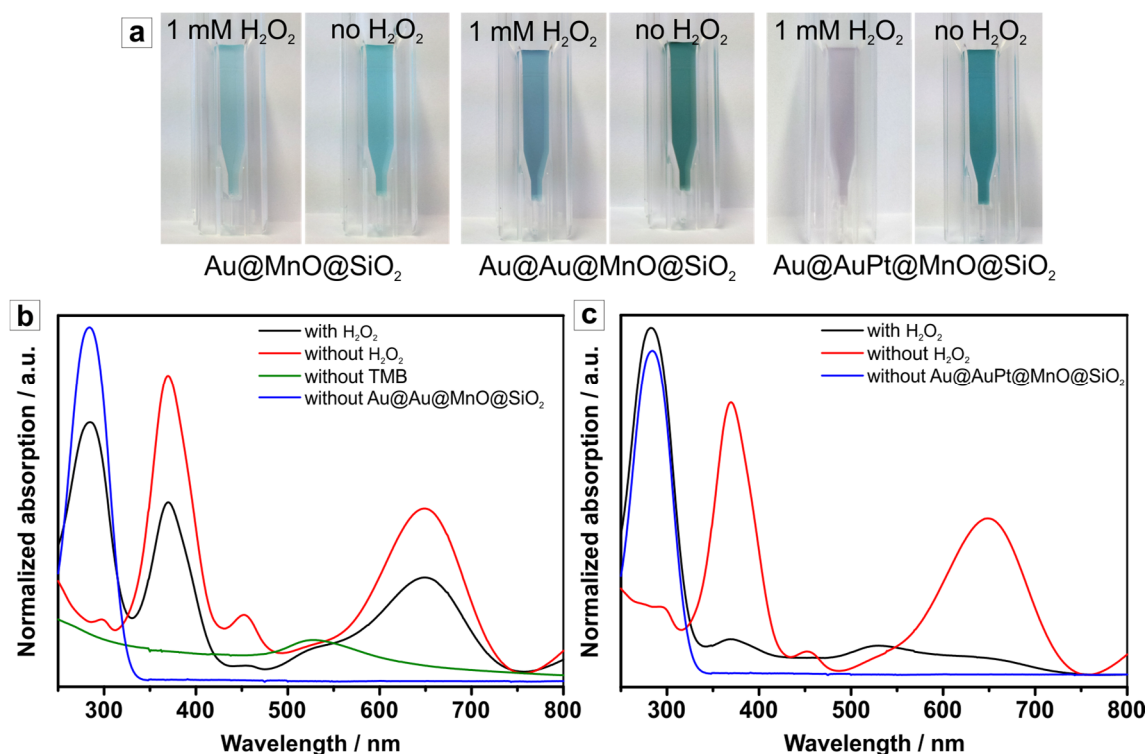


Figure 7.10: a) Pictures taken from reaction mixtures 5 min after incubation and corresponding UV-VIS spectra of b) 5  $\mu g$   $Au@Au@MnO@SiO_2$  and c) 5  $\mu g$   $Au@AuPt@MnO@SiO_2$  nanoparticles, respectively, incubated with 50  $\mu M$  TMB and 1 mM  $H_2O_2$  in 1 mL acetate buffer,  $pH = 3.7$ . The analysis was performed by [REDACTED].

These initial results concerning the pseudo-catalytic activity coming from degradation of MnO-based Janus particles issue a warning to their use in biomedical applications. Even though the MnO domain was protected from the surrounding medium by an amorphous silica shell, the leaching of  $Mn^{2+}$  ions was not efficiently suppressed. Thus, the cellular uptake of these particles might cause their degradation inside the cells and, thus, the release of  $Mn^{2+}$  ions, which are known to cause considerable stress.<sup>[46]</sup> In contrast, the inhibition of the peroxidase-like activity by incubation with  $H_2O_2$  prior to the addition of TMB holds much promise that this issue can be overcome through further investigation.

## 7.4 *In Vitro* Cytotoxicity of Janus Particles

This project was performed in collaboration with [REDACTED] and [REDACTED], [REDACTED], University Hospital, Johannes Gutenberg University, Mainz, as well as [REDACTED] and [REDACTED], University Hospital, Friedrich Schiller University, Jena. Nanoparticle design, material synthesis, and chemical characterization were performed at Johannes Gutenberg University, Mainz.

A potential biomedical use of silica-coated Janus particles, based on their optical and magnetic characteristics, is for targeted drug delivery using immune-stimulatory oligonucleotides or for application as multimodal contrast agents as described in Chapter 6. However, only a few data are available on their biological impact in human cells, in particular for Au@MnO@SiO<sub>2</sub> Janus particles, as they have not been reported before. Therefore, the cytotoxic behavior of Au@MnO@SiO<sub>2</sub> Janus particles was studied for human renal carcinoma cells (Caki-1) and human cervical carcinoma cells (HeLa). Biocompatibility and potential biomedical applications of the Au@MnO@SiO<sub>2</sub> Janus particles were assayed by co-incubating the Au@MnO@SiO<sub>2</sub> Janus particles (8@16 nm Au@MnO, SiO<sub>2</sub> shell approx. 4 nm) with Caki-1 cells for 24 hours. A cell viability assay revealed the Au@MnO@SiO<sub>2</sub> Janus particles to be non-cytotoxic, *i.e.* that in concentrations of 25, 50, and 100 µg Mn<sup>2+</sup>/mL the percentage of cell survival was 99.8 ± 5.0, 96.1 ± 4.8, and 94.4 ± 4.7, respectively (Figure 7.11).

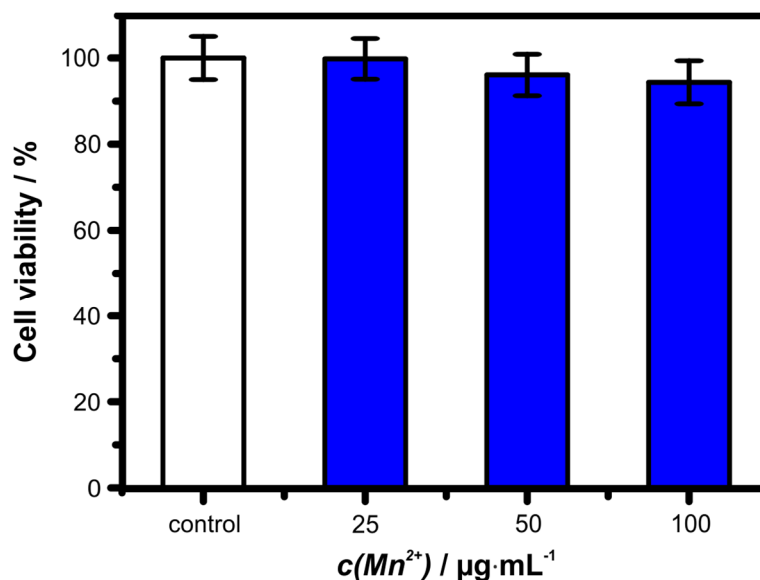


Figure 7.11: Effect of incubation and internalization of Au@MnO@SiO<sub>2</sub> Janus particles. Viability assay of Caki-1 cells, which were incubated for 24 h with increasing concentrations of Au@MnO@SiO<sub>2</sub> (referring to AAS determination). The viability assay was performed by [REDACTED].

Furthermore, cell imaging was performed using confocal laser scanning microscopy. The instrumental background was set up so that cell self-fluorescence would not interfere with our measurements. Thus, Au@MnO@SiO<sub>2</sub> Janus particles were co-incubated with HeLa cells at a concentration of 100 µg Mn<sup>2+</sup>/mL for 24 hours at 37 °C (Figure 7.12a and b). Figure 7.12c

shows a representative image of two-photon imaging, where the Au@MnO@SiO<sub>2</sub> Janus particles display a green luminescence with central emission at  $\lambda_{em} = 535$  nm. No significant auto-fluorescence was observed under similar experimental conditions or under even higher excitation laser power. This makes Au@MnO@SiO<sub>2</sub> a promising candidate for multimodal diagnostic imaging combining MRI, CT, and multi-photon microscopy.

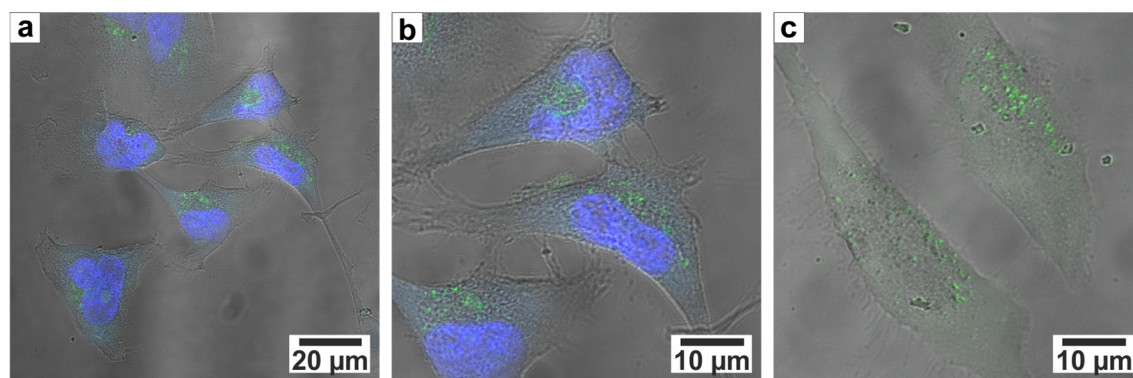


Figure 7.12: Confocal laser scanning microscopy images of HeLa cells co-incubated with 100 µg Mn<sup>2+</sup>/mL Au@MnO@SiO<sub>2</sub>-ATTO495 (green) for 24 h. The cell nuclei (blue) were stained with DAPI. The sample was excited at  $\lambda_{ex} = 488$  nm. c) Two-photon image of the same sample, excited with a two-photon laser at  $\lambda_{ex} = 970$  nm, 30 mW. The concentration of the nanoparticles referring to the concentration of Mn<sup>2+</sup> as measured by AAS. CLSM images were taken by [REDACTED].

These initial results assessing the viability of cells after only short exposure of 24 hours have to be treated with caution for two reasons: first, immortalized human carcinoma cell lines were used, which are known to be resilient to several toxins, and, second, metal nanoparticles have been shown to influence this kind of MTT/WST assay.<sup>[383,384]</sup> For this reason, the study was expanded to endothelial cells, as blood is the first contact point after intravenous injection of nanoparticles. Aside from the changes in the cell line, the surface of the applied Janus particles was varied, as the surface charge, size, and morphology are known to be crucial for internalization and impact on cellular metabolism. In most cases, nanoparticles are taken up via endocytosis, the process of uptake by enclosure into membrane vesicles.<sup>[265]</sup> Hence, a strong correlation between the interactions of nanoparticles with the cellular membrane at their uptake point is qualitatively observed. The incubation of nanoparticles with cell medium causes the formation of a protein corona, as described at the beginning of this chapter. This corona facilitates receptor-mediated endocytosis.<sup>[385]</sup> While neutral surface functionalization is commonly applied in order to prevent unwanted biological interactions, positively charged nanoparticles interact strongly with the negatively charged cell membrane. Cho *et al.* observed negatively charged and neutral nanoparticles to be taken up on much lower levels than positively charged particles.<sup>[386]</sup> Further, Villanueva and co-workers found uptake and toxicity dependent on the type of surface coating for negatively charged iron oxide nanoparticles, while neutral nanoparticles were not internalized.<sup>[387]</sup> In fact, the uptake of anionic nanoparticles is discussed to occur through nonspecific binding or clustering at cationic sites on the cellular membrane, which are scarcer than the negatively charged compartments. Cationic

nanoparticles have been shown to bind to negatively charged groups on the cell surface, which enhances their translocation across the membrane.<sup>[388]</sup> Further, slight changes concerning structure or hydrophobicity showed a strong impact on the internalization.<sup>[389]</sup> This becomes even more important for Janus particles consisting of hydrophobic and hydrophilic domains. In order to investigate the impact of (i) surface charge, (ii) Janus character, and (iii) chemical composition, we designed Au@MO<sub>x</sub>@SiO<sub>2</sub> Janus particles, where the surface charge was varied by introduction of amino groups attached to either the Au domain or the silica shell. Further, the Janus particles were compared to their spherical counterparts, namely MnO@SiO<sub>2</sub> and Fe<sub>3</sub>O<sub>4</sub>@SiO<sub>2</sub>. Finally, the metal oxide domain was either composed of MnO or Fe<sub>3</sub>O<sub>4</sub>. Table 7.2 gives an overview of the variation of measured zeta potentials  $\zeta$  as a function of the surface functionalization, domain sizes, and composition of the analyzed nanoparticles.

Table 7.2: Summary of domain sizes of Janus particles, core size of spherical control particles, and obtained zeta potentials  $\zeta$  in aqueous solution as a function of surface functionalization. The zeta potential measurements were performed by [REDACTED].

	$d(\text{Au}) / \text{nm}$	$d(\text{MO}_x) / \text{nm}$	$\zeta / \text{mV}$
ODT-Au@MnO@SiO <sub>2</sub>	8.0 ± 0.5	29.6 ± 3.0	-27.0 ± 1.8
ODT-Au@MnO@SiO <sub>2</sub>	4.5 ± 0.3	14.5 ± 1.5	-28.0 ± 1.5
ODT-Au@MnO@SiO <sub>2</sub> -NH <sub>2</sub>	4.5 ± 0.3	14.5 ± 1.5	19.0 ± 0.8
NH <sub>2</sub> -Au@MnO@SiO <sub>2</sub>	4.5 ± 0.3	14.5 ± 1.5	-24.0 ± 0.1
MnO@SiO <sub>2</sub>	---	23.7 ± 1.8	-45.0 ± 0.7
MnO@SiO <sub>2</sub> -NH <sub>2</sub>	---	23.7 ± 1.8	17.0 ± 0.2
ODT-Au@Fe <sub>3</sub> O <sub>4</sub> @SiO <sub>2</sub>	3.5 ± 0.8	18.1 ± 1.2	-35.0 ± 1.8
ODT-Au@Fe <sub>3</sub> O <sub>4</sub> @SiO <sub>2</sub> -NH <sub>2</sub>	3.5 ± 0.8	18.1 ± 1.2	21.0 ± 0.5
NH <sub>2</sub> -Au@Fe <sub>3</sub> O <sub>4</sub> @SiO <sub>2</sub>	3.5 ± 0.8	18.1 ± 1.2	-27.0 ± 0.4
Fe <sub>3</sub> O <sub>4</sub> @SiO <sub>2</sub>	---	16.1 ± 0.9	-38.0 ± 0.7
Fe <sub>3</sub> O <sub>4</sub> @SiO <sub>2</sub> -NH <sub>2</sub>	---	16.1 ± 0.9	11.0 ± 0.4

Au@Fe<sub>3</sub>O<sub>4</sub>@SiO<sub>2</sub> and Au@MnO@SiO<sub>2</sub> Janus particles were taken up to a greater extent when amino-groups were introduced at the gold domain as compared to particles bearing no amino groups or amino groups at the silica shell. This indicated an impact of the surface charge and also of the reduced hydrophobicity upon ligand exchange from 1-octadecanethiol to cysteamine. Figure 7.13 shows the influence of surface modification of Au@MnO@SiO<sub>2</sub>

Janus particles on immortalized human microvascular endothelial cells (HMEC-1). The impact on the cell metabolism was determined in terms of relative changes in the cellular ATP level, as it is an evident physiological indication of cells undergoing apoptosis.<sup>[390,391]</sup> After incubation for 72 hours, the ATP level was increased with low doses of up to 1  $\mu\text{g Mn}^{2+}/\text{mL}$ , irrespective of the surface functionalization. For higher concentrations, Janus particles bearing amino-groups showed a distinct cytotoxic effect, though it was slightly more pronounced for cysteamine-bound particles. For spherical  $\text{Fe}_3\text{O}_4@\text{SiO}_2$  and  $\text{MnO}@\text{SiO}_2$ , a higher impact was also caused by amino-functionalization. Thus, the primary cause for the stronger impact on the cellular metabolism was the increased uptake of cationic nanoparticles. The position of the amino groups and, thus, the Janus character was only secondary. As discussed earlier, cationic nanoparticles are less colloiddally stable and tend to agglomerate to a higher extent, which was also observed within this study. Consequently, the higher uptake might have also been caused by sedimentation of nanoparticle agglomerates onto the cell surface, which is equivalent to a locally increased concentration.

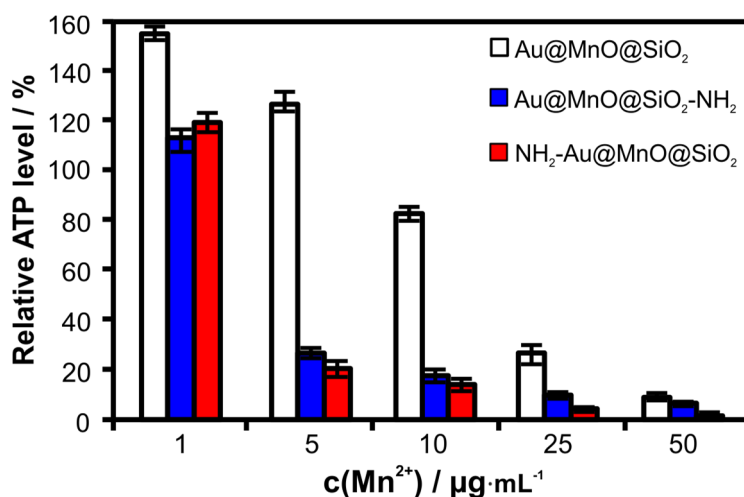


Figure 7.13: Effect of nanoparticle surface functionalization on cellular ATP level. HMEC-1 cells were incubated with increasing concentrations of  $\text{Au}@\text{MnO}@\text{SiO}_2$  Janus particles (referring to AAS determination). Relative cellular ATP levels were detected by ATPLite assay after 72 h. Data were normalized to control cells (without nanoparticle exposure). The measurements were performed by [REDACTED].

As  $\text{NH}_2\text{-Au}@\text{MnO}@\text{SiO}_2$  nanoparticles were taken up to the largest extent, their biological response was further investigated. Figure 7.14a shows a time-dependent, as well as concentration-dependent, reduction of the ATP level of HMEC-1. Incubation for 3 hours caused no significant changes for concentrations up to 50  $\mu\text{g Mn}^{2+}/\text{mL}$ , referring to concentrations determined by AAS. However, it dropped drastically for concentrations higher than 1  $\mu\text{g Mn}^{2+}/\text{mL}$  after 24 hours. In contrast, lower concentrations induced an increased ATP level at all tested incubation times. This was explained in terms of hormesis, which is known as the stimulation of growth by a low dose of toxins.<sup>[392,393]</sup> Here, the critical cytotoxic concentration of  $\text{NH}_2\text{-Au}@\text{MnO}@\text{SiO}_2$  nanoparticles was determined to be 5  $\mu\text{g Mn}^{2+}/\text{mL}$ . Further investigations by confocal laser scanning microscopy were performed using a non-toxic concentration of

1  $\mu\text{g}/\text{mL}$   $\text{Mn}^{2+}$ . Figure 7.14b - d show the co-localization of dye-labeled nanoparticles and HMEC-1 cells after 3, 24, and 48 hours, respectively. After 3 hours of incubation, an adhesion of the Janus particles was observed in z-stacking analysis. This was indicated by the green dots above the red cell membrane (see arrow in Figure 7.14e), as well as a fluorescent signal close to the outer side of the cells (Figure 7.14b). After 24 hours of incubation, the particles were fully internalized, as confirmed by z-stacking (see arrows in Figure 7.14f). These findings suggested the uptake to occur between 3 hours and 24 hours incubation time, as is reflected by the reduction of cellular ATP level. Control experiments with spherical  $\text{MnO}@/\text{SiO}_2$  nanoparticles revealed similar results, so that these effects were not specific to Janus particles.

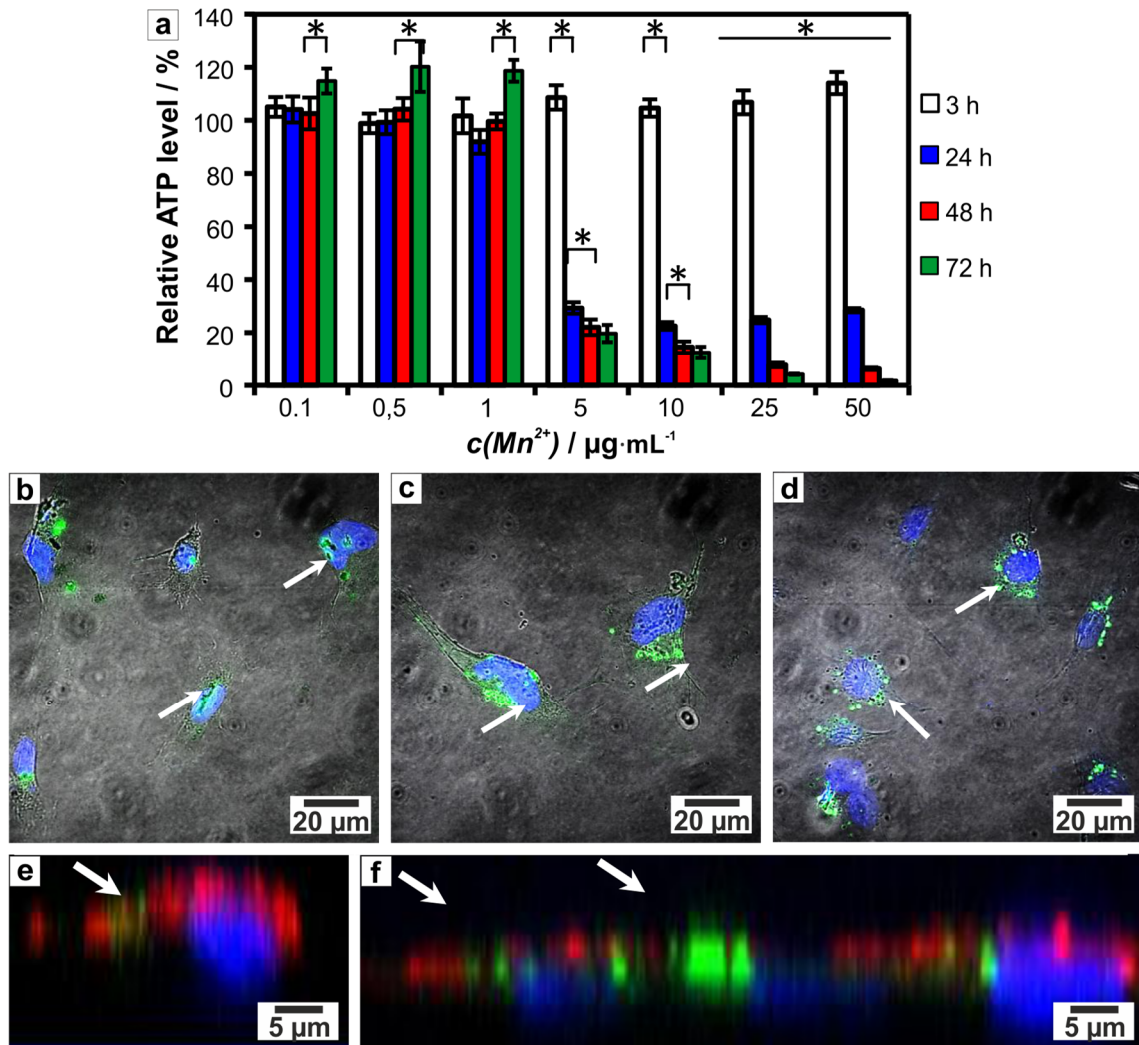


Figure 7.14: Effect of incubation time on cellular ATP level and internalization of  $\text{Au}@/\text{MnO}@/\text{SiO}_2$ -FITC Janus particles. a) Cellular ATP level of endothelial cells after 3, 24, 48, and 72 h of co-incubation with different concentrations of  $\text{NH}_2$ - $\text{Au}@/\text{MnO}@/\text{SiO}_2$ -FITC Janus particles. Data were normalized to untreated control cells.  $p^* < 0.05$ . Confocal fluorescence and bright field (overlay) images b) 3 h, c) 24 h, and d) 48 h after incubation with 1  $\mu\text{g}$   $\text{Mn}^{2+}/\text{mL}$  (referring to AAS concentration); e) and f) confocal image z-stacks showing the position of  $\text{NH}_2$ - $\text{Au}@/\text{MnO}@/\text{SiO}_2$  Janus particles after 3 h and 24 h, respectively. The nuclei (blue) were stained with Hoechst 33258, the glycocalix (red) with lectin WGA-AlexaFluor633. The measurements were performed by [REDACTED].

Moreover, a size-dependent cytotoxic potential was observed for Janus particles as well as spherical analogues (Figure 7.15). Here, the domain sizes of Au@MnO@SiO<sub>2</sub> Janus particles were varied (5@15 nm vs. 8@30 nm), as were those of MnO@SiO<sub>2</sub> (10 nm vs. 24 nm). For both types, the larger nanoparticles showed a stronger reduction of the cellular ATP levels as compared to the smaller ones. Hence, this effect was not exclusively caused by the Janus character, as this effect has been observed in other studies on size-dependent cytotoxicity. Generally, larger nanoparticles were shown to exhibit a higher toxic potential.<sup>[394–397]</sup>

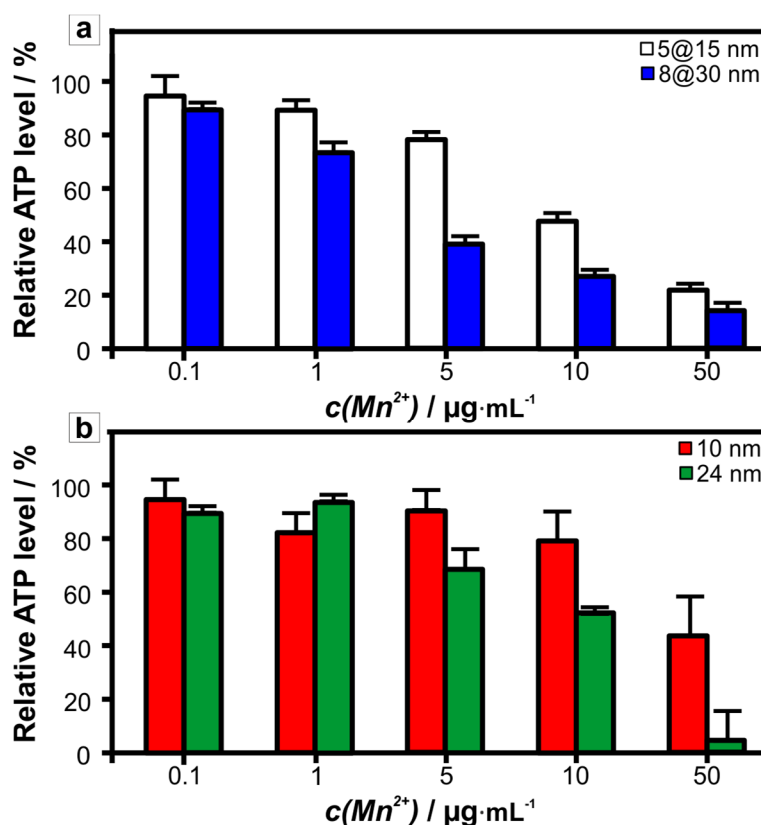


Figure 7.15: Domain size effects of MnO-based nanoparticles on cellular ATP levels. HMEC-1 cells were incubated with 0.1 - 50 µg Mn<sup>2+</sup>/mL (referring to the AAS concentration) for 24 h and the relative ATP levels were detected by the ATPLite assay for a) 5@15 nm and 8@30 nm Au@MnO@SiO<sub>2</sub> Janus particles and b) 10 nm and 24 nm spherical MnO@SiO<sub>2</sub> nanoparticles. Data were normalized to untreated cells. The measurements were performed by [redacted].

In contrast to Au@MnO@SiO<sub>2</sub>, the uptake of Au@Fe<sub>3</sub>O<sub>4</sub>@SiO<sub>2</sub> Janus particles without amino-groups induced barely any changes in the ATP level (Figure 7.16), while the degree of uptake was comparable extent, as almost all cells internalized Janus particles. For both types of Janus particles a perinuclear location was observed (see arrows in Figure 7.14a - c).



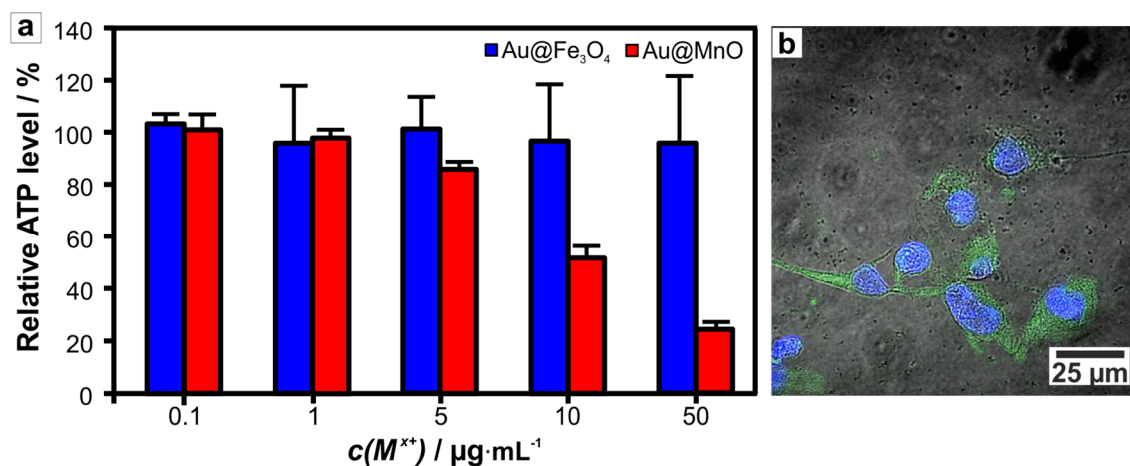


Figure 7.16: Influence of chemical composition of the metal oxide domain of Janus particles on cellular ATP levels. a) HMEC-1 cells were incubated for 24 h with Au@Fe<sub>3</sub>O<sub>4</sub>@SiO<sub>2</sub> and Au@MnO@SiO<sub>2</sub>, respectively. The relative ATP levels were measured by ATPLite assay. Data were normalized to untreated cells. b) Confocal fluorescence and bright-field (overlay) image of Au@Fe<sub>3</sub>O<sub>4</sub>@SiO<sub>2</sub> (green) internalization. The cell nuclei (blue) were stained with Hoechst 33258. The measurements were performed by [REDACTED].

Therefore, the stronger impact of the cellular metabolism cannot be ascribed to a higher uptake of Au@MnO@SiO<sub>2</sub> Janus particles, but rather to a distinct intrinsic cytotoxic potential of MnO. The reduction in the ATP level was suggested to originate from lethal cytotoxic effects, which are known to be caused by production of reactive oxygen species (ROS) and reduced mitochondrial activity.<sup>[398]</sup>

These results reflected the enhanced reactivity of Au@MnO@SiO<sub>2</sub> and related compositions of Janus particles as compared to Fe<sub>3</sub>O<sub>4</sub>-based particles, which could be due to their decreased chemical stability. This was observed while testing the peroxidase-like catalytic activity. Mn<sup>2+</sup> is a well-known neurotoxin involved in diminished motor skills and psychological disturbances similar to Parkinson's disease.<sup>[399]</sup> However, the toxicity of MnO at nanoscale is controversially discussed in literature. Hussain *et al.* described the significant toxicity, neurotransmitter depletion, and ROS formation of MnO nanoparticles.<sup>[399]</sup> Further, Gilad and co-workers investigated the use of MnO nanoparticles for MRI, although elevated concentrations needed for signal enhancement were found to be toxic.<sup>[400]</sup> In contrast, hollow MnO nanoparticles were reported not to show any significant toxicity.<sup>[360]</sup> Previous investigations by our group also confirmed the biocompatibility of polymer-coated MnO nanoparticles to Caki-1 cells, as well as MnO@SiO<sub>2</sub> nanoparticles to primary and bone marrow cells.<sup>[47,51,401]</sup> This controversy reveals the need for systematic studies of the cytotoxic potential of MnO-based nanoparticles. However, the impact of Mn<sup>2+</sup> ions on the cell metabolism, along with the observed chemical instability at low *pH*, suggested a stealth effect contributing to the observed biological response. Natural cell membranes are an efficient barrier against uptake of metal ions, though functionalized nanoparticles are easily internalized. Slight changes of the intracellular *pH* to the acidic range may cause the degradation of MnO nanoparticles, which is consistent with the dose-dependent response observed here. The release of Mn<sup>2+</sup> ions would cause biological

responses, such as oxidative stress, reduced mitochondrial activity, and, finally, cell death by apoptosis. Likewise, Hussain *et al.* observed a 10-fold increase in ROS levels for internalization of MnO nanoparticles as compared to Mn<sup>2+</sup> solutions, which could confirm this hypothesis.<sup>[399]</sup> The controversy about cytotoxicity of MnO nanoparticles might suffer from the relative chemical stability along with the storage conditions or age of the nanoparticles as potential progressive degradation, alternation, or aging prior to the incubation have to be kept in mind. Further experimental investigations are needed to examine the origin of the impact of MnO-based nanoparticles on cells, and whether it is an intrinsic characteristic or caused by degradation, which might be overcome by appropriate ligand protection.

## 7.5 Conclusion

Janus particles are emerging as a promising tool for future medical applications, as they combine two or more distinct components, which can be addressed independently from each other in order to be used for drug delivery, multimodal biomedical imaging, and biological probing. However, the combination of two inorganic nanoparticles enhances their chemical reactivity as well, such that the study introduced here is supposed to issue a warning. Aside from the desired functionalities of the Janus particles, they may activate, influence, or damage cellular metabolism as a consequence of their morphology, orthogonal surface functionalization, protein corona, and intrinsic reactivity.

Here, we analyzed the hazardous as well as advantageous potential of Janus particles for biomedical applications from three aspects: the compositional analysis of the hard protein corona, the peroxidase-like activity as enzyme mimics, and their impact on the cellular metabolism. The formation of the protein corona was observed to depend on (i) the core materials of isotropic nanoparticles, (ii) the particle morphology, and (iii) the incubation time. The orthogonal functionalization of Janus particles was reflected by a significantly increased affinity for lipoproteins, other plasma components, and proteins involved in coagulation, such as fibrinogen.

Nanoparticles serving as enzyme mimics are under current investigation, whereby the chemical stability has to be kept in mind. Here, we demonstrated chemically stable Fe<sub>3</sub>O<sub>4</sub>-based hetero-nanoparticles to exhibit a higher affinity for TMB as peroxidase substrate as compared to the single component nanoparticles. The kinetic parameters were calculated and showed an even higher catalytic potential than the natural enzyme, horseradish peroxidase. In contrast, MnO-based nanoparticles suffered from progressive degradation at reaction conditions. This has to be taken into account for any biomedical applications, as the reaction setup was designed to display physiological conditions. Despite encapsulation with an amorphous SiO<sub>2</sub>-shell, extremely fast oxidation of TMB in the absence of peroxide was ascribed to Mn<sup>2+</sup> leaching,

though this was significantly slowed down upon addition of H<sub>2</sub>O<sub>2</sub>. These results foreshadowed an increased cytotoxic potential, which was the third subject of analysis.

The impact of Janus particles on cells was mainly dependent on three factors: (i) the overall surface charge, (ii) the size of the nanoparticles, and (iii) the chemical composition of the metal oxide domain. The uptake was enhanced upon conjugation of amino groups to the surface of either the Au domain or the SiO<sub>2</sub> shell, which was ascribed to the electrostatic interaction with anionic cell membranes. Generally, amino-functionalized Janus particles showed a lower biocompatibility. Larger nanoparticles also induced a stronger effect on the cellular ATP levels irrespective of the morphology and composition of the nanoparticles. However, the chemical composition of the metal oxide domain turned out to be crucial for the biocompatibility of Janus particles, as MnO-based Janus particles revealed a stronger concentration-dependent reduction of the cellular ATP level as compared to Fe<sub>3</sub>O<sub>4</sub>-based Janus particles. These distinct effects might be caused by progressive degradation and subsequent impact on the cellular metabolism, which was suggested by the test for peroxidase-like activity.

To conclude, Janus particles were demonstrated to be promising candidates for biomedical applications as composition, morphology, and surface functionalization can be used to tailor their characteristics. Asymmetric Janus particles combine promising features for future biomedical applications, such as multifunctionality and biocompatibility. However, more information is needed in order to understand and control the interactions at the nano-bio interface, though these initial results hold a lot of promise that these issues can be overcome by further investigations.

## 7.6 Experimental Section

**Materials.** All reactions were carried out using commercially available reagents without any further purification. Cysteamine ( $\geq 98\%$ ), 3,5,3',5'-tetramethylbenzidine (TMB,  $>99\%$ ), anhydrous sodium acetate ( $>99\%$ ), dimethyl sulfoxide (DMSO, 99.8%), hydrogen peroxide (H<sub>2</sub>O<sub>2</sub>,  $\geq 35\text{ wt}\%$ ), fetal bovine serum (FBS), penicillin-streptomycin (PEST, 1000 U/mL penicillin and 10 mg/mL streptomycin), L-glutamine, MEM non-essential amino acids, and cell counting kit-8 (CCK-8) were purchased from Sigma-Aldrich. Acetone, ethanol, chloroform, glacial acid, and hexane were purchased from Fisher Scientific. MycoKill AB was purchased from PAA.

**Surface Modification of Au@MO<sub>x</sub>@SiO<sub>2</sub> NPs.** In order to control the zeta potential of Janus particles, amino groups were introduced either on the surface of the silica-encapsulated nanoparticles as described in Chapter 4.4 or by ligand exchange of the Au domain. This was performed by addition of ca 20 mg cysteamine dissolved in a mixture of 5 mL chloroform and 5 mL ethanol to Au@MO<sub>x</sub>@SiO<sub>2</sub> particles in 5 mL ethanol. The reaction mixture was stirred at

room temperature overnight. The particles were precipitated by addition of hexane, collected by centrifugation (9000 rpm, 10 min), and washed using acetone/hexane.

**Characterization.** The peroxidase-like activity of Janus particles was investigated by means of UV-VIS spectroscopy after comprehensive analysis by TEM and AAS (see Chapter 4.4.1). The interaction of nanoparticles with blood plasma was analyzed by capillary label-free liquid chromatography mass spectrometry (LC-MS). In order to determine the impact of Janus particles on the cell metabolism, cytotoxicity assays and ATPLite assays were used in combination with confocal laser scanning microscopy subsequent to thorough analysis of particle size by TEM and zeta potential measurements.

**Peroxidase-Like Catalytic Activity of NPs.** The peroxidase-like catalytic activity was determined spectrophotometrically by measuring the formation of the charge-transfer complex of partially oxidized TMB<sup>+</sup> at  $\lambda = 652$  nm using a Varian Cary 500 UV-VIS/NIR-spectrometer. The TMB oxidation activity was typically measured in 0.2 M sodium acetate buffer ( $pH = 3.7$ ) in the presence of nanoparticles (5 - 20  $\mu\text{g Mn}^{2+}$  or  $\text{Fe}^{2+/3+}$ , respectively, referring to AAS analysis) using 100  $\mu\text{M}$  TMB. A 4.16 mM stock solution of TMB was prepared by 1:9 volumetric dilution with buffer of a stock solution of TMB in DMSO (10 mg/1 mL). The exact concentration was calculated from the absorption at 288 nm ( $\epsilon = 21 \text{ mM}^{-1}\text{cm}^{-1}$ ). Hydrogen peroxide was added to start the reaction, unless stated otherwise. UV-VIS spectra were recorded after baseline correction to buffer. Buffer, aqueous nanoparticle solution, and TMB were mixed in the cuvette prior to addition of  $\text{H}_2\text{O}_2$ . The steady-state kinetics were performed by varying the concentration of TMB (0 - 500  $\mu\text{M}$ ). The reaction was carried out in 1 mL acetate buffer and monitored spectroscopically for 10 - 15 min for  $\text{Au@Fe}_3\text{O}_4\text{@SiO}_2$  and  $\text{Fe}_3\text{O}_4\text{@SiO}_2$ . The kinetic curves were analyzed utilizing the Michaelis-Menten model and Lineweaver-Burk linearization.

**LC-MS Analysis of NP Protein Corona.** All experiments were conducted using technical triplicates of each sample to ensure reproducibility. Particle suspensions were incubated with 200  $\mu\text{L}$  of human plasma for 30 min or 2 h at 37 °C. The proteins were eluted from the nanoparticles, digested by trypsin, and identified by label-free liquid chromatography mass spectrometry according to the protocol described by Tenzer and co-workers.<sup>[402]</sup> Data analysis was performed using the software tool ISOQuant.<sup>[403]</sup>

**Cell Culture.** The human renal cell carcinoma line (Caki-1) and human cervical carcinoma cell line (HeLa) were kindly provided by [REDACTED] (Institute for pharmacy and biochemistry, Johannes Gutenberg-University, Mainz). McCoy's 5A medium was used as the culture medium and was modified by addition of 10 % FBS, 1 % PEST, 2 mM *L*-glutamine, MycoKill, and MEM non-essential amino acids. Cells were routinely grown in 25 cm<sup>2</sup> sterile cell culture flasks at 37 °C, 95 % relative humidity, and 5 %  $\text{CO}_2$  until confluence was reached.

Immortalized human microvascular endothelial cells (HMEC-1; Centre for Disease Control and Prevention, USA) were cultured as described by Landgraf and co-workers.<sup>[346]</sup>

**Cytotoxicity Assay.** The cytotoxicity assay was performed according to the supplier in 96 well cell plates used under standard conditions. The density was 15 000 cells/well. For background subtraction 6 wells were only filled with media and H<sub>2</sub>O. After 24 h of cell growth, different concentrations of silica-coated nanoparticles in McCoy's 5A were added, and the incubation time was set to 24 h. The medium was then replaced by 100  $\mu$ L of a cell counting kit solution, 5.4 mL culture medium was mixed with 600  $\mu$ L CCK-8, and incubation was continued for another 3 h at 37 °C, 95 % relative humidity, and 5 % CO<sub>2</sub>. The absorption of formazan formed due to cellular activity was measured at 450 nm. All results were normalized to wells that contained media instead of cells, after background subtraction.

**Evaluation of Effects on Cell Metabolism (ATP).** The cellular levels were used as a marker for nanoparticles' effect on the cell metabolism. After incubation of HMEC-1 with different nanoparticle concentrations (0.1 - 50  $\mu$ g Mn<sup>2+</sup>/mL referring to AAS analysis) for 3 h, 24 h, 48 h, or 72 h and several washing steps, the ATPLite assay was performed according to manufacturer's instructions. A LUMIStar Galaxy system (BMG LABTECH GmbH, Ortenberg) was used to detect the fluorescence signal of the transformation of *D*-luciferin to oxyluciferin. For detailed descriptions see <sup>[346]</sup>.

**Confocal Laser Scanning Microscopy.** In order to visualize nanoparticles after their cellular uptake, CLSM was performed using either a Zeiss LSM 710 NLO or a Zeiss LSM 510 Meta microscope. Cell nuclei were stained with DAPI or Hoechst 33258, and the glycocalyx with lectin WGA-AlexaFluor633.



# 8

## Conclusion and Outlook

The general aim of this work was the two-faceted examination of Janus particles as novel dimeric hetero-nanostructures. A key point was to control their morphology, size, and chemical composition, though their subsequent selective surface functionalization was in no way subordinate in order to obtain well-defined amphiphilic nanoparticles. We placed emphasis on dumbbell-like structures composed of a metal and a metal oxide domain. The utilized materials exhibit several unique advantages useful for biomedical applications, for instance as *theranostic* agents. The metal domain composed of gold, platinum, or their alloy was selected on the basis of these metals' extraordinary optical characteristics and high contrast for computed X-ray tomography. Further, the materials of the metal oxide domain were either manganese or iron oxide, as they feature outstanding size-dependent magnetic behavior at nanoscale, which enables their use as contrast agents for magnetic resonance imaging.

The first part of the present thesis covered the sophisticated synthesis and comprehensive characterization of water-soluble multifunctional Janus particles. It was designed to be a seeding-growth process of hydrophobic heterodimer nanoparticles using preformed metal particles as seeds. Subsequently, a selective surface modification was applied, as the synthesis of hetero-nanoparticles requires an even higher degree of synthetic control as compared to single-component nanoparticles.

In the first step of the synthetic procedure, monodisperse, size-tunable Au nanoparticles were demonstrated to be easily synthesized by reduction in hydrophobic solvents, which thus met the requirements for their use as seeds for heteroepitaxial nucleation of a metal oxide domain. Their synthesis was in accordance with LaMer's model of homogeneous nucleation, as nucleation and growth were clearly separated. By controlling the reaction temperature, the particle size was adjusted in the range between 3 nm and 9 nm, while an ensuing seeding-growth technique was developed to enlarge the monodisperse nanoparticles up to 20 nm. Investigation of the structure of Au nanoparticles by HR TEM and high resolution synchrotron

powder diffraction demonstrated their polycrystallinity, which was ascribed to the tendency of Au toward twinning. Further, the high quality of Au nanoparticles enabled the formation of self-assembled superlattices, where a preference for 2D hexagonally-ordered layers over 3D self-assembled superlattices, or vice versa, was regulated by the concentration of excess ligands as well as the nanoparticle concentration itself. In order to investigate the impact of the chemical composition of the metal domain on Janus particles, we transferred the synthetic procedure to composition-tunable  $\text{Au}_x\text{Pt}_{1-x}$  alloy nanoparticles, whose characteristics were observed to represent the synergy of both Au and Pt.

Next, we established a facile synthetic approach to  $\text{Au@MnO}$  and  $\text{Au@Fe}_3\text{O}_4$  heterodimer nanoparticles with precise control over morphology and domain sizes, as investigated by (HR) TEM, DLS, and UV-VIS spectroscopy. The morphology was conclusively determined to be dumbbell-like by TEM EDX line scans as well as TEM tomography. The size of the metal oxide domains for a given diameter of Au seeds could be easily tuned in the range between 8 nm and 30 nm by variation of the amount of metal oleate used as precursor. Investigation of the reaction mechanism revealed a separation of heterogeneous nucleation and growth for  $\text{Au@MnO}$ , but a size-focusing effect for  $\text{Au@Fe}_3\text{O}_4$  heterodimer nanoparticles to be responsible for their uniformity in size. The phase composition of the as-prepared heterodimer nanoparticles was investigated by high resolution synchrotron powder diffraction data collected at the beamline 11-BM of the Advanced Photon Source (APS) of the Argonne National Laboratory. The metal oxide domains were determined to be manganosite and magnetite, respectively. This result was confirmed by magnetic data, which further indicated a Verwey transition to occur in  $\text{Au@Fe}_3\text{O}_4$  nanoparticles. The universal applicability of the chemical protocol was confirmed by its adaptation to Pt and  $\text{Au}_x\text{Pt}_{1-x}$  nanoparticles used as seeds.

Therefore, this study presented a kind of LEGO schematic, as the individual components can be combined like building blocks, while the characteristics of the heterodimers were strongly dependent on the actual chemical composition. This was found to originate from distinct interfacial communication of the individual domains across the solid state interface within the dumbbell-like nanoparticles. Aside from differences between  $\text{Au@MnO}$  and  $\text{Au@Fe}_3\text{O}_4$  regarding their synthetic procedure, UV-VIS and transient absorption spectroscopy discerned distinct interactions across the interfaces: the formation of a Schottky junction upon conjugation of Au to the semi-metal  $\text{Fe}_3\text{O}_4$  was suggested, but only a polarization at the interface with the wide band gap semiconductor MnO was observed.

Finally, a selective silica coating of the metal oxide domain was demonstrated to be a highly effective technique to convert hydrophobic heterodimer nanoparticles into multifunctional, water-soluble, and dye-labeled nanoparticles. Here, the synthetic approach of encapsulating spherical metal oxide nanoparticles was applied to heterodimer nanoparticles, as it combines the advantages of the reverse-microemulsion approach and the Stöber technique. The



subsequent introduction of additional surface functionalization, such as PEG- or  $\text{NH}_2$ -groups, enhanced the colloidal stability and the control of surface charge, respectively. Previous thiol functionalization of the Au domain resulted in solely encapsulating the metal oxide domain with a thin silica layer, leaving the vitreophobic Au domain untouched. In the absence of any thiol, the hydrophobic heterodimers were completely covered by silica. Investigation of the solution-phase behavior by dynamic light scattering revealed the amphiphilic nanoparticles to be colloidally stable in aqueous solution. Further, no indication of aggregation or flocculation was observed upon incubation in various buffer solutions and serum. Time-resolved fluorescence spectroscopy in combination with confocal laser scanning microscopy revealed  $\text{Au@MnO@SiO}_2$  heterodimers to be highly two-photon active, based on the intrinsic properties of the Au domain. As the ability of selective surface functionalization was preserved despite the silica encapsulation, these nanoparticles represent an encouraging alternative to current bioimaging nanoparticle-platforms and, further, enable the formation of well-defined Janus particles.

The second part of this thesis covered specific examples of applications of Janus particles obtained by selective surface modification, exploiting their chemically distinct faces. Upon orthogonal functionalization, the Janus particles self-assembled at air-water and oil-water interfaces, minimizing the interfacial tension by an upright orientation at the interfaces. This was shown by surface area-pressure isotherms and cryo-TEM investigation, respectively. Further, we analyzed the interaction of Janus particles with DOPC lipid bilayers, which served as a model system for the interaction with cellular membranes. These experiments demonstrated the ability of Janus particles to induce membrane tubulation under isoosmotic conditions and their enclosure in membrane vesicles, which displays a passive, artificial endocytotic uptake pathway. However, no effect was observed for membranes under tension, so that it remains unclear from these pilot experiments whether the formation of membrane tubes or vesicles may serve as an additional uptake pathway in living cells, as was suggested by Reynwar *et al.* in coarse-grained simulations.<sup>[52]</sup>

Furthermore, by virtue of their intrinsic materials' characteristics, Janus particles were exploited as contrast agents for multimodal bioimaging, combining computed X-ray tomography (CT) and magnetic resonance imaging (MRI). For this purpose, their domain sizes were adjusted by subsequent overgrowth of Au on preformed heterodimer nanoparticles. This modification was necessary due to restrictions on the size of metal seeds for the synthesis of well-defined heterodimer nanoparticles on the one hand, and, on the other hand, due to the lower sensitivity of CT as compared to MRI. The additional nucleation occurred chemo-selectively on the Au domains, independent of the chemical composition of the metal oxide domains, but a distinct difference was observed concerning the resulting morphology: in the case of  $\text{Au@MnO}$ , progressive overgrowth led to enlarged Au domains, whereas  $\text{Au@Fe}_3\text{O}_4$

heterodimer nanoparticles facilitated the nucleation of additional Au domains, resulting in Au@Au@Fe<sub>3</sub>O<sub>4</sub> heterotrimer nanoparticles. This effect might be attributed to distinct interfacial communication influencing the electronic structure of the Au domains. Independent of the morphology, the enlargement of the Au domain significantly amplified the X-ray attenuation. Here, a threshold effect was observed for low concentrations, and a linear increase in signal amplification for elevated concentrations of Janus particles. Likewise, Janus particles were demonstrated to be superior to spherical single-component metal oxide nanoparticles regarding their application as MRI contrast agents. Au@MnO@SiO<sub>2</sub> heterodimer nanoparticles significantly accelerated longitudinal relaxation processes. The increase in  $r_1$  indicated a junction effect in the dumbbell-structure, which allows facile tuning of the relaxation times by adjustment of the domain sizes. In addition to high relaxivities T<sub>1</sub> or T<sub>2</sub> being inevitable for the respective imaging technique, their ratio of relaxivities is of particular importance regarding the application as contrast agents. Detailed studies on the effect of chemical composition and morphology on transverse magnetization are underway.

Aside from their intrinsic functionalities specially designed for imaging applications, Janus particles might activate, influence, or damage the cellular metabolism due to their morphology, multifunctionality, orthogonal surface functionalization, and enhanced intrinsic reactivity. For this reason, their hazardous and advantageous potential for biomedical applications was investigated highlighting their impact on (i) the composition of the hard protein corona, (ii) their enzyme-like reactivity, and (iii) their effect on cellular metabolism in *in vitro* studies. The formation of the protein corona was observed to depend not only on the core materials and the incubation time, but also on the surface functionalization and particle morphology. The increased affinity for lipoproteins, proteins involved in coagulation, and other plasma components reflected the orthogonal surface functionalization, as these proteins are known for their strong interaction with hydrophobic surfaces. This demonstrated a significant impact of the functionalization and morphology on “what the cell sees” upon incubation with Janus particles.

The enhanced reactivity of Janus particles as compared to spherical metal oxide nanoparticles was addressed in enzyme-mimicking tests, investigating peroxidase-like activity in this particular case. Chemically stable Fe<sub>3</sub>O<sub>4</sub>-based hetero-nanoparticles showed an even higher catalytic potential than the natural enzyme horseradish peroxidase. Here, the intrinsic activity of the metal domains, as well as the interfacial activation of at least one of the two components, might contribute to the enhanced reactivity, but a differentiation remained challenging. In contrast, the high reactivity of MnO-based hetero-nanoparticles was caused by progressive degradation of MnO under reaction conditions. This has to be taken into account for any biomedical application, as the reaction setup was designed to display physiological conditions. In fact, this was confirmed by *in vitro* studies, as biocompatibility assays revealed a

significantly reduced ATP levels in HMEC-1 for MnO<sub>2</sub> as compared to Fe<sub>3</sub>O<sub>4</sub>-based nanoparticles. Further, surface charge, which was adjusted by subsequent amino-functionalization, and size were demonstrated to affect the cellular metabolism independent of the core materials. However, no increased cytotoxic potential was observed for Janus particles over spherical nanoparticles, such that a passive endocytotic cellular uptake by membrane tubulation and vesiculation could be disregarded.

Future work will comprise further examination of Janus particles for biomedical applications, as their tunable composition, morphology, and surface functionalization make them promising candidates for *theranostic* agents. Nevertheless, the interactions and reactions at the nano-bio interface are barely understood, which is a fundamental requirement for tailored cell targeting, drug delivery, and diagnostic imaging. These applications are cutting-edge technologies, where the advantages of Janus particles can be maximized: the distinct surface functionalization of the two components will be used for enhancing the target specificity of these particles as simultaneous imaging agents and drug transporters. For instance, rapidly growing tumor cells overexpress antigens, which can be targeted by a specific antibody bound to one domain of the nanoparticles surface, while the other domain of the Janus particle can be functionalized with cancer-specific chemotherapeutic agents. This is crucial in order to succeed with simultaneous imaging and therapy, while minimizing unintended accumulation and adverse effects due to high doses of nanoparticles and therapeutics. Finally, careful consideration of the intrinsic reactivity of hetero-nanoparticles is essential prior to their *in vivo* application and will be subject to comprehensive research.

Another area for intensive work will be the analysis of the underlying interactions within heterodimer nanoparticles. As the components can differ in both chemical composition and morphology, a large library of Janus particles can be made in theory from the available building blocks, which represent a kind of LEGO schematic. Nevertheless, Janus particles cannot be reduced to the morphologic combination of two domains: they are irreducibly complex as highlighted in the present dissertation. From a fundamental point of view, it will be interesting to compare heterodimer nanoparticles with regard to their interaction across the solid state interface dependent on their chemical composition and domain size ratio. For instance, conjugation of metal oxide domains composed of TiO<sub>2</sub> or ZnO to metal nanoparticles enables access to highly effective plasmonic photo-catalysts. Variation of the metal domains, on the other hand, is of particular interest for their interfacial activation upon contact with a metal oxide support. This approach will contribute to a fundamental understanding of the fascinating characteristics and widespread applications of Janus particles.



# 9

## Supporting Information

Table S.1: Measurement and refinement parameters of the synchrotron diffraction pattern of Au nanoparticles (see Figure 2.5).

	Au
Particle size measured from TEM images	5.3 nm $\pm$ 0.5 nm
Diffractometer	11-BM at the Advanced Photon Source, Argonne National Laboratory
Sample preparation	Fine powder in 0.8 mm Kapton tube
Measuring mode	Transmission
Wavelength / $\text{\AA}$	0.413715
Measuring range	$0.5 \leq 2\theta/^\circ \leq 46.5$ ; $0.1 \leq Q \cdot \text{\AA} \leq 12.0$
Refinement range	$3.3 \leq 2\theta/^\circ \leq 40.5$ ; $0.8 \leq Q \cdot \text{\AA} \leq 10.5$
Temperature / K	298
Profile fit	Rietveld refinement according to reported crystal structure models
Background	Chebyshev
Profile function	Fundamental parameters approach (WPPM, Ln_normal_sphere)
Program	TOPAS Academic V5
Total No. of parameters / Background	18 / 10
$R_{wp}$	13.43
GoF	2.30
DW	0.20
<b>Au – Phase</b>	
Space group	Fm-3m
Cell parameters / $\text{\AA}$	4.07316(7)
Crystallite size - Max / nm	0.516(5)
Crystallite size - Expected / nm	1.39(1)
Crystallite size - Variance / nm	1.82(4)
Crystallite size - Skew / nm	3.82(2)
Fraction / %wt	100.0
Biso	0.706(4)
Preferred orientation	-/-

Table S.2: Measurement and refinement parameters of the synchrotron diffraction pattern of Au@MnO (see Figure 3.4) and Au@MnO@SiO<sub>2</sub> nanoparticles (see Figure 4.5).

	Au@MnO	Au@MnO@SiO <sub>2</sub>
Particle size measured from TEM images	Au: 6.5 nm ± 0.3 nm MnO: 19.3 nm ± 1.8 nm	Au: 9.0 nm ± 0.6 nm MnO: 18.8 nm ± 0.8 nm
Diffractometer	11-BM at the Advanced Photon Source, Argonne National Laboratory	
Sample preparation	Fine powder in 0.8 mm Kapton tube	
Measuring mode	Transmission	
Wavelength / Å	0.413715	
Measuring range	0.5 ≤ 2θ/° ≤ 46.5; 0.1 ≤ Q·Å ≤ 12.0	
Refinement range	3.3 ≤ 2θ/° ≤ 40.5; 0.8 ≤ Q·Å ≤ 10.5	
Temperature / K	298	
Profile fit	Rietveld refinement according to reported crystal structure models	
Background	Chebyshev	
Profile function	Fundamental parameters approach	
Program	TOPAS Academic V5	
Total No. of parameters / Background	33 / 20	33 / 20
R <sub>wp</sub>	8.52	6.65
GoF	1.69	1.17
DW	0.37	0.76
<b>Au – Phase</b>		
Space group	<i>Fm-3m</i>	
Cell parameters / Å	4.0749(2)	4.0575(2)
Crystallite size / nm	6.4(2)	9.4(3)
Fraction / %wt	15.43(8)	39.1(4)
Biso	1.43(3)	0.91(3)
Preferred orientation	0.7445(2) in (111)	0.769(2) in (111)
<b>MnO – Phase</b>		
Space group	<i>Fm-3m</i>	
Cell parameter / Å	4.4301(1)	4.3703(6)
Crystallite size / nm	22.3(7)	6.1(5)
Fraction / %wt	84.57(8)	64.8(4)
Biso	1.43(3)	0.91(3)

Table S.3: Measurement and refinement parameters of the synchrotron diffraction pattern of Au@Fe<sub>3</sub>O<sub>4</sub> (see Figure 3.18), Pt@Fe<sub>2</sub>O<sub>3</sub>, and Au<sub>x</sub>Pt<sub>1-x</sub>@Fe<sub>2</sub>O<sub>3</sub> nanoparticles (see Figure 3.33).

	Au@Fe <sub>3</sub> O <sub>4</sub>	Pt@Fe <sub>2</sub> O <sub>3</sub>	Au <sub>x</sub> Pt <sub>1-x</sub> @Fe <sub>2</sub> O <sub>3</sub>
Particle size measured from TEM images	Au: 9.0 ± 0.7 nm Fe <sub>3</sub> O <sub>4</sub> : 15.1 ± 1.6 nm	Pt: 5.6 ± 0.5 nm Fe <sub>2</sub> O <sub>3</sub> : 12.9 ± 1.6 nm	Au <sub>x</sub> Pt <sub>1-x</sub> : 8.0 ± 0.5 nm Fe <sub>2</sub> O <sub>3</sub> : 16.1 ± 1.3 nm
Diffractometer	11-BM at the Advanced Photon Source, Argonne National Laboratory		
Sample preparation	Fine powder in 0.8 mm Kapton tube		
Measuring mode	Transmission		
Wavelength / Å	0.413715		
Measuring range	0.5 ≤ 2θ° ≤ 46.5; 0.1 ≤ Q·Å ≤ 12.0		
Refinement range	3.3 ≤ 2θ° ≤ 40.5; 0.8 ≤ Q·Å ≤ 10.5		
Temperature / K	298		
Profile fit	Rietveld refinement according to reported crystal structure models		
Background	Chebyshev		
Profile function	Fundamental parameters approach		
Program	TOPAS Academic V5		
Total No. of parameters / Background	22 / 11	21 / 11	22 / 11
R <sub>wp</sub>	11.4	8.98	11.8
GoF	1.59	1.82	2.22
DW	0.40	0.40	0.31
<b>M – Phase</b>			
Space group	Fm-3m		
Composition	Au	Pt	Au <sub>0.73</sub> Pt <sub>0.27</sub>
Cell parameters / Å	4.0553(2)	3.8934(1)	4.0111(2)
Crystallite size / nm	7.7(1)	8.5(1)	4.8(1)
Fraction / %wt	49.6(3)	24.60(1)	32.8(1)
Biso	1 (fixed)	1 (fixed)	1 (fixed)
Preferred orientation	0.774(2) in (111)	-/-	0.711(1) in (111)
<b>FeO<sub>x</sub> – Phase</b>			
Space group	P4132		
Cell parameter / Å	8.3709(4)	8.3627(2)	8.3684(3)
Crystallite size / nm	18.4(1)	18.4(3)	23.3(7)
Fraction / %wt	50.4(3)	75.40(6)	67.2(1)
Biso	1 (fixed)	1 (fixed)	1 (fixed)
Site occupation factor 8c	1 (fixed)	1 (fixed)	1 (fixed)
Site occupation factor 12d	0.99(2)	0.967(2)	0.905(4)
Site occupation factor 4a	0.89(5)	0.605(5)	0.602(1)
Approx. composition	Fe <sub>0.733(9)</sub> O ≈ Fe <sub>3</sub> O <sub>4</sub>	Fe <sub>0.679(1)</sub> O ≈ Fe <sub>2</sub> O <sub>3</sub>	Fe <sub>0.665(2)</sub> O ≈ Fe <sub>2</sub> O <sub>3</sub>





# 10

## Bibliography

- [1] L. N. Lewis, *Chemical Reviews* **1993**, *93*, 2693 – 2730.
- [2] D. Wang, T. Xie, Y. Li, *Nano Research* **2009**, *2*, 30 – 46.
- [3] A.-H. Lu, E. L. Salabas, F. Schüth, *Angewandte Chemie International Edition* **2007**, *46*, 1222 – 1244.
- [4] J. Cheon, J.-H. Lee, *Accounts of Chemical Research* **2008**, *41*, 1630 – 1640.
- [5] M. Liong, J. Lu, M. Kovoichich, T. Xia, S. G. Ruehm, A. E. Nel, F. Tamanoi, J. I. Zink, *ACS Nano* **2008**, *2*, 889 – 896.
- [6] J. Gao, H. Gu, B. Xu, *Accounts of Chemical Research* **2009**, *42*, 1097 – 1107.
- [7] M. Moros, B. Pelaz, P. López-Larrubia, M. L. García-Martin, V. Grazú, de la Fuente, J. M., *Nanoscale* **2010**, *2*, 1746 – 1755.
- [8] H. Goesmann, C. Feldmann, *Angewandte Chemie International Edition* **2010**, *49*, 1362 – 1395.
- [9] G. Ozin, *Advanced Materials* **1992**, *4*, 612 – 649.
- [10] B. Wu, H. Zhang, C. Chen, S. Lin, N. Zheng, *Nano Research* **2009**, *2*, 975 – 983.
- [11] F.-h. Lin, R.-a. Doong, *The Journal of Physical Chemistry C* **2011**, *115*, 6591 – 6598.
- [12] T. D. Schladt, T. Graf, O. Köhler, H. Bauer, M. Dietzsch, J. Mertins, R. Branscheid, U. Kolb, W. Tremel, *Chemistry of Materials* **2012**, *24*, 525 – 535.
- [13] S. T. Kochuveedu, Y. H. Jang, D. H. Kim, *Chemical Society Reviews* **2013**, *42*, 8467 – 8493.
- [14] X. Zhang, Y. L. Chen, R.-S. Liu, D. P. Tsai, *Reports on Progress in Physics* **2013**, *76*, 046401.
- [15] J. J. Storhoff, R. Elghanian, R. C. Mucic, C. A. Mirkin, R. L. Letsinger, *Journal of the American Chemical Society* **1998**, *120*, 1959 – 1964.
- [16] R. S. Norman, J. W. Stone, A. Gole, C. J. Murphy, T. L. Sabo-Attwood, *Nano Letters* **2008**, *8*, 302 – 306.
- [17] P. K. Jain, I. H. El-Sayed, M. A. El-Sayed, *Nano Today* **2007**, *2*, 18 – 29.
- [18] Thanh, Nguyen T. K., N. Maclean, S. Mahiddine, *Chemical Reviews* **2014**, 140708135221009.
- [19] D. Yoo, J.-H. Lee, T.-H. Shin, J. Cheon, *Accounts of Chemical Research* **2011**, *44*, 863 – 874.
- [20] X. Huang, M. A. El-Sayed, *Alexandria Journal of Medicine* **2011**, *47*, 1 – 9.
- [21] P. G. de Gennes, *Angewandte Chemie International Edition* **1992**, *31*, 842 – 845.
- [22] M. Lattuada, T. A. Hatton, *Nano Today* **2011**, *6*, 286 – 308.

- [23] H. Yin, C. Wang, H. Zhu, S. H. Overbury, S. Sun, S. Dai, *Chemical Communications* **2008**, 4357 – 4359.
- [24] C. Wang, H. Daimon, S. Sun, *Nano Letters* **2009**, 9, 1493 – 1496.
- [25] P. Li, Z. Wei, T. Wu, Q. Peng, Y. Li, *Journal of the American Chemical Society* **2011**, 133, 5660 – 5663.
- [26] A. Walther, M. Hoffmann, Müller, Axel H. E., *Angewandte Chemie* **2008**, 120, 723 – 726.
- [27] A. Synytska, R. Khanum, L. Ionov, C. Cherif, C. Bellmann, *ACS Applied Materials & Interfaces* **2011**, 3, 1216 – 1220.
- [28] C. Xu, B. Wang, S. Sun, *Journal of the American Chemical Society* **2009**, 131, 4216 – 4217.
- [29] J. Hu, S. Zhou, Y. Sun, X. Fang, L. Wu, *Chemical Society Reviews* **2012**, 41, 4356 – 4378.
- [30] H. Zhou, J. Lee, T. J. Park, S. J. Lee, J. Y. Park, J. Lee, *Sensors and Actuators B: Chemical* **2012**, 163, 224 – 232.
- [31] A. Walther, A. E. Müller, *Soft Matter* **2008**, 4, 663.
- [32] S. Jiang, Q. Chen, M. Tripathy, E. Luijten, K. S. Schweizer, S. Granick, *Advanced Materials* **2010**, 22, 1060 – 1071.
- [33] K. J. Lee, J. Yoon, J. Lahann, *Current Opinion in Colloid & Interface Science* **2011**, 16, 195 – 202.
- [34] A. Kumar, B. J. Park, F. Tu, D. Lee, *Soft Matter* **2013**, 9, 6604 – 6617.
- [35] A. R. Tao, S. Habas, P. Yang, *Small* **2008**, 4, 310 – 325.
- [36] L. Carbone, P. D. Cozzoli, *Nano Today* **2010**, 5, 449 – 493.
- [37] C. Wang, C. Xu, H. Zeng, S. Sun, *Advanced Materials* **2009**, 21, 3045 – 3052.
- [38] M. J. Alvarez, J. T. Khoury, T. G. Schaaff, M. N. Shafiqullin, I. Vezmar, R. L. Whetten, *The Journal of Physical Chemistry B* **1997**, 101, 3706 – 3712.
- [39] N. J. Durr, T. Larson, D. K. Smith, B. A. Korgel, K. Sokolov, A. Ben-Yakar, *Nano Letters* **2007**, 7, 941 – 945.
- [40] J. F. Hainfeld, D. N. Slatkin, T. M. Focella, H. M. Smilowitz, *British Journal of Radiology* **2006**, 79, 248 – 253.
- [41] Q. Y. Cai, S. Kim, K. S. Choi, S. Y. Kim, S. J. Byun, K. W. Kim, S. H. Park, S. K. Juhng, K.-H. Yoon, *Investigative Radiology* **2007**, 42, 797 – 806.
- [42] R. Popovtzer, A. Agrawal, N. A. Kotov, A. Popovtzer, J. Balter, T. E. Carey, R. Kopelman, *Nano Letters* **2008**, 8, 4593 – 4596.
- [43] Y. Liu, K. Ai, L. Lu, *Accounts of Chemical Research* **2012**, 45, 1817 – 1827.
- [44] D. Xi, S. Dong, X. Meng, Q. Lu, L. Meng, J. Ye, *RSC Advances* **2012**, 2, 12515.
- [45] C. Sun, Lee, J. S. H., M. Zhang, *Advanced Drug Delivery Reviews* **2008**, 60, 1252 – 1265.
- [46] H. B. Na, I. C. Song, T. Hyeon, *Advanced Materials* **2009**, 21, 2133 – 2148.
- [47] T. D. Schladt, K. Schneider, M. I. Shukoor, F. Natalio, H. Bauer, M. N. Tahir, S. Weber, L. M. Schreiber, H. C. Schröder, Müller, Werner E. G. *et al.*, *Journal of Materials Chemistry* **2010**, 20, 8297 – 8304.
- [48] H. Yang, Y. Zhuang, H. Hu, X. Du, C. Zhang, X. Shi, H. Wu, S. Yang, *Advanced Functional Materials* **2010**, 20, 1733 – 1741.
- [49] R. Hao, R. Xing, Z. Xu, Y. Hou, S. Gao, S. Sun, *Advanced Materials* **2010**, 22, 2729 – 2742.
- [50] D. Ho, X. Sun, S. Sun, *Accounts of Chemical Research* **2011**, 44, 875 – 882.

- [51] T. D. Schladt, K. Koll, S. Prüfer, H. Bauer, F. Natalio, O. Dumele, R. Raidoo, S. Weber, U. Wolfrum, L. M. Schreiber *et al.*, *Journal of Materials Chemistry* **2012**, 22, 9253 – 9262.
- [52] B. J. Reynwar, G. Illya, V. A. Harmandaris, M. M. Müller, K. Kremer, M. Deserno, *Nature* **2007**, 447, 461 – 464.
- [53] A. Alexeev, W. E. Uspal, A. C. Balazs, *ACS Nano* **2008**, 2, 1117 – 1122.
- [54] I. Schick, S. Lorenz, D. Gehrig, A.-M. Schilmann, H. Bauer, M. Panthöfer, K. Fischer, D. Strand, F. Laquai, W. Tremel, *Journal of the American Chemical Society* **2014**, 136, 2473 – 2483.
- [55] M. Faraday, *Philosophical Transactions of the Royal Society of London* **1857**, 147, 145 – 181.
- [56] I. Freestone, N. Meeks, M. Sax, C. Higgitt, *Gold Bulletin* **2007**, 4, 270 – 277.
- [57] The British Museum, London,  
[http://www.britishmuseum.org/explore/highlights/highlight\\_objects/pe\\_mla/t/the\\_lycurgus\\_cup.aspx](http://www.britishmuseum.org/explore/highlights/highlight_objects/pe_mla/t/the_lycurgus_cup.aspx)  
(accessed 25.6.2014).
- [58] A. Maynard, <http://2020science.org/2009/04/29/control-at-the-nanoscale-smallness-strangeness-and-sophistication/#ixzz33Tg9U7aL> (accessed 30.6.2014).
- [59] G. Mie, *Annalen der Physik* **1908**, 3, 377 – 445.
- [60] R. Narayanan, M. A. El-Sayed, *The Journal of Physical Chemistry B* **2005**, 109, 12663 – 12676.
- [61] S. L. Suib (Ed.) "*New and Future Developments in Catalysis*", Elsevier, Amsterdam, **2013**.
- [62] S. Jeong, K. Woo, D. Kim, S. Lim, J. S. Kim, H. Shin, Y. Xia, J. Moon, *Advanced Functional Materials* **2008**, 18, 679 – 686.
- [63] A. W. Sanders, D. A. Routenberg, B. J. Wiley, Y. Xia, E. R. Dufresne, M. A. Reed, *Nano Letters* **2006**, 6, 1822 – 1826.
- [64] C. A. Mirkin, R. L. Letsinger, R. C. Mucic, J. J. Storhoff, *Nature* **1996**, 382, 607 – 609.
- [65] T. A. Taton, *Science* **2000**, 289, 1757 – 1760.
- [66] N. Nath, A. Chilkoti, *Analytical Chemistry* **2002**, 74, 504 – 509.
- [67] H. Cang, T. Sun, *Optics Letters* **2005**, 30, 3048 – 3050.
- [68] X. Yang, S. E. Skrabalak, Z.-Y. Li, Y. Xia, L. V. Wang, *Nano Letters* **2007**, 7, 3798 – 3802.
- [69] E. C. Dreaden, A. M. Alkilany, X. Huang, C. J. Murphy, M. A. El-Sayed, *Chemical Society Reviews* **2012**, 41, 2740.
- [70] Y. Xia, Y. Xiong, B. Lim, S. E. Skrabalak, *Angewandte Chemie International Edition* **2009**, 48, 60 – 103.
- [71] V. LaMer, R. H. Dinegar, *Journal of American Chemical Society* **1950**, 72, 4847 – 4854.
- [72] J. Park, J. Joo, S. G. Kwon, Y. Jang, T. Hyeon, *Angewandte Chemie International Edition* **2007**, 46, 4630 – 4660.
- [73] H. Hiramatsu, F. E. Osterloh, *Chemistry of Materials* **2004**, 16, 2509 – 2511.
- [74] N. R. Jana, L. Gearheart, C. J. Murphy, *Langmuir* **2001**, 17, 6782 – 6786.
- [75] T. K. Sau, C. J. Murphy, *Journal of the American Chemical Society* **2004**, 126, 8648 – 8649.
- [76] J. Zhang, H. Liu, Z. Wang, N. Ming, *Advanced Functional Materials* **2007**, 17, 3295 – 3303.
- [77] J. Pérez-Juste, I. Pastoriza-Santos, L. M. Liz-Marzán, P. Mulvaney, *Coordination Chemistry Reviews* **2005**, 249, 1870 – 1901.
- [78] M. Hu, J. Chen, Z.-Y. Li, L. Au, G. V. Hartland, X. Li, M. Marquez, Y. Xia, *Chemical Society Reviews* **2006**, 35, 1084 – 1094.

- [79] D. Boyer, P. Tarmarat, A. Maali, B. Lounis, M. Orrit, *Science* **2002**, 297, 1160 – 1163.
- [80] I.-C. Sun, D.-K. Eun, J. H. Na, S. Lee, I.-J. Kim, I.-C. Youn, C.-Y. Ko, H.-S. Kim, D. Lim, K. Choi *et al.*, *Chemistry - A European Journal* **2009**, 15, 13341 – 13347.
- [81] X. Huang, I. H. El-Sayed, W. Qian, M. A. El-Sayed, *Journal of the American Chemical Society* **2006**, 128, 2115 – 2120.
- [82] E. B. Dickerson, E. C. Dreaden, X. Huang, I. H. El-Sayed, H. Chu, S. Pushpanketh, J. F. McDonald, M. A. El-Sayed, *Cancer Letters* **2008**, 269, 57 – 66.
- [83] V. Salgueiriño-Maceira, M. A. Correa-Duarte, M. Farle, *Small* **2005**, 1, 1073 – 1076.
- [84] C.-H. Jun, Y. J. Park, Y.-R. Yeon, J.-r. Choi, W.-r. Lee, S.-j. Ko, J. Cheon, *Chemical Communications* **2006**, 1619 – 1621.
- [85] S. Kang, G. X. Miao, S. Shi, Z. Jia, D. E. Nikles, J. W. Harrell, *Journal of the American Chemical Society* **2006**, 128, 1042 – 1043.
- [86] M. I. Bodnarchuk, M. V. Kovalenko, H. Groiss, R. Resel, M. Reissner, G. Hesser, R. T. Lechner, W. Steiner, F. Schäffler, W. Heiss, *Small* **2009**, 5, 2247 – 2252.
- [87] M. I. Shukoor, F. Natalio, M. N. Tahir, V. Ksenofontov, H. A. Therese, P. Theato, H. C. Schröder, Müller, Werner E. G., W. Tremel, *Chemical Communications* **2007**, 4677 – 4679.
- [88] J. Luo, M. M. Maye, V. Petkov, N. N. Kariuki, L. Wang, P. Njoki, D. Mott, Y. Lin, C.-J. Zhong, *Chemistry of Materials* **2005**, 17, 3086 – 3091.
- [89] J. A. Creighton, D. G. Eadon, *Journal of the Chemical Society, Faraday Transactions* **1991**, 87, 3881 – 3891.
- [90] D. Wang, Y. Li, *Advanced Materials* **2011**, 23, 1044 – 1060.
- [91] D. Wang, Q. Peng, Y. Li, *Nano Research* **2010**, 3, 574 – 580.
- [92] S. E. Habas, H. Lee, V. Radmilovic, G. A. Somorjai, P. Yang, *Nature Materials* **2007**, 6, 692 – 697.
- [93] Y.-C. Lu, Z. Xu, H. A. Gasteiger, S. Chen, K. Hamad-Schifferli, Y. Shao-Horn, *Journal of the American Chemical Society* **2010**, 132, 12170 – 12171.
- [94] U. Banin, *Nature Materials* **2007**, 6, 625 – 626.
- [95] Z. L. Wang, M. B. Mohamed, S. Link, M. A. El-Sayed, *Surface Science* **1999**, 440, 809 – 814.
- [96] B. Nikoobakht, M. A. El-Sayed, *Chemistry of Materials* **2003**, 15, 1957 – 1962.
- [97] C. Wang, Z. Ma, T. Wang, Z. Su, *Advanced Functional Materials* **2006**, 16, 1673 – 1678.
- [98] L. Vigderman, B. P. Khanal, E. R. Zubarev, *Advanced Materials* **2012**, 24, 4811 – 4841.
- [99] S. Narayanan, B. N. Sathy, U. Mony, M. Koyakutty, S. V. Nair, D. Menon, *ACS Applied Materials & Interfaces* **2012**, 4, 251 – 260.
- [100] Z. Wang, S. Zong, J. Yang, J. Li, Y. Cui, *Biosensors and Bioelectronics* **2011**, 26, 2883 – 2889.
- [101] Z. Zhang, L. Wang, J. Wang, X. Jiang, X. Li, Z. Hu, Y. Ji, X. Wu, C. Chen, *Advanced Materials* **2012**, 24, 1418 – 1423.
- [102] J. Turkevich, P. C. Stevenson, J. Hillier, *Discussions of the Faraday Society* **1951**, 11, 55 – 75.
- [103] G. Schmid, R. Pfeil, R. Boese, F. Bändermann, S. Meyer, G. Calis, van der Welden, Jan W.A., *Chemische Berichte* **1981**, 114, 3634 – 3642.
- [104] M. Brust, M. Walker, D. Bethell, D. J. Schiffrin, R. Whyman, *Journal of the Chemical Society, Chemical Communications*, 1994, 801 – 802.

- [105] N. Zheng, J. Fan, G. D. Stucky, *Journal of the American Chemical Society* **2006**, *128*, 6550 – 6551.
- [106] S. Peng, Y. Lee, C. Wang, H. Yin, S. Dai, S. Sun, *Nano Research* **2008**, *1*, 229 – 234.
- [107] C. B. Murray, C. R. Kagan, M. G. Bawendi, *Science* **1995**, *270*, 1335 – 1338.
- [108] S. I. Stoeva, Prasad, B. L. V., S. Uma, P. K. Stoimenov, V. Zaikovski, C. M. Sorensen, K. J. Klabunde, *The Journal of Physical Chemistry B* **2003**, *107*, 7441 – 7448.
- [109] O. C. Compton, F. E. Osterloh, *Journal of the American Chemical Society* **2007**, *129*, 7793 – 7798.
- [110] N. R. Jana, L. Gearheart, C. J. Murphy, *Chemistry of Materials* **2001**, *13*, 2313 – 2322.
- [111] G. Carrot, J. C. Valmalette, C. Plummer, S. M. Scholz, J. Dutta, H. Hofmann, J. G. Hilborn, *Colloid & Polymer Science* **1998**, *276*, 853 – 859.
- [112] S. Meltzer, R. Resch, B. E. Koel, M. E. Thompson, A. Madhukar, Requicha, Aristides A. G., P. Will, *Langmuir* **2001**, *17*, 1713 – 1718.
- [113] M.-C. Daniel, D. Astruc, *Chemical Reviews* **2004**, *104*, 293 – 346.
- [114] K. L. Kelly, E. Coronado, L. L. Zhao, G. C. Schatz, *The Journal of Physical Chemistry B* **2003**, *107*, 668 – 677.
- [115] U. Kreibig, L. Genzel, *Surface Science* **1985**, *156*, 678 – 700.
- [116] S. L. Logunov, T. S. Ahmadi, M. A. El-Sayed, *The Journal of Physical Chemistry B* **1997**, *101*, 3713 – 3719.
- [117] T. P. Martin, *Physics Reports* **1996**, *273*, 199 – 241.
- [118] W. A. de Heer, *Reviews of Modern Physics* **1993**, *65*, 611 – 676.
- [119] A. Henglein, *J. Phys. Chem. (The Journal of Physical Chemistry)* **1993**, *97*, 5457 – 5471.
- [120] T. D. Schladt, Dissertation, "Design of Multifunctional Magnetic Nanomaterials for Biomedical Applications", Johannes Gutenberg-Universität, Mainz, **2010**.
- [121] X. Peng, J. Wickham, A. P. Alivisatos, *Journal of the American Chemical Society* **1998**, *120*, 5343 – 5344.
- [122] C. E. Ashley, E. C. Carnes, G. K. Phillips, D. Padilla, P. N. Durfee, P. A. Brown, T. N. Hanna, J. Liu, B. Phillips, M. B. Carter *et al.*, *Nature Materials* **2011**, *10*, 389 – 397.
- [123] M. R. Rasch, E. Rossinyol, J. L. Hueso, B. W. Goodfellow, J. Arbiol, B. A. Korgel, *Nano Letters* **2010**, *10*, 3733 – 3739.
- [124] M. Grzelczak, P. Mulvaney, L. M. Liz-Marzán, *Chemical Society Reviews* **2008**, *37*, 1783 – 1791.
- [125] K. Bishop, C. E. Wilmer, S. Soh, B. A. Grzybowski, *Small* **2009**, *5*, 1600 – 1630.
- [126] S. C. Glotzer, M. J. Solomon, *Nature Materials* **2007**, *557* – 562.
- [127] M. P. Pileni, *Journal of Colloid and Interface Science* **2012**, *388*, 1 – 8.
- [128] Zhang, S. C. Glotzer, *Nano Letters* **2004**, *4*, 1407 – 1413.
- [129] C. B. Murray, C. R. Kagan, M. G. Bawendi, *Annual Review of Materials Research* **2000**, *30*, 545 – 610.
- [130] H. Alaeian, J. A. Dionne, *Optics Express* **2012**, *20*, 15781 – 15796.
- [131] J. V. Sanders, *Acta Crystallographica* **1968**, *A24*, 427 – 434.
- [132] C. Hrelescu, J. Stehr, M. Ringler, R. A. Sperling, W. J. Parak, T. A. Klar, J. Feldmann, *The Journal of Physical Chemistry C* **2010**, *114*, 7401 – 7411.

- [133] A. Sanchot, G. Baffou, R. Marty, A. Arbouet, R. Quidant, C. Girard, E. Dujardin, *ACS Nano* **2012**, *6*, 3434 – 3440.
- [134] K. Shimizu, W. Woo, B. Fisher, H. Eisler, M. Bawendi, *Physical Review Letters* **2002**, *89*.
- [135] K. Okamoto, S. Vyawahare, A. Scherer, *Journal of the Optical Society of America B* **2006**, *23*, 1674 – 1678.
- [136] R. Alvarez-Puebla, L. M. Liz-Marzán, García de Abajo, F. Javier, *The Journal of Physical Chemistry Letters* **2010**, *1*, 2428 – 2434.
- [137] A. Sánchez-Iglesias, P. Aldeanueva-Potel, W. Ni, J. Pérez-Juste, I. Pastoriza-Santos, R. A. Alvarez-Puebla, B. N. Mbenkum, L. M. Liz-Marzán, *Nano Today* **2010**, *5*, 21 – 27.
- [138] Z. Nie, A. Petukhova, E. Kumacheva, *Nature Nanotechnology* **2009**, *5*, 15 – 25.
- [139] T. P. Bigioni, X.-M. Lin, T. T. Nguyen, E. I. Corwin, T. A. Witten, H. M. Jaeger, *Nature Materials* **2006**, *5*, 265 – 270.
- [140] Y. Min, M. Akbulut, K. Kristiansen, Y. Golan, J. Israelachvili, *Nature Materials* **2008**, *7*, 527 – 538.
- [141] B. Prasad, C. M. Sorensen, K. J. Klabunde, *Chemical Society Reviews* **2008**, *37*, 1871.
- [142] Z. L. Wang, *Advanced Materials* **1998**, *10*, 13 – 30.
- [143] J. Chen, T. Herricks, Y. Xia, *Angewandte Chemie International Edition* **2005**, *44*, 2589 – 2592.
- [144] C. Wang, H. Daimon, T. Onodera, T. Koda, S. Sun, *Angewandte Chemie International Edition* **2008**, *47*, 3588 – 3591.
- [145] M. R. Buck, J. F. Bondi, R. E. Schaak, *Nature Chemistry* **2011**, *4*, 37 – 44.
- [146] S. Chen, K. Kimura, *The Journal of Physical Chemistry B* **2001**, *105*, 5397 – 5403.
- [147] J. Chen, T. Herricks, M. Geissler, Y. Xia, *Journal of the American Chemical Society* **2004**, *126*, 10854 – 10855.
- [148] A. Demortière, P. Launois, N. Goubet, P.-A. Albouy, C. Petit, *The Journal of Physical Chemistry B* **2008**, *112*, 14583 – 14592.
- [149] C. Wang, W. Tian, Y. Ding, Y.-q. Ma, Z. L. Wang, N. M. Markovic, V. R. Stamenkovic, H. Daimon, S. Sun, *Journal of the American Chemical Society* **2010**, *132*, 6524 – 6529.
- [150] C. Wang, H. Yin, R. Chan, S. Peng, S. Dai, S. Sun, *Chemistry of Materials* **2009**, *21*, 433 – 435.
- [151] I. Schick, S. Lorenz, D. Gehrig, S. Tenzer, W. Storck, K. Fischer, D. Strand, F. Laquai, W. Tremel, *Beilstein Journal of Nanotechnology* **2014**, *submitted*.
- [152] H. Zeng, S. Sun, *Advanced Functional Materials* **2008**, *18*, 391 – 400.
- [153] H. Yu, M. Chen, P. M. Rice, S. X. Wang, R. L. White, S. Sun, *Nano Letters* **2005**, *5*, 379 – 382.
- [154] H. Gu, R. Zheng, X. Zhang, B. Xu, *Journal of the American Chemical Society* **2004**, *126*, 5664 – 5665.
- [155] C. Wang, Y. Wei, H. Jiang, S. Sun, *Nano Letters* **2009**, *9*, 4544 – 4547.
- [156] B. Nakhjavan, M. N. Tahir, F. Natalio, H. Gao, K. Schneider, T. Schladt, I. Ament, R. Branscheid, S. Weber, U. Kolb *et al.*, *Journal of Materials Chemistry* **2011**, *21*, 8605 – 8611.
- [157] B. Nakhjavan, M. N. Tahir, M. Panthöfer, H. Gao, T. Gasi, V. Ksenofontov, R. Branscheid, S. Weber, U. Kolb, L. M. Schreiber *et al.*, *Chemical Communications* **2011**, *47*, 8898 – 8900.
- [158] B. Nakhjavan, M. N. Tahir, F. Natalio, M. Panthöfer, H. Gao, M. Dietzsch, R. Andre, T. Gasi, V. Ksenofontov, R. Branscheid *et al.*, *Nanoscale* **2012**, *4*, 4571 – 4577.
- [159] C. Wang, H. Yin, S. Dai, S. Sun, *Chemistry of Materials* **2010**, *22*, 3277 – 3282.

- [160] H. Gu, Z. Yang, J. Gao, C. K. Chang, B. Xu, *Journal of the American Chemical Society* **2005**, *127*, 34 – 35.
- [161] T. Teranishi, M. Saruyama, M. Kanehara, *Nanoscale* **2009**, *1*, 225 – 228.
- [162] Y. Jang, J. Chung, S. Kim, S. W. Jun, B. H. Kim, D. W. Lee, B. M. Kim, T. Hyeon, *Physical Chemistry Chemical Physics* **2011**, *13*, 2512 – 2516.
- [163] C. Xu, J. Xie, D. Ho, C. Wang, N. Kohler, E. G. Walsh, J. R. Morgan, Y. E. Chin, S. Sun, *Angewandte Chemie International Edition* **2008**, *47*, 173 – 176.
- [164] Y. Wei, Bishop, Kyle J. M., J. Kim, S. Soh, B. A. Grzybowski, *Angewandte Chemie International Edition* **2009**, *48*, 9477 – 9480.
- [165] F.-h. Lin, W. Chen, Y.-H. Liao, R.-a. Doong, Y. Li, *Nano Research* **2011**, *4*, 1223 – 1232.
- [166] B. Wu, S. Tang, M. Chen, N. Zheng, *Chemical Communications* **2014**, *50*, 174 – 176.
- [167] G. Lopes, J. M. Vargas, S. K. Sharma, F. Béron, K. R. Pirola, M. Knobel, C. Rettori, R. D. Zysler, *The Journal of Physical Chemistry C* **2010**, *114*, 10148 – 10152.
- [168] T. D. Schladt, M. I. Shukoor, K. Schneider, M. N. Tahir, F. Natalio, I. Ament, J. Becker, F. D. Jochum, S. Weber, O. Köhler *et al.*, *Angewandte Chemie International Edition* **2010**, *49*, 3976 – 3980.
- [169] L. Zhang, Y.-H. Dou, H.-C. Gu, *Journal of Colloid and Interface Science* **2006**, *297*, 660 – 664.
- [170] Y.-w. Jun, J.-w. Seo, J. Cheon, *Accounts of Chemical Research* **2008**, *41*, 179 – 189.
- [171] T. D. Schladt, K. Schneider, H. Schild, W. Tremel, *Dalton Transactions* **2011**, *40*, 6315.
- [172] N. Kamaly, Z. Xiao, P. M. Valencia, A. F. Radovic-Moreno, O. C. Farokhzad, *Chemical Society Reviews* **2012**, *41*, 2971 – 3010.
- [173] Y. Jun, J. Lee, J. Cheon, *Angewandte Chemie International Edition* **2008**, *47*, 5122 – 5135.
- [174] H. B. Na, J. H. Lee, K. An, Y. I. Park, M. Park, I. S. Lee, D.-H. Nam, S. T. Kim, S.-H. Kim, S.-W. Kim *et al.*, *Angewandte Chemie International Edition* **2007**, *46*, 5397 – 5401.
- [175] N. R. Jana, Y. Chen, X. Peng, *Chemistry of Materials* **2004**, *16*, 3931 – 3935.
- [176] Y. Chen, E. Johnson, X. Peng, *Journal of the American Chemical Society* **2007**, *129*, 10937 – 10947.
- [177] T. D. Schladt, T. Graf, W. Tremel, *Chemistry of Materials* **2009**, *21*, 3183 – 3190.
- [178] S. Mourdikoudis, L. M. Liz-Marzán, *Chemistry of Materials* **2013**, *25*, 1465 – 1476.
- [179] L. M. Bronstein, X. Huang, J. Retrum, A. Schmucker, M. Pink, B. D. Stein, B. D. D. Dragnea, *Chemistry of Materials* **2007**, *19*, 3624 – 3632.
- [180] L. M. Liz-Marzán, M. Giersig, P. Mulvaney, *Langmuir* **1996**, *12*, 4329 – 4335.
- [181] H.-Y. Park, M. J. Schadt, Wang, I.-I. S. Lim, P. N. Njoki, S. H. Kim, M.-Y. Jang, J. Luo, C.-J. Zhong, *Langmuir* **2007**, *23*, 9050 – 9056.
- [182] E. V. Shevchenko, M. I. Bodnarchuk, M. V. Kovalenko, D. V. Talapin, R. K. Smith, S. Aloni, W. Heiss, A. P. Alivisatos, *Advanced Materials* **2008**, *20*, 4323 – 4329.
- [183] Y. Wei, R. Klajn, A. O. Pinchuk, B. A. Grzybowski, *Small* **2008**, *4*, 1635 – 1639.
- [184] M. Ghosh, K. Biswas, A. Sundaresan, Rao, C. N. R., *Journal of Materials Chemistry* **2006**, *16*, 106 – 111.
- [185] W.-r. Lee, M. G. Kim, J.-r. Choi, J.-I. Park, S. J. Ko, S. J. Oh, J. Cheon, *Journal of the American Chemical Society* **2005**, *127*, 16090 – 16097.

- [186] R. J. Hill, C. J. Howard, *Journal of Applied Crystallography* **1987**, *20*, 467 – 474.
- [187] W. S. Seo, H. H. Jo, K. Lee, B. Kim, S. J. Oh, J. T. Park, *Angewandte Chemie International Edition* **2004**, *43*, 1115 – 1117.
- [188] B. Martinez, X. Obradors, L. Balcells, A. Rouanet, C. Monty, *Phys. Rev. Lett.* **1998**, *80*, 181 – 184.
- [189] J. Nogués, J. Sort, V. Langlais, V. Skumryev, S. Suriñach, J. S. Muñoz, M. D. Baró, *Physics Reports* **2005**, *422*, 65 – 117.
- [190] J. Park, K. An, Y. Hwang, J.-G. Park, H.-J. Noh, J.-Y. Kim, J.-H. Park, N.-M. Hwang, T. Hyeon, *Nature Materials* **2004**, *3*, 891 – 895.
- [191] S. Cheong, P. Ferguson, K. W. Feindel, I. F. Hermans, P. T. Callaghan, C. Meyer, A. Slocombe, C.-H. Su, F.-Y. Cheng, C.-S. Yeh *et al.*, *Angewandte Chemie International Edition* **2011**, *50*, 4206 – 4209.
- [192] D. Kim, M. K. Yu, T. S. Lee, J. J. Park, Y. Y. Jeong, S. Jon, *Nanotechnology* **2011**, *22*, 155101.
- [193] C. Hoskins, Y. Min, M. Gueorguieva, C. McDougall, A. Volovick, P. Prentice, Z. Wang, A. Melzer, A. Cuschieri, L. Wang, *Journal of Nanobiotechnology* **2012**, *10*, 27.
- [194] J. Salado, M. Insausti, L. Lezama, Muro, I. Gil de, M. Moros, B. Pelaz, V. Grazu, Fuente, Jesús M. de la, T. Rojo, *Nanotechnology* **2012**, *23*, 315102.
- [195] E. Umut, F. Pineider, P. Arosio, C. Sangregorio, M. Corti, F. Tabak, A. Lascialfari, P. Ghigna, *Journal of Magnetism and Magnetic Materials* **2012**, *324*, 2373 – 2379.
- [196] D. K. Kirui, D. A. Rey, C. A. Batt, *Nanotechnology* **2010**, *21*, 105105.
- [197] Y. Sheng, J. Xue, *Journal of Colloid and Interface Science* **2012**, *374*, 96 – 101.
- [198] Wang, J. Luo, Q. Fan, M. Suzuki, I. S. Suzuki, M. H. Engelhard, Y. Lin, N. Kim, J. Q. Wang, C.-J. Zhong, *The Journal of Physical Chemistry B* **2005**, *109*, 21593 – 21601.
- [199] W. Gao, L. Ji, L. Li, G. Cui, K. Xu, P. Li, B. Tang, *Biomaterials* **2012**, *33*, 3710 – 3718.
- [200] M. V. Kovalenko, M. I. Bodnarchuk, R. T. Lechner, G. Hesser, F. Schäffler, W. Heiss, *Journal of the American Chemical Society* **2007**, *129*, 6352 – 6353.
- [201] S. Sun, H. Zeng, D. B. Robinson, S. Raoux, P. M. Rice, S. X. Wang, G. Li, *Journal of the American Chemical Society* **2004**, *126*, 273 – 279.
- [202] A. F. Oliveri, E. W. Elliott, M. E. Carnes, J. E. Hutchison, D. W. Johnson, *ChemPhysChem* **2013**, *14*, 2655 – 2661.
- [203] W. Shi, H. Zeng, Y. Sahoo, T. Y. Ohulchanskyy, Y. Ding, Z. L. Wang, M. Swihart, P. N. Prasad, *Nano Letters* **2006**, *6*, 875 – 881.
- [204] S. G. Kwon, Y. Piao, J. Park, S. Angappane, Y. Jo, N.-M. Hwang, J.-G. Park, T. Hyeon, *Journal of the American Chemical Society* **2007**, *129*, 12571 – 12584.
- [205] X. Sun, N. Frey Huls, A. Sigdel, S. Sun, *Nano Letters* **2012**, *12*, 246 – 251.
- [206] B. H. Kim, N. Lee, H. Kim, K. An, Y. I. Park, Y. Choi, K. Shin, Y. Lee, S. G. Kwon, H. B. Na *et al.*, *Journal of the American Chemical Society* **2011**, *133*, 12624 – 12631.
- [207] E. Lima, A. L. Brandl, A. D. Arelaro, G. F. Goya, *Journal of Applied Physics* **2006**, *99*, 083908.
- [208] R. Müller, R. Hergt, S. Dutz, M. Zeisberger, W. Gawalek, *Journal of Physics: Condensed Matter* **2006**, *18*, 2527 – 2542.
- [209] F. Walz, *Journal of Physics: Condensed Matter* **2002**, *14*, R285 – R340.



- [210] V. Subramanian, E. E. Wolf, P. V. Kamat, *Journal of the American Chemical Society* **2004**, *126*, 4943 – 4950.
- [211] Y.-S. Chen, H. Choi, P. V. Kamat, *Journal of the American Chemical Society* **2013**, *135*, 8822 – 8825.
- [212] Y. H. Jang, Y. J. Jang, S. T. Kochuveedu, M. Byun, Z. Lin, D. H. Kim, *Nanoscale* **2014**, *6*, 1823 – 1832.
- [213] T. Hirakawa, P. V. Kamat, *Journal of the American Chemical Society* **2005**, *127*, 3928 – 3934.
- [214] Y. Lee, M. A. Garcia, Frey Huls, Natalie A., S. Sun, *Angewandte Chemie* **2010**, *122*, 1293 – 1296.
- [215] A. Furube, L. Du, K. Hara, R. Katoh, M. Tachiya, *Journal of the American Chemical Society* **2007**, *129*, 14852 – 14853.
- [216] Z. Xu, Y. Hou, S. Sun, *Journal of the American Chemical Society* **2007**, *129*, 8698 – 8699.
- [217] I. Thomann, B. A. Pinaud, Z. Chen, B. M. Clemens, T. F. Jaramillo, M. L. Brongersma, *Nano Letters* **2011**, *11*, 3440 – 3446.
- [218] K. Korobchevskaya, C. George, A. Diaspro, L. Manna, R. Cingolani, A. Comin, *Applied Physics Letters* **2011**, *99*, 011907.
- [219] C. George, A. Genovese, F. Qiao, K. Korobchevskaya, A. Comin, A. Falqui, S. Marras, A. Roig, Y. Zhang, R. Krahne *et al.*, *Nanoscale* **2011**, *3*, 4647 – 4654.
- [220] A. Comin, K. Korobchevskaya, C. George, A. Diaspro, L. Manna, *Nano Letters* **2012**, *12*, 921 – 926.
- [221] C. Wang, Y. Hou, J. Kim, S. Sun, *Angewandte Chemie International Edition* **2007**, *46*, 6333 – 6335.
- [222] P. Dutta, A. Manivannan, M. Seehra, N. Shah, G. Huffman, *Physical Review B* **2004**, *70*, 174428.
- [223] M. Hatakeyama, H. Kishi, Y. Kita, K. Imai, K. Nishio, S. Karasawa, Y. Masaike, S. Sakamoto, A. Sandhu, A. Tanimoto *et al.*, *Journal of Materials Chemistry* **2011**, *21*, 5959 – 5966.
- [224] R. Mout, D. F. Moyano, S. Rana, V. M. Rotello, *Chemical Society Reviews* **2012**, *41*, 2539 – 2544.
- [225] S. K. Basiruddin, A. Saha, N. Pradhan, N. R. Jana, *The Journal of Physical Chemistry C* **2010**, *114*, 11009 – 11017.
- [226] N. T. Thanh, L. A. Green, *Nano Today* **2010**, *5*, 213 – 230.
- [227] B. Pelaz, S. Jaber, de Aberasturi, Dorleta Jimenez, V. Wulf, T. Aida, Fuente, Jesús M. de la, J. Feldmann, H. E. Gaub, L. Josephson, C. R. Kagan *et al.*, *ACS Nano* **2012**, *6*, 8468 – 8483.
- [228] C. Graf, Q. Gao, I. Schütz, C. N. Noufele, W. Ruan, U. Posselt, E. Korotianskiy, D. Nordmeyer, F. Rancan, S. Hadam *et al.*, *Langmuir* **2012**, *28*, 7598 – 7613.
- [229] S. Santra, H. Yang, D. Dutta, J. T. Stanley, P. H. Holloway, W. Tan, B. M. Moudgil, R. A. Mericle, *Chemical Communications* **2004**, 2810.
- [230] D. C. Lee, F. V. Mikulec, J. M. Pelaez, B. Koo, B. A. Korgel, *The Journal of Physical Chemistry B* **2006**, *110*, 11160 – 11166.
- [231] G. A. Sotiriou, A. M. Hirt, P.-Y. Lozach, A. Teleki, F. Krumeich, S. E. Pratsinis, *Chemistry of Materials* **2011**, *23*, 1985 – 1992.
- [232] R. P. Bagwe, L. R. Hilliard, W. Tan, *Langmuir* **2006**, *22*, 4357 – 4362.
- [233] S. M. Moghimi, A. C. Hunter, J. C. Murry, *Pharmacological Reviews* **2001**, *53*, 283 – 318.

- [234] M. A. Dobrovolskaia, P. Aggarwal, J. B. Hall, S. E. McNeil, *Molecular Pharmaceutics* **2008**, *5*, 487 – 495.
- [235] M. A. Correa-Duarte, M. Giersig, L. M. Liz-Marzán, *Chemical Physics Letters* **1998**, *286*, 497 – 501.
- [236] A. L. Rogach, D. Nagesha, J. W. Ostrander, M. Giersig, N. A. Kotov, *Chemistry of Materials* **2000**, *12*, 2676 – 2685.
- [237] S. Santra, R. Tapeç, N. Theodoropoulou, J. Dobson, A. Hebard, W. Tan, *Langmuir* **2001**, *17*, 2900 – 2906.
- [238] Y. Kobayashi, M. A. Correa-Duarte, L. M. Liz-Marzán, *Langmuir* **2001**, *17*, 6375 – 6379.
- [239] T. Tago, T. Hatsua, K. Miyajima, M. Kishida, S. Tashiro, K. Wakabayashi, *J. Am. Ceram. Soc.* **2002**, *85*, 2188 – 2194.
- [240] A. Schroedter, H. Weller, *Angewandte Chemie International Edition* **2002**, *41*, 3218 – 3221.
- [241] Y. Chan, J. P. Zimmer, M. Stroh, J. S. Steckel, R. K. Jain, M. G. Bawendi, *Advanced Materials* **2004**, *16*, 2092 – 2097.
- [242] A. Guerrero-Martínez, J. Pérez-Juste, L. M. Liz-Marzán, *Advanced Materials* **2010**, *22*, 1182 – 1195.
- [243] T. Kim, E. Momin, J. Choi, K. Yuan, H. Zaidi, J. Kim, M. Park, N. Lee, M. T. McMahon, A. Quinones-Hinojosa *et al.*, *Journal of the American Chemical Society* **2011**, *133*, 2955 – 2961.
- [244] W. Stöber, A. Fink, E. Bohn, *Journal of Colloid and Interface Science* **1968**, *26*, 62 – 69.
- [245] Y. Kobayashi, H. Katakami, E. Mine, D. Nagao, M. Konno, L. M. Liz-Marzán, *Journal of Colloid and Interface Science* **2005**, *283*, 392 – 396.
- [246] Y. Han, J. Jiang, S. S. Lee, J. Y. Ying, *Langmuir* **2008**, *24*, 5842 – 5848.
- [247] D. Gerion, F. Pinaud, S. C. Williams, W. J. Parak, D. Zanchet, S. Weiss, A. P. Alivisatos, *The Journal of Physical Chemistry B* **2001**, *105*, 8861 – 8871.
- [248] T. Nann, P. Mulvaney, *Angewandte Chemie International Edition* **2004**, *43*, 5393 – 5396.
- [249] C. C. Berry, A. Curtis, *Journal of Physics D: Applied Physics* **2003**, *36*, R198-R206.
- [250] D. K. Yi, S. T. Selvan, S. S. Lee, G. C. Papaefthymiou, D. Kundaliya, J. Y. Ying, *Journal of the American Chemical Society* **2005**, *127*, 4990 – 4991.
- [251] S. T. Selvan, T. T. Tan, J. Y. Ying, *Advanced Materials* **2005**, *17*, 1620 – 1625.
- [252] M. Darbandi, R. Thomann, T. Nann, *Chemistry of Materials* **2005**, *17*, 5720 – 5725.
- [253] E. Amstad, S. Zurcher, A. Mashaghi, J. Y. Wong, M. Textor, E. Reimhult, *Small* **2009**, *5*, 1334 – 1342.
- [254] T. L. Doane, C. Burda, *Chemical Society Reviews* **2012**, *41*, 2885 – 2911.
- [255] D.-E. Lee, H. Koo, I.-C. Sun, J. H. Ryu, K. Kim, I. C. Kwon, *Chemical Society Reviews* **2012**, *41*, 2656 – 2672.
- [256] E. M. Sevick-Muraca, J. P. Houston, M. Gurfinkel, *Current Opinion in Chemical Biology* **2002**, *6*, 642 – 650.
- [257] A. van Blaaderen, A. Vrij, *Langmuir* **1992**, 2921 – 2931.
- [258] A. Imhof, M. Megens, J. J. Engelberts, de Lang, D. T. N., R. Sprik, W. L. Vos, *The Journal of Physical Chemistry B* **1999**, *103*, 1408 – 1415.

- [259] L. Wang, K. Wang, S. Santra, X. Zhao, L. R. Hilliard, J. E. Smith, Y. Wu, W. Tan, *Analytical Chemistry* **2006**, 647 – 654.
- [260] J. Xie, C. Xu, N. Kohler, Y. Hou, S. Sun, *Advanced Materials* **2007**, 19, 3163 – 3166.
- [261] C. A. Simpson, A. C. Agrawal, A. Balinski, K. M. Harkness, D. E. Cliffler, *ACS Nano* **2011**, 5, 3577 – 3584.
- [262] B. Derjaguin, L. Landau, *Acta Physicochim. URSS* **1941**, 14, 633.
- [263] E. Verwey, J. Overbeek, "Theory of the stability of lyophobic colloids. The interaction of sol particles having an electric double layer", Elsevier, Amsterdam, **1948**.
- [264] E. Verwey, J. Overbeek, *Kolloid-Zeitschrift* **1955**, 141, 44 – 45.
- [265] A. E. Nel, L. Mädler, D. Velegol, T. Xia, Hoek, Eric M. V., P. Somasundaran, F. Klaessig, V. Castranova, M. Thompson, *Nature Materials* **2009**, 8, 543 – 557.
- [266] C. Schneider, Dissertation, "The Surface Charge of Soft and Hard Sphere Colloidal Particles", University Bayreuth, Berlin, **2010**.
- [267] F. Natalio, A. Kashyap, S. Lorenz, H. Kerschbaumer, M. Dietzsch, M. N. Tahir, H. Duschner, S. Strand, D. Strand, W. Tremel, *Nanoscale* **2012**, 4, 4680 – 4686.
- [268] Y. Yang, M. Y. Gao, *Advanced Materials* **2005**, 17, 2354 – 2357.
- [269] F. Laquai, Y.-S. Park, J.-J. Kim, T. Basché, *Macromolecular Rapid Communications* **2009**, 30, 1203 – 1231.
- [270] J. Wang, B. H. Toby, P. L. Lee, L. Ribaud, S. M. Antao, C. Kurtz, M. Ramanathan, R. B. von Dreele, M. A. Beno, *Review of Scientific Instruments* **2008**, 79, 085105.
- [271] P. L. Lee, D. Shu, M. Ramanathan, C. Preissner, J. Wang, M. A. Beno, R. B. von Dreele, L. Ribaud, C. Kurtz, S. M. Antao *et al.*, *Journal of Synchrotron Radiation* **2008**, 15, 427 – 432.
- [272] C. Preissner, D. Shu, B. H. Toby, P. Lee, J. Wang, D. Kline, K. Goetze, Nuclear Instruments and Methods in Physics Research Section A: Accelerators, Spectrometers, Detectors and Associated Equipment **2009**, in press.
- [273] L. R. Dalesio, J. O. Hill, M. Kraimer, S. Lewis, D. Murray, S. Hunt, W. Watson, M. Clausen, J. Dalesio, *Nuclear Instruments & Methods in Physics Research Section A* **1994**, 352, 179 – 184.
- [274] A. Coelho, "TOPAS Academic V5", Coelho Software, Brisbane, Australia, **2007**.
- [275] A. Walther, Müller, Axel H. E., *Chemical Reviews* **2013**, 113, 5194 – 5261.
- [276] N. Zhao, M. Gao, *Advanced Materials* **2009**, 21, 184 – 187.
- [277] T. Mokari, *Science* **2004**, 304, 1787 – 1790.
- [278] D. Rodríguez-Fernández, L. M. Liz-Marzán, *Particle & Particle Systems Characterization* **2013**, 30, 46 – 60.
- [279] Y. J. Jang, D. H. Kim, *Chemistry - A European Journal* **2011**, 17, 540 – 545.
- [280] Z. W. Seh, S. Liu, M. Low, S.-Y. Zhang, Z. Liu, A. Mlayah, M.-Y. Han, *Advanced Materials* **2012**, 24, 2310 – 2314.
- [281] C. Wang, J. Irudayaraj, *Small* **2010**, 6, 283 – 289.
- [282] J. Lim, S. A. Majetich, *Nano Today* **2013**, 8, 98 – 113.
- [283] C. Casagrande, P. Fabre, E. Raphael, M. Veyssié, *Europhysics Letters* **1989**, 9, 251 – 255.
- [284] L. Hong, S. Jiang, S. Granick, *Langmuir* **2006**, 22, 9495 – 9499.
- [285] S. Jiang, M. J. Schultz, Q. Chen, J. S. Moore, S. Granick, *Langmuir* **2008**, 24, 10073 – 10077.

- [286] A. Perro, F. Meunier, V. Schmitt, S. Ravaine, *Colloids and Surfaces A: Physicochemical and Engineering Aspects* **2009**, 332, 57 – 62.
- [287] Z. Nie, W. Li, M. Seo, S. Xu, E. Kumacheva, *Journal of the American Chemical Society* **2006**, 128, 9408 – 9412.
- [288] K.-H. Roh, D. C. Martin, J. Lahann, *Nature Materials* **2005**, 4, 759 – 763.
- [289] A. Klinkova, H. Therien-Aubin, R. M. Choueiri, M. Rubinstein, E. Kumacheva, *Proceedings of the National Academy of Sciences* **2013**, 110, 18775 – 18779.
- [290] Y. Song, S. Chen, *Langmuir* **2014**, 30, 6389 – 6397.
- [291] P. R. Sajanlal, T. S. Sreeprasad, A. K. Samal, T. Pradeep, *Nano Reviews* **2011**, 2, 53.
- [292] D. Hirsemann, S. Shylesh, De Souza, Roger A., B. Diar-Bakerly, B. Biersack, D. N. Mueller, M. Martin, R. Schobert, J. Breu, *Angewandte Chemie International Edition* **2012**, 51, 1348 – 1352.
- [293] S. Weiss, D. Hirsemann, B. Biersack, M. Ziadeh, A. H. Müller, J. Breu, *Polymer* **2013**, 54, 1388 – 1396.
- [294] W. Ramsden, *Proceedings of the Royal Society of London A* **1903**, 72, 156 – 164.
- [295] S. Pickering, *Journal of the Chemical Society, Transactions* **1907**, 91, 2001 – 2021.
- [296] P. Pieranski, *Physical Review Letters* **1980**, 45, 569 – 572.
- [297] A. Böker, J. He, T. Emrick, T. P. Russell, *Soft Matter* **2007**, 3, 1231.
- [298] B. P. Binks, P. Fletcher, *Langmuir* **2001**, 17, 4708 – 4710.
- [299] N. Glaser, D. J. Adams, A. Böker, G. Krausch, *Langmuir* **2006**, 22, 5227 – 5229.
- [300] S. Förster, T. Plantenberg, *Angewandte Chemie International Edition* **2012**, 41, 688 – 714.
- [301] J. N. Israelachvili, *"Intermolecular and surface forces"*, Academic Press, Burlington, MA, **2011**.
- [302] L. Zhang, A. Eisenberg, *Science* **1995**, 268, 1728 – 1731.
- [303] C. A. Tolman, *Chemical Reviews* **1977**, 77, 313 – 348.
- [304] C. Xu, K. Xu, H. Gu, R. Zheng, H. Liu, X. Zhang, Z. Guo, B. Xu, *Journal of the American Chemical Society* **2004**, 126, 9938 – 9939.
- [305] J. Xie, C. Xu, Z. Xu, Y. Hou, K. L. Young, S. X. Wang, N. Pourmond, S. Sun, *Chemistry of Materials* **2006**, 18, 5401 – 5403.
- [306] M. D. Shultz, J. U. Reveles, S. N. Khanna, E. E. Carpenter, *Journal of the American Chemical Society* **2007**, 129, 2482 – 2487.
- [307] C. G. Pierpont, C. W. Lange, *"The Chemistry of Transition Metal Complexes Containing Catechol and Semiquinone Ligands"*, John Wiley & Sons, Inc., Hoboken, NJ, USA, **2007**.
- [308] B. P. Binks, *Current Opinion in Colloid & Interface Science* **2002**, 7, 21 – 41.
- [309] B. J. Park, T. Brugarolas, D. Lee, *Soft Matter* **2011**, 7, 6413.
- [310] L. Botto, E. P. Lewandowski, M. Cavallaro, K. J. Stebe, *Soft Matter* **2012**, 8, 9957.
- [311] Q. Guo, X. Teng, S. Rahman, H. Yang, *Journal of the American Chemical Society* **2003**, 125, 630 – 631.
- [312] I. Langmuir, *Journal of the Franklin Institute* **1934**, 218, 143 – 171.
- [313] H. Riegler, K. Spratte, *Thin Solid Films* **1992**, 210-211, 9 – 12.
- [314] J. Rother, Dissertation, "Dynamics and mechanics of adherent cells in the context of environmental cues", Georg-August-University Göttingen, Göttingen, **2014**.

- [315] M. Tarantola, A. Pietuch, D. Schneider, J. Rother, E. Sunnick, C. Rosman, S. Pierrat, C. Sönnichsen, J. Wegener, A. Janshoff, *Nanotoxicology* **2011**, *5*, 254 – 268.
- [316] Y. Zhang, N. Kohler, M. Zhang, *Biomaterials* **2002**, *23*, 1553 – 1561.
- [317] X. Jiang, A. Musyanovych, C. Röcker, K. Landfester, V. Mailänder, G. U. Nienhaus, *Nanoscale* **2011**, *3*, 2028.
- [318] H.-m. Ding, Y.-q. Ma, *Nanoscale* **2012**, *4*, 1116.
- [319] W. Römer, L. Berland, V. Chambon, K. Gaus, B. Windschiegl, D. Tenza, Aly, Mohamed R. E., V. Fraissier, J.-C. Florent, D. Perrais *et al.*, *Nature* **2007**, *450*, 670 – 675.
- [320] P. R. Leroueil, S. Hong, A. Mecke, J. R. Baker, B. G. Orr, Banaszak Holl, Mark M., *Accounts of Chemical Research* **2007**, *40*, 335 – 342.
- [321] Y.-C. Li, Y.-S. Lin, P.-J. Tsai, C.-T. Chen, W.-Y. Chen, Y.-C. Chen, *Analytical Chemistry* **2007**, *79*, 7519 – 7525.
- [322] P. Sharma, A. Singh, S. C. Brown, N. Bengtsson, G. A. Walter, S. R. Grobmyer, N. Iwakuma, S. Santra, E. W. Scott, B. M. Moudgil, *624*, 67 – 81.
- [323] X. Wu, T. Ming, X. Wang, P. Wang, J. Wang, J. Chen, *ACS Nano* **2010**, *4*, 113 – 120.
- [324] H. Jans, Q. Huo, *Chemical Society Reviews* **2012**, *41*, 2849.
- [325] C. Xu, G. A. Tung, S. Sun, *Chemistry of Materials* **2008**, *20*, 4167 – 4169.
- [326] D. Weishaupt, V. D. Koechli, B. Marineck, "Wie funktioniert MRI. Eine Einführung in Physik und Funktionsweise der Magnetresonanzbildgebung", Springer Berlin Heidelberg, Berlin, Heidelberg, **2009**.
- [327] P. C. Lauterbur, *Nature* **1973**, *242*, 190 – 191.
- [328] A. P. Koretsky, A. C. Silva, *NMR in Biomedicine* **2004**, *17*, 527 – 531.
- [329] D. Pan, S. D. Caruthers, A. Senpan, A. H. Schmieder, S. A. Wickline, G. M. Lanza, *Wiley Interdisciplinary Reviews: Nanomedicine and Nanobiotechnology* **2011**, *3*, 162 – 173.
- [330] Y.-K. Peng, C.-W. Lai, C.-L. Liu, H.-C. Chen, Y.-H. Hsiao, W.-L. Liu, K.-C. Tang, Y. Chi, J.-K. Hsiao, K.-E. Lim *et al.*, *ACS Nano* **2011**, *5*, 4177 – 4187.
- [331] Z. Zhen, *Theranostics* **2012**, *2*, 45 – 54.
- [332] Z. Li, P. W. Yi, Q. Sun, H. Lei, H. Li Zhao, Z. H. Zhu, S. C. Smith, M. B. Lan, Lu, Gao Qing Max, *Advanced Functional Materials* **2012**, *22*, 2387 – 2393.
- [333] K. C.-F. Leung, S. Xuan, X. Zhu, D. Wang, C.-P. Chak, S.-F. Lee, W. K.-W. Ho, B. C.-T. Chung, *Chemical Society Reviews* **2012**, *41*, 1911 – 1928.
- [334] H. Cai, K. Li, M. Shen, S. Wen, Y. Luo, C. Peng, G. Zhang, X. Shi, *Journal of Materials Chemistry* **2012**, *22*, 15110 – 15120.
- [335] M. Yang, K. Cheng, S. Qi, H. Liu, Y. Jiang, H. Jiang, J. Li, K. Chen, H. Zhang, Z. Cheng, *Biomaterials* **2013**, *34*, 2796 – 2806.
- [336] K. C. Briley-Saebo, V. Mani, F. Hyafil, J.-C. Cornily, Z. A. Fayad, *Magnetic Resonance in Medicine* **2008**, *59*, 721 – 730.
- [337] Y.-W. J. Wang, *Quant Imaging Med Surg* **2011**, *1*, 35 – 40.
- [338] J. Zhu, Y. Lu, Y. Li, J. Jiang, L. Cheng, Z. Liu, L. Guo, Y. Pan, H. Gu, *Nanoscale* **2014**, *6*, 199.
- [339] A. Radomski, P. Jurasz, D. Alonso-Escolano, M. Drews, M. Morandi, T. Malinski, M. W. Radomski, *British journal of pharmacology* **2005**, *146*, 882 – 893.

- [340] R. D. Ross, L. E. Cole, Tilley, Jennifer M. R., R. K. Roeder, *Chemistry of Materials* **2014**, *26*, 1187 – 1194.
- [341] NIST Physics Laboratory Home Page, NIST Standard Reference Database 126, <http://www.nist.gov/pml/data/xraycoef/> (accessed 10.07.2014).
- [342] P. A. Jackson, Rahman, Wan Nordiana W. Abd., C. J. Wong, T. Ackerly, M. Geso, *European Journal of Radiology* **2010**, *75*, 104 – 109.
- [343] N. Yusa, M. Jiang, K. Mizuno, M. Uesaka, *Radiological Physics and Technology* **2009**, *2*, 33 – 39.
- [344] K. E. Kellar, D. K. Fujii, W. Gunther, K. C. Briley-Saebo, M. Spiller, S. H. Koenig, *Magnetic Resonance Materials in Physics, Biology and Medicine* **1999**, *8*, 207 – 213.
- [345] S. H. Koenig, K. E. Kellar, *Magnetic Resonance in Medicine* **1995**, *34*, 227 – 233.
- [346] L. Landgraf, P. Ernst, I. Schick, O. Köhler, H. Oehring, W. Tremel, I. Hilger, *Biomaterials* **2014**, *35*, 6986 – 6997.
- [347] L. Haslauer, I. Müller, P. Ernst, M. Schäfer, I. Schick, O. Köhler, H. Oehring, T. Basché, C. Sönnichsen, W. Tremel *et al.*, *Beilstein Journal of Nanotechnology* **2014**, *submitted*.
- [348] R. André, F. Natálio, W. Tremel in *New and Future Developments in Catalysis* (Ed.: S. L. Suib), Elsevier, Amsterdam, **2013**.
- [349] T. Cedervall, I. Lynch, S. Lindman, T. Berggård, E. Thulin, H. Nilsson, K. A. Dawson, S. Linse, *Proceedings of the National Academy of Sciences* **2007**, *104*, 2050 – 2055.
- [350] M. P. Monopoli, D. Walczyk, A. Campbell, G. Elia, I. Lynch, F. Baldelli Bombelli, K. A. Dawson, *Journal of the American Chemical Society* **2011**, *133*, 2525 – 2534.
- [351] M. Rahman, S. Laurent, N. Tawil, L. Yahia, M. Mahmoudi (Eds.) *Springer Series in Biophysics*", Springer Berlin Heidelberg, Berlin, Heidelberg, **2013**.
- [352] L. Vroman, A. L. Adams, G. C. Fischer, P. C. Munoz, *Blood* **1980**, *55*, 156 – 159.
- [353] D. Walczyk, F. B. Bombelli, M. P. Monopoli, I. Lynch, K. A. Dawson, *Journal of the American Chemical Society* **2010**, *132*, 5761 – 5768.
- [354] E. Casals, T. Pfaller, A. Duschl, G. J. Oostingh, V. F. Puentes, *Small* **2011**, *7*, 3479 – 3486.
- [355] S. Milani, F. Baldelli Bombelli, A. S. Pitek, K. A. Dawson, J. Rädler, *ACS Nano* **2012**, *6*, 2532 – 2541.
- [356] M. Rahman, S. Laurent, N. Tawil, L. Yahia, M. Mahmoudi in *Springer Series in Biophysics* (Eds.: M. Rahman, S. Laurent, N. Tawil, L. Yahia, M. Mahmoudi), Springer Berlin Heidelberg, Berlin, Heidelberg, **2013**.
- [357] N. A. Kotov, *Science* **2010**, *330*, 188 – 189.
- [358] C. H. Liu, Z. D. Zhou, X. Yu, B. Q. Lv, J. F. Mao, D. Xiao, *Inorganic Materials* **2008**, *44*, 291 – 295.
- [359] T. Zhou, B. Wu, D. Xing, *Journal of Materials Chemistry* **2011**, *22*, 470 – 477.
- [360] J. Shin, R. M. Anisur, M. K. Ko, G. H. Im, J. H. Lee, I. S. Lee, *Angewandte Chemie International Edition* **2009**, *48*, 321 – 324.
- [361] S. V. Patwardhan, F. S. Emami, R. J. Berry, S. E. Jones, R. R. Naik, O. Deschaume, H. Heinz, C. C. Perry, *Journal of the American Chemical Society* **2012**, *134*, 6244 – 6256.
- [362] V. Puddu, C. C. Perry, *ACS Nano* **2012**, *6*, 6356 – 6363.
- [363] V. Puddu, C. C. Perry, *Langmuir* **2014**, *30*, 227 – 233.

- [364] T. Cedervall, I. Lynch, M. Foy, T. Berggård, S. C. Donnelly, G. Cagney, S. Linse, K. A. Dawson, *Angewandte Chemie International Edition* **2007**, *46*, 5754 – 5756.
- [365] F. D. Sahné, C. Scoglio, J. Riviere, D. Roccatano, *PLoS ONE* **2013**, *8*, e64690.
- [366] F. Manea, F. B. Houillon, L. Pasquato, P. Scrimin, *Angewandte Chemie* **2004**, *43*, 6165 – 6169.
- [367] R. Bonomi, F. Selvestrei, V. Lombardo, C. Sissi, S. Polizzi, F. Mancin, U. Tonellato, P. Scrimin, *Journal of American Chemical Society* **2008**, *130*, 15744 – 15745.
- [368] L. Pasquato, F. Rancan, P. Scrimin, F. Mancin, C. Frigeri, *Chemical Communications* **2000**, 2253 – 2254.
- [369] D. Kisailus, M. Najarian, J. C. Weaver, D. E. Morse, *Advanced Materials* **2005**, *17*, 1234 – 1239.
- [370] Y. Lin, J. Ren, X. Qu, *Advanced Materials* **2014**, DOI: 10.1002/adma.201400238.
- [371] W. Luo, C. Zhu, S. Su, Di Li, Y. He, Q. Huang, C. Fan, *ACS Nano* **2012**, *4*, 7451 – 7458.
- [372] M. Comotti, C. Della Pina, R. Matarrese, M. Rossi, *Angewandte Chemie International Edition* **2004**, *43*, 5812 – 5815.
- [373] M. Comotti, C. Della Pina, E. Falletta, M. Rossi, *Advanced Synthesis & Catalysis* **2006**, *348*, 313 – 316.
- [374] W. He, Y.-T. Zhou, W. G. Wamer, X. Hu, X. Wu, Z. Zheng, M. D. Boudreau, J.-J. Yin, *Biomaterials* **2013**, *34*, 765 – 773.
- [375] S. Wang, W. Chen, A.-L. Liu, L. Hong, H.-H. Deng, X.-H. Lin, *ChemPhysChem* **2012**, *13*, 1199 – 1204.
- [376] Y. Jv, B. Li, R. Cao, *Chemical Communications* **2010**, *46*, 8017.
- [377] H. Fenton, *Chemistry News* **1876**, *33*, 190.
- [378] H. Fenton, *Journal of the Chemical Society, Faraday Transactions* **1894**, *65*, 899.
- [379] L. Gao, J. Zhuang, L. Nie, J. Zhang, Y. Zhang, N. Gu, T. Wang, J. Feng, D. Yang, S. Perrett *et al.*, *Nature Nanotechnology* **2007**, *2*, 577 – 583.
- [380] P. D. Josephy, Eling, T., R. P. Mason, *The Journal of Biological Chemistry* **1981**, *257*, 3669 – 3675.
- [381] X. Sun, S. Guo, C.-S. Chung, W. Zhu, S. Sun, *Advanced Materials* **2013**, *25*, 132 – 136.
- [382] D. Xu, Z. Liu, H. Yang, Q. Liu, J. Zhang, J. Fang, S. Zou, K. Sun, *Angewandte Chemie International Edition* **2009**, *48*, 4217 – 4221.
- [383] D.-W. Han, S. C. Hong, J. H. Lee, J. Lee, H. Y. Kim, J. Y. Park, Cho, J. Lee, *International Journal of Nanomedicine* **2011**, 3219.
- [384] C. Hoskins, L. Wang, W. Cheng, A. Cuschieri, *Nanoscale Research Letters* **2012**, *7*, 77.
- [385] J. A. Khan, B. Pillai, T. K. Das, Y. Singh, S. Maiti, *ChemBioChem* **2007**, *8*, 1237 – 1240.
- [386] E. C. Cho, J. Xie, P. A. Wurm, Y. Xia, *Nano Letters* **2009**, *9*, 1080 – 1084.
- [387] A. Villanueva, M. Cañete, A. G. Roca, M. Calero, S. Veintemillas-Verdaguer, C. J. Serna, del Puerto Morales, María, R. Miranda, *Nanotechnology* **2009**, *20*, 115103.
- [388] A. Verma, F. Stellacci, *Small* **2010**, *6*, 12 – 21.
- [389] Z.-J. Zhu, P. S. Ghosh, O. R. Miranda, R. W. Vachet, V. M. Rotello, *Journal of the American Chemical Society* **2008**, *130*, 14139 – 14143.
- [390] S. Crouch, R. Kozlowski, K. J. Slater, J. Fletcher, *Journal of Immunological Methods* **1993**, *160*, 81 – 88.

- [391] Y. Eguchi, S. Shimizu, Y. Tsujimoto, *Cancer Research* **1997**, *57*, 1835 – 1840.
- [392] A. Stebbing, *Science of The Total Environment* **1982**, *22*, 213 – 234.
- [393] E. J. Calabrese, L. A. Baldwin, *Annual Review of Pharmacology and Toxicology* **2003**, *43*, 175 – 197.
- [394] B. D. Chithrani, A. A. Ghazani, W. Chan, *Nano Letters* **2006**, *6*, 662 – 668.
- [395] W. Jiang, Kim, Betty Y. S., J. T. Rutka, Chan, Warren C. W., *Nature Nanotechnology* **2008**, *3*, 145 – 150.
- [396] J. Rejman, V. Oberle, I. S. Zuhorn, D. Hoekstra, *Biochemical Journal* **2004**, *377*, 159 – 169.
- [397] A. L. Doiron, B. Clark, K. D. Rinker, *Biotechnology and Bioengineering* **2011**, *108*, 2988 – 2998.
- [398] A. Chomposor, K. Saha, P. S. Ghosh, D. J. Macarthy, O. R. Miranda, Z.-J. Zhu, K. F. Arcaro, V. M. Rotello, *Small* **2010**, *6*, 2246 – 2249.
- [399] S. M. Hussain, *Toxicological Sciences* **2006**, *92*, 456 – 463.
- [400] A. A. Gilad, P. Walczak, M. T. McMahon, H. B. Na, J. H. Lee, K. An, T. Hyeon, van Zijl, Peter C.M., J. W. Bulte, *Magnetic Resonance in Medicine* **2008**, *60*, 1 – 7.
- [401] K. Koll, Dissertation, "Functionalization and Characterization of Magnetic Nanoparticles for Biomedical Applications", Johannes Gutenberg-Universität, Mainz, **2011**.
- [402] S. Tenzer, D. Docter, S. Rosfa, A. Wlodarski, J. Kuharev, A. Rekić, S. K. Knauer, C. Bantz, T. Nawroth, C. Bier *et al.*, *ACS Nano* **2011**, *5*, 7155 – 7167.
- [403] J. Kuharev, S. Tenzer, "ISOQuant", Mainz, **2009-2014**.



## Curriculum Vitae

### ■ PERSÖNLICHE DATEN

Geburtstag: 12.01.1988

Geburtsort: Wiesbaden

Staatsangehörigkeit: Deutsch

### ■ AUSBILDUNG

10/2011 – heute Promotion im Fachbereich Chemie  
Johannes Gutenberg-Universität Mainz

10/2006 – 07/2011 Studium der Chemie  
Johannes Gutenberg-Universität Mainz  
Abschluss: Diplom

09/2004 – 06/2006 Internatsschule Schloss Hansenberg, Johannisberg  
Abschluss: Abitur

08/1998 – 07/2003 Gymnasium Eltville, Eltville am Rhein

09/1994 – 07/1998 Freiherr-vom-Stein-Grundschule, Eltville am Rhein

### ■ WISSENSCHAFTLICHER LEBENS LAUF

10/2011 – heute Forschung im Rahmen der Doktorarbeit an der Johannes  
Gutenberg-Universität Mainz in Kollaboration mit:  
Georg-August-Universität Göttingen, Friedrich Schiller  
Universität Jena, MPI für Polymerforschung Mainz,  
Universitätsmedizin der Johannes Gutenberg-Universität Mainz

04/2014 – heute Stipendium der Graduate School of Excellence Mainz *MAINZ*

04/2012 – 03/2014 Chemiefonds-Doktoranden-Stipendium des Verbandes der  
Chemischen Industrie VCI

04/2012 – 03/2014 Kollegiatin der Graduate School of Excellence *MAINZ*

01/2012 – 03/2012 Stipendium der Graduate School of Excellence Mainz *MAINZ*

06/2012 MLP Förderpreis der Chemie 2012 als Auszeichnung für die  
Diplomarbeit "Funktionalisierte Au@MnO-Janus-Partikel"

01/2011 – 07/2011 Forschung im Rahmen der Diplomarbeit an der Johannes  
Gutenberg-Universität Mainz

08/2009 – 03/2010 ISAP-DAAD-Stipendium für einen Forschungsaufenthalt an der  
*University of Toronto*, Toronto, Ontario, Kanada